University of Southampton

Faculty of Engineering and Physical Sciences

Optoelectronics Research Centre

High-Energy Ultrafast Ytterbium-doped Fibre Laser Technologies

by

Jikun Yan

Thesis for the degree of Doctor of Philosophy

March 2026

University of Southampton

Abstract

Faculty of Engineering and Physical Sciences

Optoelectronics Research Centre

Degrees for Doctor of Philosophy

High-Energy Ultrafast Ytterbium-Doped Fibre Laser Technologies

by

Jikun Yan

This thesis investigates the design and dynamics of high-energy ultrafast fibre lasers, with a particular emphasis on Mamyshev oscillators (MOs). Steady-state (SS) and dynamic (Dy) models based on rate equations were developed to analyse both the steady-state output and the transient evolution of these systems. Through systematic modelling and experimental validation, practical strategies were established for optimizing filter separation, gain distribution, and cavity architecture, enabling femtosecond pulse generation with energies up to the hundreds of nanojoules directly from oscillators. Beyond oscillator optimization, the work extends high-energy fibre lasers through the integration of advanced fibre technologies. Hollow-core nested antiresonant nodeless fibres (NANFs) were implemented both intracavity and extracavity. Within the cavity, NANF provided a flexible means of reducing the repetition rate to the megahertz regime, yielding more than 20% enhancement in pulse energy. Outside the cavity, they acted as efficient delivery channels and linear compressors, achieving stable compression of ~500 nJ MO pulses to sub-50 fs durations with ~86% overall efficiency, while avoiding nonlinear spectral distortions. These results underline the potential of NANFs as a route toward fully fibre-integrated, high-energy ultrafast pulse generation and delivery. The thesis also addresses the critical challenge of initiating mode-locking in MOs. Using dispersive Fourier transform (DFT), the spectral evolution from seed injection to stable mode-locking was directly captured under different initial inversion conditions. This approach revealed the pulse buildup dynamics, including the role of gain competition and noise evolution, and provided practical guidelines for achieving robust single-pulse operation. Finally, multicore fibres (MCFs) were explored as a prospective route for further pulse energy scaling. By enabling coherent coupling across multiple cores, MCFs offer a promising strategy to surpass the limitations of single-core designs while preserving beam quality and stability. To sum up, the combination of validated theoretical models, targeted experimental demonstrations, and the integration of advanced fibre platforms establishes a comprehensive framework for the development of next-generation high-energy ultrafast fibre lasers. The findings not only deepen the understanding of Mamyshev oscillators but also chart practical pathways toward their deployment in scientific, industrial, and biomedical applications.

Table of Contents

Table of Tables

Table of Figures

Research Thesis: Declaration of Authorship

Print name: Jikun Yan

Title of thesis: High-Energy Ultrafast Ytterbium-Doped Fibre Lasers

I declare that this thesis and the work presented in it are my own and has been generated by me as the result of my own original research.

I confirm that:

1. This work was done wholly or mainly while in candidature for a research degree at this University;
2. Where any part of this thesis has previously been submitted for a degree or any other qualification at this University or any other institution, this has been clearly stated;
3. Where I have consulted the published work of others, this is always clearly attributed;
4. Where I have quoted from the work of others, the source is always given. With the exception of such quotations, this thesis is entirely my own work;
5. I have acknowledged all main sources of help;
6. Where the thesis is based on work done by myself jointly with others, I have made clear exactly what was done by others and what I have contributed myself;

Parts of this work have been published as: [see list of publications]

Signature: ..... Date:.....

Acknowledgements

As I reach the conclusion of writing my thesis, I am struck by the realization that my student life is truly coming to an end. Four years ago, when my master's advisor, Professor Jiahui Peng, enthusiastically introduced me to the opportunity of pursuing a PhD at the University of Southampton with funding from the China Scholarship Council (CSC), I simply saw it as a chance to explore the world while I was still young. I could not have imagined how profoundly this advice would shape the course of my life. The influence of both my supervisor and the CSC has been invaluable. They planted the seeds of my PhD journey, and I extend my heartfelt gratitude to them.

I arrived in Southampton while the global COVID-19 pandemic was still ongoing. Given the unusual circumstances and the unfamiliarity of a new country, the early days were inevitably challenging. However, I was fortunate to encounter many wonderful people. Yi Sui and Zishen Fu, who were on the same flight before I even set foot in the UK, have remained close friends and companions through difficult times. On my very first day at 300 Burgess Road, I was welcomed with a generous dinner prepared by Dr. Chuang Sun, Dr. Xiangyu Qu, and Dr. Xin Liu. Along with Mr. Chao Wang and Dr. Peng Jiang, they have offered me invaluable support and guidance throughout my time here. I will always remember the festivals and countless barbecues we shared together.

My first group meeting was held online, and I could hardly have foreseen the strong bonds I would later form with colleagues I initially knew only through a screen. My supervisor, Professor David Richardson, is a remarkably wise and inspiring mentor. I have always admired his personal integrity and ability, and I was particularly touched by his advice to take time to connect with the people and culture of Southampton. Despite his extremely busy schedule, and even after joining Microsoft, Professor Richardson continued to provide me with valuable guidance and feedback. I am deeply grateful not only for his supervision but also for his vision in fostering an open, inclusive, and collaborative research group that brought together such outstanding colleagues.

I would also like to thank Professor Di Lin, Dr. Yongmin Jung, and Dr. Lin Xu for their guidance and pragmatic advice, which has greatly influenced my own way of thinking. I am further indebted to my group members Dr. Qiang Fu, Dr. Sijing Liang, Dr. Duanyang Xu, Dr. Yudi Wu, Dr. Kunhao Ji, Dr. Xin Huang, and also to Professor Francesco Poletti, Professor Johan Nilsson, Dr. Meng Ding, Dr. Hao Liu, Dr. Hans Christian Mulvad, Dr. Kyle Bottrill, and Dr. Qiubai Yang from the ORC for their assistance, both in experiments and academic discussions.

Above all, I owe my deepest gratitude to my parents. For them, who had never flown before, traveling across eight time zones was a challenge, and my absence made it hard to meet the

expectations of a son in both physical and emotional presence. Yet, they have always given me unconditional support and provided a solid emotional foundation. I am also grateful to my extended family back home, who supported my parents both emotionally and practically during these years.

There is an old Chinese saying, “At thirty, one should stand firm” (三十而立), meaning that by the age of thirty, one is expected to have achieved something in life. Perhaps obtaining a doctoral degree can be regarded as a milestone on my academic path, signifying my formal entry into the realm of scholarship. Yet I still feel that it is not enough. For me, living within the campus environment for so long has indeed been a truly rewarding experience, but this joy has come at the cost of a certain detachment from wider society, slowing my steps in engaging with and understanding the world. I am by no means denying the value of my doctoral years; on the contrary, I cherish them deeply, as they have provided me with a rare opportunity to continue my pursuit of truth. Four years ago, when I applied for my PhD, I envisioned becoming an independent researcher. Today, I find myself very close to that goal. Now, the key to the future is in my hands, and I look forward with great anticipation to the path ahead.

Definitions and Abbreviations

CW ..... Continuous-wave

MOPA ..... Master oscillator power amplifier

CPA ..... Chirped pulse amplification

MO ..... Mamyshev oscillator

SPM ..... Self-phase modulation

AOM ..... Acousto-optic modulator

HCF ..... Hollow-core fibre

NANF ..... Nested antiresonant nodeless fibre

MCF ..... Multicore fibre

TS-DFT ..... Time-stretched dispersive Fourier transform

DFT ..... Dispersive Fourier transform

SS ..... Steady-state

Dy ..... Dynamic

FEL ..... Free-electron laser

YDFL ..... Ytterbium-doped fibre laser

LMA ..... Large-mode-area

KLM ..... Kerr-lens mode locking

SPM ..... Self-phase modulation

FWM ..... Four-wave mixing

NPR ..... Nonlinear polarization rotation

NPE ..... Nonlinear polarization evolution

PM ..... Polarization-maintaining

NOLM ..... Nonlinear optical loop mirror

NALM ..... Nonlinear amplifying loop mirror

NPS ..... Nonlinear phase shift

SESAM ..... Semiconductor saturable absorber mirror

CNT ..... Carbon nanotube

DCF ..... Double-cladding fibre

PCF ..... Photonic crystal fibre

CBC ..... Coherent beam combining

GVD ..... group-velocity dispersion

ANDi ..... all-normal-dispersion

TL ..... Transform-limited

YDF ..... ytterbium-doped fibre

SAM ..... Saturable absorber mirror

STML ..... Spatiotemporal mode-locking

MMF ..... Multimode fibre

SRS ..... Stimulated Raman scattering

TOD ..... Third-order dispersion

NLSE ..... Nonlinear Schrödinger equation

GNLSE ..... Generalized nonlinear Schrödinger equation

DMS ..... Dispersion-managed soliton

CGLE ..... Complex Ginzburg-Landau equation

SSFM ..... Split-step Fourier method

RK4 ..... Fourth-order Runge-Kutta

PF ..... Passive fibre

FFT ..... Finite-Fourier-transfrom

MFD ..... Mode field diameter

NA ..... Numerical aperture

SLD ..... Superluminescent diode

LD ..... Laser diode

BPF ..... Band-pass filter

WHP ..... Half-wave plate

ISO ..... Isolator

ACF ..... Autocorrelation function

FWHM..... Full-width at half-maximum

RF..... Radio-frequency

SNR ..... Signal-to-noise ratio

SMF ..... Single mode fibre

GDD ..... Group delay dispersion

YDFA..... Ytterbium-doped fibre amplifier

CM..... Chirped mirror

SLM ..... Spatial light modulator

PB-HCF..... Bandgap HCF

OSA ..... Optical spectrum analyzer

MMF ..... Multimode fibre

DSF..... Dispersion-shifted fibre

EOM ..... Electro-optic modulator

LC..... Liquid crystal

LCoS..... Liquid crystal on silicon

CMOS ..... Complementary metal-oxide-semiconductor

BS..... Beam splitter

Chapter 1 Introduction

1.1 Motivation

The development of ultrafast fibre lasers has long been driven by both frontier science and real-world applications. Compact and robust femtosecond fibre sources now underpin diverse fields, from nonlinear multiphoton microscopy for deep-tissue biological imaging, to precision micromachining of brittle and transparent materials, to femtosecond-laser-assisted mass spectrometry[1-4]. In all these cases, the decisive advantage of ultrashort pulses lies in their ability to deliver high peak intensities with minimal thermal load, enabling interactions and processing outcomes that conventional continuous-wave (CW) or nanosecond lasers cannot achieve. At the same time, these applications highlight stringent demands on pulse energy, duration, and repetition rate. For example, lowering repetition rates helps suppress thermal accumulation in micromachining and reduces photodamage also improve imaging depth in biomedical imaging, while avoiding space-charge saturation in mass spectrometry[4-7].

Typically, high-energy ultrafast fibre lasers are realised through a master oscillator power amplifier (MOPA) architecture, combining a femtosecond oscillator with chirped pulse amplification (CPA) stages. While this system is stable and mature, gain narrowing limits the compressed pulse duration to ~200 fs, and multiple amplification stages are often required to reach megawatt-level peak powers, at the cost of increased complexity and reduced robustness. The Mamyshev oscillator (MO) offers a breakthrough alternative. By incorporating offset spectral filters that act as an artificial saturable absorber with a near-100% effective modulation depth, the Mamyshev oscillator enables the direct generation of sub-30 fs, microjoule-level pulses with peak powers exceeding 10 MW, approaching or even surpassing the performance of titanium–sapphire oscillators[8, 9]. This innovation redefines the role of the fibre oscillator, transforming it from a seed source into a standalone high-energy femtosecond platform. It also expands the scope of ultrafast fibre lasers toward applications that prioritise high peak power over high average power, thereby stimulating widespread research interest.

As a compact high-energy femtosecond source, the MO offers unique advantages but also poses design constraints. Nonlinear effects such as self-phase modulation (SPM) and normal dispersion are both essential to MO operation and restrictive for its design space, making optimisation a delicate balance of competing effects. In contrast, the MOPA framework provides greater design flexibility through its amplification stages, where elements such as acousto-optic modulators (AOMs) can adjust the repetition rate or tailor the output. It is therefore natural to ask

how the compactness and intrinsic high-energy capability of the MO can be combined with the versatility of broader fibre laser design strategies.

Recent advances in fibre technology provide promising routes. A kind of hollow-core fibre (HCF), hollow-core nested antiresonant nodeless fibres (NANFs), with their broadband guidance, low attenuation, and unique dispersion properties[10], enable intracavity repetition-rate reduction and efficient energy extraction, while also offering extracavity benefits for pulse delivery and nearly linear compression. This flexibility makes them an attractive platform for adapting oscillator design to application-specific requirements. Multicore fibres (MCFs) represent another route, enabling coherent combination across multiple cores to scale pulse energy beyond single-core limits and to generate novel structured beams. In parallel, time-stretched dispersive Fourier transform (TS-DFT), also called dispersive Fourier transform (DFT) provides a powerful diagnostic tool for probing MO startup dynamics, offering insights that can guide reliable single-pulse operation and improved system robustness.

These considerations motivate the central theme of this thesis: advancing high-energy ultrafast fibre lasers through the combined development of MOs, advanced fibre technologies such as NANFs and MCFs, and real-time diagnostics of nonlinear dynamics.

1.2 Outline of thesis

The thesis is organized as follows:

Part I (Chapters 1-2): Background and motivation. Chapter 1 states the motivation, frames the problem of high-energy ultrafast fibre lasers, and outlines the thesis structure and contributions. Chapter 2 provides the background: evolution of laser and fibre-laser technologies, ultrafast operation in fibres, mode-locking mechanisms, pulse dynamics, and the development of the MO, together with enabling fibre platforms (HCF, MCF).

Part II (Chapters 3-4): Theory and modelling framework. Chapter 3 develops the theoretical basis for ultrafast pulse propagation in fibres and reviews pulse-evolution regimes including solitons, dissipative solitons, and similaritons, culminating in the physical mechanism of the Mamyshev oscillator as a filtering-based mode-locking scheme characterized by a step-like transmission response. Chapter 4 presents the simulation toolkit used throughout the thesis: steady-state (SS) and dynamic (Dy) rate-equation models, split-step Fourier propagation, and gain/dispersion modelling used to predict operating windows and guide design.

Part III (Chapters 5-7): High-energy MO design, implementation, and compression. Chapter 5 reports the 20 MHz MO design and construction, simulation-experiment comparisons, and optimization guided by the modelling framework. Chapter 6 shows further investigates intracavity

integration of NANF to reduce repetition rate to the ~1 MHz class and to enhance pulse energy, establishing a 1 MHz operation within the MO architecture. Chapter 7 demonstrates extracavity use of NANF for high-efficiency, flexible, and fidelity-preserving compression of MO pulses, together with fibre-based energy delivery. The focus is on linear, low-distortion compression performance and system-level efficiency.

Part IV (Chapters 8-9): Technology reserve and forward directions. Chapter 8 presents DFT-based, seed-injected startup studies of the MO, providing initial, real-time observations of pulse buildup under controlled initial conditions and informing reliable single-pulse operation. Chapter 9 explores MCF coupling as a prospective route for coherent scaling and structured-beam capabilities, establishing an experimental platform and design considerations for future high-energy fibre systems.

Part V (Chapters 10):Chapter 10 concludes the thesis, summarizing the main findings and outlining future work, with emphasis on integrating MO, NANF, and MCF technologies and on leveraging real-time diagnostics for robust, application-oriented ultrafast sources.

Chapter 2 Background

2.1 Evolution of laser technologies

The invention of the ruby laser by Theodore Maiman in 1960 marked the beginning of the laser era[11], demonstrating the principle of stimulated emission in practice[12]. While ruby lasers are now of mainly historical interest, they established the foundation for all subsequent developments. The helium-neon (He-Ne) laser followed in 1961[13], offering stable CW emission at 632.8 nm and becoming the archetypal "red laser" in laboratories and classrooms before being displaced by compact diode lasers[14-17]. By 1964, the neodymium-doped yttrium aluminum garnet (Nd:YAG) laser had established itself as a robust solid-state source[18], combining efficiency and good beam quality[19, 20] with broad utility in industrial processing and medicine[21-24]. In the same year, the carbon dioxide (CO_2) laser provided efficient infrared output at 10.6 μm[25] and reached power levels in the tens of kilowatts[26, 27], making it the workhorse for heavy-duty materials processing, particularly of non-metals[21, 28-30]. During the 1970s, excimer lasers emerged as pulsed ultraviolet sources based on rare-gas halide compounds[31, 32]. Their short wavelengths proved indispensable in semiconductor lithography and also revolutionized refractive eye surgery[33-38]. In parallel, dye lasers introduced the first broadly tunable platform[39-41] and enabled picosecond and femtosecond pulse generation[42-44], but were eventually superseded by titanium-doped sapphire (Ti:sapphire) lasers in the 1990s[45]. First demonstrated in 1986[46], Ti:sapphire combined solid-state reliability with an exceptionally broad gain bandwidth, rapidly establishing itself as the benchmark platform for femtosecond pulse generation and enabling pulse durations of only a few femtoseconds[47, 48]. It also remains the medium of choice for petawatt-class lasers[49, 50]. Meanwhile, semiconductor diode lasers, first demonstrated in the 1960s[51, 52], matured into compact and efficient sources. They now dominate in production volume, serve numerous consumer and industrial applications, and provide the primary pump source for both solid-state and fibre lasers[53-55]. At the frontier of photon science, free-electron lasers (FELs), first demonstrated in the late 1970s[56], employ relativistic electron beams in undulators to generate coherent radiation across the electromagnetic spectrum, enabling unique applications in structural biology and ultrafast magnetization dynamics[57, 58]. Their reliance on kilometer-scale accelerators, however, limits them to a handful of international facilities[59].

The first fibre laser was demonstrated in the early 1960s by Snitzer and colleagues[60-62]. Subsequent advances in silica fibre fabrication, driven largely by optical telecommunications, improved fibre quality and doping techniques[63-65]. A true turning point then came in the mid-1980s with the advent of reliable semiconductor diode lasers, which provided an efficient route

to optical pumping[66]. Building on these developments, Payne and co-workers highlighted the potential of rare-earth-doped fibres, not only as laser gain media but also as highly efficient optical amplifiers, culminating in the erbium-doped fibre amplifier that transformed telecommunications[67]. At the same time, fibre-based lasers began to establish themselves more broadly, benefiting from the intrinsic advantages of the waveguide geometry[68]. The introduction of cladding-pumped fibre architectures in the late 1980s provided the first scalable route to high powers by allowing multimode pump diodes to efficiently excite single-mode fibre cores[69-71]. With the advent of high-brightness pump diodes in the 1990s[72], ytterbium emerged as the preferred dopant for power scaling, owing to its low quantum defect, tolerance to high doping concentrations, and broad absorption band[73, 74]. These advantages quickly established ytterbium-doped fibre lasers (YDFLs) as the leading platform for high-power operation. A decisive milestone was reached in 1999 with the demonstration of a single-mode YDFL delivering more than 100 W of output[75]. Continued progress in large-mode-area (LMA) fibre design, pump technology, and tandem-pumping strategies further extended performance into the kW and even 10 kW regime in CW operation[76-79]. Together, these developments firmly positioned YDFLs as a robust and effective solution for single-channel high-power lasers. This historical trajectory illustrates how successive laser platforms have fulfilled distinct scientific and technological needs, leaving enduring legacies in research, industry, and medicine. Within this broader landscape, fibre lasers have emerged as a versatile and increasingly important technology. They combine excellent beam quality with outstanding efficiency in both optical gain and electrical-to-optical conversion. Their all-fibre architecture provides compact and alignment-free operation while ensuring effective thermal management, features that distinguish them from bulk solid-state lasers. In addition, the waveguide geometry facilitates strong light-matter interactions, offering a natural platform for nonlinear optics.[68]. These combined attributes have established fibre lasers as a uniquely robust and versatile platform in modern photonics.

2.2 Ultrafast lasers

The historical trajectory of laser development was initially dominated by the pursuit of higher average power. CW solid-state and fibre lasers were scaled to the kilowatt level, enabling applications in industrial materials processing and telecommunications. Yet it soon became clear that average power alone does not grant access to the nonlinear regimes of light-matter interaction[80]. Entering these regimes, from nonlinear optics to strong-field physics with high-harmonic generation as a prominent example, depends critically on peak power, jointly determined by pulse energy and duration[81-83]. Ultrafast lasers, or more accurately, ultrafast pulse lasers, employ mode-locking techniques to produce pulses with durations in the

femtosecond (fs) or picosecond (ps) range, offered a transformative capability. Their extremely short temporal widths yield exceptionally high peak powers and enable light-matter interactions on timescales comparable to electronic and vibrational dynamics[84]. This combination not only drives nonlinear absorption and frequency conversion but also minimizes thermal diffusion, allowing high-precision material processing with negligible collateral damage[85].

The concept of mode-locking was first demonstrated in 1964 on Nd:glass lasers by Hargrove and his colleagues[86]. A decade later, in 1972, dye lasers exploited their broad gain bandwidth to reach ~1.5 ps pulses[43]. These early experimental advances were accompanied by significant theoretical progress. Kuizenga and Siegman provided the first comprehensive theory of active mode-locking, elucidating the distinct roles of amplitude and internal phase modulation in establishing phase coherence among longitudinal modes[87, 88] . Their work demonstrated that phase modulation alone can support pulse formation in homogeneously broadened lasers, challenging the conventional amplitude-gating picture. Building on this foundation, Haus later formulated the theory of forced mode-locking, introducing a master-equation approach that unified time- and frequency-domain descriptions of mode-locked lasers and paved the way for subsequent developments in passive and nonlinear mode-locking regimes [89]. These theoretical foundations proved essential for the later transition toward passive mode-locking schemes, which ultimately enabled the dramatic pulse-shortening achieved in dye and Ti:sapphire lasers. Soon, in 1981, the pulse duration of dye systems was pushed into the femtosecond regime[44]. However, dye systems required complex dye circulation and gas-laser pumping, which limited their stability and practical use. In the 1980s, Ti:sapphire lasers extended this frontier: their ultrabroad gain bandwidth, spanning 660-1180 nm, supported pulses of only a few femtoseconds, approaching the optical cycle of visible light[46]. A decisive step came in 1990, when Ishida et al. demonstrated passive mode-locking with an intracavity saturable absorber dye, producing stable 190 fs pulses[90], and shortly thereafter Sibbett's group achieved 60 fs pulses from a Ti:sapphire laser by Kerr-lens mode locking (KLM) regme[47]. Subsequent improvements with intracavity dispersion control and chirped dielectric mirrors pushed pulse durations below 10 fs by the mid-1990s[91] and to ~5 fs in the early 2000s[48]. Ti:sapphire oscillators rapidly became the workhorses of ultrafast laboratories, providing stable femtosecond sources for spectroscopy and nonlinear optics[92, 93]. The decisive breakthrough came with CPA in the mid-1980s[94], a technique later recognized with the 2018 Nobel Prize in Physics. In CPA, an ultrashort pulse is first stretched in time to reduce its peak intensity, then safely amplified to high energy, and finally recompressed to its original femtosecond duration, enabling the amplification of femtosecond pulses to millijoule and joule energies[95, 96]. In combination with Ti:sapphire's broad gain bandwidth, CPA established a technology base that has powered advances ranging

from multiphoton microscopy[97] to frequency combs[98, 99], attosecond metrology[100], and relativistic plasma physics[101].

Yet, despite their unrivalled performance, bulk solid-state systems remained bulky, alignment-sensitive, and thermally limited, restricting their accessibility and hindering deployment beyond specialized laboratories[102, 103]. Fibre lasers, by contrast, offer intrinsic benefits for ultrafast operation: long interaction lengths enable nonlinear effects such as SPM and four-wave mixing (FWM) for pulse shaping and spectral broadening [104, 105], while the high surface-area-to-volume ratio ensures efficient thermal management at high average powers [106, 107]. These attributes allowed YDFLs to emerge as natural successors for high-energy ultrafast light sources.

The development of pulsed fibre lasers dates back to 1983, when partial mode-locking was first observed in a Nd-doped fibre laser[108]. In the following years, improved techniques enabled picosecond and even femtosecond pulses from Nd-fibre systems[109, 110]. However, interest in ultrafast Nd-doped fibres gradually diminished as other dopants with more favourable properties emerged. Ultrafast fibre lasers are now primarily based on four spectral regions: Yb-fibre lasers around 1.03 μm, Er-fibre lasers around 1.55 μm, Tm/Ho-fibre lasers around 2 μm, and Er fluoride fibre lasers around 3.0 μm. Among these, Yb-fibre systems have become the dominant platform for high-energy operation, enabled by the adoption of CPA in MOPA architectures[68]. To date, the highest pulse energy from a diffraction-limited monolithic Yb-fibre CPA system is approximately 1.7 mJ, as reported by Bingham et al.[111], while the earliest application of CPA in fibre systems can be traced back to 1993 in Er-doped fibre[112]. The development of ultrafast fibre lasers has been guided not only by the quest for higher performance but also by the need for practical utility. In many applications, specific requirements on parameters such as repetition rate, spectral bandwidth, pulse duration, and wavelength tunability have motivated tailored designs[113]. Nevertheless, the ability to increase output power, pulse energy, and peak power remains the central driver, as these ultimately define access to nonlinear and high-field regimes.

2.3 Key advances in ultrafast fibre lasers

From a technological perspective, progress in this field has been propelled by three converging directions: innovations in mode-locking mechanisms, which enabled stable femtosecond pulse generation in fibre configuration; advances in fibre design and fabrication, which provided the physical platform for scaling energy and power; and the exploration of new pulse evolution regimes, which allowed these systems to overcome fundamental limitations and reach unprecedented performance.

2.3.1 Mode-locking mechanisms

The refinement of mode-locking techniques has been central to the progress of ultrafast fibre lasers. Early demonstrations relied on active mode-locking with externally driven modulators, but the limited modulation bandwidth restricted pulse durations to the hundred-picosecond regime [114]. The need for shorter pulses and fully fibre-integrated implementations motivated the exploration of passive mode-locking schemes based on the intrinsic optical nonlinearity of fibres. In the early 1990s, this effort led to the development of Kerr-effect-based self-starting mode-locking mechanisms, including additive pulse mode-locking and, more prominently, nonlinear polarization rotation (NPR) [115, 116]. The broader framework of nonlinear polarization evolution (NPE) exploits intensity-dependent polarization changes induced by the Kerr effect, which are converted into effective amplitude modulation by polarizing elements [117]. These mechanisms enabled the direct generation of femtosecond pulses from fibre oscillators and supported higher pulse energies than those achievable with semiconductor saturable absorbers. However, NPR/NPE schemes typically rely on polarization-sensitive and often non-reciprocal elements to convert Kerr-induced polarization changes into effective amplitude modulation. As a result, they are generally less compatible with polarization-maintaining (PM) fibre architectures and tend to exhibit increased sensitivity to environmental perturbations compared to fully PM or absorber-based mode-locking schemes [118]. To overcome these drawbacks, loop-mirror geometries such as nonlinear optical loop mirrors (NOLMs) and nonlinear amplifying loop mirrors (NALMs) were developed[119-123]. By replacing free-space polarization optics with fibre interferometers, they exploit intensity-dependent phase shifts to achieve passive mode-locking while being inherently compatible with PM fibres. In particular, NALMs enhance the nonlinear phase shift (NPS) by incorporating a gain segment in the loop, lowering the threshold and improving stability. This capability motivated their widespread adoption for environmentally robust ultrafast oscillators, especially in industrial and commercial systems. Nevertheless, approaches such as incorporating Faraday rotator mirrors [115] or cross-splicing sections of PM fibre [124] have been demonstrated to mitigate group-velocity mismatch, which originates from the intrinsic birefringence of PM fibres, and thereby make NPE viable in PM fibre configurations. In parallel, semiconductor saturable absorber mirrors (SESAMs) provided a compact and user-friendly alternative, with engineered modulation depth and recovery times that offered stable, self-starting femtosecond operation[125]. SESAM-based mode-locking proved indispensable for the commercialization of ultrafast fibre lasers, although the relatively low damage threshold of semiconductor absorbers limited their use in high-energy systems. More recently, nanomaterial-based saturable absorbers have expanded the toolbox. Carbon nanotubes (CNTs) allow spectral tuning of the absorption band via their diameter and chirality, offering sub-picosecond recovery times [126], while graphene provides intrinsically broadband absorption and ultrafast carrier

recovery on the order of hundreds of femtoseconds[127]. These materials not only extend mode-locking to new spectral regions, such as 2 μm Tm/Ho-fibre lasers, but also offer higher damage tolerance and ease of integration. Together, these innovations have progressively addressed the competing demands of high pulse energy, environmental stability, and operational simplicity, thereby establishing a diverse set of mode-locking mechanisms tailored to different ultrafast fibre laser platforms.

2.3.2 Fibre Design and fabrication

In parallel, The introduction of double-cladding fibres (DCF) in the late 1980s provided the first scalable route to high powers by allowing multimode pump diodes to efficiently excite single-mode doped cores[69]. This geometry enabled brightness enhancement factors of 3-5 orders of magnitude from pump to signal[128, 129]. In the field of ultrashort pulses, an all-fibre linearly polarized CPA system using ordinary Yb-doped DCF achieved a single pulse energy of up to 112uJ and an average power of 440.6W after compression[130, 131]. The development of LMA fibres and microstructured designs such as photonic crystal fibres (PCFs) enabled effective mode areas of thousands of square micrometres, thereby suppressing nonlinear phase accumulation (B-integral) and mitigating optical damage, while preserving near-diffraction-limited beam quality. These advances allowed femtosecond fibre amplifiers to reach pulse energies beyond 1 mJ[132, 133]. The same microstructured design philosophy also inspired the first hollow-core PCFs based on photonic bandgap guidance, which demonstrated typically transmission losses of ~1 dB/km and limited spectral windows[134]. Building on this foundation, HCFs have evolved into hollow-core NANFs, which combine broad transmission windows with record-low attenuation (~0.01 dB/km at 1550 nm) [135]. In contrast to photonic bandgap fibres, which offered only narrow guidance bands and relatively high loss, HCFs provide lower loss, broader bandwidth, reduced bend sensitivity, and structural simplicity, making them attractive candidates for ultrafast fibre systems. Gas-filled HCFs, in particular, have become standard tools for nonlinear spectral broadening and pulse compression, with millijoule-level pulses compressed to below 5 fs[136]. These capabilities have established HCFs as enabling platforms for generating few-cycle driving pulses that underpin high-harmonic generation [137]. HCFs extend these capabilities by offering improved transmission performance and scalability across wavelength ranges, raising the prospect of more efficient energy delivery and pulse manipulation directly within fibre platforms. Nevertheless, many challenges remain, like integration with existing fibre architectures, and significant research is still required before HCFs can fully realize their potential. MCFs extend fibre laser scaling by integrating multiple amplification channels into a single cladding, which greatly suppresses relative phase fluctuations compared to arrays of discrete fibres. This facilitates coherent beam combining (CBC) with reduced stabilization requirements[138]. Proof-

of-principle demonstrations have shown phase-locked operation of 7-core fibres[139], while more recent rod-type MCF CPA systems have achieved hundreds of watts average power and pulse energies of several hundred microjoules in the femtosecond regime[140]. Beyond energy scaling through phase-locked combination, MCFs also enable reconfigurable structured light generation by controlling the amplitude, phase, and polarization across multiple cores, thus offering a route to high-power tailored beams for advanced applications[141]. PM fibres employ built-in stress elements to induce strong birefringence, which suppresses coupling between orthogonal polarization modes and thereby preserves a well-defined state of polarization along the fibre length[142]. For ultrafast fibre lasers, the impact of PM technology has been decisive: it eliminates polarization drifts, stabilizes nonlinear mode-locking mechanisms, and enables reproducible pulse dynamics. Together with advances in all-fibre splicing, PM fibres allow the complete removal of free-space sections, yielding compact, environmentally robust oscillators and amplifiers. Commercial PM-fibre-based oscillators can now deliver sub-100 fs pulses with μJ-level energies directly from alignment-free cavities. Their reliability and stability have made PM fibres indispensable for translating laboratory ultrafast performance into industrial and field-deployable systems[103]. These advances in fibre design have provided the technological foundation that enables modern ultrafast fibre lasers to combine high energy, excellent beam quality, and robust operation across diverse application scenarios.

2.3.3 Pulse evolution regimes

Beyond advances in mode-locking and fibre design, the study of pulse dynamics in fibre cavities uncovered a sequence of ultrafast regimes that fundamentally shaped the development of high-energy fibre lasers. The earliest demonstrations in the anomalous-dispersion regime gave rise to soliton mode-locking, where the balance between group-velocity dispersion (GVD) and SPM produced stable femtosecond pulses with the characteristic Kelly sidebands[115, 143, 144]. However, the soliton area theorem imposes strict energy limits, and as energy is increased, instabilities including breather states and pulse splitting appear. These phenomena have been well documented in early observations of breathing solitons and in theoretical analyses of soliton stability[145]. To overcome these intrinsic limits, designs exploiting normal dispersion were introduced in the early 1990s. The stretched-pulse fibre laser (Tamura et al., 1993) represented the first breakthrough, enabling pulse energies of order 1 nJ by allowing periodic broadening and recompression inside the cavity[146, 147]. A further advance came with the discovery of self-similar parabolic pulse evolution (“similaritons”), where pulses propagate with linear chirp and remarkable resilience against wave breaking, reaching pulse energies near 10 nJ[148, 149]. The decisive shift arrived with the development of all-normal-dispersion (ANDi) cavities supporting dissipative solitons, in which spectral filtering, saturable absorption, and gain stabilization broke

free from the soliton energy limit[150-152]. This enabled pulse energies beyond 20 nJ directly from oscillators, reaching levels comparable to those of standard Ti:sapphire oscillators in terms of pulse energy and peak power[153]. These pulses were strongly chirped inside the cavity and required external compression to near transform-limited (TL) durations, but they demonstrated that fibre oscillators could sustain orders-of-magnitude higher energies than conventional soliton lasers. Together, these regimes transformed YDFLs into natural testbeds for positive-dispersion pulse dynamics. Both soliton-derived and dissipative-soliton oscillators have been used as seed sources for CPA, where pulse energies are routinely scaled from the nanojoule level to millijoules[132]. Nevertheless, pushing oscillator energies directly into the hundreds of nanojoules or even microjoule regime remains especially significant, as it reduces reliance on complex multi-stage amplification and enables simpler, more robust ultrafast systems.

2.3.4 Mamyshev oscillators

A further breakthrough in the pursuit of high-energy fibre oscillators came with the introduction of the MO. The operating principle underlying the MO can be traced back to earlier studies on pulse shaping through nonlinear spectral broadening combined with spectral filtering. In 1994, Piché demonstrated through mathematical analysis and numerical simulation that the combination of self-phase modulation in a nonlinear fibre and offset spectral filtering could lead to effective pulse shaping and mode-locking [154]. Building on this concept, P. V. Mamyshev introduced in 1998 a regenerator consisting of a nonlinear fibre segment followed by an offset bandpass filter, which exhibited strong noise discrimination and pulse reshaping capabilities [155]. Although this scheme was originally developed in the context of optical signal regeneration in fibre communication systems, it established the physical foundation for what later became known as Mamyshev filtering. The extension of Mamyshev filtering to laser cavities enabled a new class of passively mode-locked fibre lasers. Early demonstrations of Mamyshev-type filtering in fibre cavities date back to 2008 [156], while the first laser implementations delivering nanojoule-level pulses appeared around 2015 [157]. The practical impact of the concept became widely recognized in 2017, when the Cornell group reported an ytterbium-fibre MO producing compressed pulses with peak powers exceeding 1 MW [158]. The MO can be regarded as a passively mode-locked fibre laser whose effective transmission function mimics that of a saturable absorber with nearly step-like characteristics. This behavior provides an exceptionally large modulation depth and distinguishes the MO from conventional mode-locking approaches such as NPE or SESAMs. While NPE typically offers modulation depths on the order of 70%, the effective modulation depth of the MO is significantly higher, enabling much stronger noise discrimination and improved tolerance to large nonlinear phase shifts [159]. As a result,

compared with other fibre-laser mode-locking schemes, the MO offers distinct advantages for generating femtosecond pulses with high peak power.

An impressive MO was reported by Wright et al. (2017), employing a ytterbium-doped fibre (YDF) with a 6-μm core. They obtained ~50 nJ pulses which, after external compression, reached ~40 fs duration and nearly 1 MW peak power[158]. This result established the feasibility of the MO as a high-energy femtosecond oscillator. Subsequent progress was made by the same group: in 2018, Sidorenko, Fu, Wright et al. extended the design to a 10-μm-core fibre, thereby enlarging the mode area and relaxing nonlinear phase accumulation. This configuration supported ~190 nJ compressed pulses with peak powers up to 3 MW[160]. The study not only confirmed the scalability of the MO but also highlighted the adoption of larger mode areas as a straightforward route to higher energies. These predictions were soon validated by Liu et al. (2019), who implemented an MO based on a 29-μm-core PCF and combined it with a multi-pass cell to extend the cavity length and lower the repetition rate. This design overcame pump-power limitations while preserving stability, ultimately yielding compressed pulses with ~1 μJ energy and peak powers up to 13 MW, the highest reported at the time[8]. Further progress was reported in 2022, by Lin et al., who employed a 33-μm-core, high-concentration ytterbium fibre of 0.8 m length to deliver compressed pulses with ~1.2 μJ energy while maintaining femtosecond compressibility[9]. Due to its energy superiority, the MO structure was quickly extended to other bands. In 2019, Olivier et al. demonstrated the first erbium-doped MO in the 1.55 μm telecom band, generating pulses with ~31 nJ energy compressible to ~100 fs[161]. More recently, in 2022, Zheng et al. reported an all-fibre Er-MO with a low mode-locking threshold, directly delivering sub-90 fs pulses[162]. In 2020, Repgen et al. realized the first Tm-fibre MO at 2 μm, generating pulses of ~3.5 nJ energy, thereby demonstrating the feasibility of mode-locking in MO at longer wavelengths despite anomalous-dispersion conditions. In 2024, Wen et al. extended the concept to ~1.7 μm using thulium-doped fibre[163].

The pursuit of all-fibre MOs represents a key step toward practical ultrafast sources, aiming to combine the high-energy capability of the MO with the robustness of spliced, alignment-free fibre architectures. The first all-fibre implementation of the MO was reported in 2016 by Nikita of Aston University, they achieved self-starting via dissipative Faraday instability, This is also the earlist MO operating at telecom wavelength[164]. Another work reported in 2017 by Samartsev et al., who demonstrated an environmentally stable YDF-based oscillator designed as a seed source for high-power ultrafast systems. The cavity, fully spliced and alignment-free, delivered pulses with energies up to 15 nJ, compressible to sub-200 fs durations, and exhibited remarkable stability against temperature, humidity, vibration, and shock[165]. Although the energy was modest, this work established the feasibility of implementing MO in a robust all-fibre format. The first clear step toward high-energy femtosecond operation came in 2021, when Wang et al. reported an all-

PM-fibre Yb MO delivering ~83 nJ pulses, compressible to 56 fs with peak powers exceeding 1 MW[166]. This confirmed that a fully fibre-integrated architecture could sustain hundred-nanojoule-level femtosecond pulses. In 2022, Haig et al. advanced the design by incorporating custom fibre-integrated filters and output couplers, enabling a self-starting all-fibre MO. Their oscillator generated ~110 nJ pulses, compressible to 40 fs (~80 nJ after compression), corresponding to ~1.5 MW peak power, while operating stably without manual perturbation[167]. Further scaling was achieved in 2023, when Wang et al. demonstrated an all-fibre Yb MO operating in two regimes. In the high-energy regime, it produced 153 nJ pulses at 9.8 MHz, compressible to 73 fs with 122 nJ energy and 1.7 MW peak power. In the high-average-power regime, the same oscillator delivered 3.4 W average power at 44 MHz with ~100 fs duration[168]. Most recently, in 2025, Yang et al. extended the all-fibre MO concept to the 2 μm band, demonstrating a Tm-doped configuration that delivered 0.9 nJ, 309 fs pulses after compression[169]. Although the energy remains modest, this result highlights the spectral universality of the MO and opens pathways toward mid-infrared applications.

Another widely studied direction is the starting of the MO. Because the MO employs offset spectral filters that approximate a step-like transmission function, it exhibits unusually high modulation depth. While this makes it an efficient artificial saturable absorber, it also renders self-starting difficult: low-level fluctuations are typically suppressed rather than amplified, unlike in conventional mode-locked lasers. Early implementations therefore relied on external seed injection, where pulses from a separate laser were coupled into the cavity to initiate mode-locking. This method proved straightforward and robust, and was widely adopted in both free-space and all-fibre MOs, but required an external oscillator and manual operation[9, 157, 158]. To simplify operation, researchers introduced auxiliary starting arms, typically incorporating a saturable absorber mirror (SAM) or a NPE arm, which temporarily reduced the modulation depth and facilitated Q-switching [160, 161, 170]. However, these schemes relied on free-space components, making them complex, environmentally sensitive, and difficult to maintain.[171]. Another approach was pump modulation, typically combined with a tunable filter[172]. In this scheme, the filter separation is initially kept small, and pump current is modulated to generate Q-switched or noisy broadband emission that can evolve into a stable mode-locked state. Once mode-locking is established, the filter separation is increased to restore full modulation depth. A subsequent improvement removed the need for pump modulation: by setting a larger initial overlap between the filter passbands, CW light can pass through both filters and evolve into mode-locked pulses under suitable pump power. After stable operation is reached, the filter separation is increased to the desired value[173, 174]. Despite their effectiveness, both strategies share a practical limitation: because the filters are located within the cavity, the method is inconvenient and less suitable for large-scale or industrial applications.

The focus on pulse buildup has also motivated the use of DFT techniques to study the pulse buildup dynamics in MOs. In 2023, Li et al. employed DFT to study the pulse buildup in a seeded MO, revealing that gain competition among multiple injected seed pulses necessitates higher pump power for ignition and often results in multipulse operation. They further showed that using strongly modulated seed pulses can mitigate this effect and promote clean single-pulse starting[175]. In 2025, Xu et al. employed DFT to capture the full buildup sequence, revealing the transition from amplified spontaneous emission, through noisy spectral broadening, to the establishment of stable femtosecond pulses[176]. Beyond their role as high-energy ultrafast sources, MOs have also become valuable platforms for studying nonlinear pulse dynamics. Using DFT, researchers have revealed phenomena ranging from soliton ststes to multipulse states and chaotic behavior[177-182]. These studies highlight the MO not only as a practical femtosecond fibre laser architecture but also as a versatile testbed for exploring coherence and complexity in dissipative laser systems.

With power scaling firmly established, MO have also been extended toward ultrabroadband and few-cycle operation. Their combination of high pulse energies and noise-robust filtering enables strong nonlinear interactions directly in fibre, without the fragility of bulk systems. In 2020, Ma et al. generated octave-spanning spectra in a Yb-fibre MO, approaching the single-cycle limit[183]. In 2024, Kang et al. compressed 10 nJ MO pulses to 9.1 fs at 90 MHz, achieving spectral coverage from 800-1350 nm[184]. At longer wavelengths, Luo et al. realized intracavity supercontinuum generation in an Er-doped MO, spanning 1330-2030 nm without external amplification[185]. These results underline the MO's versatility as a compact fibre platform for few-cycle and ultrabroadband sources. Beyond spectral broadening, the MO has also been used to structure light in spatial and temporal degrees of freedom. High-energy MOs have directly produced femtosecond cylindrical vector beams and optical vortices with megawatt peak powers, offering compact routes to vectorial light for advanced imaging and micromachining[186, 187]. In parallel, multimode implementations have enabled spatiotemporal mode-locking (STML). In 2022, Cao et al. demonstrated self-starting STML using Mamyshev regenerators in a multimode fibre (MMF) cavity[188], while in 2024 Liu et al. reported an all-fibre Er/Yb multimode MO delivering ~171 nJ, 30 kW spatiotemporal solitons[189]. These advances highlight the MO not only as a high-energy femtosecond source, but also as a versatile platform for generating structured and high-dimensional light fields.

2.4 Conclusion

This chapter has traced the evolution of laser science from its origins in the ruby and helium-neon lasers to the diverse families of gas, dye, solid-state, semiconductor, and fibre lasers. Particular emphasis was placed on the progression from CW operation toward ultrafast sources,

highlighting how innovations in mode-locking transformed lasers into powerful tools for exploring nonlinear and strong-field physics. Building on this, the discussion turned to the rise of fibre lasers, which combine rare-earth-doped gain with the thermal and guiding advantages of the fibre geometry. The development of cladding-pumped designs, LMA fibres, and advanced architectures such as MCFs and HCFs established fibre lasers as the most scalable and practical high-power laser platform. In parallel, the exploration of pulse dynamics, including soliton, dissipative soliton and self-similar regimes, provided pathways to overcome intrinsic energy limits. Within this landscape, the MO has emerged as a pivotal architecture. By combining spectral broadening with offset filtering, it enables pulse energies in the 100-nJ to μJ range directly from fibre oscillators, while offering robust self-starting and compatibility with all-fibre integration. Recent demonstrations have extended the concept across multiple wavelength bands, explored its initiation and dynamical behaviour, and applied it to few-cycle pulse generation, supercontinuum, and structured beams.

In summary, these developments converge on the central theme of this thesis: the realization of high-energy ultrafast YDFLs. Among the various platforms, Yb-fibre combines high quantum efficiency, broad gain bandwidth, and operation in the normal-dispersion regime, making it uniquely suited for advancing ultrafast performance. The following chapters build directly on this foundation, focusing on ytterbium-fibre systems as both practical femtosecond sources and experimental platforms for exploring nonlinear light-matter interactions.

Chapter 3 Background theory

3.1 Introduction

Ultrafast fibre lasers have emerged as indispensable tools in both fundamental science and industrial applications owing to their compact geometry, high efficiency, and exceptional pulse quality. Among the rare-earth doped fibres, ytterbium (Yb^{3+}) stands out as the most widely used gain medium because of its simple energy-level structure, broad gain bandwidth, high quantum efficiency. These features make Yb-doped fibre lasers particularly suitable for generating high-energy femtosecond pulses, which are essential for applications such as precision material processing, biomedical imaging, and nonlinear optics.

To establish a foundation for the experimental and numerical studies presented in later chapters, this chapter provides a systematic overview of the physical principles underpinning Yb-doped ultrafast fibre lasers. We begin by introducing the gain dynamics through a four-level rate-equation model, which can be reduced to an effective two-level system under typical operating conditions. This framework enables the description of population inversion, gain saturation, and the steady-state solutions relevant to practical amplifiers and oscillators. Next, we discuss the role of dispersion and nonlinear optical effects in fibres, which govern the propagation, shaping, and stability of ultrashort pulses. Particular attention is given to GVD, higher-order dispersion, and key nonlinear processes such as SPM and self-steepening. Building on this background, the mode-locking mechanisms are reviewed, including soliton, breathing soliton, dissipative soliton formation, similariton, and the specific case of the MO. These mechanisms highlight the intricate balance of gain, dispersion, and nonlinearity that enables stable ultrafast pulse generation. Finally, the technique of DFT is introduced as a powerful real-time diagnostic method. By mapping optical spectra into the temporal domain, DFT allows single-shot spectral measurements with high resolution and has become an essential tool for studying transient dynamics in mode-locked fibre lasers.

Overall, this chapter establishes the theoretical background required for understanding and analysing the subsequent experimental investigations of ultrafast fibre lasers and amplifiers.

3.2 Gain dynamics in Yb-doped fibres

Rare-earth ion Yb^{3+} is widely employed in high-power and ultrafast fibre lasers due to its relatively simple energy-level structure and broad absorption and emission bands. As illustrated in Fig. (a), the manifold of $^2F_{7/2}$ (ground-state multiplet) and $^2F_{5/2}$ (excited-state multiplet) is split into several Stark sublevels in a glass host. Upon optical pumping, ions are excited to the higher Stark

sublevels of $^2F_{5/2}$, and then rapidly relax nonradiatively via phonon-assisted transitions to the lowest sublevel of this manifold within a picosecond to nanosecond timescale. This lowest sublevel acts as the upper laser level. Similarly, radiative transitions terminate on an excited sublevel of $^2F_{7/2}$, which also undergoes ultrafast relaxation back to the ground state.

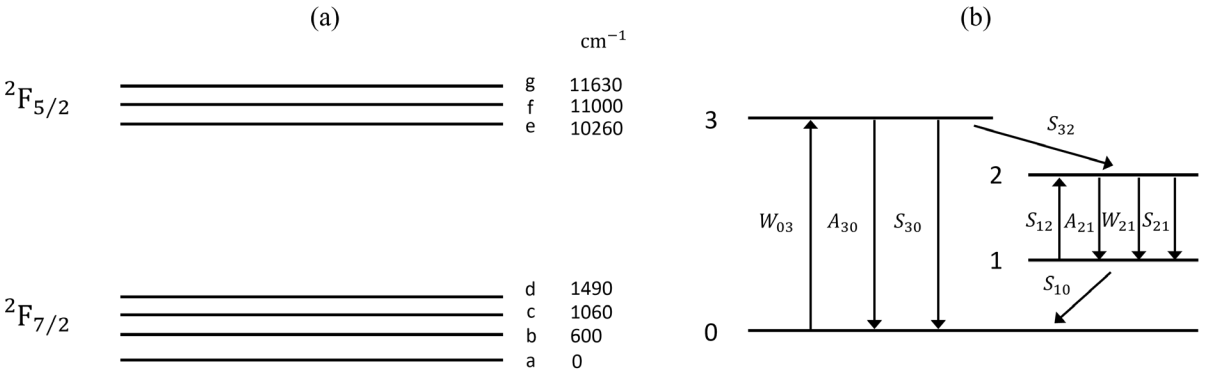

Figure 3.1 Energy-level structure and effective four-level model of Yb^{3+} ions in glass hosts. (a) Stark-split manifolds of the ground $^2F_{7/2}$ and excited $^2F_{5/2}$ states. (b) Simplified four-level scheme used for rate-equation modeling: level 0 is the ground state, level 1 the lower laser level, level 2 the upper laser level, and level 3 the pump level. Pump absorption occurs at 0→3, followed by ultrafast nonradiative relaxation into level 2. Stimulated emission 2→1 and signal absorption 1→2 form the laser transition. Because the populations of levels 3 and 1 decay on timescales much shorter than the upper-state lifetime, they can be adiabatically eliminated, reducing the system to an effective two-level model (N_0 and N_2). This effective model provides the basis for the subsequent derivation of the rate equations and the gain expression.

The Yb^{3+} gain medium can be represented by four levels, as in Fig. (b): level 0 is the ground state; level 1 is the lower laser level within the $^2F_{7/2}$ manifold; level 2 is the upper laser level (lowest Stark sublevel of $^2F_{5/2}$; level 3 is a pump level in the $^2F_{5/2}$ manifold. Pump stimulated absorption from 0→3 occurs at the rate W_{03}. Population in level 3 decays rapidly either radiatively to 0 at spontaneous emission rate A_{30} or nonradiatively at rates S_{30} and S_{32}. The laser transition is 2↔1: stimulated emission 2→1 proceeds at rate W_{21}, while signal-induced absorption 1→2 proceeds at rate S_{21}. In addition, level-2 undergoes spontaneous emission to level-1 at rate A_{21}, and the level-1 population relaxes to level-0 at rate S_{10} or back to level-2 at S_{12}. In typical Yb-doped glasses the nonradiative relaxations S_{32} and S_{10} are picosecond/ nanosecond processes, whereas the upper-state fluorescence lifetime is milliseconds. Consequently, levels 3 and 1 do not provide significant population storage: N_3 is negligible, and N_1 rapidly returns to level 0. All ions pumped from level 0 are effectively transferred to the upper laser level 2. Eliminating the fast

variables yields an effective two-level scheme with only N_0 (ground) and N_2 (upper) retained. the temporal evolution of the populations (N_0 and N_2) can be written as:

$$\begin{cases} \frac{dN_2}{dt} = W_{03}N_0 - (W_{21} + A_{21} + S_{21})N_2 \\ N_0 + N_2 = N_T \end{cases} \tag{3-1}$$

where N_T is the total dopant concentration.

At steady state ($dN_2/dt = 0$), and substituting $N_0 = N_T - N_2$, the inversion becomes：

$$N_2 = N_T \frac{W_{03}}{W_{03} + W_{21} + A_{21} + S_{21}}. \tag{3-2}$$

It is convenient to express the transition rates via the absorption and emission cross sections σ and the photon flux densities $\phi = P/(Ahv)$, where P is the optical power at the pump or signal wavelength, A is the effective cross-sectional area of the optical mode within the doped region and v is the optical frequency. The pump and signal transition rates are written as：

$$W_{03} = \sigma_{a,p}\phi_p, \qquad W_{21} = \sigma_{e,s}\phi_s, \tag{3-3}$$

where $\sigma_{a,p}$ is the pump absorption cross section and $\sigma_{e,s}$ is the stimulated emission cross section at the signal wavelength. The upper-state fluorescence lifetime can be defined as $\tau_f \approx 1/(A_{21} + S_{21})$. Substituting these relations, the fractional inversion is obtained as

$$\frac{N_2}{N_T} = \frac{\sigma_{a,p}\phi_p}{\sigma_{a,p}\phi_p + \sigma_{e,s}\phi_s + 1/\tau_f}. \tag{3-4}$$

The net gain coefficient at the signal wavelength is determined by the balance of stimulated emission and reabsorption:

$$g = \sigma_{e,s}N_2 - \sigma_{a,s}N_0 = N_T\left[\sigma_{e,s}\frac{N_2}{N_T} - \sigma_{a,s}\left(1 - \frac{N_2}{N_T}\right)\right], \tag{3-5}$$

where $\sigma_{a,s}$ denotes the signal absorption cross section.

3.3 Dispersion and nonlinear effects

The propagation of ultrashort pulses in optical fibres is governed by the interplay between dispersion and nonlinear effects. Dispersion arises from the frequency dependence of the refractive index and leads to temporal broadening or compression, depending on its sign and order. Nonlinear effects originate from the intensity dependence of the refractive index and from delayed molecular responses of the medium, giving rise to phenomena such as SPM, stimulated Raman scattering (SRS), and self-steepening. In realistic fibre systems, these effects act

simultaneously; their relative impact is determined by pulse duration, peak power, fibre length, and the dispersion profile. Understanding these mechanisms is essential for modeling and optimizing the spectral and temporal evolution of pulses in MOs and related ultrafast fibre laser architectures.

3.3.1 Dispersion

When a pulse propagates in a dispersive medium, different frequency components travel at different group velocities. The propagation constant $\beta(\omega)$ can be expanded as a Taylor series around the carrier frequency ω_0:

$$\beta(\omega) = \beta_0 + \beta_1(\omega - \omega_0) + \frac{\beta_2}{2!}(\omega - \omega_0)^2 + \frac{\beta_3}{3!}(\omega - \omega_0)^3 + \cdots \quad (3\text{-}6)$$

Here, β_1 is the inverse of the group velocity, β_2 is the GVD parameter, and β_3 represents third-order dispersion (TOD). For broadband ultrashort pulses, higher-order terms can become non-negligible.

Chromatic dispersion is the combined effect of material dispersion and waveguide dispersion. In silica fibres, material dispersion arises from the wavelength-dependent refractive index of silica (and is influenced by dopants), whereas waveguide dispersion is governed by the guiding geometry. The commonly used dispersion parameter is:

$$D(\lambda) = -\frac{2\pi c}{\lambda^2}\beta_2(\lambda) \quad (3\text{-}7)$$

typically reported in ps/(nm·km). In the normal-dispersion regime ($\beta_2 > 0$), longer wavelengths travel faster; in the anomalous regime ($\beta_2 < 0$), the opposite occurs.

Material dispersion can be well approximated using the Sellmeier model. Using the standard three-term Sellmeier coefficients for fused silica, $D(\lambda)$ over 800-1600 nm is readily computed [190] (see Fig. 2.1). Around the Yb emission band (~1000-1100 nm), fused-silica material dispersion lies in the normal-dispersion region. Waveguide dispersion depends on the fibre design (e.g., core radius a, index contrast Δ, refractive-index profile) and can be engineered to be positive or negative, enabling dispersion-shifted, dispersion-compensating, or dispersion-flattened fibres.

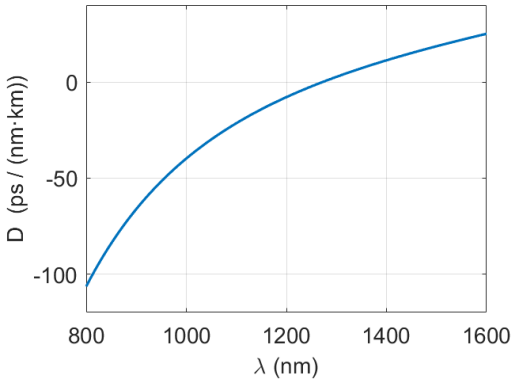

Figure 3.2 Chromatic dispersion D(λ) of fused silica computed from the three-term Sellmeier model over 800-1600 nm. The Yb band lies in the normal-dispersion region.

When the pulse spectral span is large, especially near the zero-dispersion wavelength, third-order dispersion (β_3) becomes important. TOD introduces asymmetric temporal and spectral distortions (pre-/post-pulses and oscillations). During pulse compression, imperfect TOD compensation limits the attainable pulse quality even when GVD is well managed. Therefore, broadband compression typically requires careful dispersion management across orders, and including β_3 in simulations is necessary to faithfully model ultrashort, broadband pulses.

3.3.2 Self phase modulation

SPM arises from the instantaneous Kerr nonlinearity of the fibre medium, in which the refractive index depends on the optical intensity:

$$n(I) = n_0 + n_2 I \tag{3-8}$$

This effect induces a time-dependent phase shift $\phi_{NL}(t) = \gamma P(t) L_{eff}$, where γ is the nonlinear coefficient, $P(t)$ is the instantaneous power, and L_{eff} is the effective interaction length. The corresponding instantaneous frequency change $\delta\omega(t) = -\partial\phi_{NL}/\partial t$ yields spectral broadening that is ideally symmetric about the carrier. Both the shape and chirp state of the initial pulse affect SPM broadening. Super-Gaussian pulses and Gaussian pulsess, exhibit multi-peak structures, but most of their energy remains within the central peak in Super-Gaussian pulses. Positive pre-chirp tends to smooth spectral oscillations, whereas sufficiently negative pre-chirp may lead to partial spectral narrowing. In ultrafast fibre lasers, SPM is often the dominant mechanism for bandwidth generation, and the resulting chirp can be partially or fully compensated to produce shorter pulses.

3.3.3 Stimulated Raman scattering

In addition to the instantaneous electronic response, silica fibres exhibit a delayed nonlinear response associated with molecular vibrations, known as the Raman response. When the optical peak power is sufficiently high, the delayed Raman response can lead to SRS, in which energy is transferred from higher to lower frequencies within the pulse. For ultrashort pulses, this manifests as an asymmetric broadening of the optical spectrum toward longer wavelengths, often referred to as the intrapulse Raman self-frequency shift. In practice, SRS acts alongside other nonlinear effects such as SPM and self-steepening; its qualitative role is to bias otherwise symmetric broadening toward longer wavelengths

3.3.4 Self-steepening

The self-steepening effect arises from the intensity dependence of the group velocity and becomes significant when the pulse duration approaches a few optical cycles or the spectral bandwidth is large. The self-steepening effect derives its name from the fact that it makes the pulse trailing edge steeper. The most obvious characteristic of the self-steepening effect is the asymmetric broadening of the spectrum: manifested in a stronger redshift peak than a blueshift peak and a wider spectral broadening at the blue end. While usually secondary to SPM in fibres, self-steepening can imprint fine high-frequency features and a blue-side spectral bias, especially when combined with higher-order dispersion and Raman effects.

3.4 Pulse evolution regimes

The evolution of mode-locking strategies in ultrafast fibre lasers can be viewed as a progressive response to two overarching demands: increasing the extractable pulse energy and maintaining stability under high nonlinearity. Early designs operated in the soliton regime within all-anomalous-dispersion cavities, where the interplay between GVD and SPM produced pulses close to the fundamental soliton solution of the nonlinear Schrödinger equation (NLSE). While such “average solitons” offered TL durations and simple implementation, their pulse energy was strictly constrained by the soliton area theorem, and NPS beyond π triggered soliton fission or resonant dispersive wave emission. To relax this limitation, dispersion mapping was introduced, alternating segments of normal and anomalous dispersion so that the pulse “breathed” in duration and bandwidth within each round trip. This stretched-pulse or dispersion-managed-soliton regime reduced the average peak power, allowing larger B-integral ($\gtrsim 2\pi$) and energies in the multi-nanojoule range while preserving compressibility to near-transform limits. A major advance was the introduction of ANDi cavities supporting dissipative solitons. In this regime, the interplay of SPM with normal GVD is counterbalanced by spectral filtering, saturable absorption,

and the finite gain bandwidth, leading to the formation of strongly chirped pulses inside the cavity. The resulting broad temporal width lowers the peak power for a given pulse energy, which allows the system to tolerate NPS exceeding 10π and to support pulse energies in the tens of nanojoules. In parallel, the self-similar evolution (similariton) regime emerged, particularly in fibre segments with distributed gain, where pulses evolve toward a parabolic intensity profile with linear frequency sweep. This attractor state allows wave-breaking-free spectral broadening and high-energy operation and is often combined with dissipative soliton shaping for further performance gains. Building on these developments, the Mamyshev oscillator implements a filtering-based mode-locking mechanism using two offset bandpass filters separated by a nonlinear spectral broadening in the gain fibre. Only pulses whose spectra have been sufficiently broadened can pass to the next filter, providing an effective saturable absorber without recovery-time or modulation-depth limitations. This architecture supports NPS exceeding 20π and pulse energies in the 100-nJ to microjoule range, with external compression to sub-100-fs durations. As such, the MO represents the current state-of-the-art in energy-scalable mode-locked fibre oscillators, combining the broadening capacity of high-nonlinearity stages with the selectivity of spectral filtering to achieve both stability and performance.

From a theoretical perspective, the pulse evolution regimes discussed in this section are commonly described using different classes of evolution models, depending on the relative roles of dispersion, nonlinearity, gain, loss, and spectral filtering. Conservative regimes are typically captured by the NLSE, which in its simplest form can be written as

$$\frac{\partial A}{\partial z} = -\frac{\alpha}{2}A + i\frac{\beta_2}{2}\frac{\partial^2 A}{\partial t^2} + i\gamma|A|^2 A \tag{3-9}$$

where A is the slowly varying pulse envelope, $\beta_2$is the group-velocity dispersion coefficient, and γ is the Kerr nonlinearity. NLSE governs soliton and dispersion-managed soliton dynamics. When gain, loss, and spectral filtering are included, the dynamics can be described by dissipative extensions such as the complex Ginzburg–Landau equation (CGLE), which admits dissipative soliton and self-similar solutions. Strongly filtered systems such as the MO are more naturally described using cavity map models, in which nonlinear propagation governed by the the generalized nonlinear Schrödinger equation (GNLSE) is combined with discrete gain and filtering operators. The detailed numerical framework adopted in this thesis is introduced in Chapter 4.

3.4.1 Soliton

The soliton regime occurs in all-anomalous-dispersion cavities where pulse dynamics are well described by the conservative NLSE. The stationary solution is the fundamental soliton with a sech^2 temporal profile as:

$$I(t) = I_0 sech^2(t/T_0) \tag{3-10}$$

where, T_0 is the pulse width, and nearly flat instantaneous frequency (minimal chirp). Its existence is governed by the soliton order

$$N^2 = \frac{\gamma P_0 T_0^2}{|\beta_2|} \tag{3-11}$$

with $N = 1$ for the fundamental state; higher N values produce periodic breathing and, under perturbations, soliton fission. The corresponding "area" relation for energy,

$$E = \frac{2|\beta_2|}{\gamma T_0} \tag{3-12}$$

illustrates the intrinsic energy-duration-dispersion scaling and the limited energy headroom of conservative solitons.

Figure 3.3 and Figure 3.4 illustrate the intrinsic relationship between pulse energy, duration, and dispersion, as well as the characteristic temporal-spectral evolution of a soliton fibre laser. In the fundamental soliton regime, the cavity operates with net anomalous dispersion, and the local dispersion along the propagation path remains constant and negative. Under these conditions, the effects of GVD are exactly balanced by SPM, leading to a stationary pulse in both temporal and spectral domains. As shown in Figure 3.3, the pulse duration remains constant throughout the cavity, reflecting this balance, while the local dispersion curve indicates a uniform anomalous dispersion environment. Figure 3.4 presents a numerical example of such a cavity, where the temporal and spectral envelopes are preserved over successive round trips, highlighting the stability and invariance of soliton operation.

In practice, the maximum tolerable NPS (B-integral) is on the order of π. Beyond this, resonant dispersive waves or wave breaking appear, particularly when higher-order dispersion (e.g., β_3) introduces asymmetry. While soliton lasers are valued for simplicity and TL output, their strict energy ceiling motivated the search for dispersion management strategies.

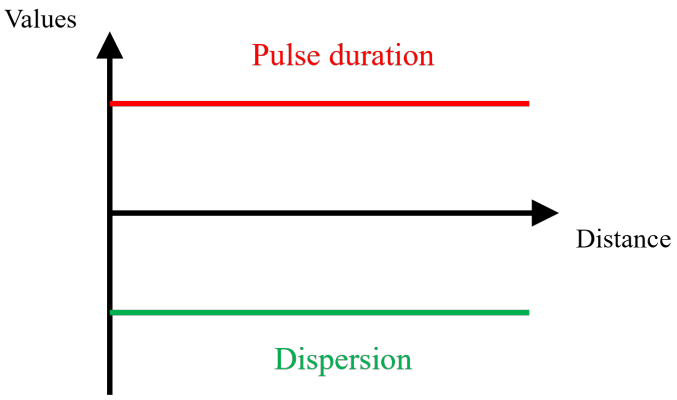

Figure 3.3 Schematic of local dispersion (green) and pulse duration (red) evolution in a fundamental soliton fibre laser. The local dispersion remains constant and anomalous along the cavity, enabling a fixed pulse duration through the balance of GVD and SPM.

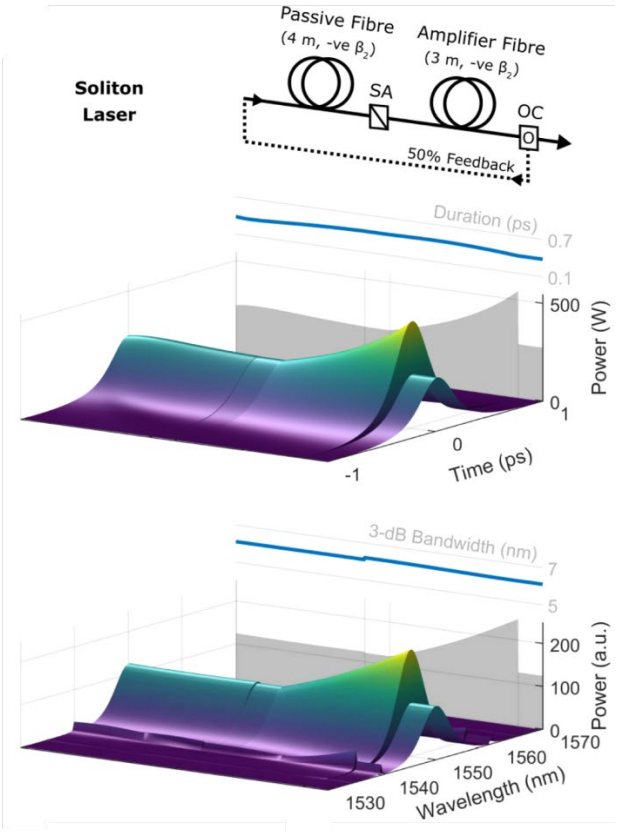

Figure 3.4 Numerical illustration of temporal and spectral evolution in a soliton regime[191]. Both envelopes remain invariant over successive round trips, characteristic of a conservative soliton solution.

3.4.2 Dispersion-managed soliton

Dispersion-managed solitons (DMS) arise in fibre laser cavities where the local dispersion alternates periodically between anomalous and normal segments, forming a dispersion map with near-zero net dispersion over one period. This periodic alternation causes the pulse to breathe in

both temporal duration and spectral bandwidth during each round trip, yet return to its initial shape after a full map period. The breathing reduces the peak power over a significant fraction of the cavity, enabling larger nonlinear phase accumulation ($B \gtrsim 2\pi$) and thus higher pulse energies than stationary solitons, while maintaining good compressibility at the output. The dynamics can be interpreted via an "average soliton" model with modified effective dispersion and nonlinearity. Stable operation requires careful control of the map strength and segment lengths: excessive stretching suppresses nonlinear interaction, while insufficient stretching risks wave breaking. In practice, higher-order dispersion (β_3) and finite gain bandwidth further influence stability and compressibility. Typical DMS systems produce few-nJ pulses that can be externally compressed to sub-100-fs durations.

Figure 3.5 and Figure 3.6 show the dispersion map and pulse evolution for a DMS fibre laser. As depicted in Figure 3.5, the local dispersion (green) alternates between anomalous and normal segments, while the pulse duration (red) breathes periodically within each dispersion period. Figure 3.6 presents a numerical example of temporal and spectral breathing dynamics. The reduced peak power over most of the cavity length allows for larger nonlinear phase accumulation before instability, enabling higher pulse energies than stationary solitons while maintaining good compressibility at the output.

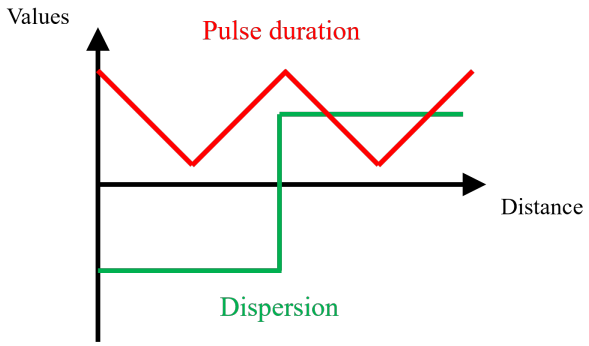

Figure 3.5 Schematic of local dispersion (green) and pulse duration (red) evolution in a DMS fibre laser. The local dispersion alternates between anomalous and normal segments, producing periodic breathing in temporal width.

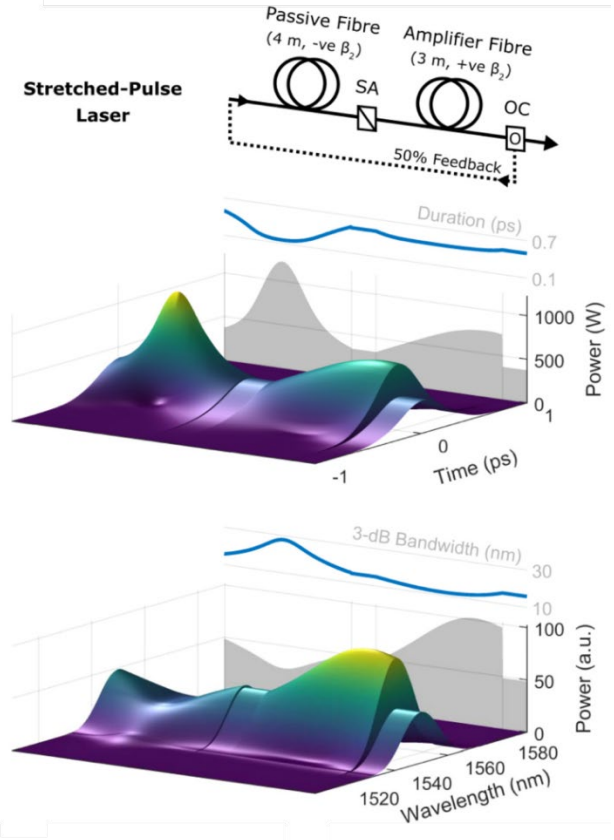

Figure 3.6 Numerical illustration of pulse evolution in a DMS regime[191]. Temporal and spectral breathing over each dispersion period reduces peak power for most of the cavity, allowing larger nonlinear phase accumulation before instability.

3.4.3 Dissipative soliton

Dissipative solitons form in fibre laser cavities with net-normal dispersion, where the combined action of SPM, normal GVD, spectral filtering, saturable absorption, and finite gain bandwidth produces stable attractor solutions of the CGLE. Unlike conservative solitons, which are nearly TL in-cavity, dissipative solitons are strongly chirped during propagation. This chirp, together with their broad temporal width, keeps the peak power relatively low for a given pulse energy, allowing tolerance to accumulated NPS well beyond 10π. As a result, dissipative solitons can achieve pulse energies an order of magnitude higher than those in soliton or DMS regimes, while maintaining stable single-pulse operation and robustness to environmental perturbations.

In a typical dissipative soliton cavity, SPM and normal GVD act together to broaden the spectrum, while the spectral filter truncates and reshapes it. The saturable absorber and gain bandwidth define the energy and amplitude stability, ensuring that the pulse evolves toward a self-consistent attractor each round trip. The resulting spectra are often near-rectangular with steep edges determined by the filter passband, and the in-cavity pulses remain highly chirped. External compression can then yield clean, high-quality pulses in the 50-200 fs range. However, the flat-

topped spectra may introduce residual sidelobes upon compression, which can be mitigated by spectral apodization or higher-order dispersion compensation. Apart from dissipative solitons, ANDi cavities can also sustain self-similar pulse evolution, known as the similariton regime, which is discussed in the following section.

Figure 3.7 and Figure 3.8 illustrate the dispersion profile and pulse evolution in a dissipative soliton fibre laser. As shown in Figure 3.7, the cavity exhibits a net-normal dispersion profile, and the pulse maintains a relatively broad temporal width within the fibre segments, limiting peak power for a given energy. The apparent narrowing of the pulse in the middle of the map is caused by the spectral filter located at the output position, which reduces the pulse width before it is re-injected into the cavity. Figure 3.8 presents a numerical example of the temporal and spectral evolution, showing the characteristic strong in-cavity chirp and near-rectangular spectrum associated with the dissipative soliton regime.

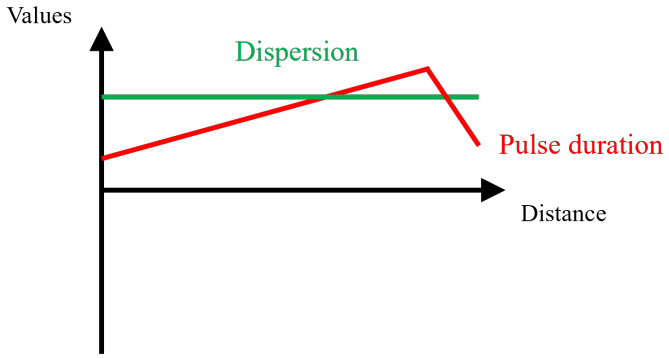

Figure 3.7 Schematic of local dispersion (green) and pulse duration (red) evolution in a dissipative soliton fibre laser operating in an ANDi cavity. Gain, spectral filtering, and SPM collectively shape the pulse toward a strongly chirped steady state.

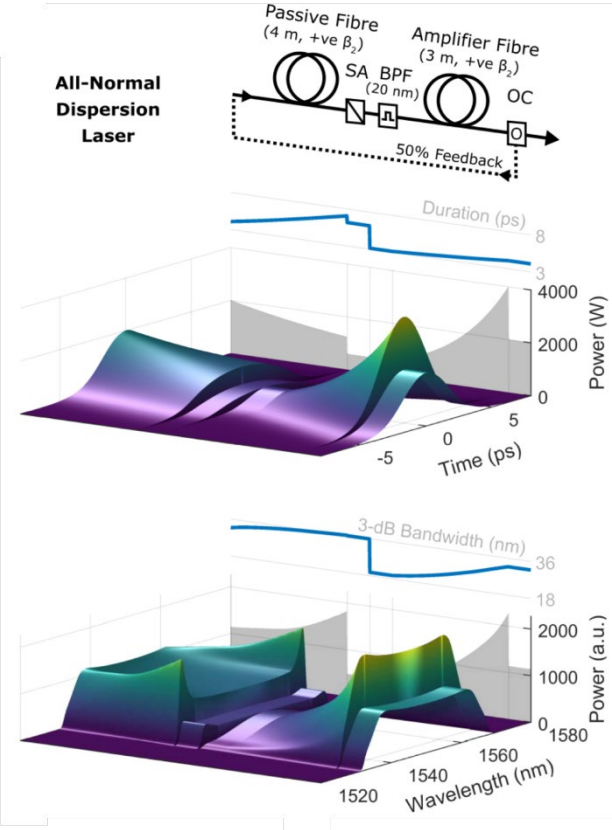

Figure 3.8 Numerical illustration of pulse evolution in a dissipative soliton regime[191]. The pulse remains broad and strongly chirped in fibre segments, with narrowing occurring at the intracavity filter before re-amplification.

3.4.4 Self-similar (Similariton)

In addition to dissipative solitons, ANDi cavities can also support self-similar pulse evolution. Similaritons arise in normally dispersive fibre segments under strong nonlinear phase accumulation, typically in the presence of distributed gain (amplifier similariton). They evolve toward a parabolic temporal intensity profile with a linear frequency chirp, which represents an attractor solution of the governing equations. This self-similar evolution enables wave-breaking-free spectral broadening and supports high pulse energies without compromising stability. In an amplifier similariton, the pulse duration, bandwidth, and chirp scale monotonically with propagation distance. In oscillator implementations, a narrowband filter is often placed within the cavity to truncate the spectrum and reset the pulse for the next round trip. When embedded in ANDi cavities, similariton dynamics can be combined with dissipative shaping to suppress multi-pulsing and CW breakthrough. In this regime, the tolerance to NPS can match or exceed that of dissipative solitons, provided that gain distribution and dispersion are appropriately matched.

Figure 3.9 shows a numerical example in which both temporal and spectral profiles broaden steadily in the gain segment, approaching the self-similar attractor before being reshaped by intracavity elements for the next round trip.

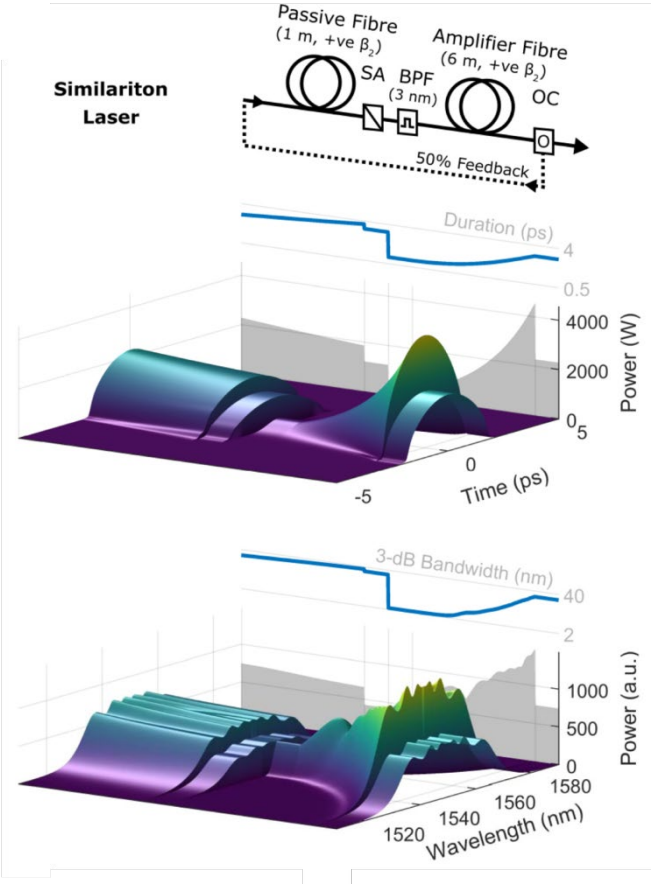

Figure 3.9 Numerical illustration of pulse evolution in a similariton regime[191]. Temporal and spectral profiles broaden monotonically in the gain segment, approaching the self-similar attractor before being reset by intracavity shaping elements.

3.4.5 Mamyshev oscillator

A MO employs offset spectral filtering between two bandpass filters whose passbands are separated by several nanometers. Between the filters, a length of gain fibre induces strong SPM-driven spectral broadening. Only pulses with sufficient peak power to broaden across the filter offset can pass to the next stage, while low-intensity background and CW components are rejected. This spectral gating mechanism functions as an artificial saturable absorber with a near-100% effective modulation depth and no recovery time, since both Kerr-induced spectral broadening and spectral filtering are instantaneous on the timescale of the pulse. As a result, it avoids the limitations associated with finite modulation depth and saturation fluence in material-based absorbers. In contrast to soliton-like attractors described by the complex Ginzburg–Landau equation, the Mamyshev oscillator operates as a strongly dissipative system dominated by highly selective, filter-induced spectral losses. Its steady states are therefore less universal

but exhibit exceptional robustness for energy scaling. This mechanism enables the cavity to sustain extremely large NPS ($B > 20\pi$) and pulse energies in the 100-nJ to μJ range. Intra-cavity pulses are strongly chirped and exhibit flat-topped spectra due to filter truncation, allowing external compression to durations below 100 fs. MOs thus represent the current state-of-the-art in energy-scalable mode-locked fibre lasers, combining the large-broadening capacity of high-nonlinearity gain segments with the selectivity of spectral filtering to achieve both stability and high performance.

Figure 3.10 presents a numerical simulation of intracavity propagation between the two offset filters, highlighting the monotonic temporal and spectral broadening within the gain fibre, followed by abrupt spectral narrowing at the filter due to the step-like spectral filtering.

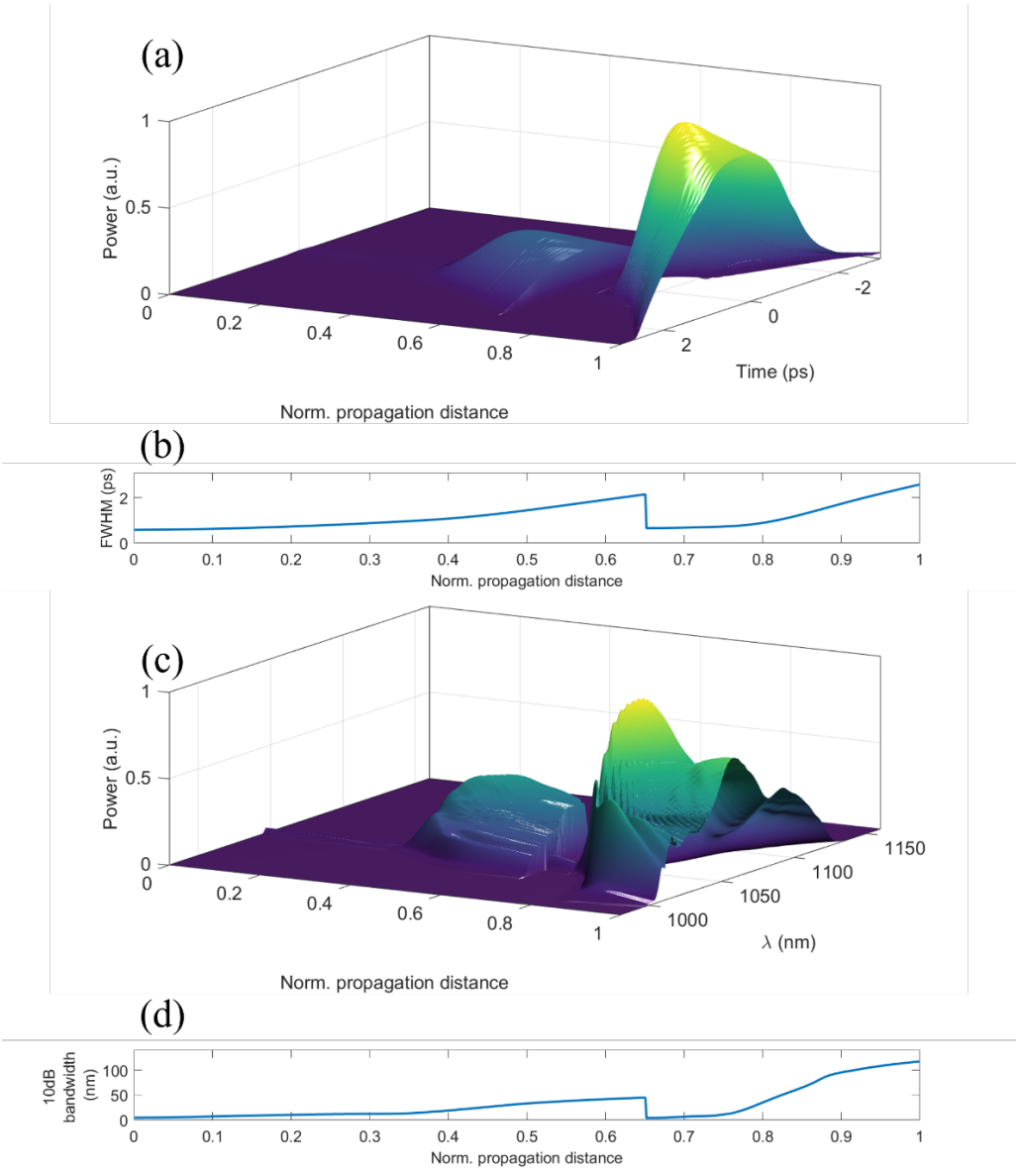

Figure 3.10 Temporal and spectral evolution in a MO, obtained from numerical simulation of propagation between two offset spectral filters. (a) Simulated temporal intensity

evolution over one filter-to-filter segment. (b) Full-width at half-maximum (FWHM) pulse duration versus normalized propagation distance, showing monotonic broadening in the gain fibre followed by abrupt narrowing at the filter. (c) Simulated spectral evolution over the same segment, illustrating strong SPM-induced broadening. (d) 10-dB spectral bandwidth versus normalized propagation distance, with sudden reduction at the filter due to the step-like spectral gating.

3.4.6 Technology Comparison

Comparing MO with other similar fibre laser technologies can more intuitively demonstrate its technical characteristics. Here, MO technology will be compared with other oscillator technologies and laser amplification technologies in multiple dimensions.

Table 3.1 performance summary of SMF-based ytterbium-doped fibre oscillators for different pulse evolutions.

Pulse Evolution	Nonlinear Phase	Typical Performance	Best Performance
Soliton	~0	0.1 nJ, 300 fs	0.5 nJ, 100 fs
Dispersion-managed soliton	0 – π	1 nJ, 100 fs	up to 3 nJ, down to 50 fs
Passive similariton	2π – 10π	6 nJ, 150 fs	15 nJ, 100 fs
Dissipative soliton	2π – 10π	6 nJ, 150 fs	up to 20 nJ, down to 70 fs
Amplifier similariton	4π – 10π	3 nJ, 70 fs	up to 8 nJ, 40 fs
MO	>60π (in simulation: > 140π)		experiment: 50 nJ, 40 fs (in simulation: >190 nJ, <20 fs)

The Table 3.1, from ref [179], demonstrates the superior performance of the MO oscillator in the field of fibre optic oscillators. It can tolerate nonlinear phase shifts several times greater than other oscillators, thus achieving the highest pulse energy, the shortest pulse width and also highest peak power with consistent fibre core diameter. Therefore, the MO is comparable in performance to fibre lasers with pulse amplifiers. Table 3.2 lists the widely used ultrashort pulse amplification techniques in fibre media and, to my knowledge, the best results in terms of peak power, comparing them with the results from MO. The most mature technique, CPA, benefits from advantages in gain fibre, primarily in the size of the effective mode field area, enabling it to

achieve the highest output power and peak power of a single fibre to date. CPA is a linear amplification technique, and the output pulse spectrum is limited by the gain narrowing effect, resulting in pulse durations often in the hundreds of femtoseconds. Pre-chirp managed amplification, as a nonlinear amplification technique, can generate pulses in the hundreds of femtoseconds range. Another recently emerging nonlinear amplification technique, gain-managed amplification, can achieve pulses as short as sub-50 fs. From the results, MO is similar to gain-managed amplification, capable of producing pulses as short as sub-50 fs, and the highest peak power achieved so far is also close to 10-20 MW. Overall, MO still lags behind the best amplification results, but compared to nonlinear amplification techniques, this gap is not insurmountable; further design optimizations in fibre optics are expected to narrow this gap. Based on this, MO, as a simple oscillator, becomes particularly unique and structurally simple.

Table 3.2 Performance summary of different ytterbium-doped fibre amplifications and MO.

Pulse Evolution	Best Performance	Gain fibre used in Main ampflifer	Number of amfplifier stages
CPA[133]	2.2 mJ, 480 fs, 3.8GW	An Yb-doped Large-Pitch PCF with a core diameter of 108 μm and an affective MFD of 105 μm	4
Pre-chirp managed amplification[192]	27 μ J, 172 fs, 113MW	An Yb-doped LMA-PCF with a core diameter of 40 μm	5
Gain-managed amplification[193]	2.7 μ J, 76 fs, 28MW	An Yb-doped PCF with core/cladding diameter of 40/200 μm	3
MO[9]	1.2uJ, 58fs, 13MW	An in-house fabricated step-index YDF with a large core diameter of ~33 μm	0

3.5 Dispersive Fourier transform

The DFT is a real-time spectroscopic technique that maps the optical spectrum of an ultrashort pulse into a temporal waveform via GVD. As illustrated in Figure 3.11, when a broadband pulse

propagates through a highly dispersive medium, different spectral components acquire distinct group delays, leading to a temporally stretched output pulse whose intensity profile reproduces the input spectrum. Under the temporal Fraunhofer approximation, written as $t_0^2 \ll |2\beta_2 z|$ where t_0 is the pulse duration, this frequency-to-time mapping becomes linear, and the general relation between time T and angular frequency ω is

$$T(\omega) = \sum_{m=2}^{\infty} \frac{\beta_m z}{(m-1)!} \omega^{m-1} \tag{3-13}$$

where β_m are the m-th order dispersion coefficients and z is the propagation length. In the ideal case where higher-order dispersion terms ($m > 3$) are negligible, this relation reduces to the second-order form $T(\omega) \approx \beta_2 z\omega$.

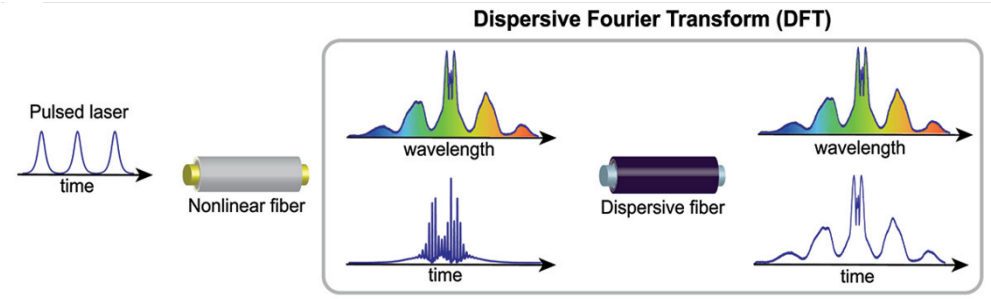

Figure 3.11 Principle of DFT measurements[194]. A broadband ultrashort pulse undergoes linear propagation in a highly dispersive fibre, where different spectral components experience distinct group delays. This frequency-to-time mapping enables direct reconstruction of the optical spectrum from the temporally stretched pulse intensity waveform, provided the temporal Fraunhofer approximation is satisfied.

Following the basic principle of frequency-to-time mapping, the performance of a DFT system is ultimately determined by a set of interdependent parameters that link the optical source, dispersive medium, and detection system. Specifically, the spectral resolution, scan rate, and number of data points acquired per spectrum are closely related. The scan rate R is simply the repetition rate of the laser pulses. When a pulse is stretched by GVD, the mapping between wavelength and time is described by $\Delta\tau = |D|z\Delta\lambda$, where $\Delta\lambda$ is the optical bandwidth, D is the GVD per unit length (in $ps \cdot nm^{-1} \cdot km^{-1}$), and $\Delta\tau$ is the temporal span of the mapped spectrum. To avoid temporal overlap between adjacent stretched pulses, $\Delta\tau$ must remain smaller than R^{-1}. The number of sampled points in the time-stretched waveform is given by $N = f\Delta\tau = f|D|z\Delta\lambda$, where f is the sampling rate of the digitizer. The achievable spectral resolution is limited by several factors: the digitizer sampling rate, yielding $\delta\lambda_{dig} = (f|D|z)^{-1}$; the analog bandwidth B of the detection system, giving $\delta\lambda_{det} = (B|D|z)^{-1}$; and the GVD itself, which imposes a far-field-equivalent limit $\delta\lambda_{GVD} = \lambda_0\sqrt{2/(c|D|z)}$, where λ_0 is the center wavelength and c is the speed of

light. In practice, the overall spectral resolution is determined by the most restrictive among these limits. While this analysis assumes that β_2 dominates, higher-order dispersion terms (β_3, β_4, ⋯) can distort the frequency-to-time mapping, particularly for broadband ultrashort pulses or extremely large dispersion. Such terms break the strict linear wavelength-time relation, leading to spectral warping and asymmetric stretching, most pronounced at the spectral edges. These effects can be mitigated by careful selection of dispersive media, such as dispersion-compensating fibre or chirped fibre Bragg gratings, and by operating within the temporal far-field regime so that higher-order terms remain negligible compared to β_2.

Owing to its simplicity and ability to acquire spectra at the laser repetition rate, the DFT has become an indispensable tool in ultrafast laser research. In real-time measurements, consecutive stretched pulses are detected by a high-speed photodiode and digitized for direct single-shot spectral retrieval, enabling statistical analysis of shot-to-shot variations. In the field of ultrashort pulse lasers, this capability has enabled real-time observation of mode-locking startup and noise evolution, tracking of soliton interactions and breathing dynamics, monitoring of multi-pulsing transitions, measurement of spectral broadening in nonlinear fibres and chirped-pulse amplification systems, and single-shot detection of rare phenomena such as soliton explosions and optical rogue waves.

3.6 Conclusion

In this chapter, we have developed the theoretical framework necessary for the study of Yb-doped ultrafast fibre lasers. The gain dynamics were first described using a four-level rate-equation model, which was simplified into an effective two-level system under the assumption of fast relaxation of pump and lower-laser levels. This treatment enabled the derivation of steady-state population inversion and gain expressions, providing the foundation for amplifier and oscillator modelling.

The propagation of femtosecond pulses in fibres was examined, with emphasis on the interplay between dispersion and nonlinear effects that dictates pulse evolution. The inclusion of both second- and higher-order dispersion, together with SPM and related nonlinear processes, forms the basis for understanding pulse broadening, compression, and spectral shaping. Subsequently, the mechanisms of mode-locking were reviewed, with emphasis on soliton, breathing, and dissipative regimes. The MO was introduced as a representative example of dissipative mode-locking, illustrating how strong spectral filtering combined with nonlinear broadening can stabilise ultrashort pulses. Finally, we introduced the concept of DFT, a real-time diagnostic technique that provides unprecedented access to the transient and stochastic behaviour of ultrafast lasers. Together, these elements establish the physical principles that underpin the

experimental and numerical investigations presented in later chapters. By combining gain dynamics, nonlinear fibre optics, mode-locking mechanisms, and advanced diagnostics, we are equipped with a comprehensive framework to understand and control the operation of Yb-doped ultrafast fibre systems.

Chapter 4 Numerical simulation of ultrafast pulses in fibres

4.1 Introduction

The simulation of ultrafast pulse propagation in fibre laser systems requires accurate modeling of dispersion, nonlinearity, and gain. This chapter establishes the numerical framework used throughout this thesis, focusing on solving the GNLSE and incorporating both SS and Dy gain models for rare-earth-doped fibres. Two numerical solvers are implemented to handle the nonlinear propagation: the split-step Fourier method (SSFM), which treats linear and nonlinear effects in alternating domains, and the fourth-order Runge-Kutta (RK4) method, which enables more accurate integration of the nonlinear operator and longitudinally varying effects such as gain or Raman response. The appropriate solver is selected based on simulation demands for precision or efficiency. Special emphasis is placed on modeling the gain dynamics in YDFs, which play a central role in pulse amplification and MO operation. A SS model is first introduced, where the upper-state population is calculated directly from time-averaged pump and signal powers, allowing fast estimation of the gain profile with minimal computation. To address situations where gain recovery and depletion vary within and between pulses, a Dy gain model is developed, which solves the time-dependent rate equations in tandem with pulse propagation. A modular simulation structure is employed, allowing for flexible construction of full cavity models from independently defined components. The two gain models are compared in terms of accuracy and computational load, using test cases at different repetition rates. The final section provides a unified set of simulation parameters used in later chapters, including dispersion, nonlinearity, and gain fibre specifications.

4.2 Background: the GNLSE and common numerical solvers

4.2.1 The generalized nonlinear Schrödinger equation

To accurately simulate ultrashort pulse evolution in fibre-based systems, a comprehensive physical model is required to describe the effects of dispersion, nonlinearity, and optical gain. These effects collectively govern the temporal and spectral dynamics of femtosecond pulses, especially under high peak power and broad bandwidth conditions.

In particular, the propagation of an ultrashort pulse in an optical fibre is governed by the GNLSE, which accounts for the combined effects of dispersion, Kerr nonlinearity, Raman scattering, and fibre loss. The GNLSE in the time domain is expressed as[105]:

$$\frac{\partial A}{\partial z} = -\frac{\alpha}{2}A + i\sum_{k=2}^{n}\frac{i^k i\beta_k}{k!}\frac{\partial^k A}{\partial T^k} + i\gamma|A|^2A - \frac{\gamma}{\omega_0}\frac{\partial}{\partial T}(|A|^2A) - i\gamma T_R A\frac{\partial|A|^2}{\partial T} \quad (4\text{-}1)$$

Here, A is the slowly varying envelope of the pulse and α represents the linear loss. The second term on the right-hand side is the dispersion term. β_k is the kth-order dispersion coefficient. It is usually enough to consider high to third order dispersion for most conditions. The last three terms correspond to SPM, self-steepening and Raman effects. This equation is expressed in a retarded time frame defined by: $T = t - z/v_g$, where $v_g = 1/\beta_1$ is the group velocity. The nonlinear coefficient $\gamma = \frac{n_2\omega_0}{A_{eff}}$, where the nonlinear-index coefficient n_2 is set to $2.1 \times 10^{-20}\, m^2/W$ for a silica fibre, ω_0 is the centre optical frequency and the A_{eff} is the effective core area. Raman effect related T_R is defined as[105]:

$$T_R \equiv \int_{-\infty}^{\infty} tR(t)dt = f_R\int_{-\infty}^{\infty} th_R(t)dt = f_R\frac{d\left(Im\widetilde{h_R}\right)}{d(\Delta\omega)}\bigg|_{\Delta\omega=0} \quad (4\text{-}2)$$

The response function $R(t)$ consists of an instantaneous electronic response and a delayed Raman response: $R(t) = (1 - f_R)\delta(t) + f_R h_R(t)$, where f_R denotes the fractional contribution of the delayed Raman. Based on experimental measurements, $f_R \approx 0.18$ for silica fibres. A widely used analytic form of $h_R(t)$ is [105]:

$$h_R(t) = \frac{\tau_1^2 + \tau_2^2}{\tau_1\tau_2^2}e^{-t/\tau_2}sin(-t/\tau_1), t \geq 0 \quad (4\text{-}3)$$

with $\tau_1 = 12.2fs$ and $\tau_2 = 32fs$.

The above equation can be used to model the pulse evolution in passive fibres (PFs). To model pulse evolution in gain fibres, a position- and frequency- dependent gain term is added:

$$\frac{\partial A}{\partial z} = -\frac{\alpha}{2}A + \frac{g(z,\omega)}{2}A + i\sum_{k=2}^{n}\frac{i^k i\beta_k}{k!}\frac{\partial^k A}{\partial T^k} + i\gamma|A|^2A - \frac{\gamma}{\omega_0}\frac{\partial}{\partial T}(|A|^2A) - i\gamma T_R A\frac{\partial|A|^2}{\partial T} \quad (4\text{-}4)$$

The four-level system can be used to describe the $g(z,\omega)$ of YDF as:

$$g(z,\omega) = \frac{\sigma_e(\omega)\Delta N(z) - \sigma_a(\omega)\left(N - \Delta N(z)\right)}{2} \quad (4\text{-}5)$$

Here, $\sigma_a(\omega)$ and $\sigma_e(\omega)$ are absorption cross section and emission cross section, respectively, as shown in Figure 4.1. ΔN is the population difference between upper and lower energy levels. Since the relaxation times are very short in the four-energy level system, it can be simplified that the sum of the ion numbers of these two energy levels is the total number of doped ions N. Here, the value of N is set to $5 \times 10^{25}/m^3$

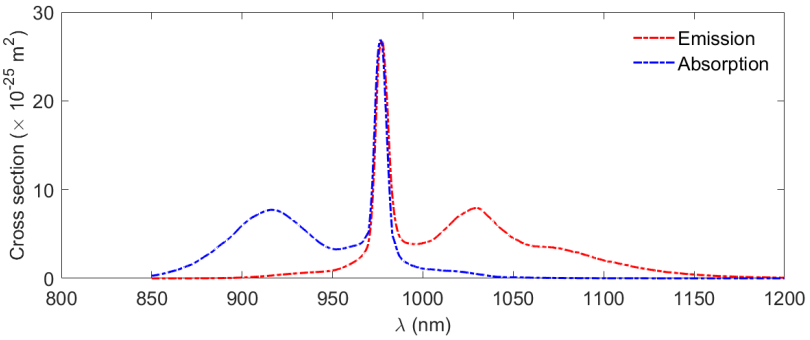

Figure 4.1 Absorption (blue curve) and emission (red curve) section spectrum of Yb-doped fibre.

4.2.2 Split-step Fourier and Runge-Kutta methods

4.2.2.1 Split-Step Fourier Method

The SSFM is a widely used numerical scheme for solving the GNLSE. It exploits the fact that dispersion and nonlinearity act independently over short propagation steps. The total evolution over one step Δz is approximated by sequentially applying the linear (dispersive) and nonlinear operators:

$$A(z+\Delta z,T) \approx exp\left(\widehat{D}\cdot\frac{\Delta z}{2}\right)\exp\left(\widehat{N}\cdot\Delta z\right)exp\left(\widehat{D}\cdot\frac{\Delta z}{2}\right)A(z,T) \tag{4-6}$$

Here, $\widehat{D}$ represents the linear dispersion operator, including dispersions, loss and gain, and is applied in the frequency domain via finite-Fourier-transfrom (FFT). The nonlinear operator $\widehat{N}$ is applied in the time domain and includes SPM, self-steepening, and Raman effects.

The implementation steps are:

1. Transform $A(z,T)$ to the frequency domain to apply the linear operator $exp\left(\widehat{D}\cdot\frac{\Delta z}{2}\right)$.

2. Transform back to the time domain and apply the nonlinear operator $\widehat{N}$ over Δz.

3. Transform to frequency domain again and apply $exp\left(\widehat{D}\cdot\frac{\Delta z}{2}\right)$ to complete the step.

This symmetric form ensures second-order accuracy. SSFM is computationally efficient and suitable for long-distance steady-state simulations, but its accuracy diminishes in highly nonlinear or strongly coupled systems.

4.2.2.2 Runge-Kutta Method

The RK4 method is a widely used numerical integrator for solving ordinary differential equations with high accuracy. In the context of ultrafast pulse simulation, RK4 provides a robust and flexible framework for computing nonlinear evolution in the GNLSE, particularly when combined with the

split-step method. The classical RK4 method is a widely used algorithm for numerically solving ordinary differential equations of the form

$$\frac{dy}{dz} = f(z, y) \tag{4-7}$$

over discrete steps of size Δz. Within each step, the RK4 procedure proceeds as follows:

1. Compute the first estimate of the slope:

$$k_1 = \Delta z \cdot f(z, y) \frac{dy}{dz} = f(z, y) \tag{4-8}$$

2. Estimate at the midpoint using k_1:

$$k_2 = \Delta z \cdot f\left(z + \frac{\Delta z}{2}, y + \frac{k_1}{2}\right) \tag{4-9}$$

3. Repeat midpoint evaluation with k_2:

$$k_3 = \Delta z \cdot f\left(z + \frac{\Delta z}{2}, y + \frac{k_2}{2}\right) \tag{4-10}$$

4. Estimate the slope at the endpoint using k_3:

$$k_4 = \Delta z \cdot f(z + \Delta z, y + k_3) \tag{4-11}$$

5. Update the solution:

$$y(z + \Delta z) = y(z) + \frac{1}{6}(k_1 + 2k_2 + 2k_3 + k_4) \tag{4-12}$$

In this study, the RK4 method is employed for two main purposes: 1. Nonlinear Operator Evaluation: Within each split-step interval, the linear and nonlinear effects are separated. The linear dispersive terms are evaluated in the frequency domain, while the nonlinear terms, including SPM, self-steepening, Raman scattering, and gain, are treated in the time domain using the RK4 scheme. 2. Pump Power Evolution: A standard RK4 routine is employed to solve a set of coupled differential equations describing the longitudinal evolution of pump and signal powers along the fibre. These equations are governed by the local population inversion $\Delta N(z)$, which itself depends on both pump and signal intensities. This approach enables accurate modeling of the spatially varying gain profile in active fibres such as Yb-doped fibre amplifiers.

The RK4 method provides fourth-order accuracy, with global error scaling as $\mathcal{O}(\Delta z^4)$. It offers a good balance between accuracy and computational efficiency. RK4 is explicit and stable for a wide range of step sizes, making it suitable for nonlinear systems with spatially varying parameters.

4.3 Modeling strategies for pulse evolution

4.3.1 Steady-state gain modelling and numerical implementation

4.3.1.1 Physical model and assumptions

In fibre-based amplification and resonant cavity systems, the evolution of the optical field is governed by the interaction between dispersion, Kerr nonlinearity, and optical gain. The latter is determined by the population inversion of the active medium, which depends on the balance between pump-induced excitation and signal-induced depletion. In this work, the gain medium is described using a SS gain approximation, which assumes that the population inversion adjusts quasi-instantaneously to the locally averaged optical intensities. This approximation is well justified under stable operating conditions, including CW amplification, quasi-CW pumping of pulsed systems, and mode-locked fibre cavities operating near steady state. In such regimes, the upper-state lifetime τ is typically orders of magnitude longer than the optical pulse duration, while remaining short compared to the timescale over which average pump and signal powers vary along the fibre. The main assumptions of the SS gain model used throughout this thesis are summarized as follows:

1. scalar model: All quantities depend only on the propagation coordinate z. Radial dependence of the optical modes and spatial hole burning effects are neglected. The polarization is ignored. Mode overlap is incorporated through a constant confinement factor Γ.
2. Steady-state population inversion: The population inversion is described by a time-averaged equilibrium value $\Delta N(z)$, rather than time-resolved carrier dynamics within individual pulses.
3. Equivalent average-power treatment of pulsed signals: For pulsed operation, the effect of the signal on the inversion is approximated by its local average power or spectral energy density, avoiding explicit resolution of ultrafast gain depletion and recovery during each pulse.
4. No dynamic gain transients: Gain recovery, relaxation oscillations, and Q-switching-like dynamics are not explicitly modeled. These effects may become relevant during startup transients or strong perturbations but are outside the scope of the present SS framework.
5. Uniform dopant distribution and fixed material parameters: The total dopant density N, emission and absorption cross-sections $\sigma_e(\omega)$, $\sigma_a(\omega)$, and upper-state lifetime τ are assumed constant along the fibre.

Within these assumptions, the SS gain model provides a computationally efficient yet physically consistent description of energy exchange between pump, signal, and the gain medium.

4.3.1.2 Steady-state population inversion

We denote the populations of the upper and lower laser levels by $N_E(z)$ and $N_G(z)$, respectively, such that the total dopant density satisfies

$$N = N_E(z) + N_G(z). \tag{4-13}$$

The population inversion is defined as

$$\Delta N(z) = N_E(z) - N_G(z). \tag{4-14}$$

Under steady-state conditions, the rate equations for the two-level system admit a closed-form solution for $\Delta N(z)$, obtained by balancing stimulated absorption, stimulated emission, and spontaneous decay. Using the notation introduced in Chapter 3, the inversion at position z can be written as

$$\Delta N(z) = \frac{\sum_i \Gamma \sigma_a(\omega_i) I(z,\omega_i)/\hbar\omega_i}{\sum_i \frac{\Gamma\big(\sigma_a(\omega_i) + \sigma_e(\omega_i)\big) I(z,\omega_i)}{\hbar\omega_i} + 1/\tau} \tag{4-15}$$

where $I(z,\omega_i)$ represents the local optical intensity (or spectral intensity) at frequency ω_i, including contributions from both pump and signal fields. The summation index i runs over all discrete spectral components included in the numerical model. This expression yields the local equilibrium inversion corresponding to the instantaneous average optical intensities at position z. Importantly, no temporal derivatives appear in Eq. (4-15), reflecting the steady-state nature of the approximation.

4.3.1.3 Gain spectrum and coupling to field propagation

Once $\Delta N(z)$ is obtained, the frequency-dependent gain coefficient is calculated as

$$g(z,\omega) = \Gamma\{\sigma_e(\omega)\Delta N(z) - \sigma_a(\omega)[N - \Delta N(z)]\} \tag{4-16}$$

This gain spectrum enters the linear operator of the field propagation equation and determines the amplification or attenuation of each spectral component. In this work, the optical field envelope $A(z,t)$ is propagated using the GNLSE, solved numerically by the SSFM. The linear operator includes dispersion up to the required order and the gain term $g(z,\omega)$, while the nonlinear operator accounts for Kerr nonlinearity and, where relevant, self-steepening. The spectral bandwidth considered in this thesis typically exceeds several tens of nanometers (corresponding to pulse durations in the few-tens-of-femtoseconds regime), which necessitates inclusion of higher-order dispersion terms beyond β_2, as well as self-steepening effects. These

contributions become non-negligible when the pulse bandwidth approaches a significant fraction of the carrier frequency or spans regions of rapidly varying dispersion.

4.3.1.4 Numerical implementation and cavity algorithm

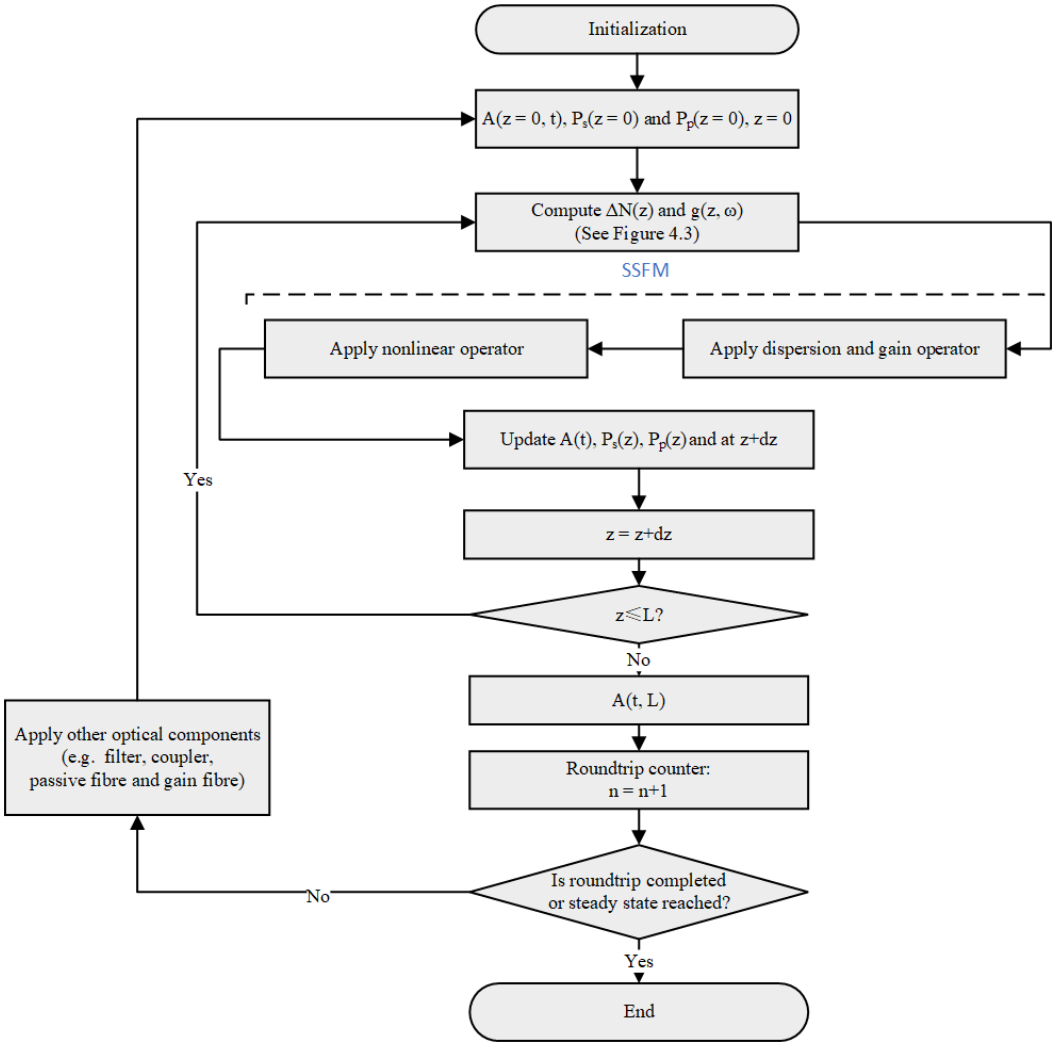

Figure 4.2 Flowchart of the resonant cavity simulation under the steady-state gain approximation. Each active fibre segment is solved using the SSFM with locally updated dispersion, nonlinearity, and gain operators. The population inversion $\Delta N(z)$ is computed at each spatial step. The round-trip loop continues until convergence or a predefined iteration count is reached.

The complete resonant cavity simulation is implemented using a modular round-trip propagation framework, as schematically illustrated in Figure 4.2. Each optical component in the cavity, including active fibres, PFs, filters, and couplers, is treated as an independent module and sequentially applied in a round-trip loop. The algorithm proceeds as follows:

1. Initialization: The optical field $A(z = 0, t)$, pump power $P_p(z = 0)$, and signal power $P_s(z = 0)$are initialized. The spatial coordinate is set to $z = 0$, and the round-trip counter is initialized.

2. Active fibre propagation: For each active fibre segment, the field is propagated along the fibre length using the SSFM. At each spatial step Δz: The local pump and signal powers $P_p(z)$ and $P_s(z)$ are first updated. Based on these values, the population inversion $\Delta N(z)$ is computed using Eq. (4-15) , and the corresponding gain spectrum $g(z,\omega)$ is evaluated using Eq. (4-16). Subsequently, the linear operator, including dispersion and gain, and the nonlinear operator are applied sequentially to update the field envelope $A(z,t)$.
3. Passive components: For PFs and other passive elements, the same SSFM framework is used, but gain-related calculations are omitted. Only dispersion and nonlinear effects are applied.
4. Round-trip update: After the field traverses all cavity components, the round-trip index is incremented, and the output field $A(t,L)$ is fed back as the input for the next round trip.
5. Termination criterion: The simulation continues until either a predefined number of round trips is reached or a steady state is achieved, defined by convergence of output energy, spectral shape, or temporal waveform.

The subroutine responsible for computing $\Delta N(z)$and $g(z,\omega)$at each spatial step is detailed in Figure 4.3.

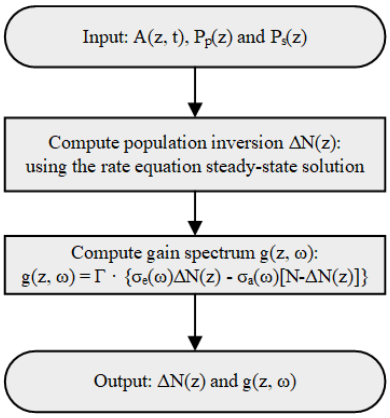

Figure 4.3 Subroutine for computing the local steady-state population inversion and gain spectrum. The inversion $\Delta N(z)$is obtained from the steady-state solution of the rate equations using local pump and signal powers, and subsequently used to calculate the frequency-dependent gain coefficient $g(z,\omega)$.

4.3.1.5 Limitations and outlook toward advanced modelling

While the SS gain approximation enables efficient simulation of complex resonant cavities, it inherently neglects spatial and temporal gain dynamics. A more complete description would require solving the full time-dependent rate equations, potentially coupled to transverse mode dynamics, leading to spatio-temporal or even spatio-spectral models. Such approaches, while more accurate during transients or strong perturbations, are computationally demanding and

often impractical for long cavity simulations involving hundreds or thousands of round trips. Alternative numerical strategies include reduced-order models, adaptive time-scale separation methods, or hybrid schemes in which dynamic gain is resolved only during critical phases (e.g., startup or perturbation events). In this context, data-driven or AI-assisted approaches may play a supporting role, for example by accelerating parameter sweeps, identifying attractor states, or learning surrogate models that approximate gain dynamics without explicitly solving the full rate equations. However, such methods should be regarded as complementary tools rather than replacements for physically grounded modelling.

4.3.2 Dynamic gain modelling and numerical implementation

4.3.2.1 Motivation and scope of the dynamic gain model

While the SS gain approximation provides an efficient description of energy exchange under near-equilibrium conditions, it inherently neglects the temporal evolution of the population inversion. This limitation becomes critical in systems where strong gain depletion, significant recovery between pulses, or non-equilibrium operation play an essential role, such as during startup dynamics, low-repetition-rate operation, or perturbative studies of resonant cavities. To address these effects, we implement a Dy gain model, in which the evolution of the upper-state population is explicitly tracked over successive round trips. The Dy model retains the modular cavity structure and field propagation framework used in the SS approach, but replaces the static inversion profile with a round-trip–resolved population dynamics model based on the rate equations. The key idea is to decouple the ultrafast signal-induced gain depletion, occurring on the timescale of the optical pulse, from the slow pump-induced gain recovery, occurring over the inter-pulse interval. This separation is justified by the large disparity between the pulse duration (fs–ps) and the repetition period (ns–μs) under CW pumping.

4.3.2.2 Definition of population inversion variables

In the Dy gain model, the evolution of the gain medium within each round trip is described by explicitly separating signal-induced depletion and pump-induced recovery of the population inversion. To this end, three inversion-related quantities are introduced at each spatial position z. The initial inversion $\Delta N_i(z)$is defined as the population inversion immediately before the arrival of the optical pulse. It represents the available upper-state population and is used to compute the local gain spectrum during pulse amplification. During pulse propagation, stimulated emission extracts energy from the gain medium. The corresponding depleted inversion amount, denoted as $\Delta N_e(z)$, quantifies the reduction of the population inversion induced by the signal. Importantly, $\Delta N_e(z)$represents a consumed inversion amount, rather than a population state. After pulse amplification, the remaining population inversion is given by

$$\Delta N_{\text{after\_amp}}(z) = \Delta N_i(z) - \Delta N_e(z), \tag{4-17}$$

which describes the population inversion immediately after the pulse has passed through the gain medium. This formulation allows the Dy model to explicitly capture the asymmetric roles of gain depletion during pulse amplification and gain recovery during the inter-pulse interval, while maintaining computational efficiency.

4.3.2.3 Gain spectrum evaluation and depletion step

At each spatial position z within an active fibre segment, the gain spectrum $g(z, \omega)$ is computed using the initial inversion $\Delta N_i(z)$ by Eq. (4-16). This gain coefficient is applied to the optical field during propagation using the SSFM, in combination with dispersion and nonlinear effects. During this step, the signal extracts energy from the gain medium, leading to a reduction in the population inversion. The exhausted inversion $\Delta N_e(z)$is then computed by integrating the rate equation over the pulse interaction, accounting explicitly for signal-induced stimulated emission. In contrast to the SS model, no assumption of instantaneous equilibrium is made during this step.

4.3.2.4 Gain recovery between round trips

After completion of a full round trip, the remaining inversion $\Delta N_{\text{after\_amp}}(z)$ serves as the initial condition for gain recovery during the inter-pulse interval. The recovery process is simulated at a fixed pump power P_p, assuming no signal is present during this time window. By integrating the rate equation over the inter-pulse duration, the population inversion is increased by a recovery amount $\Delta N_{\text{recovery}}(z)$. As a result, the initial inversion for the subsequent round trip is updated according to

$$\Delta N_i^{(n+1)}(z) = \Delta N_{\text{after\_amp}}^{(n)}(z) + \Delta N_{\text{recovery}}^{(n)}(z), \tag{4-18}$$

where the recovery term is governed by pump absorption and spontaneous decay. This decoupled treatment of depletion and recovery is justified by the large separation between the ultrafast pulse duration and the inter-pulse spacing under continuous-wave pumping.

4.3.2.5 Numerical algorithm and cavity implementation

The overall Dy gain simulation follows the same modular round-trip structure as the SS model, with additional steps introduced to account for population dynamics. The algorithm proceeds as follows:

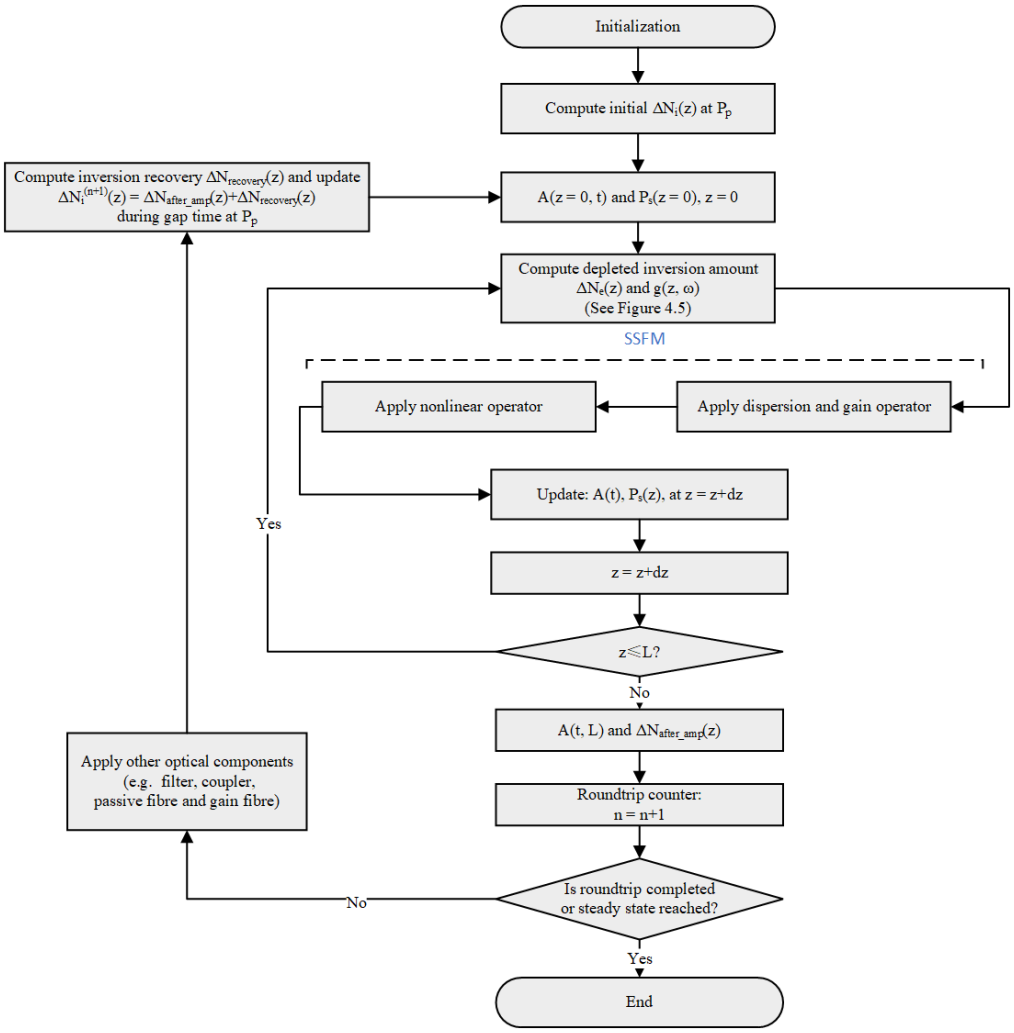

Figure 4.4 Flowchart of the resonant cavity simulation under the dynamic gain model. The algorithm explicitly separates signal-induced gain depletion and pump-induced recovery of the population inversion. At each spatial step, the gain spectrum is computed from the initial inversion $\Delta N_i(z)$, while the depleted inversion amount $\Delta N_e(z)$ is evaluated during pulse amplification, yielding the post-amplification inversion $\Delta N_{\text{after\_amp}}(z)$. Gain recovery during the inter-pulse interval is then used to update $\Delta N_i(z)$ for the next round trip.

1. Initialization: An initial inversion profile $\Delta N_i(z)$ is computed at the pump power P_p. The optical field $A(z = 0, t)$ and spatial coordinate are initialized.
2. Active fibre propagation: For each spatial step Δz, the gain spectrum $g(z, \omega)$ is computed from $\Delta N_i(z)$. The optical field is then propagated using SSFM, including dispersion, nonlinearity, and gain. The depleted inversion amount $\Delta N_e(z)$ is evaluated from the rate equation, and the post-amplification inversion $\Delta N_{\text{after\_amp}}(z)$ is obtained.
3. Passive components: Passive fibres and other cavity elements are treated identically to the SS model, with gain-related calculations disabled.

4. Gain recovery: After completion of the round trip, gain recovery is simulated over the inter-pulse interval to compute $\Delta N_{\text{recovery}}(z)$ and update $\Delta N_i(z)$ for the next iteration.
5. Iteration and convergence: The round-trip counter is incremented, and the process repeats until either a predefined number of round trips is reached or a steady state is achieved.

The complete simulation flow is illustrated in Figure 4.4, while the gain calculation subroutine is detailed in Figure 4.5.

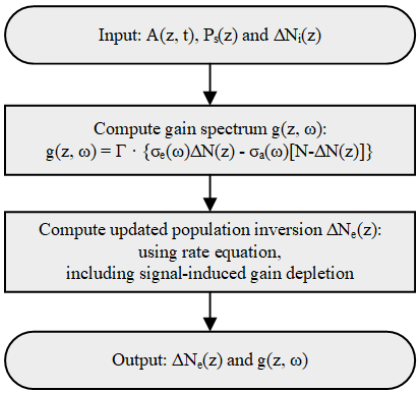

Figure 4.5 Subroutine for dynamic gain calculation. The gain spectrum is computed from the initial inversion $\Delta N_i(z)$. Signal-induced gain depletion yields the exhausted inversion $\Delta N_e(z)$, which is subsequently used to simulate pump-driven recovery before the next round trip.

4.3.2.6 Model capabilities and limitations

Compared to the SS approximation, the Dy gain model enables simulation of strong gain depletion and recovery effects, arbitrary pulse sequences and repetition rates, non-equilibrium initial inversion profiles, and transient dynamics during startup or perturbation. However, the model remains one-dimensional and neglects transverse spatial effects, spatial hole burning, and mode competition. Full spatio-temporal modelling would require solving coupled Maxwell–Bloch or multimode GNLSE–rate-equation systems, which are computationally prohibitive for long-cavity simulations involving many round trips. Reduced-order or hybrid approaches may offer a practical compromise between physical fidelity and computational efficiency.

4.3.3 Simulation parameters

The numerical simulations presented throughout this thesis rely on a consistent set of physical, fibre-specific, and numerical control parameters, which are summarized in Table 4.1, Table 4.2, and Table 4.3, respectively. Together, these parameters form the basis for modeling dispersion, nonlinearity, gain, and loss in both passive and active fibre segments. Table 4.1 lists the key material constants used for modeling YDFs, including the upper-state lifetime τ, nonlinear

refractive index n_2, dopant concentration N, and the emission and absorption cross sections. These quantities are held fixed across all simulations involving gain media, ensuring consistency in the evaluation of population inversion and the associated gain dynamics. Table 4.2 summarizes the geometric and dispersion-related properties of the fibre types used in the simulations, including the mode field diameter (MFD), cladding radius, fibre loss α, second-order dispersion coefficient β_2, and third-order dispersion coefficient β_3. The values correspond to typical specifications of commercially available fibres and are chosen to best reproduce the experimentally observed pulse characteristics. In addition, Table 4.3 provides the numerical parameters controlling the simulations, such as the temporal window, sampling resolution, spatial step size, and round-trip limits. These parameters are selected to ensure numerical stability and accuracy of the SSFM, and are applied consistently in both the SS and Dy gain models. Unless stated otherwise, the same parameter sets are used across the SS and Dy gain simulations to ensure direct comparability under different gain modeling assumptions. The specific role and sensitivity of selected parameters will be discussed in the context of individual simulation cases in later chapters.

Table 4.1 Key physical parameters used for simulating Yb-doped fibre segments.

τ	n_2	N
$0.85\ ms$	$2.1 \times 10^{-20}\ m^2/W$	$5.0 \times 10^{25}\ ions/m^3$

Table 4.2 Fibre parameters used in the simulations, including mode size, dispersion, and loss.

Fibre type	MFD (μm)	Cladding radius (μm)	α (dB/km)	β_2 (fs^2/mm)	β_3 (fs^3/mm)
PM-10/125[195]	11.6	62.5	0.5	23	58
PM-25/250[196]	20.6	125	0.5	20	62
PLMA-25/250[197]	20.6	125	0.5	20	62
PLMA-30/250[198]	23.4	125	0.5	20	62

Table 4.3 Numerical control parameters used in the SS and Dy cavity simulations.

Parameter	Symbol	Value / Range
Time window	T_{win}	62.5
Number of points	N_t	4096
Spatial step	Δz	2mm

Max round trips	N_{max}	5000
Repetition period (Dy)	T_R	$50ns - 1\mu s$

4.4 Comparative analysis of steady-state and dynamic gain models

To evaluate the impact of gain model selection on amplification accuracy, we perform a comparative simulation using both the SS and Dy gain models. The test case involves the continuous injection of a 500 fs Gaussian pulse with 20 pJ energy and a central wavelength of 1040 nm into a 1-m-long PLMA-25/250 gain fibre. Forward pumping is applied with a fixed pump power of 5 W. Given the upper-state lifetime $\tau = 0.85\ ms$, we examine two representative repetition rates: 10 kHz and 1 MHz. These cases correspond to markedly different recovery conditions between successive pulses, complete recovery at 10 kHz and strong depletion at 1 MHz, thus highlighting the regimes where Dy modeling becomes necessary. Figure 4.6 and Figure 4.7 compare the SS amplification results after convergence for the two repetition rates. Each figure includes the following panels: spectral evolution, spatial distribution of population inversion $N_2(z)$, pulse energy evolution, output spectrum and temporal waveform, and the gain depletion and recovery profiles used in the Dy model to determine whether stable amplification has been achieved. At 10 kHz, both models yield nearly identical results, validating the SS approximation for low-repetition-rate systems. In contrast, at 1 MHz, the SS model significantly overestimates gain, as it fails to account for incomplete inversion recovery between pulses. The Dy model accurately captures the reduced gain, spectral narrowing, and output pulse energy resulting from insufficient recovery time, making it essential for modeling high-repetition-rate amplification. However, this improved accuracy comes at the cost of significantly increased computational effort. The SS model requires only a single calculation. As shown in the captions of Figure 4.6 and Figure 4.7, the Dy model requires 40 and 2888 pulse injection iterations to reach convergence at 10 kHz and 1 MHz, respectively. At higher repetition rates, even more iterations are needed to achieve stability. Moreover, each iteration involves additional computations to resolve the population inversion $N_2(z)$ within a single pulse amplification cycle.

In general, the SS model remains an efficient and practical tool, and it is extensively employed in the MO simulations presented in Chapter 5, Chapter 6 and Chapter 7. Cross-comparison with experimental results confirms its accuracy in modeling amplification paths and pulse evolution. However, it should be noted that the SS model tends to underestimate the required pump power in high-repetition-rate scenarios. For the study of high-speed cavity dynamics in Chapter 8, where transient gain behavior plays a crucial role, the SS model becomes inadequate, and the Dy model is adopted to simulate the mode-locking establishment process of the MO.

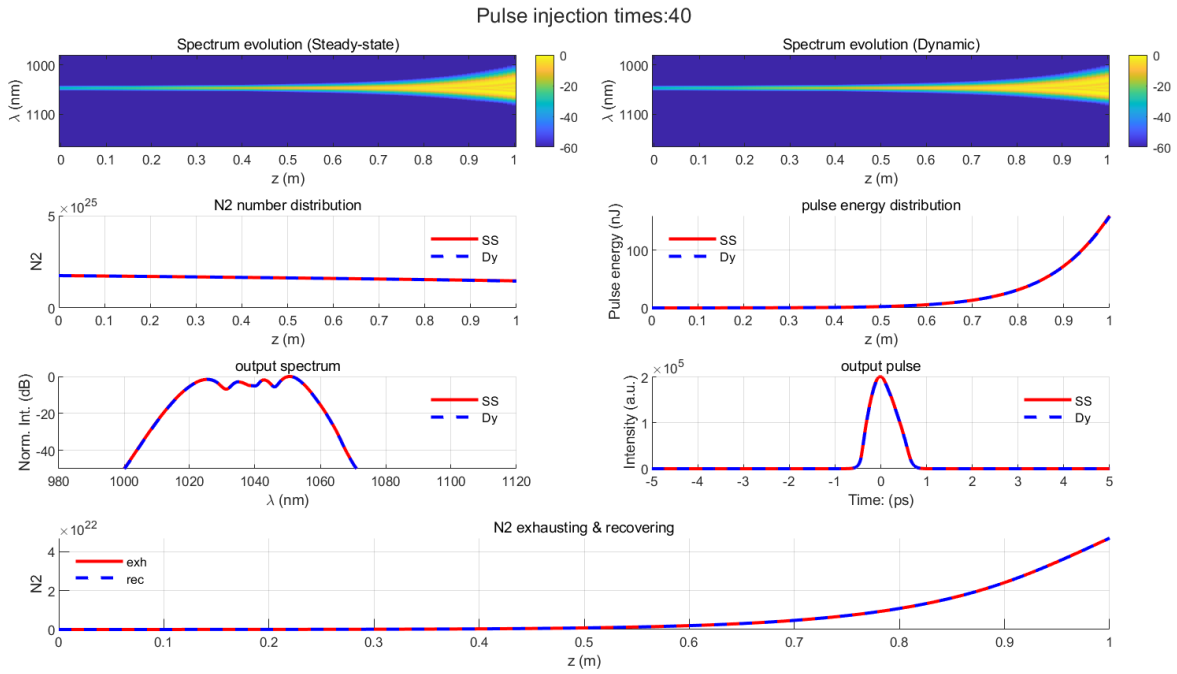

Figure 4.6 Comparison of SS and Dy gain models for 10 kHz pulse repetition rate. All results converge after 40 pulse injections in the Dy model. The negligible difference between SS and Dy confirms that the SS model remains valid under full recovery conditions.

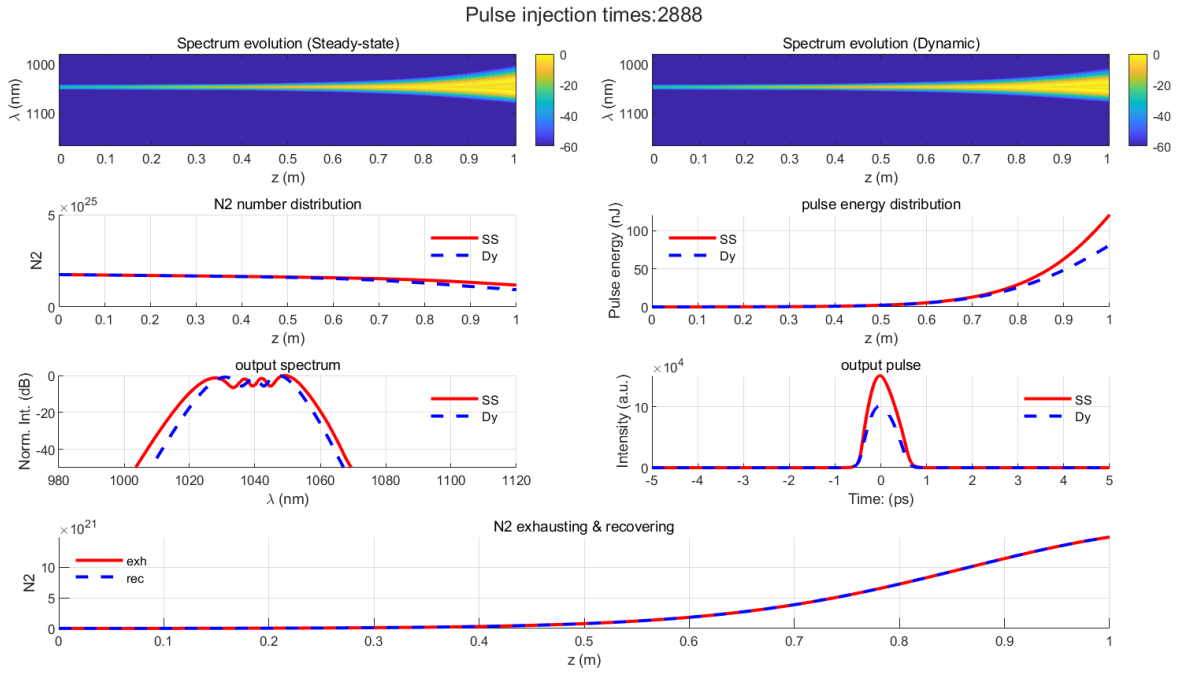

Figure 4.7 Comparison at 1 MHz repetition rate. The Dy model requires 2888 pulse injections to reach SS. The SS model significantly overestimates gain due to neglecting gain depletion. The Dy model reveals reduced pulse energy and spectral narrowing caused by incomplete inversion recovery.

4.5 Conclusion

This chapter provides a robust computational foundation for modeling ultrafast pulse propagation and amplification in fibre-based systems. By combining the GNLSE with efficient numerical solvers and physically realistic gain models, the simulation framework is capable of capturing both SS and time-dependent dynamics of high-energy pulse evolution. The SS gain model offers a computationally efficient approach that remains accurate in low-repetition-rate systems or conditions with complete inversion recovery. In contrast, the Dy gain model is necessary to simulate gain saturation and recovery effects in high-repetition-rate or strongly depleted regimes. A comparative analysis between these models highlights their respective strengths and limitations, guiding their application in later chapters. The tools and models established here form the basis for the optimization and experimental validation of MOs in Chapter 5 and Chapter 7, and for modeling cavity dynamics and mode-locking behavior in Chapter 8.

Chapter 5 High energy femtosecond Mamyshev oscillator

5.1 Introduction

Ultrafast fibre lasers based on the MO architecture have attracted considerable attention due to their exceptional pulse-energy scalability and robustness. The unique spectral-filtering mechanism in MOs, enabled by offset bandpass filters and strong nonlinear spectral broadening, allows stable mode-locked operation without the need for additional saturable absorbers. While the fundamental principles of MOs have been extensively studied, practical optimization strategies for achieving higher output energy and improved pulse quality remain active areas of research. In this chapter, we design and experimentally demonstrate a high-performance MO operating at 20 MHz. The oscillator configuration, seed source, and output characteristics are first described. Numerical modelling is then employed to guide energy optimization, analyzing the influence of gain-fibre length, pump-power distribution, filter offset, passive-fibre length, and dispersion. These simulations provide clear guidance for experimental optimization and design. The modelling framework is further extended to the seed laser, where the effects of pulse energy, central wavelength, pulse duration, and chirp on MO performance are systematically assessed. Based on these results, a simplified femtosecond fibre oscillator is proposed as a practical seed option, offering reduced system complexity without compromising output performance. Overall, this chapter presents a comprehensive study of a 20 MHz MO, combining experimental validation with numerical modelling to optimize both cavity parameters and seed-laser characteristics. It establishes a detailed experimental and theoretical foundation for further investigations of MO systems.

5.2 20MHz Mamyshev oscillator

5.2.1 Mamyshev oscillator setup

Based on the principle of MO, the experimental configuration of the oscillator is schematically illustrated in Figure 5.1. The MO was built comprising two active fibre amplifiers (the pre-amplifier and the main amplifier), two spectral filters and some free-space and PF cavity sections. The pre-amplifier consisted of a 2.5-m length of double-clad PM YDF (PM YDF; PLMA-YDF-25/250-VIII, Coherent) that had a numerical aperture (NA) of 0.065/0.46 for the core/cladding, respectively. The V-number of the fibre at 1 μm was estimated to be 5.1. To suppress high-order transverse modes and ensure single-mode operation, the fibre was coiled with a bending diameter of 7 cm.

According to the datasheet, the fibre cladding absorption is estimated to be approximately 1.7 dB/m at 915 nm and around 5.1 dB/m near 975 nm, respectively. The YDF in the pre-amplifier was forward pumped through a pump/signal combiner since the pre-amplifier only needed to provide low-power amplification to overcome the intracavity loss and to generate sufficient spectral broadening to enable MO operation. The YDF used in the main-amplifier is the same YDF in the pre-amplifier, but has a shorter length, 2m. The main-amplifier provided the main power amplification within the MO. Hence, to reduce the NPS accumulation in the main-amplifier, the YDF was backward cladding-pumped using free-space coupling. By injecting light from a superluminescent diode (SLD), the amplified spectra of the two gain stages were measured and are shown in Figure 5.2. The blue curve represents the input spectrum from the SLD, while the red and green curves correspond to the amplified spectra of the pre-amplifier and main amplifier, respectively. Notably, the gain peak of pre-amplifier is observed to be red shifted, which can be attributed to the longer fibre length. This slight separation in the gain peak is beneficial for effective mode locking as it allows for the spectral separation of two spectral filters.

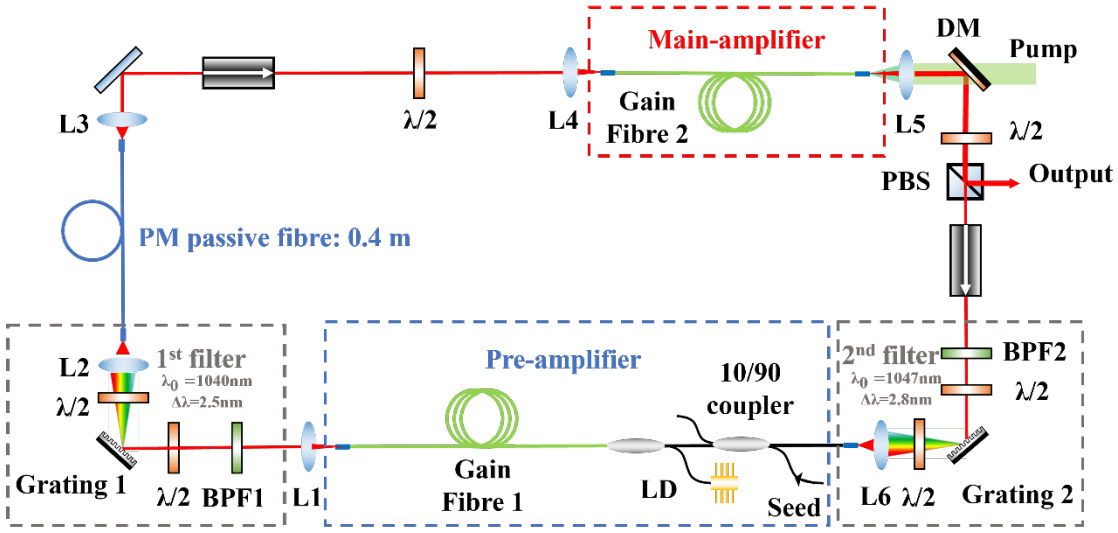

Figure 5.1 Schematic diagram of the MO used in the experiment. The cavity includes two spectrally offset bandpass filters and two Yb-doped fibre amplifiers to enable mode-locking. A 0.4 m PM PF is inserted between the pre-amplifier and the main amplifier. Both amplifiers are pumped by 975 nm multimode laser diodes (LDs). The oscillator is externally seeded to facilitate self-starting of the mode-locking process. Optical components: L, lens; DM, dichroic mirror; PBS, polarization beam splitter; λ/2, half-wave plate; BPF, bandpass filter.

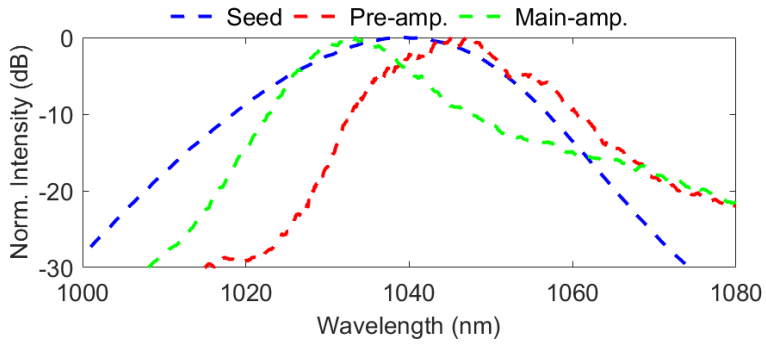

Figure 5.2 Input spectrum of the SLD and amplified spectra of the gain fibres. The blue, red, and green curves represent the SLD seed, pre-amplifier output, and main amplifier output, respectively.

The gain fibres used in this experiment were pumpedby multimode laser diodes (LDs) centered at a wavelength of 975 nm. Figure 5.3 (a) shows the measured pump power of the main amplifier as a function of LD drive current. Since the pump light is not fully absorbed by the active fibres, the absorbed pump power was determined by subtracting the residual (unabsorbed) pump power from the injected pump power. This method enables an accurate estimation of the pump power effectively coupled into the active fibre core. It is estimated that approximately 90% of the launched pump light is coupled into the main amplifier. In the setup, the main amplifier is pumped by four identical LDs (each rated at 60 W), while the pre-amplifier is pumped by a single LD of the same type. Figure 5.3 (b) presents the estimated absorbed pump powers for both amplifiers over a range of drive currents from 0.6 A to 3.0 A.

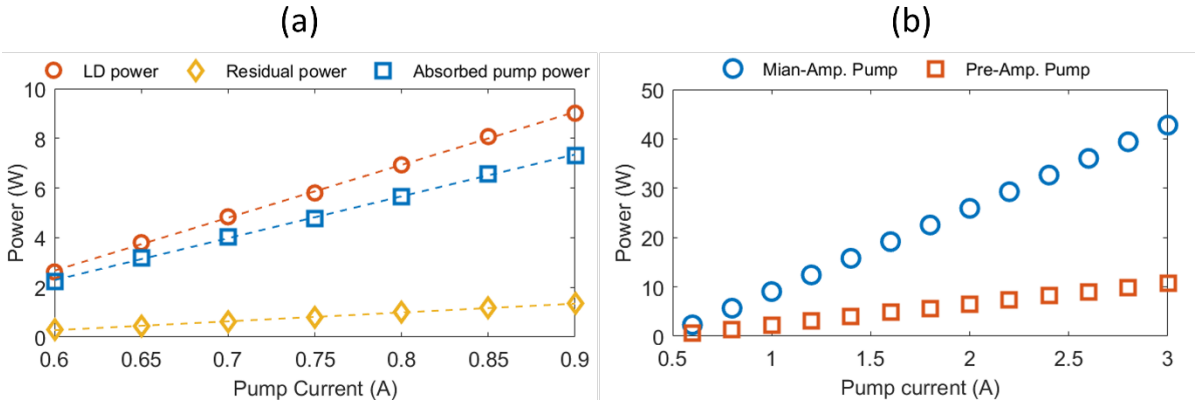

Figure 5.3 (a) Measured LD output, residual, and absorbed pump powers for the main amplifier as functions of LD drive current. (b) Estimated absorbed pump powers for the pre-amplifier (P_1) and main amplifier (P_2).

Fibre optic components used in the cavity are also constructed with PM fibres. The PFs have a core/cladding diameter of 10/125 μm (FUD-3460, Coherent), except for the fibre section directly spliced with pre-amplifier, which has a diameter of 25/250 μm (PLMA-GDF-25/250-M, Coherent). The length of PF that between L6 and gain fibre 1, PF1, and between L2 and L3, PF2, are 2.0 m and 0.4 m, respectively. To maximize the coupling efficiency within the cavity, different focal lengths

of aspherical lens pairs are employed. For the above-mentioned cavity, the focal length information of the lenses used can be found in Table 5.1. If the core size of the fibre used in the cavity changes, the focal length of the lens used must also be changed accordingly.

Table 5.1 The focal length of the aspherical lens in the MO.

Lens	1	2	3	4	5	6
Focal length (mm)	18.4	8.0	11.0	25.4	25.4	11.0

Diffraction gratings were employed to spatially distribute the spectrum before coupling into the single-mode fibres, thereby forming narrow-band spectral filters with Gaussian-shaped transmission profiles, which is an important feature to enable good MO performance[158]. The centre wavelengths and bandwidths of the filters can be tuned by changing the angle of grating and position of receiving fibre. The groove density of the grating 1 used in 1st filter and the grating 2 in 2nd filter are 300 line/mm and 1000 line/mm, respectively. Dielectric-coated band-pass filters (BPFs) with a bandwidth of 4 nm were placed before the gratings to enhance the spectral filtering extinction ratio and suppress parasitic lasing. It was measured that the spectral filtering extinction ratio was increased from 40 dB to over 60 dB with the insertion of the BPFs, which effectively suppressed the parasitic lasing during the high-power operation of the MO. As referenced in Figure 5.1, the 1st filter was set to be centered at 1040 nm with a 3 dB bandwidth of 2.5 nm, while the 2nd filter was centered at 1047 nm with a bandwidth of 2.8 nm. The measured transmission spectra of both filters are presented in Figure 5.4. The influence of these filter settings on mode-locking performance will be further discussed in Section 5.3. Half-wave plates (HWPs) are used to align the beam polarization and to ensure alignment with the principal axis of the PM fibre components (e.g. PM fibres, isolators, ISOs, and gratings). The output coupling ratio is adjusted at ~90% using a combination of a HWP and a PBS. The total optical cavity path length was measured to be ~ 15 m, corresponding to a fundamental repetition rate of ~ 20 MHz. A 10/90 fibre coupler was used to couple and inject an external seed laser at the 10% port into the cavity to initiate the mode-locked operation.

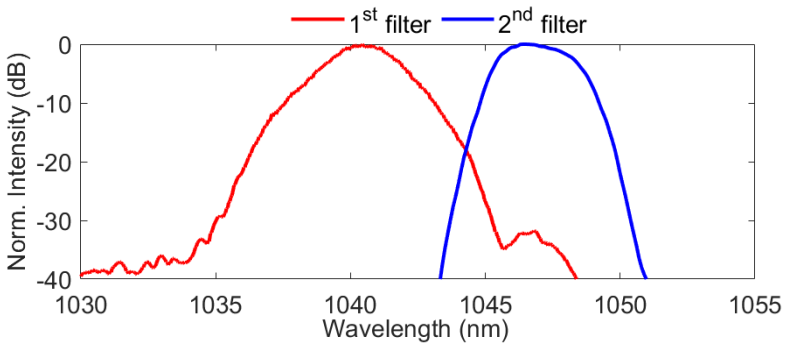

Figure 5.4 Measured transmission spectra of the 1st filter (red) and the 2nd filter (blue).

Single-pulse mode-locking was achieved when the pump powers of both the pre-amplifier and main amplifier exceeded their respective thresholds. Figure 5.5 (a) presents the output power of the MO as a function of the absorbed pump power of the main amplifier, with the pre-amplifier pump power held constant throughout the measurement. The absorbed power was calculated by subtracting the residual power from the launched pump power. A maximum output power of 7.6 W was recorded. At maximum pump power, the output spectrum, which is shown in Figure 5.5 (b), was centered at 1062 nm with a 10 dB bandwidth of 120 nm.

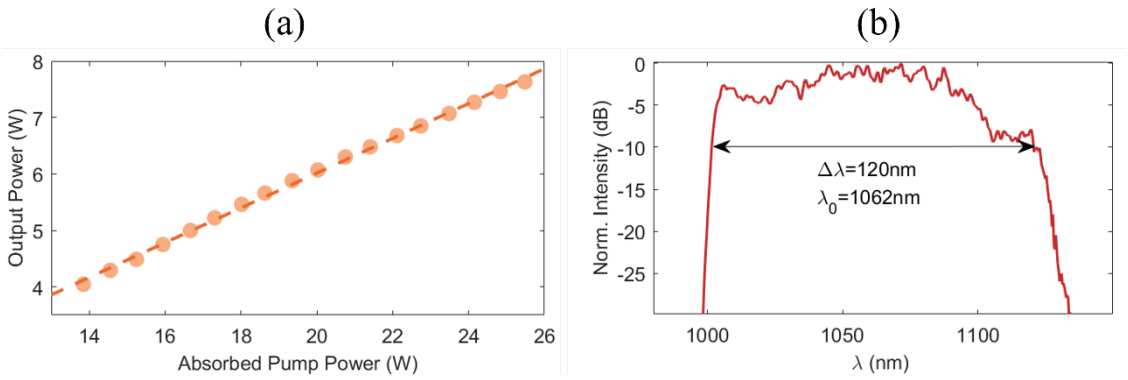

Figure 5.5 (a) Average output power of the MO as a function of absorbed pump power in the main amplifier. (b) Output optical spectrum at maximum pulse energy (381 nJ), centered at 1062 nm with a 10-dB bandwidth of 120 nm.

An external pulse compressor based on a pair of transmission gratings (1250 lines/mm, Ibsen) was implemented, as shown in Figure 5.6. The total transmission efficiency of the compressor was measured to be approximately 67% at full MO output power. To protect the autocorrelator from excessive power during measurement, the output beam was attenuated using a HWP and a PBS before entering the compressor. Figure 5.7 (a) shows the measured autocorrelation function (ACF) of the compressed pulse, along with the calculated TL ACF derived from the output spectrum. The measured and calculated ACFs had Full-width at half-maximum (FWHM) values of 51.7 fs and 42.8 fs, respectively. Assuming a Gaussian pulse shape, the actual pulse duration of the compressed pulse was estimated to be 36.7 fs. The measured ACF exhibits small pedestals, likely due to nonlinear chirp generated in the amplification stage that could not be fully compensated by the grating-based compressor. Based on the ACF, 74% of the total pulse energy was concentrated within the main lobe. Figure 5.7 (b) shows a broader time scan, confirming the absence of side pulses, further validating stable single-pulse operation. The radio-frequency (RF) spectrum, which is shown in Figure 5.8 (a) verifies a fundamental repetition rate of 20.03 MHz, with a signal-to-noise ratio (SNR) of 65.48 dB measured using a resolution bandwidth of 1 Hz and a span of 700 Hz. These results confirm the stable single-pulse mode-locked operation. Based on the measured output power and repetition rate, the maximum pulse energy was calculated to be 381 nJ.

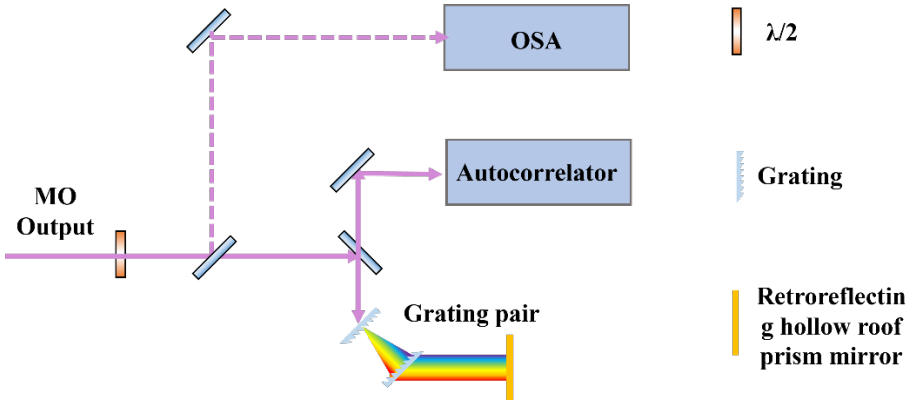

Figure 5.6 Schematic of the external pulse compressor used for characterizing the output of the MO. A pair of transmission gratings provides dispersion compensation.

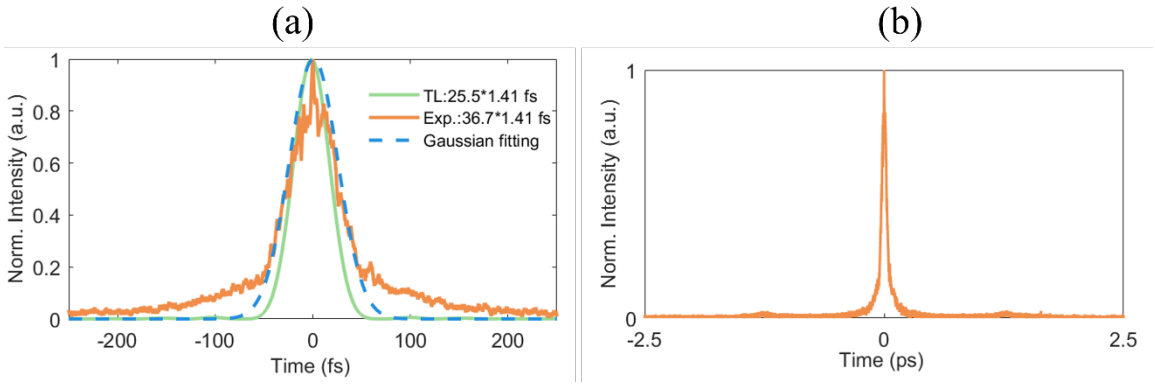

Figure 5.7 (a) Measured ACF (orange) of the compressed pulse and the calculated TL ACF (green). Blue dashed line: Gaussian fit. (b) Measured ACF of the compressed pulse over a 5 ps span, showing no evidence of side pulses.

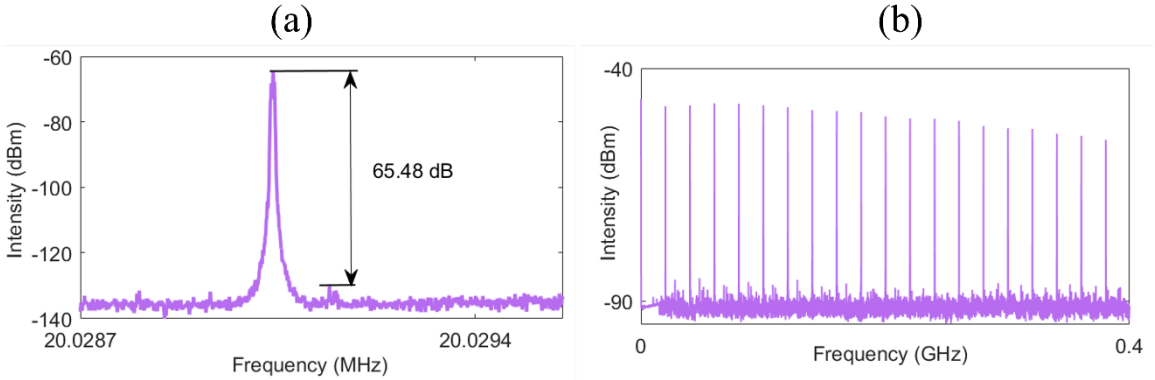

Figure 5.8 (a) RF spectrum measured at 20.03 MHz with a 1 Hz resolution bandwidth and 700 Hz span. (b) A wider span RF spectrum showing fundamental repetition rate and harmonics.

5.2.2 Seed laser

Due to the unique characteristics of the mode-locking process in the MO, special measures are typically required to initiate mode-locking. Several common approaches include: (1) injecting an external seed laser [158], (2) modulating the pump power [172], and (3) incorporating an external configuration for assistance [8]. In our case, mode-locking was initiated by injecting an external seed pulse.

The structure of the seed source is illustrated in Figure 5.9. It consists of four main modules: a SESAM-based mode-locked fibre laser, a fibre amplifier, a pulse compressor, and a pulse spectrum broadener. The seed generates a high-peak-power pulse train with a broad optical spectrum. The mode-locked fibre laser provides stable picosecond pulses. Figure 5.10 (a) shows the output power as a function of pump current. The working current was set to 244 mA. This particular value was chosen as further increasing the pump current would result in pulse splitting and the occurrence of double-pulse mode locking. The corresponding repetition rate under single-pulse operation is ~19.64 MHz, as shown in Figure 5.10 (b). The output spectrum at highest energy single-pulse mode-locking is presented in Figure 5.10 (c). The generated pulse is then amplified by a fibre amplifier, yielding an output power of ~60 mW. A pulse compressor is used to shorten the pulse duration. The ACF of the shortest pulse is shown in Figure 5.11 (b), with a FWHM of 422 fs, corresponding to a pulse duration of ~300 fs assuming a Gaussian profile. The compressed pulse is subsequently injected into a ~1.5 m segment of single mode fibre (SMF) to induce spectral broadening through SPM. As shown in Figure 5.11 (c), the 10-dB spectral width is broadened from 14.3 nm to 24.9 nm. Due to coupling losses in the seed system, the average power coupled into the MO is approximately 0.5 mW.

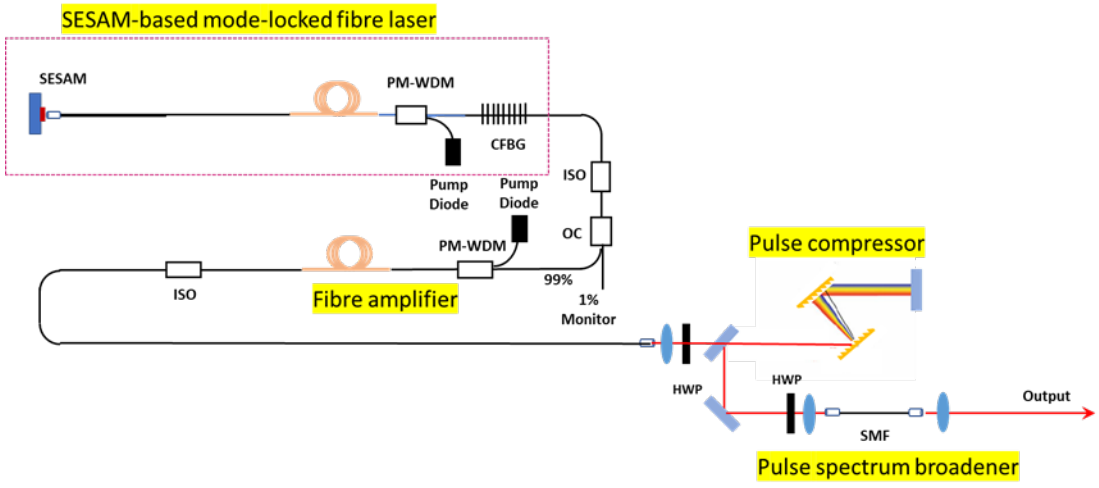

Figure 5.9 Schematic of the external seed source used to initiate mode-locking in the MO. The system comprises four modules: a SESAM-based mode-locked fibre laser, a fibre amplifier, a grating-based pulse compressor, and a nonlinear pulse spectrum

broadener. The spectrum broadening stage utilizes ~1.5 m of SMF to induce SPM. Optical components: SESAM, semiconductor saturable absorber mirror; PM-WDM, PM wavelength division multiplexer; CFBG, chirped fibre Bragg grating; ISO, isolator; OC, optical coupler.

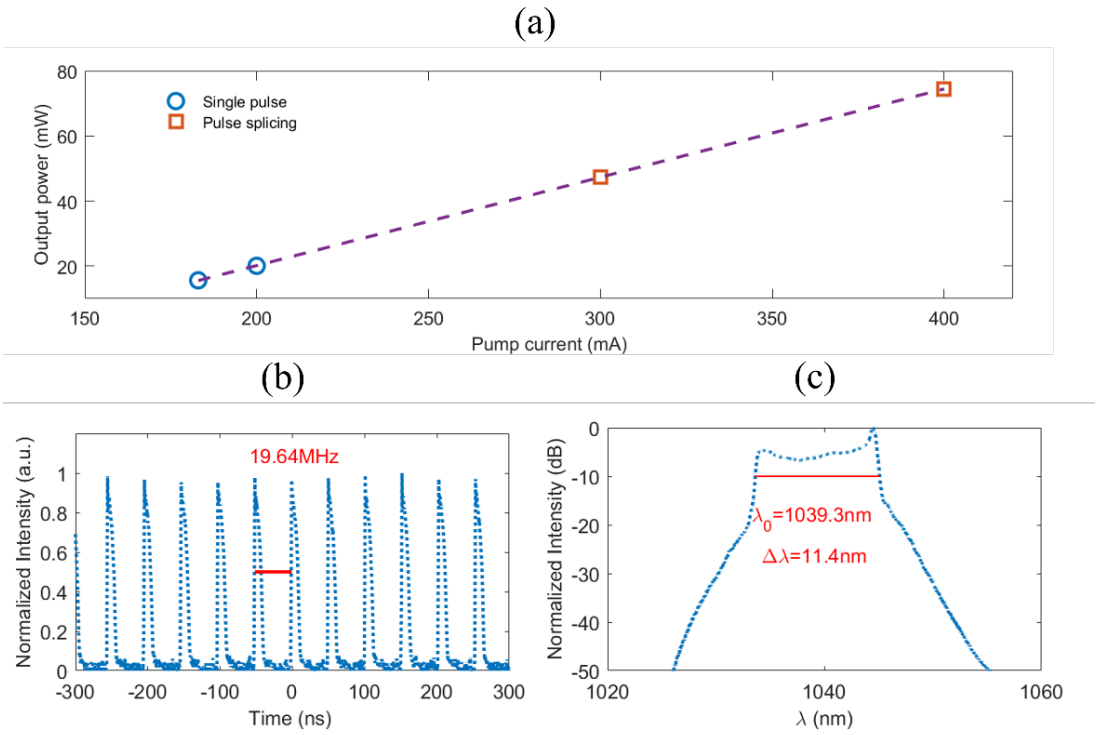

Figure 5.10 Single-pulse characteristics of the SESAM-based mode-locked fibre laser. (a) Output power as a function of pump current; (b) Pulse train measured on an oscilloscope, showing a repetition rate of ~19.64 MHz; (c) Optical spectrum at the operating point for single-pulse operation.

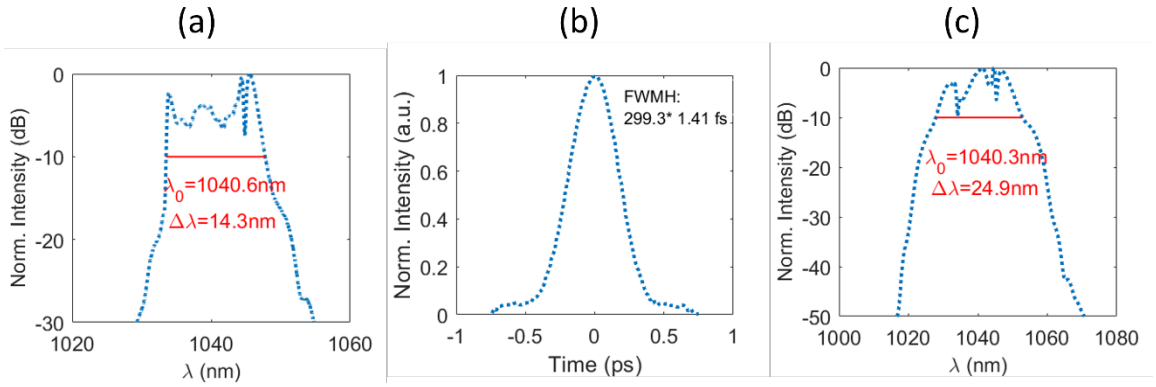

Figure 5.11 Performance of the seed pulse after amplification and compression. (a) Spectrum of the amplified pulse before compression; (b) Autocorrelation trace of the shortest compressed pulse, with an FWHM of 422 fs; (c) Optical spectrum after nonlinear spectral broadening in single-mode fibre, showing an increased 10-dB bandwidth from 14.3 nm to 24.9 nm.

5.3 Simulation and optimization

MO is a complex system whose operating characteristics are affected by many factors such as filtering, gain, and nonlinear effects. Therefore, the optimization direction to improve its output characteristics is not intuitive. Compared with experiments, it is more efficient and economical to use numerical simulation to determine the optimization settings. In this part, I performed numerical simulation on the afore-mentioned MO, compared it with the experimental results, and confirmed the reliability of the numerical simulation. With the help of numerical simulation, I investigated the effects of the main amplifier gain fibre length, PF length, pre-amplifier power, and filter combination on the maximum output energy in the MO, as well as the effect of the seed pulse on the start-up of the MO.

5.3.1 Simulation (steady-stete gain modeling) V.S. experiment

Table 5.2 lists the values of some key parameters in the numerical simulation. Their corresponding elements in the experimental setup shown in Figure 5.1 are defined as follows: L_{PF1}, refers to the length of PF 1(i.e., the PF between lens L6 and gain fibre 1); L_{PF2} denotes the length of PF 2 (between lenses L2 and L3); $L_{GF1}$and L_{GF2} are the lengths of the pre-amplifier and main-amplifier gain fibres, respectively; P_1 and P_2 represent the pump powers for the pre-amplifier and main-amplifier; λ_{c1} and λ_{c2} are the center wavelengths of the 1st and 2nd filters, with corresponding 3-dB bandwidths $\Delta_{\lambda 1}$ and $\Delta_{\lambda 2}$.

The seed pulse used in the simulation shares the same spectrum as shown in Figure 5.11 (c), with a energy of 2.5 pJ. The simulation yielded an output pulse energy of 384 nJ, which agrees very well with the experimental value of 381 nJ. Figure 5.12 (a) compares the simulated and experimental spectra, showing close agreement in bandwidth and shape. Since it is difficult to retrieve spectral phase information experimentally, the simulated output was numerically compressed for comparison. As shown in Figure 5.12 (b), the ACFs of the compressed pulses from simulation and experiment are also highly consistent. These comparisons confirm that the simulation accurately reproduces both the spectral and temporal characteristics of the experimental pulse, indicating that the numerical model is reliable for further investigation and design optimization.

Table 5.2 Parameters setting in simulation compared to experiment.

L_{PF1}	L_{PF2}	L_{GF1}	L_{GF2}	P_1	P_2	λ_{c1}	λ_{c2}	$\Delta_{\lambda 1}$	$\Delta_{\lambda 2}$
m	m	m	m	W	W	nm	nm	nm	nm
2.0	0.4	2.5	2.0	4.0	13.8	1040.0	1047.0	2.5	2.8

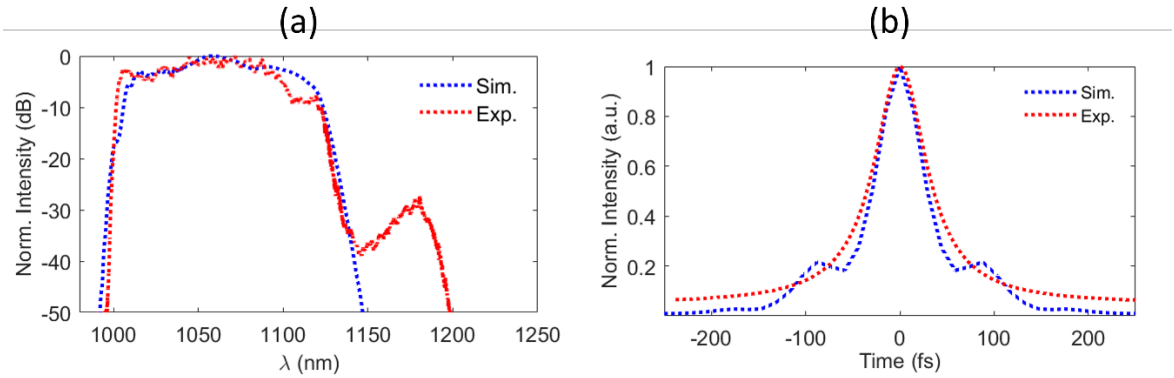

Figure 5.12 Comparison between simulation (blue dashed curve) and experiment (red dashed curve). (a) Output spectrum; (b) Autocorrelation of compressed pulse.

5.3.2 Optimization for maximum output energy

5.3.2.1 Main amplifier gain fibre length

The main amplifier plays a critical role in pulse amplification. Therefore, the first parameter considered here is the length of the gain fibre in the main amplifier, denoted as L_{GF2}, and its influence on the maximum achievable output pulse energy. Although MOs exhibit strong tolerance to NPS accumulation, the accumulated NPS, quantified by the B-integral, remains a key factor limiting the maximum pulse energy.

To evaluate this limit, I fixed the output pulse energy at 384 nJ and varied L_{GF2} from 1.0 m to 5.0 m. The required pump power P_2 was adjusted accordingly to maintain the same output energy, while other parameters remained constant. Figure 5.13 (a) shows that the B-integral increases monotonically with fibre length, indicating a positive correlation. This means shorter gain fibres can tolerate higher pulse energies before nonlinear effects become detrimental. The reasoning is straightforward: longer fibres allow more distance for NPS to accumulate. Interestingly, despite identical output pulse energy, the output spectra differ significantly. As shown in Figure 5.13 (b), increasing the gain fibre length leads to a redshift in the central wavelength, which is attributed to increased spectral evolution in the longer fibre. This observation offers a potential method for tailoring the output spectrum by adjusting the fibre length.

In summary, shortening the gain fibre in the main amplifier reduces the accumulated NPS, which in turn allows for higher pulse energy scaling in MOs. Additionally, the gain fibre length also affects the spectral profile of the output pulse, offering a degree of flexibility for tailoring spectral characteristics in oscillator design.

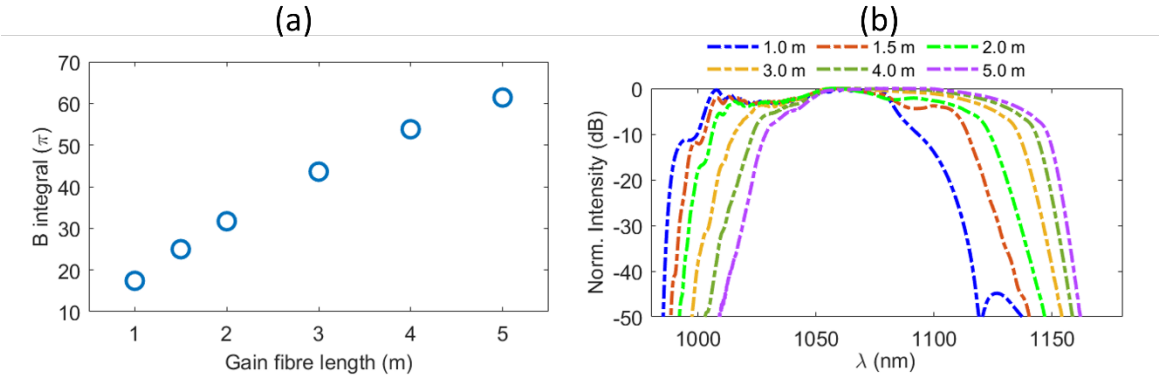

Figure 5.13 (a) B-integral values versus gain fibre length in the main amplifier, with fixed output energy of 384 nJ. (b) Corresponding output spectra for different gain fibre lengths, showing a redshift of the central wavelength with increasing fibre length.

5.3.2.2 Pre-amplifier power

The pre-amplifier, as the first gain stage within the oscillator cavity, plays an essential role in determining the final output. During experiments, we observed a phenomenon that lowering the P_1 often allows a higher P_2 without disrupting mode-locking, thereby enabling higher output pulse energy. To verify and explain this observation, numerical simulations were performed.

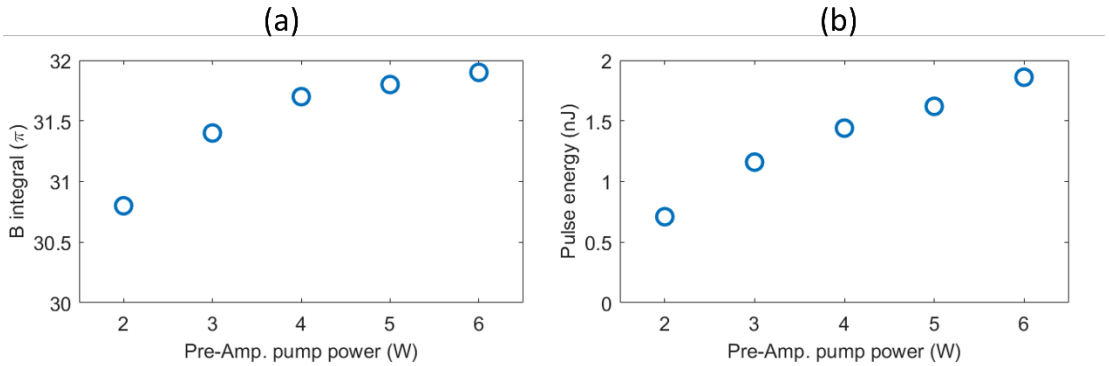

Figure 5.14 (a) Simulated B-integral in the main amplifier and (b) pulse energy injected into the main amplifier, plotted as functions of the P_1. Output pulse energy was fixed at 384 nJ.

In the simulation, the P_1 was varied from 2 W to 6 W, while the P_2 was adjusted accordingly to maintain a constant output pulse energy of 384 nJ. Figure 5.14 (a) shows that the B-integral increases with increasing P_1, confirming the experimental observation: reducing P_1 lowers nonlinear phase accumulation in the main amplifier. To understand this further, Figure 5.14 (b) plots the pulse energy entering the main amplifier as a function of P_1. It can be seen that a lower pre-amplifier pump power results in lower seed energy injected into the main amplifier, which helps suppress nonlinear effects and allows for stronger pumping in the main amplifier without excessive NPS. However, it is important to note that the P_1 cannot be reduced indefinitely.

Sufficient gain is still required to (1) initiate mode-locking from the injected seed, and (2) ensure adequate spectral broadening within the pre-amplifier to support filter-based pulse shaping.

In summary, optimizing the pump power of the pre-amplifier can effectively reduce NPS accumulation in the main amplifier, thus enabling higher pulse energy output without compromising mode-locking stability.

5.3.2.3 Filters setting

In earlier, less systematic attempts, it was noticed that the center wavelength settings of the filters significantly affect the maximum achievable output pulse energy. This section presents a more detailed analysis of this relationship. As shown in Figure 5.15, λ_{c1} was varied from 1030 nm to 1040 nm in the simulation, while the λ_{c2} was fixed at 1047 nm. Interestingly, when the output energy was fixed at 384 nJ, the results shown in Figure 5.15 (a) reveal that the B integral fluctuates around 32π as λ_{c1} changes. Conversely, when the B integral was fixed at 35π, the results in Figure 5.15 (b) indicate that the output energy first decreases and then increases as λ_{c1} shifts from 1030 nm to 1040 nm.

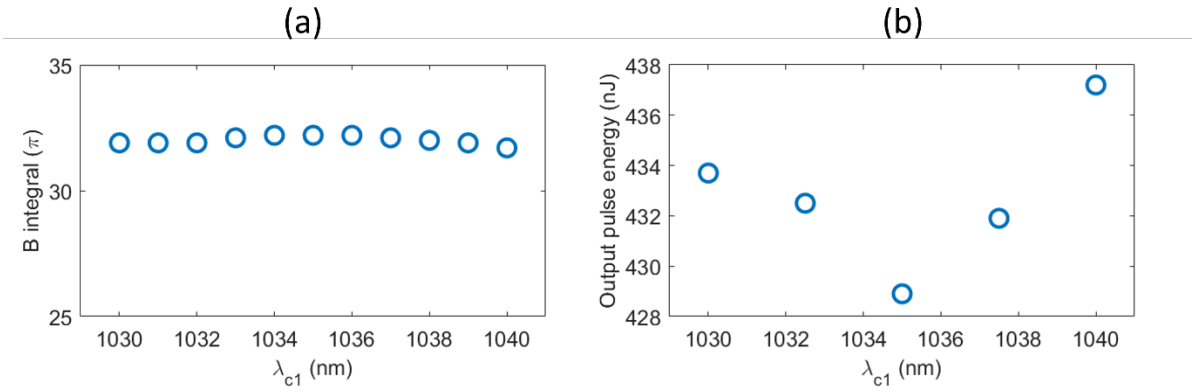

Figure 5.15 (a) B integral as a function of the center wavelength of the λ_{c1}, with output energy fixed at 384 nJ;(b) Output pulse energy as a function of λ_{c1}, with the B integral fixed at 35 π. In both cases, the pre-amplifier pump power P_1 was fixed at 4.0 W.

It is worth noting that in the simulations shown in Figure 5.15, the P_1 was fixed at 4.0 W, which represents a relatively high value. As concluded in Section 5.3.2.2, lowering P_1 can increase the maximum output energy. Therefore, by reducing P_1 from 4.0 W to 1.5 W, the results shown in Figure 5.16 were obtained. Under different λ_{c1} values and corresponding P_2 settings, the relationship between the B integral and output energy was calculated, as shown in Figure 5.16 (a). The fitted trends for each λ_{c1} value indicate that, at a lower P_1, a larger spectral separation between the two filters (i.e., a smaller λ_{c1} relative to λ_{c2} = 1047 nm) allows higher output energy at the same B integral. This trend can be understood by considering the seed pulse injected into the main amplifier. In the MO cavity, a portion of the main amplifier output is filtered by the 2nd

filter into a Gaussian-shaped pulse centered at 1047 nm, which is then sent through the pre-amplifier and used as the new seed. Figure 5.16 (b) shows the spectral broadening of this seed under two different P_1 values (1.5 W and 4.0 W). When P_1 is reduced to 1.5 W, the resulting spectrum is narrower and has greater intensity contrast between 1030 nm and 1040 nm compared to that under 4.0 W. This leads to a weaker seed being injected into the main amplifier, which in turn suppresses the NPS accumulation and enables higher amplification.

In summary, the maximum output energy of the MO is strongly influenced by the injected seed energy. A lower seed energy results in reduced nonlinear effects in the main amplifier and thus enables higher output pulse energies, provided the seed can still be sufficiently amplified. This relationship offers insight into optimizing both the spectral filtering scheme and the pump power configuration.

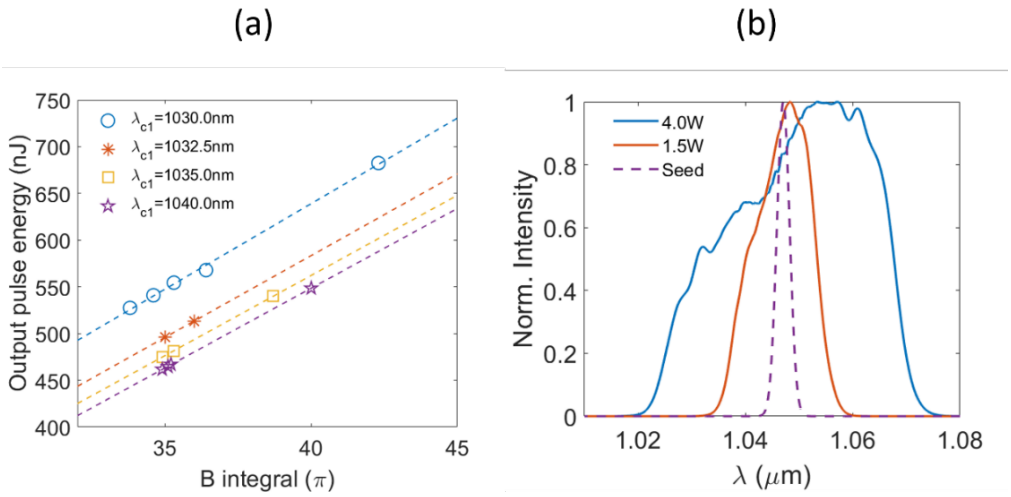

Figure 5.16 (a) Output pulse energy versus B integral for various values of λ_{c1}, with P_1 = 1.5 W. Data series: blue circles (1030.0 nm), orange asterisks (1032.5 nm), yellow squares (1035.0 nm), purple stars (1040.0 nm). (b) Spectral broadening of the seed pulse in the pre-amplifier for P_1 = 1.5 W (orange) and 4.0 W (blue). The original seed spectrum (purple dashed) is also shown for reference.

5.3.2.4 Passive fibre length

Based on the previous analysis, the main amplifier primarily determines the final output characteristics of the MO. Therefore, the L_{PF2} plays a crucial role and cannot be ignored. Simulations were performed for four different values of L_{PF2}: 0.4 m, 2.0 m, 5.0 m, and 7.0 m. The pump power P_2 was adjusted to maintain a fixed output pulse energy of 384 nJ, while all other parameters remained consistent with Table 5.2. As shown in Figure 5.17 (a), the B integral in the main amplifier decreased significantly from 31.7 π to 12.9 π as L_{PF2} increased. However, this reduction is not caused by a decrease in the seed energy injected into the main amplifier. On the contrary, as L_{PF2} increases from 0.4 m to 7.0 m the repetition rate decreases from 21.7 MHz to

12.8 MHz, resulting in an increase in the seed pulse energy from 1.4 nJ to 2.6 nJ, as shown in Figure 5.17 (b). This might appear contradictory to earlier results, but it's not. According to the B integral definition, the critical factor is the peak power, not the pulse energy.

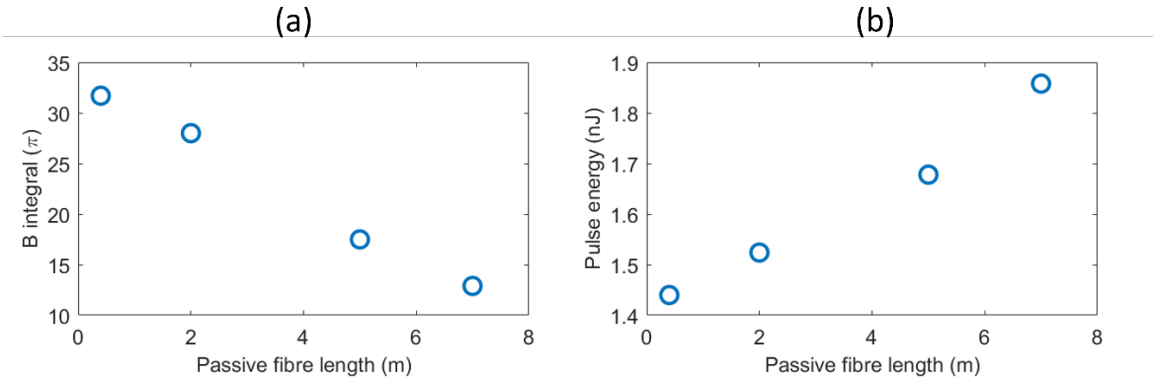

Figure 5.17 (a) Accumulated B-integral in the main amplifier and (b) pulse energy injected into the main amplifier as functions of the L_{PF2}, under a fixed output energy of 384 nJ.

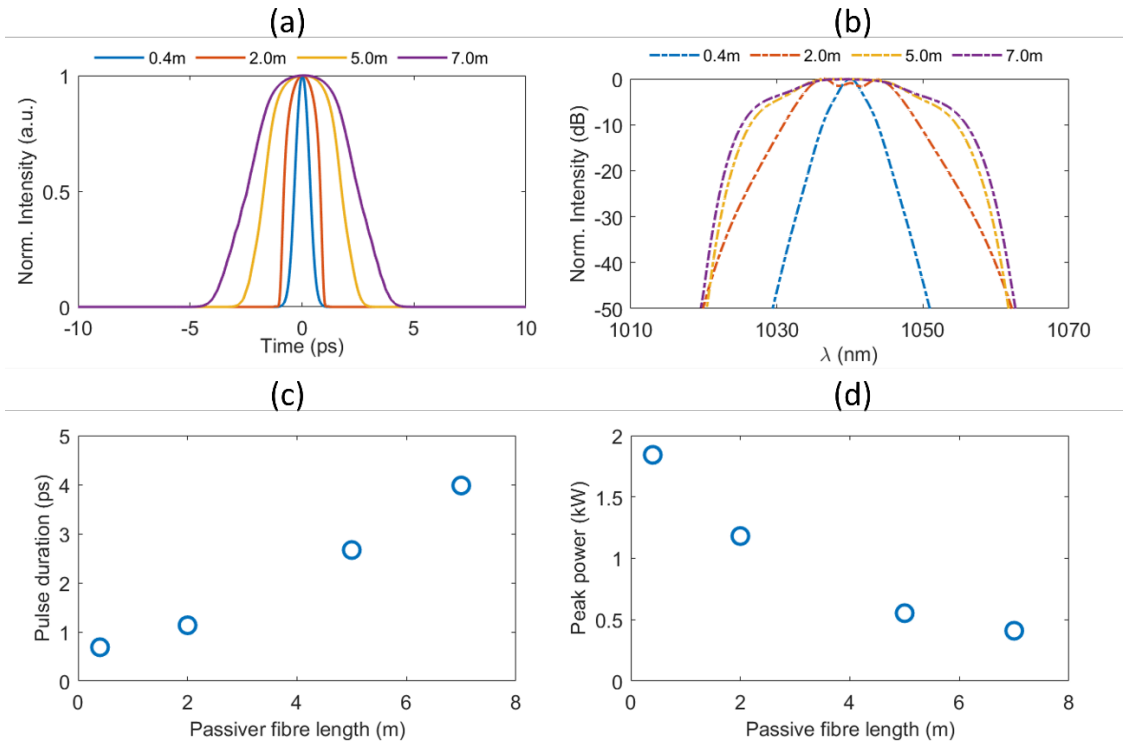

Figure 5.18 Influence of the L_{PF2} on the pulse characteristics before entering the main amplifier. (a) Temporal pulse profiles and (b) corresponding spectra for different L_{PF2} values. (c) Extracted pulse durations and (d) peak powers as functions of L_{PF2}.

Figure 5.18 (a) and Figure 5.18 (b) show that as L_{PF2} increases, the pulse broadens both temporally and spectrally. As depicted in Figure 5.18 (c), the pulse duration broadens from 0.69 ps to 3.98 ps, while the corresponding peak power decreases from 1.84 kW to 0.41 kW, as illustrated in Figure 5.18 (d). This explains the reduction in NPS accumulation despite higher pulse energy. In previous analyses without additional dispersion, the peak power was approximately

proportional to the pulse energy. Moreover, increasing L_{PF2} leads to a gradual transformation of the seed pulse shape in the main amplifier. As seen in Figure 5.18 (a) and (b), a Gaussian-shaped pulse evolves into a parabolic-like pulse, which significantly alters the spectral broadening behavior in the main amplifier. Figure 5.19 shows spectral evolution at different L_{PF2} values. At L_{PF2}=0.4 m, the spectrum exhibits asymmetric broadening with a redshift; at L_{PF2}=7.0 m, it maintains a symmetric profile; and at L_{PF2}=2.0 m, it still maintains a certain degree of asymmetric evolution.

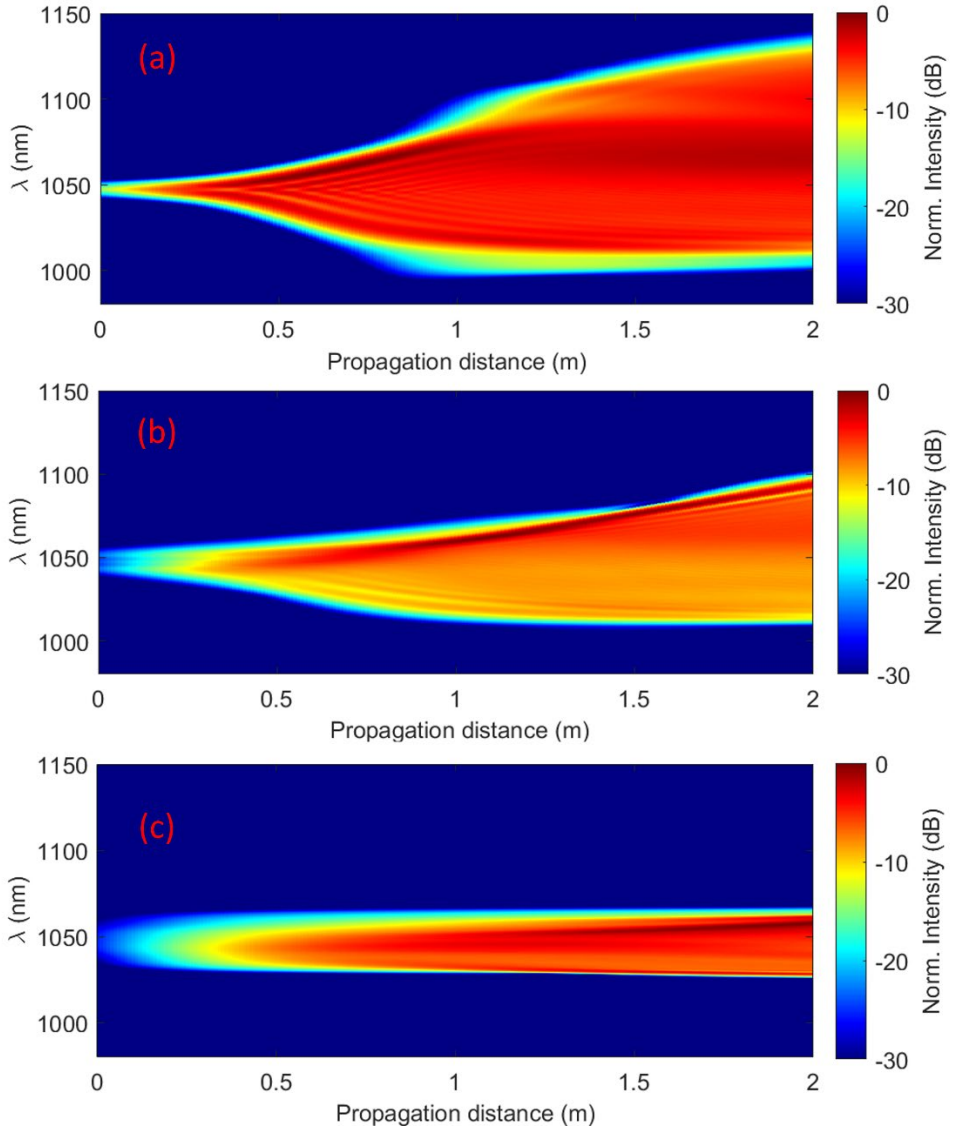

Figure 5.19 Simulated spectral evolution in the main amplifier for different L_{PF2}. (a) Spectral evolution for L_{PF2} = 0.4 m, showing significant asymmetry. (b) Evolution for L_{PF2} = 2.0 m, with reduced asymmetry. (c) Evolution for L_{PF2} = 7.0 m, where the spectrum remains highly symmetric.

In summary, changing L_{PF2} introduces several coupled effects: it alters the cavity length and repetition rate, and introduces additional dispersion and nonlinearity before the main amplifier. These effects complicate the analysis of whether the change is beneficial. In particular, when

L_{PF2} is further extended to 10.0 m (with other parameters unchanged and output fixed at 384 nJ), the output pulse becomes severely distorted. The corresponding time-domain envelope and spectrum are presented in Figure 5.20.

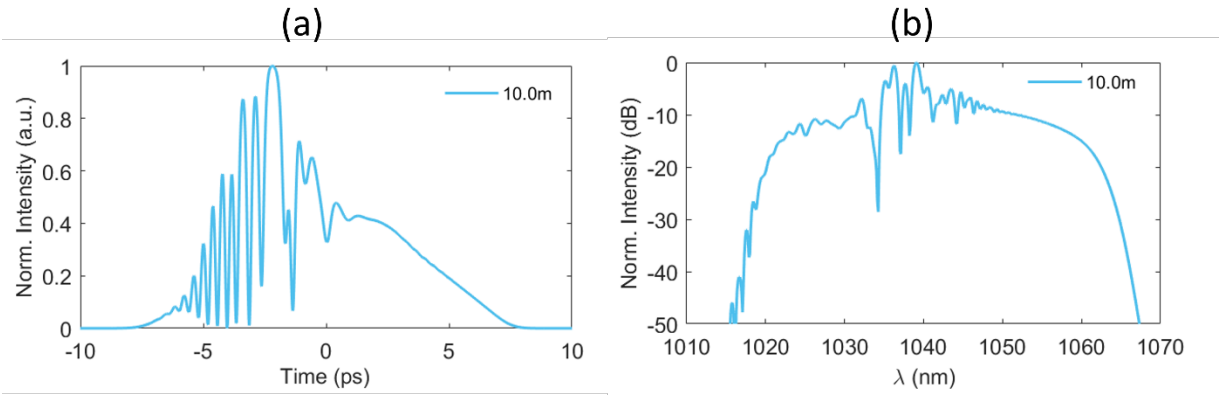

Figure 5.20 Simulated output pulse characteristics of the MO with an extended PF length L_{PF2} = 10.0 m. (a) Temporal intensity profile. (b) Corresponding optical spectrum.

5.3.2.5 Dispersion

To decouple the influence of L_{PF2} discussed in Section 5.3.2.4, which mainly affects the pulse peak power through dispersion, we independently investigate the impact of dispersion in this section. To isolate the role of dispersion, the PF lengthL_{PF2} is fixed at 0 m, and the P_1 was set to 0.5 W to reflect the high-energy operation regime. Five group delay dispersion (GDD) values are considered: $\pm$0.4ps^2, $\pm$0.2ps^2 and 0ps^2, representing increasing levels of positive, negative, and zero dispersion. Figure 5.21 shows the relationship between the output pulse energy and the B-integral under these dispersion conditions. While numerical limitations prevent access to results at very high peak powers, the trends are still evident: increasing the absolute amount of dispersion, whether positive or negative, reduces peak power and thus slows the accumulation of NPS, ultimately enabling higher output pulse energy. Notably, positive dispersion appears to be more effective than negative dispersion of equal magnitude in suppressing the B-integral. This phenomenon is further elucidated by the spectral evolution of the pulse within the main amplifier, as shown in Figure 5.22. For a fixed output energy (~850 nJ), the spectrum under negative dispersion (GDD = -0.2 ps^2) narrows near a propagation length of 0.5 m, a signature of amplification of a negatively chirped pulse in a positively dispersive Yb-doped fibre. This spectral narrowing is absent under positive dispersion (GDD = +0.2 ps^2). The corresponding temporal behavior is illustrated in Figure 5.23. As shown in Figure 5.23 (a), the pulse duration under negative dispersion decreases up to 0.55 m and subsequently increases, while under positive dispersion, the duration increases monotonically. Figure 5.23 (b) demonstrates that although both pulses achieve similar output energies, the pulse with negative dispersion consistently

exhibits higher peak power throughout the amplification process, and thus accumulates more NPS.

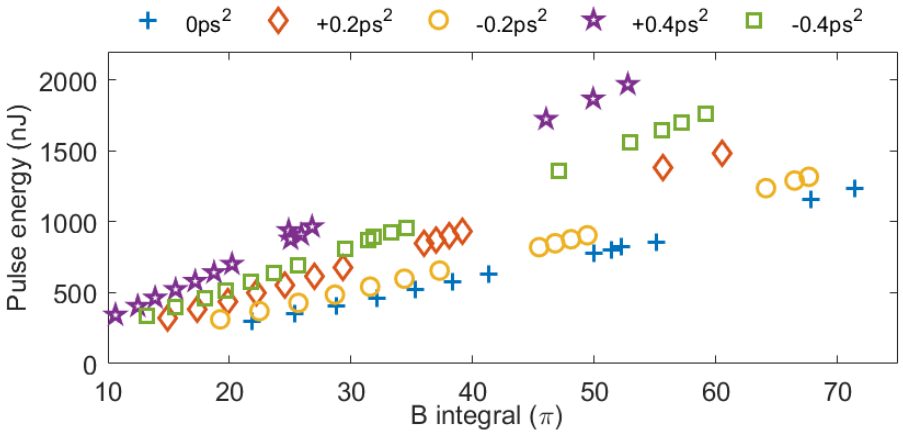

Figure 5.21 Output pulse energy as a function of B-integral under different values of GDD: 0 ps^2 (blue cross), +0.2 ps^2 (red diamond), -0.2 ps^2 (yellow circle), +0.4 ps^2 (purple star), and -0.4 ps^2 (green square).

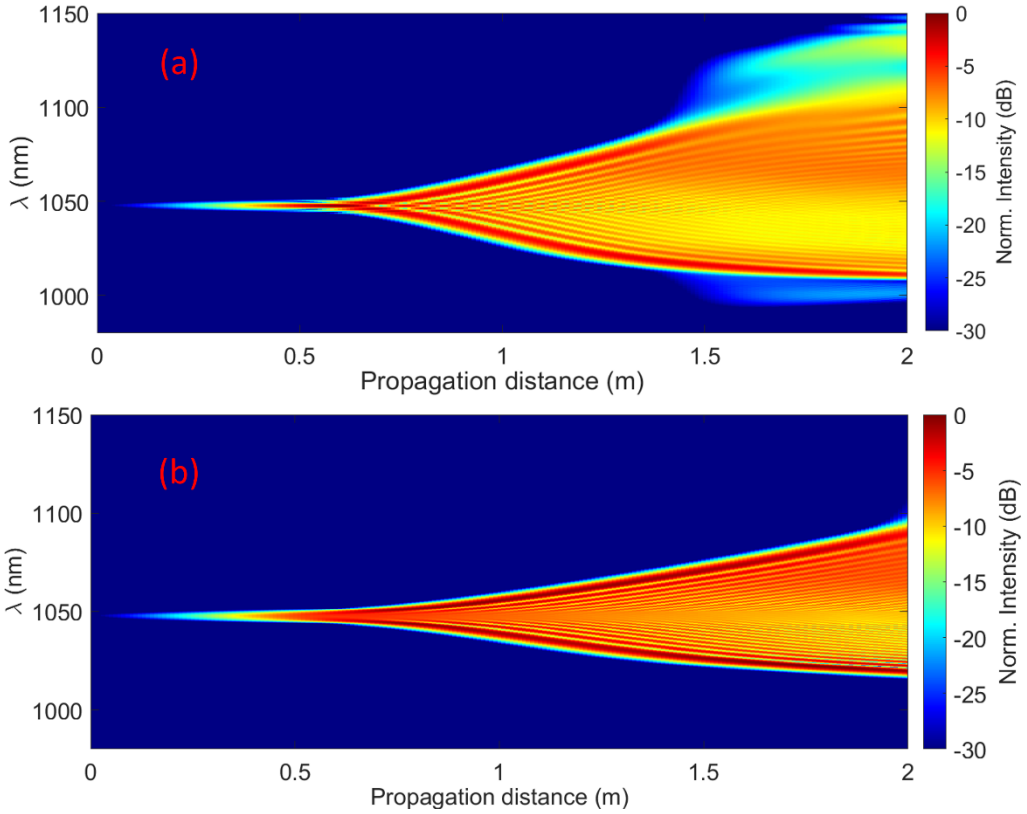

Figure 5.22 Spectral evolution of the pulse in the main amplifier at an output energy of ~850 nJ under (a) GDD = -0.2 ps^2 and (b) GDD = +0.2 ps^2. Positive dispersion suppresses spectral narrowing compared to negative dispersion.

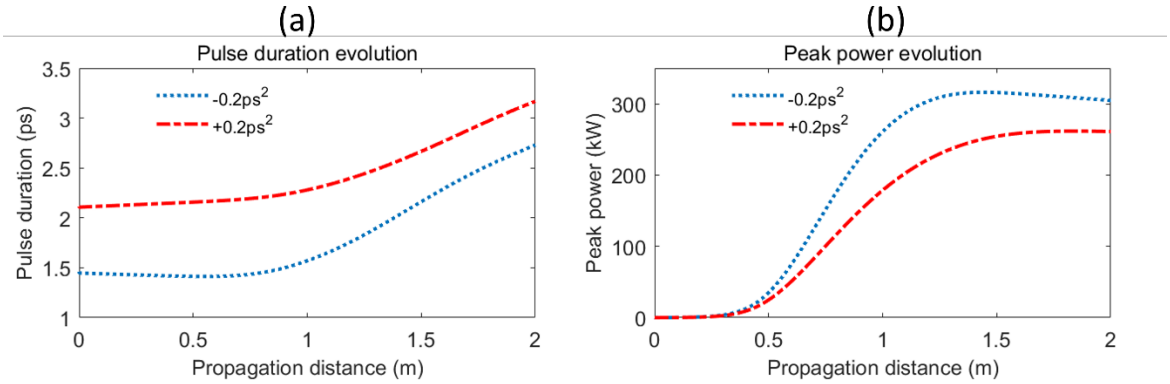

Figure 5.23 (a) Pulse duration evolution and (b) peak power evolution during amplification for GDD values of -0.2 ps^2 (blue dotted curve) and +0.2 ps^2 (red dash-dotted curve). Positive dispersion leads to lower peak power throughout the amplifier length.

In summary, introducing moderate dispersion prior to the main amplifier can enhance the achievable pulse energy by suppressing NPS accumulation. Positive dispersion is found to be more effective in this role than negative dispersion of equal magnitude. However, whether this dispersion control affects the maximum peak power remains an open question, limited by the current simulation model. Additionally, determining the upper bound of applicable dispersion before entering the chirped-pulse amplification regime is a subject worth further exploration.

5.3.2.6 Optimization in the experiment

In the experimental stage, optimization efforts were focused on adjusting the filter settings and the pump power of the pre-amplifier. The corresponding results are presented in this section. Initially, the center wavelength separation, $\Delta\lambda_c$, between the two filters was set to 7 nm, under which the maximum pulse energy achieved was 381 nJ. Two alternative filter configurations were subsequently explored. In the first configuration, the center wavelengths were set to λ_{c1} = 1035.5 nm and λ_{c2} = 1044.2 nm, yielding a $\Delta\lambda_c$ of 8.7 nm. In the second configuration, λ_{c1} = 1032.1 nm and λ_{c2} = 1047.2 nm, resulting in $\Delta\lambda_c$ = 15.1 nm. The corresponding transmission spectra of both configurations were experimentally measured and are shown in Figure 5.24 (a) and (b), respectively.

For the $\Delta\lambda_c$ = 8.7 nm case, different values of P_1 (6.52 W, 7.05 W, and 7.59 W) were tested, and the respective stable mode-locking ranges of the main amplifier pump power P_2 were recorded, as listed in Table 5.3. The results show that lower values of P_1 lead to wider mode-locking ranges and allow higher P_2 values. Moreover, it was observed experimentally that during stable mode-locking operation, the output pulse energy is primarily determined by P_2, and the influence of P_1 becomes negligible. no matter how P_1 changes, as long as MO remains in a stable mode-locked state, the output pulse energy can be be roughly judged simply determined by the value of P_2.

These observations are consistent with the simulation results presented in Section 5.3.2.2, which suggest that minimizing P_1 is beneficial for enhancing the maximum output energy of the MO.

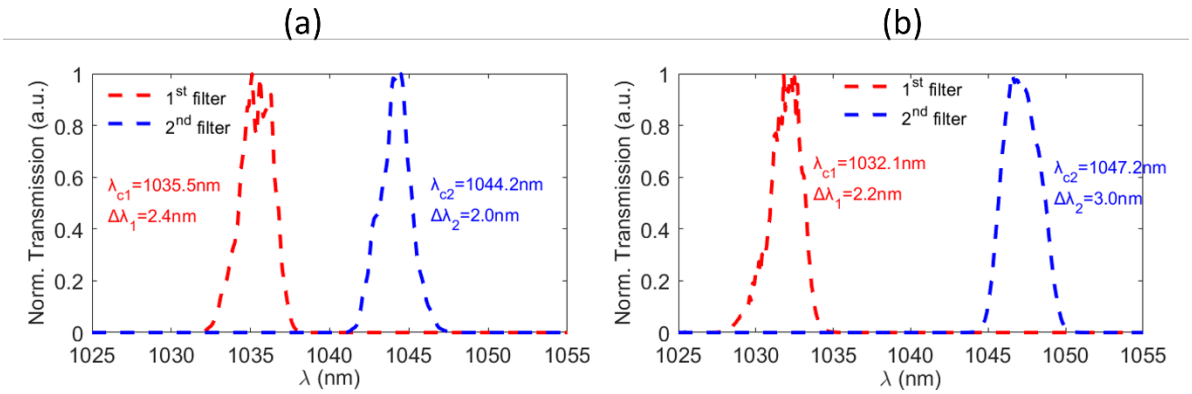

Figure 5.24 Measured transmission spectra of the two filter combinations used in the optimization experiments. (a) Combination with a central wavelength separation $\Delta\lambda_c$ of 8.7 nm, where the 1st and 2nd filters are centered at 1035.5 nm and 1044.2 nm, respectively. (b) Combination with $\Delta\lambda_c$ = 15.1 nm, corresponding to central wavelengths of 1032.1 nm and 1047.2 nm for the 1st and 2nd filters, respectively.

Table 5.3 Measured stable mode-locking ranges of the P_2 under different P_1 for $\Delta\lambda_c$ = 8.7 nm.

P_1 (W)	Mode-locking range of P_2 (W)
6.52	4.58-22.59
7.05	4.58-13.51
7.59	4.58-11.16

Figure 5.25 (a) illustrates the dependence of the output pulse energy on the absorbed pump energy under two $\Delta\lambda_c$ conditions: 8.7 nm (blue circles) and 15.1 nm (red stars). The maximum pulse energies achieved were 377 nJ and 426 nJ, respectively, indicating that increasing $\Delta\lambda_c$ leads to an enhancement of approximately 50 nJ in maximum output energy. This result supports the simulation conclusions drawn in Section 5.3.2.3. In these experiments, the pump power P_1 was set to 6.52 W for $\Delta\lambda_c$ = 8.7 nm and 7.59 W for $\Delta\lambda_c$ = 15.1 nm, as a higher $\Delta\lambda_c$ required a higher threshold P_1 to initiate mode-locking. Since the objective is to compare the maximum output energy at different $\Delta\lambda_c$ values, P_1 was not kept constant. Instead, for each $\Delta\lambda_c$, the lowest possible P_1 value was used. It is worth noting that the 377 nJ result under $\Delta\lambda_c$ = 8.7 nm is slightly lower than the 381 nJ obtained in Section5.2.1 using a $\Delta\lambda_c$ of 7.0 nm. This discrepancy may stem from differences in the MO cavity alignment at the time of measurement, as the experimental setup involves numerous spatial optical components and the measurements were taken several months apart. Another possible factor could be minor deviations in the setting of λ_{c2}. Figure 5.25

(b) presents the output spectra of the pulses corresponding to their respective maximum energies for the two $\Delta\lambda_c$ values. The spectral bandwidth at the −10 dB level was measured to be 116.2 nm for $\Delta\lambda_c$ = 8.7 nm and 126.7 nm for $\Delta\lambda_c$ = 15.1 nm. These results confirm that a larger $\Delta\lambda_c$ not only facilitates higher output pulse energy, as predicted by simulations, but also leads to broader spectral bandwidths. Figure 5.26 displays the ACFs of the compressed pulses under both spectral conditions shown in Figure 5.25 (b). The TL traces are shown as blue dashed lines, while the experimentally measured traces are plotted in red dotted lines. In Figure 5.26 (a), corresponding to $\Delta\lambda_c$ = 8.7 nm, the measured pulse duration was 44.8 fs, with a TL duration of 26.8 fs (assuming a Gaussian temporal profile). In Figure 5.26 (b), for $\Delta\lambda_c$ = 15.1 nm, the compressed pulse duration was reduced to 35.2 fs, with a TL duration of 24.2 fs. Compression was achieved using a grating-based compressor that was independently optimized for each spectral configuration.

These findings demonstrate that efficient compression of MO output pulses is achievable under both spectral configurations. Increasing the spectral separation $\Delta\lambda_c$ leads to higher pulse energy, broader output spectra, shorter compressed pulse durations, and increased peak power. At the same time, this scaling strategy introduces important trade-offs associated with spectral filtering inside the Mamyshev oscillator. A fraction of the spectrally broadened energy is inevitably rejected by the offset bandpass filters. However, under stable mode-locking conditions, the unselected spectral components could be in principle be accessed through additional output ports. From a system-design standpoint, increasing $\Delta\lambda_c$ therefore involves a balance between stability. While larger filter separations enhance output performance, they also increase the threshold pump power during the startup, leading to a higher pump-power requirement for starting and a reduced pump power range of stable mode-locking. Experimentally, when$\Delta\lambda_c$ was increased to more than 15.1 nm, reliable mode-locking became significantly more difficult to achieve, with the system operating close to the multi-pulsing regime. As a result, further increases in $\Delta\lambda_c$ were found to offer diminishing practical benefit under the present experimental conditions. Numerical simulations performed within the explored parameter range did not reveal a clear fundamental limit to this scaling trend. Instead, the observed constraints are primarily practical, arising from startup dynamics, pump-power availability, and the narrowing stability margin between single-pulse and multi-pulse operation. If these startup and stability limitations can be mitigated through improved cavity design, further exploration of larger filter separations may become viable. These considerations highlight important directions for future optimization, where the trade-offs between energy scaling, efficiency, and operational robustness must be carefully balanced.

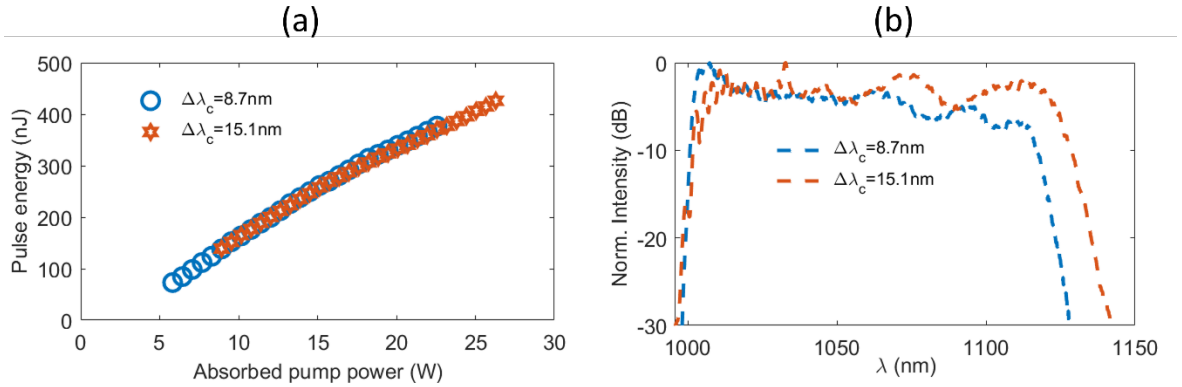

Figure 5.25 (a) Output pulse energy as a function of absorbed pump power under two different filter settings: $\Delta\lambda_c$ = 8.7 nm (blue circles) and $\Delta\lambda_c$ = 15.1 nm (red hexagrams). The maximum output energies achieved were 377 nJ and 426 nJ, respectively. (b) Normalized output spectra corresponding to the maximum output energies under the two filter settings. The -10 dB bandwidths were measured as 116.2 nm for $\Delta\lambda_c$ = 8.7 nm and 126.7 nm for $\Delta\lambda_c$ = 15.1 nm.

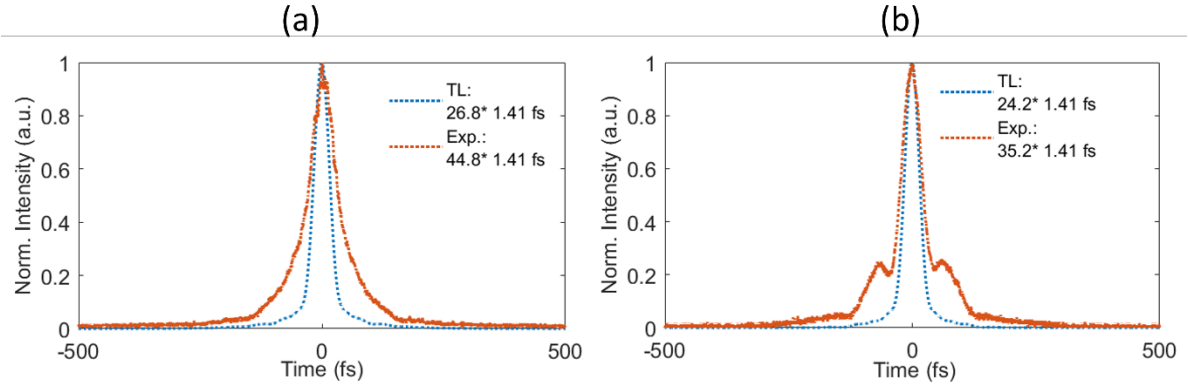

Figure 5.26 ACFs of compressed pulses corresponding to the spectra shown in Figure 5.25 (b). (a) Pulse under $\Delta\lambda_c$ = 8.7 nm condition: experimentally measured pulse duration is 44.8 fs with a TL duration of 26.8 fs. (b) Pulse under $\Delta\lambda_c$ = 15.1 nm condition: compressed to 35.2 fs with a TL duration of 24.2 fs. Blue dashed lines represent the calculated TL traces, and red dotted lines are the measured ACFs. All pulse durations are deconvolved assuming Gaussian temporal profiles.

5.3.3 Optimization for simplifying seed laser

The seed laser shown in Section 5.2.2 consists of four parts: a femtosecond fibre laser, a laser amplifier, a pulse compressor, and a spectrum stretcher. This seed is very complex and contains many spatial components, which needs large footprint, but also requires continuous maintenance. In this section, the requirements for seed parameters for starting MO will be studied in order to achieve better integration and more stable use of the seed laser.

The seed pulse used in the simulation in Section 5.3.1 and 5.3.2 has a spectrum measured in the experiment as shown in Figure 5.11 (c) and a energy of 25 pJ, which worked well in the above simulation. To facilitate the design of various parameters, the seed pulse is assumed to have a Gaussian spectrum in this section. Table 5.4 lists the reference parameters of the Gaussian seed pulse used in the simulation, including the central wavelength $\lambda_{\mathrm{seed\_c}}$, pulse energy E_{seed}, pulse duration τ_{seed}, and chirp value (group delay dispersion, GDD). These parameters serve as the baseline configuration unless otherwise stated. Each symbol defined here will be used consistently in the following sections, where the influence of varying each parameter on the MO system performance will be systematically investigated. The stable output of MO is determined by the parameters of the MO cavity itself. The role of the seed pulse is only to provide a relatively strong perturbation to promote the self-reproduction of MO. Therefore, in this part of the simulation, more attention is paid to the mode-locking threshold power of P_1, and the results of the first roundtrip after the seed pulse is injected into the MO, especially the characteristics of the pulse injected into the cavity as the input of the second roundtrip. The P_1 and P_2 are set at a low state to maximize the influence of the parameters of the seed pulse itself. The rest parameters of the MO are consistent with Table 5.2.

Table 5.4 Reference parameters of the Gaussian seed pulse used in the simulations, including central wavelength $\lambda_{\mathrm{seed\_c}}$, pulse energy E_{seed}, pulse duration τ_{seed}, and chirp (GDD). These values serve as the baseline configuration for the seed laser in Section 5.3.3.

$\lambda_{\mathrm{seed\_c}}$	E_{seed}	τ_{seed}	Chrip
nm	pJ	ps	ps^2
1040	25	0.5	0

5.3.3.1 Pulse energy

It is undoubted that higher seed pulse energy makes it easier to start MO. The significance of studying it is to find out where the upper limit of this performance improvement is, and also to find out what the intrinsic threshold pump energy is for a MO cavity with specific parameters.

P_2 was set to 4.0 W, which is a low value. Seed pulse energies, E_{seed}, ranging from 2.5 pJ to 25 nJ were tried in the simulations and the corresponding pre-amplifier threshold pump powers, P_{1_thr}, are listed in Table 5.5. When the E_{seed} increases from 2.5 pJ to 7 pJ, the P_{1_thr} gradually decreases from 0.61 W to a minimum of 0.55 W. When the E_{seed} further increases, the P_{1_thr} remains at 0.55 W without any change. Therefore, it can be considered that 0.55 W is the intrinsic P_{1_thr} for the this MO setting, that is, P_2 = 4.0 W, λ_{c1} =1040.0nm, λ_{c2} =1047.0nm. Table 5.6 lists the pulse energies injected into the second roundtrip after seed pulses, E_{2rd}, of different E_{seed} evolve

through the first roundtrip when P_1 = 0.55 W and P_2 = 4.0 W. When the E_{seed} increases from 2.5 pJ to 7 pJ, the E_{2rd} gradually increases from 158 pJ to a maximum of 562 pJ. When the E_{seed} further increases, the E_{2rd} fluctuated in a wide range exceeding 600 pJ. This fluctuation originates from sufficient spectral broadening in the main amplifier. It can also be inferred that the threshold E_{2rd} for achieving MO mode-locking in this pumping state is in the range of 485 pJ to 562 pJ. This can provide an evaluation criterion for analyzing the effect of seed pulse parameters on the start of MO mode locking.

Table 5.5 Pre-amplifier threshold pump power $P_{\mathrm{1\_thr}}$ as a function of seed pulse energy E_{seed}.

E_{seed}	2.5 pJ	5 pJ	6 pJ	7 pJ	8 pJ	25 pJ	250 pJ	2.5 nJ	25 nJ
$P_{\mathrm{1\_thr}}$	0.61 W	0.58 W	0.56 W	0.55 W	0.55 W	0.55 W	0.55 W	0.55 W	0.55 W

Table 5.6 Pulse energy injected into the second roundtrip E_{2rd} as a function of seed pulse energy E_{seed}.

E_{seed}	2.5 pJ	5 pJ	6 pJ	7 pJ	8 pJ	25 pJ	250 pJ	2.5 nJ	25 nJ
E_{2rd}	158 pJ	444 pJ	485 pJ	562 pJ	631 pJ	1002 pJ	689 pJ	679 pJ	685 pJ

5.3.3.2 Central wavelength

In the practical MO, the λ_{c1} can be customized. However, for the sake of consistency and controllability in the simulation, this λ_{c1} is fixed at 1040.0 nm. Instead, the $\lambda_{\mathrm{seed\_c}}$ is varied from 1030.0 nm to 1045.0 nm with a step of 1.0 nm to investigate the impact of spectral offset between the $\lambda_{\mathrm{seed\_c}}$ and the λ_{c1}. Two representative seed energies, 25 pJ and 250 pJ, are considered in this study. The 25 pJ level corresponds to the typical output of a standard femtosecond fibre oscillator, which is readily achievable without further amplification. In contrast, reaching 250 pJ usually requires additional pre-amplification stages, which inevitably increase system complexity, cost and footprint. Comparing these two levels allows for a clearer understanding of the system's sensitivity to spectral offset under different seed conditions. Figure 5.27 shows the variation of E_{2rd} as a function of the seed center wavelength $\lambda_{\mathrm{seed\_c}}$ under two different seed energies: 25 pJ (blue circles) and 250 pJ (orange squares). A clear threshold region, indicated by the shaded red area labeled as $P_{\mathrm{1\_thr}}$, is observed. When the E_{seed} is low (25 pJ), E_{2rd} exceeds the threshold only for wavelengths around λ_{c1}, from 1038.0 nm to 1043.0 nm, whereas higher E_{seed} (250 pJ) enables a broader spectral range. The fluctuation of these E_{2rd} above the threshold is attributed to the reduction in power spectral density caused by spectral broadening in the main amplifier. The

results highlight the wavelength dependence of the amplification process and the significant influence of seed energy on crossing the efficiency threshold.

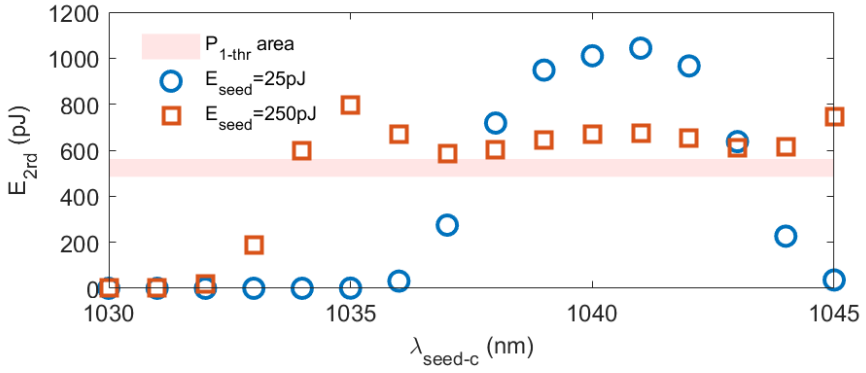

Figure 5.27 Dependence of $E_{2\mathrm{rd}}$ on the $\lambda_{\mathrm{seed\_c}}$ for two E_{seed} levels: 25 pJ (blue circles) and 250 pJ (orange squares). The shaded red region indicates the threshold level P_{1_thr}.

5.3.3.3 Pulse duration

The previous investigation demonstrated the strong influence of E_{seed} on solving offset between $\lambda_{\mathrm{seed\_c}}$ and λ_{c1}, which is primarily attributed to the spectral broadening SPM. SPM-induced spectral broadening is highly dependent on the peak power of the seed pulse. Varying the τ_{seed} is another effective way to influence the peak power while keeping the pulse energy constant. Therefore, this section focuses on examining the effect of τ_{seed} on the start of the mode-locking of the MO.

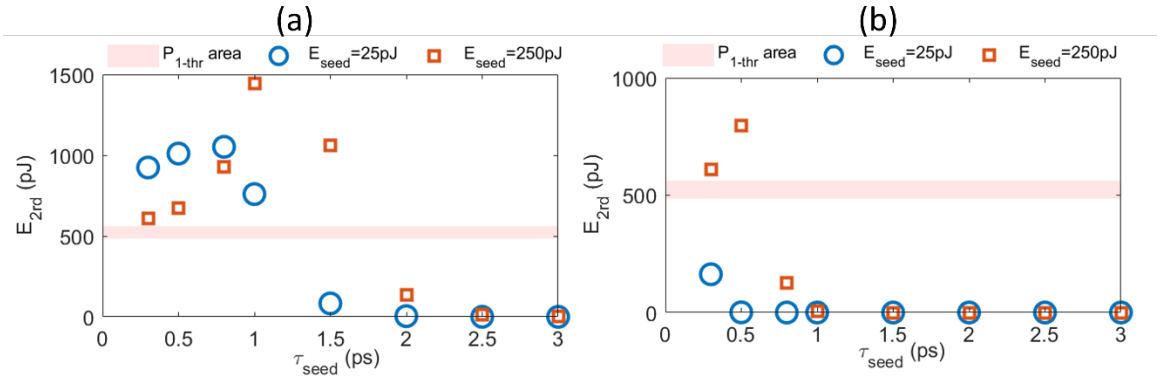

Figure 5.28 Influence of τ_{seed} on the $E_{2\mathrm{rd}}$ under (a) spectral overlap condition, $\lambda_{\mathrm{seed\_c}}$=1040.0 nm, and (b) spectral offset condition, $\lambda_{\mathrm{seed\_c}}$=1035.0 nm. Blue circles: E_{seed} =25 pJ; red squares: E_{seed}=250 pJ. The shaded area indicates the P_{1_thr} for the mode-lcoking of the MO.

A series of τ_{seed} are selected for comparison, including 0.3 ps, 0.5 ps, 0.8 ps, 1.0 ps, 1.5 ps, 2.0 ps, 2.5 ps, and 3.0 ps. These values are representative of durations that can be directly obtained from femtosecond oscillators or amplifier systems, or alternatively realized through proper pulse

compression. Figure 5.28 compares the dependence of $E_{2\mathrm{rd}}$ on the seed pulse duration τ_{seed} under two different spectral offset conditions between $\lambda_{\mathrm{seed\_c}}$ and λ_{c1}. In both cases, simulations are performed using two seed energy levels: 25 pJ and 250 pJ. In Figure 5.28 (a), the $\lambda_{\mathrm{seed\_c}}$ is set to 1040.0 nm, which is exactly overlap to the λ_{c1}. Under this spectral overlap condition, $E_{2\mathrm{rd}}$ exceeds the threshold for both seed energy levels when the τ_{seed} is short. As τ_{seed} increases, the reduced peak power leads to a rapid drop in $E_{2\mathrm{rd}}$. For the 25 pJ case, the output energy falls below the threshold when the pulse duration exceeds 1.5 ps. In contrast, for the 250 pJ case, the threshold can still be met up to $\tau_{\mathrm{seed}} \approx$ 2.0 ps, indicating that higher seed energy allows greater tolerance to longer pulse durations. In contrast, Figure 5.28 (b) shows the case where the $\lambda_{\mathrm{seed\_c}}$ is detuned to 1035.0 nm. Here, the spectral offset significantly suppresses the $E_{2\mathrm{rd}}$, and only high-energy short pulses succeed to exceed the shaded P_{1_thr} region. Spectral overlap between the $\lambda_{\mathrm{seed\_c}}$ and the λ_{c1} reduces the system's dependence on E_{seed} and τ_{seed}, enabling efficient pulse regeneration even with relatively low-energy or long-duration pulses. In contrast, when spectral offset is present, the seed must maintain sufficiently high peak powe.

5.3.3.4 Pulse chirp

In practical systems, femtosecond oscillators often generate pulses with chirp due to uncompensated dispersion or intentional design. Therefore, understanding the influence of chirp on MO performance is essential.

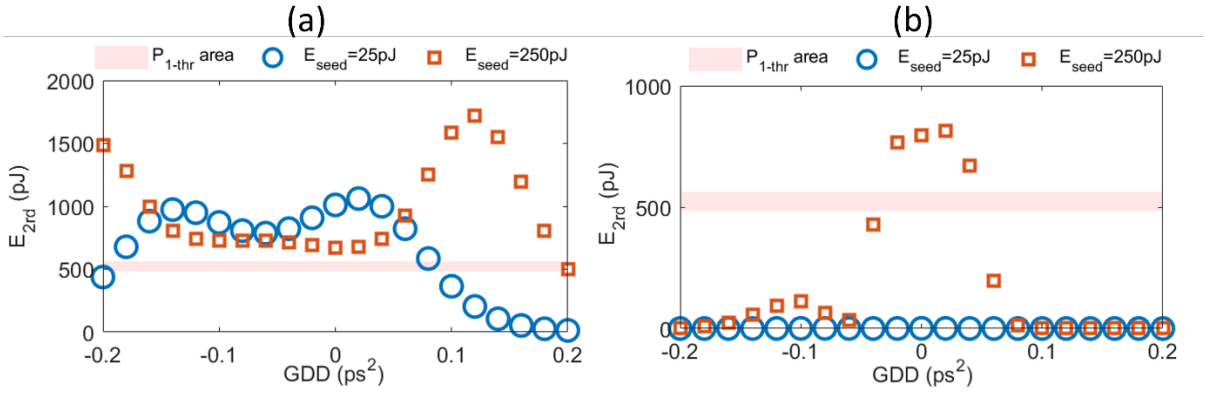

Figure 5.29 Influence of seed pulse chirp (GDD) on the extracted energy $E_{2\mathrm{rd}}$ under (a) spectral overlap condition, $\lambda_{\mathrm{seed\_c}}$=1040.0 nm, and (b) spectral offset condition, $\lambda_{\mathrm{seed\_c}}$ =1035.0 nm. Blue circles: E_{seed} =25 pJ; red squares: E_{seed}=250 pJ. The shaded area indicates the P_{1_thr} for the mode-lcoking of the MO.

Figure 5.29 illustrates the effect of seed pulse chirp, represented by its GDD, from -2.0 ps^2 to +2.0 ps^2 with a step of 0.2 ps^2, on the $E_{2\mathrm{rd}}$ under under conditions of (a), spectral overlap, and (b), spectral offset. In Figure 5.29 (a), where the $\lambda_{\mathrm{seed\_c}}$=1040.0 nm, the MO exhibits moderate tolerance to GDD variations of the seed pulse. For both seed energy levels, $E_{2\mathrm{rd}}$ remains above

the threshold in a relatively broad GDD range. Additionally, exhibits a notable asymmetry in tolerance to positive and negative GDD. Specifically, the introduction of positive dispersion (GDD > 0) causes more severe degradation in MO performance compared to the same magnitude of negative dispersion. This is evident in the 250 pJ seed energy case, where the only configuration that fails to reach the threshold occurs at GDD = +0.2 ps^2. Similarly, for the 25 pJ seed case, $E_{2\mathrm{rd}}$ falls below threshold when GDD ≥ +0.1 ps^2 and GDD = -0.2 ps^2. This suggests that positive chirp is more detrimental to the MO startup condition. One explanation for this asymmetry is that, in the simulation, the seed pulse propagates through a 2 m long PF before entering the preamplifier, which is used to simulate the pigtail of the optical fibre device. This PF introduces a total GDD of approximately 0.044 ps^2. As a result, negatively chirped seed pulses experience partial compensation, whereas positively chirped pulses accumulate additional chirp, further degrading the system performance. In contrast, Figure 5.29 (b) presents the case with a 5 nm spectral offset ($\lambda_{\mathrm{seed\_c}}$=1035.0 nm). Here, the $E_{2\mathrm{rd}}$ is significantly suppressed for most GDD values, and only a narrow region around unchirped or slightly negative chirp allows the start of the mode-locking of the MO, only in the high-energy (250 pJ) case. This confirms that spectral offset significantly narrows the chirp tolerance and increases the reliance on the amplifier for seed laser.

In summary, in the case of spectral overlap, a seed pulse with small chirp facilitates the start of the MO, with negative dispersion providing an even greater benefit. In contrast, under spectral offset conditions, the effect of the chirp of the seed pulse will be small and more dependent on the E_{seed}.

5.3.3.5 Simplified seed laser

Based on the above simulations, a femtosecond oscillator producing output pulses with reduced chirp (Figure 5.30) was constructed as the seed source for MO generation. Since realizing a soliton oscillator in the 1 μm wavelength band is theoretically challenging, this design still follows the architecture shown in Figure 5.9 but employs a shorter cavity length, resulting in a net intracavity dispersion of approximately - 0.1 ps^2. This configuration establishes a dispersion distribution suitable for DMS operation. The oscillator operates at a central wavelength of 1041.4 nm, consistent with the optical modulator wavelength λ_{c1}, as shown in Figure 5.31 (a). The spectral profile of the new oscillator exhibits relatively smooth edges, which is distinctly different from dissipative solitons that are characterized by pronounced and abrupt spectral edges. Oscilloscope measurements indicate a repetition frequency of approximately 40.24 MHz, as shown in Figure 5.31 (b). The maximum average output power is about 6 mW, corresponding to a single-pulse energy of ~ 150 pJ. Because this pulse energy is insufficient for direct pulse width measurement, the output was first amplified by a Ytterbium-doped fibre amplifier (YDFA) and subsequently dispersion-compensated using a grating pair based compressor (1000 lines/mm).

Full compensation was achieved with a grating separation of 3.5 cm. For comparison, the oscillator described in Figure 5.9 required a 16.5 cm grating spacing to achieve full dispersion compensation. Considering the additional positive dispersion introduced by the amplifier, this indicates that the output chirp of the optimized oscillator is much closer to zero. The oscillator output was directly coupled into the optical modulator via a patch cable and an FC/APC connector. Despite its relatively low pulse energy, this oscillator enabled an all-fibre method to starting the stable mode-locking of MO. Importantly, this optimized seed source eliminates the need for additional amplifiers and bulky pulse compressors in MO startup.

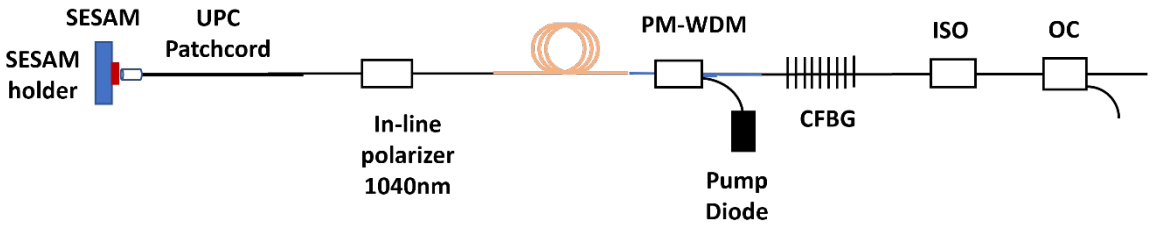

Figure 5.30 Schematic of the simplified femtosecond seed laser used to initiate the MO. The oscillator adopts a similar structure to that in Figure 5.9, with a shortened cavity length to provide net intracavity dispersion of approximately -0.1 ps^2, facilitating dispersion compensation in the downstream PF.

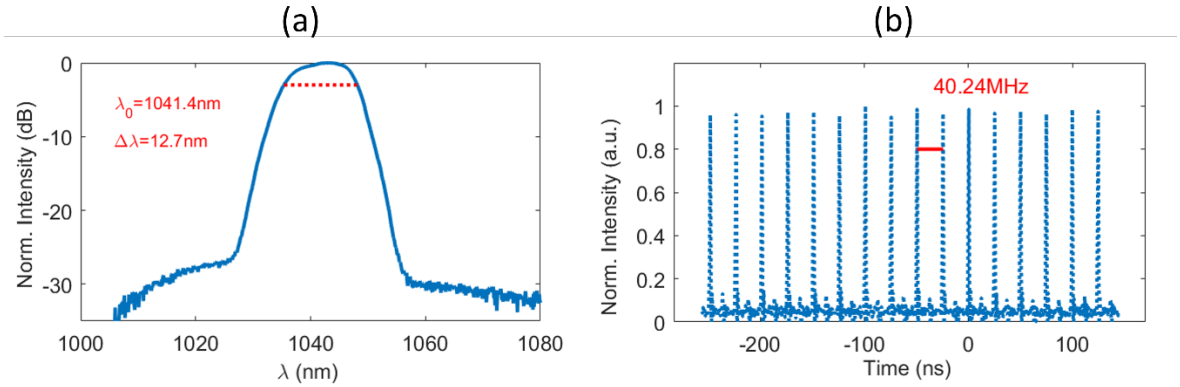

Figure 5.31 Characterization of the simplified femtosecond seed oscillator. (a) Optical spectrum of the oscillator output centered at 1041.4 nm with a full width at -10 dB of 12.7 nm. (b) Oscilloscope trace showing a pulse repetition rate of 40.24 MHz.

5.4 Conclusion

In this chapter, a comprehensive study of a 20 MHz MO was presented, combining experimental demonstration with numerical modelling to explore energy-scaling strategies and seed-laser simplification. The simulations revealed that increasing the detuning between spectral filters and reducing the pre-amplifier pump power can significantly enhance the output pulse energy, and these results were validated experimentally. The optimized oscillator delivered compressed

pulses with energies exceeding 420 nJ and durations below 40 fs. Furthermore, the modelling framework was extended to the seed source, where the influence of pulse energy, central wavelength, duration, and chirp was systematically analyzed. Guided by these results, a compact femtosecond fibre oscillator with low chirp was implemented and shown to initiate stable mode locking in the MO without the need for an external amplifier or stretcher. Overall, this chapter establishes both theoretical and experimental foundations for optimizing MOs, providing a compact and robust platform for high-energy ultrafast pulse generation.

Chapter 6 1MHz Mamyshev oscillator based on hollow-core fibre

6.1 Introduction

Ultrafast fibre lasers based on the MO architecture can deliver high-energy femtosecond pulses at megahertz-level repetition rates, but further energy scaling is fundamentally constrained by the cavity length and nonlinear phase accumulation. For applications such as precision micromachining, nonlinear microscopy, and mass spectroscopy, lasers with low repetition rates ($\leqslant$1 MHz) and high pulse energy are often required to suppress thermal accumulation, mitigate photodamage, and improve process efficiency. Conventional methods for lowering the repetition rate, such as external pulse picking or extending silica-fibre cavities, either reduce system efficiency or introduce excessive dispersion and nonlinearity, thus limiting the achievable pulse energy and duration. To overcome these limitations, we investigate the hollow-core NANFs into the MO cavity. Unlike conventional solid-core fibres, NANFs guide light in air rather than glass, resulting in a nonlinearity more than two orders of magnitude lower and a dispersion typically more than one order of magnitude smaller than silica fibres[199]. Moreover, NANFs naturally provide anomalous dispersion over a broad wavelength range, e.g., the zero-dispersion wavelength of the NANF used in our experiments is near 950 nm, making them well suited for managing pulse chirping in YDF-based MOs [200]. In this chapter, we demonstrate a low-repetition-rate MO enabled by a 240-m NANF segment, achieving stable mode locking at 1 MHz with an output energy exceeding 500 nJ. Numerical modelling reveals the favourable pulse-evolution dynamics supported by the anomalous-dispersion NANF, and experimental validation confirms substantial energy scaling. To the best of our knowledge, this represents the highest pulse energy and shortest pulse duration reported to date for a low-repetition-rate ultrafast fibre oscillator, corresponding to a peak power of ~6.4 MW, which is two orders of magnitude higher than previously demonstrated values. This NANF-based MO establishes a new pathway for energy scaling in ultrafast fibre lasers.

6.2 Background and motivation for low-repetition-rate operation

The optical cavities of mode-locked fibre lasers, including MOs, are typically several meters long and hence operate at repetition rates in the range from tens to hundreds of MHz. However, high-energy ultrafast lasers with a low repetition rate ($\leqslant$1 MHz) are preferred in some applications. For example, in high-precision micromachining processes, the low pulse repetition frequency can effectively mitigate the building up of residual heat being generated by individual ultrashort

pulses during the ablation process, avoiding possible damage to the material around the machining area and thus improving the machining quality[5]. Similarly, thermal accumulation effects appear in high-order nonlinear microscopy based biomedical imaging, therefore, decreasing the pulse repetition rate can effectively reduce phototoxic effects, such as photobleaching and photodamages[7, 201]. Beyond that, reducing the repetition rate can also improve imaging depth[6]. In femtosecond laser-assisted chemical ionization mass spectroscopy, high repetition rate lasers could generate an accumulation of ions in the ionization region, resulting in space charge saturation and therefore reducing the ionization efficiency from the subsequent pulse[4]. For the same purpose, there are similar 1MHz works in the field of CPA[202].

A common method of reducing the pulse repetition rate of an ultrafast fibre laser is to employ an external pulse picker. However, this not only decreases energy efficiency but also increases the complexity of the laser system. In principle, increasing the length of silica fibres in the mode-locked cavity can reduce the pulse repetition rate, however, this will result in large dispersion and high nonlinearity, restricting the maximum achievable pulse energy as well as the minimum achievable pulse duration. Various previous works on long-cavity ultrafast fibre lasers, including conventional mode-locked oscillators[203-205] and giant-chirp oscillators[206, 207], have shown that it is challenging to achieve a peak power more than 50 kW in the low repetition rate (≤1MHz) operation. MOs, offering larger tolerance to the NPS accumulation than other laser techniques to favor high-energy output, have also been investigated for low-repetition-rate operation. X. Luo, et al. reported a fibre MO with a cavity length of 65 m and demonstrated a 3.18-MHz pulse repetition rate at 1560 nm. A minimum pulse duration of 230 fs was obtained; however, the maximum pulse energy was only 18 nJ due to the long SMFs used inside the cavity[171]. M. Olivier, et al. presented a fibre MO with a 100-m cavity length, operating at 1030 nm. Although a low repetition rate of 939 kHz was realized, the maximum pulse energy was still relatively low (20 nJ), and the compressed pulse duration was quite long (436 fs)[208]. Regrettably, still limited to silica fibre, the standard method of increasing fibre length to reduce pulse repetition rate in MOs does not fulfil the combined need for high pulse energy and short pulse duration.

6.3 Hollow-core fibre

Hollow-core NANFs are a novel class of optical fibres that guide light predominantly in an air core by utilizing the antiresonant reflection mechanism. Compared with conventional solid-core silica fibres, NANFs offer several compelling advantages. Firstly, NANFs exhibit ultra-low transmission loss. Through the development of advanced cladding designs such as nodeless and nested-tube structures, researchers have achieved record-low losses down to 0.08 ± 0.03 dB/km[135], surpassing the attenuation of commercial single-mode fibres and demonstrating the potential of

NANFs for long-distance, high-fidelity optical transmission. Secondly, NANFs support broad and low-loss transmission windows. A recent breakthrough demonstrated that a double NANF can maintain attenuation below 0.1 dB/km across the entire 1200-1650 nm range, corresponding to a usable optical bandwidth of over 68 THz[10]. This represents the first time such a broad low-loss window has been experimentally verified in HCFs, making NANFs particularly attractive for wavelength-division multiplexing and ultrafast photonics applications. Thirdly, NANFs offer extremely low chromatic dispersion and nonlinear effects. Since light propagates mainly in air, the nonlinear refractive index is nearly negligible, and material dispersion is greatly reduced. This enables distortion-free propagation of high-peak-power femtosecond pulses and is particularly beneficial for supercontinuum generation and ultrafast light sources[209]. In addition, NANFs feature low transmission latency due to the high speed of light in air, and their air-guiding nature provides excellent thermal stability, which is crucial for precise optical frequency transmission[210]. The structural flexibility of NANFs, including variations in the number, shape, and arrangement of cladding tubes, also allows for optimization of modal properties and further suppression of higher-order modes, though these aspects are secondary compared to their fundamental optical benefits.

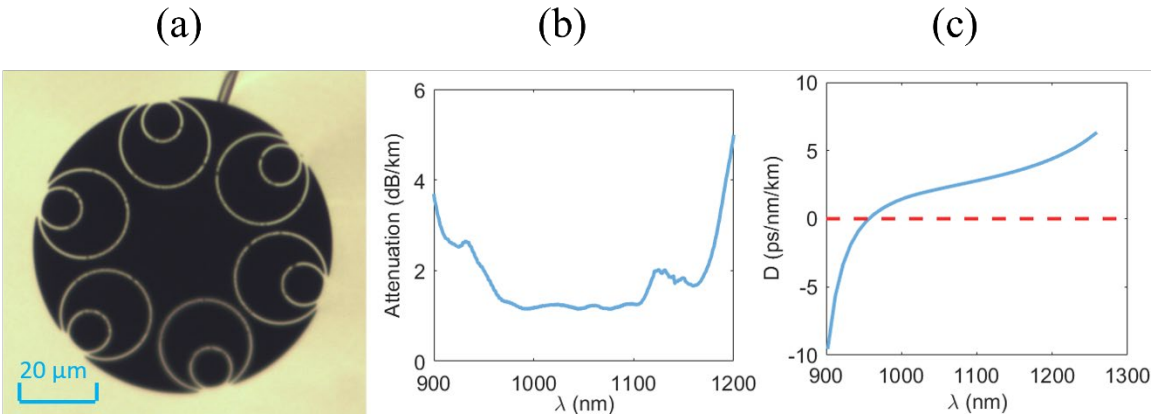

Figure 6.1 Structural and optical properties of the in-house fabricated NANF, a type of antiresonant HCF. (a) Optical microscope image of the fibre cross-section showing the nested antiresonant structure. (b) Measured loss spectrum, exhibiting a minimum attenuation of 1.3 dB/km near 1040 nm. (c) Simulated dispersion profile showing anomalous dispersion (D = 2.36 ps/(nm·km)) at the laser operating wavelength.

The unique properties of NANFs make them a promising solution for repetition rate reduction in ultrafast oscillators, particularly in scenarios where low dispersion, minimal nonlinearity, and low loss are essential. Figure 6.1 presents the structural and optical properties of an in-house fabricated NANF, a specific type of antiresonant HCFs. The fibre features a MFD of 21 µm, a loss of 1.3 dB/km, and a dispersion coefficient of 2.36 ps/(nm·km) at the operating wavelength. The measured transmission window of the NANF aligns well with the spectral region of the MO output,

and the fibre exhibits anomalous dispersion at those wavelengths. These characteristics render the NANF a suitable candidate for intracavity dispersion management.

6.4 1MHz MO experiment

To evaluate the potential of the NANF for repetition rate reduction in MOs, we replaced the 0.4 m PM PF after the 1st filter in Figure 5.1 with a 12.5 m-long NANF, as shown in Figure 6.2. To improve the mode field matching between the fibres, the focal lengths of Lens 2 and Lens 3 were adjusted to 18.4 mm and 25.4 mm, respectively. In addition, the λ_{c1} was tuned to 1036 nm with a bandwidth of 2.0 nm, as shown in Figure 6.3 (a), to optimize the output pulse characteristics. The rest of the MO cavity remained unchanged. This configuration was seeded by the laser described in Section 5.2.2. Figure 6.3 (a) illustrates that stable single-pulse mode-locking was achieved at a repetition rate of 11.24 MHz with pump powers of P_1= 6.5 W and P_2=10.0 W. With P_2 increased, the output pulse energy grew nearly linearly, as shown in Figure 6.3 (c), reaching a maximum of 359 nJ. Beyond this pump level, mode-locking was lost. When P_1 was increased to 8.1 W, only dual-pulse mode-locking could be sustained.

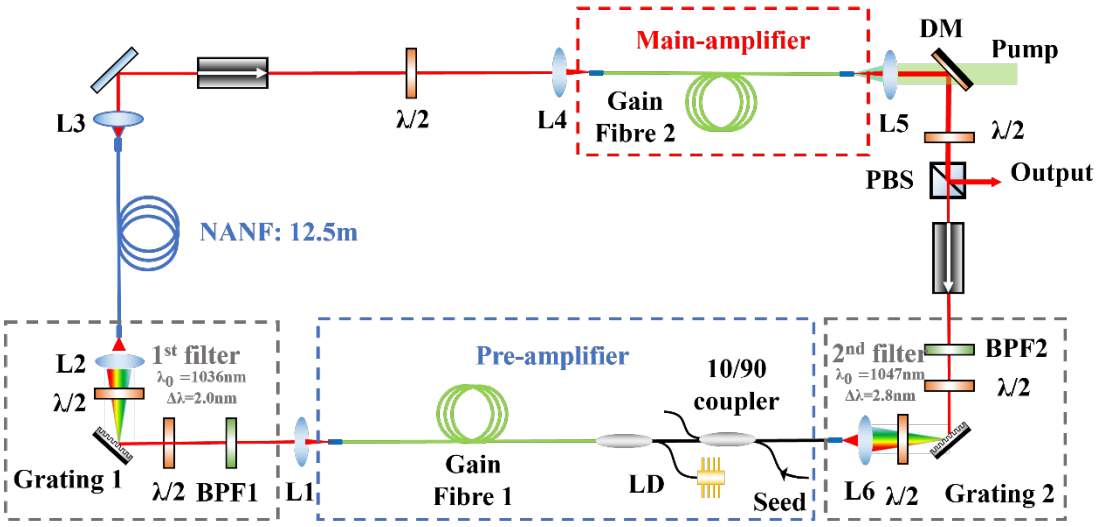

Figure 6.2 Experimental setup and performance of the MO incorporating a 12.5 m-long NANF for repetition rate reduction.

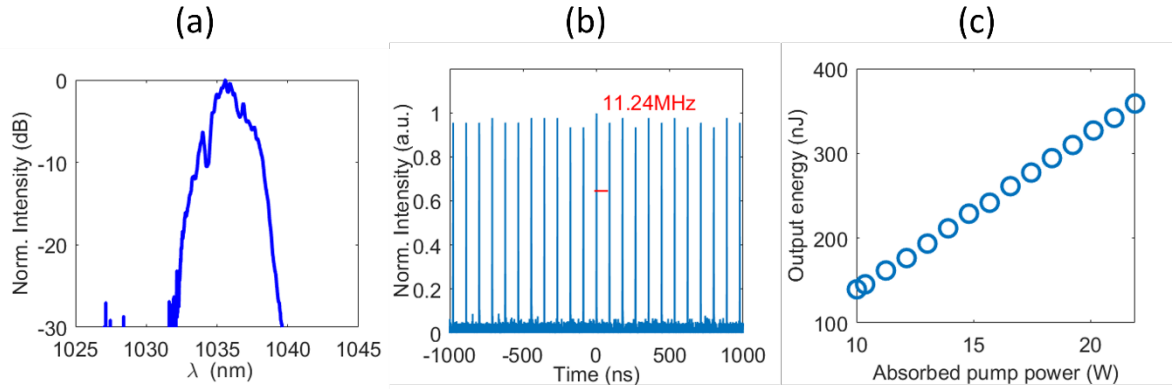

Figure 6.3 (a) Transmission spectrum of the 1st filter. (b) Detected pulse train showing stable single-pulse mode-locking at a repetition rate of 11.24 MHz. (c) Output pulse energy as a function of absorbed pump power P_2, showing a nearly linear dependence.

The primary objective of demonstrating the feasibility of using NANF in the MO cavity to reduce the repetition rate was successfully achieved. Previous attempts using PM PFs of comparable length failed to initiate mode locking. In contrast, stable mode locking was readily obtained with a 12.5 m-long NANF. Building on this result, the NANF length was further increased to 35 m and 107 m, corresponding to repetition rates of approximately 6 MHz and 2.5 MHz, respectively, both successfully supporting stable mode-locking.

Encouraged by these results, the NANF length was ultimately increased to ~240 m in subsequent experiments to further reduce the repetition rate (the structure and implementation are shown in Figure 6.4). As a result, the total optical length of the cavity increased to approximately 254 m, yielding a reduced repetition rate of ~1.18 MHz. In the experiment, the polarization extinction ratio (PER) was observed to degrade from 30 dB to 14 dB after the NANF, probably due to the asymmetric tension caused by fibre bending. To address this, PBS1 was included to maintain a high PER for the main-amplifier. Multi-pulse mode locking was initially observed at the onset of MO operation when absorbed pump powers were increased to 6.3 W and 20.8 W in the pre-amplifier and the main-amplifier, respectively. However, stable single-pulse mode locking could be obtained when pump powers were reduced selectively for the two amplifiers. In the single-pulse mode-locked operation, the absorbed pump power was fixed at 3.8 W in the pre-amplifier while was adjusted between 4.6 W and 6.4 W in the main-amplifier to change the output power from the MO. This multi-pulsed mode-locking for the MO with NANF is attributed to the large mismatch in pulse repetition rates between the seed laser and the MO cavity. Nevertheless, the pump threshold of the MO with the NANF was substantially lower than the MO without NANF.

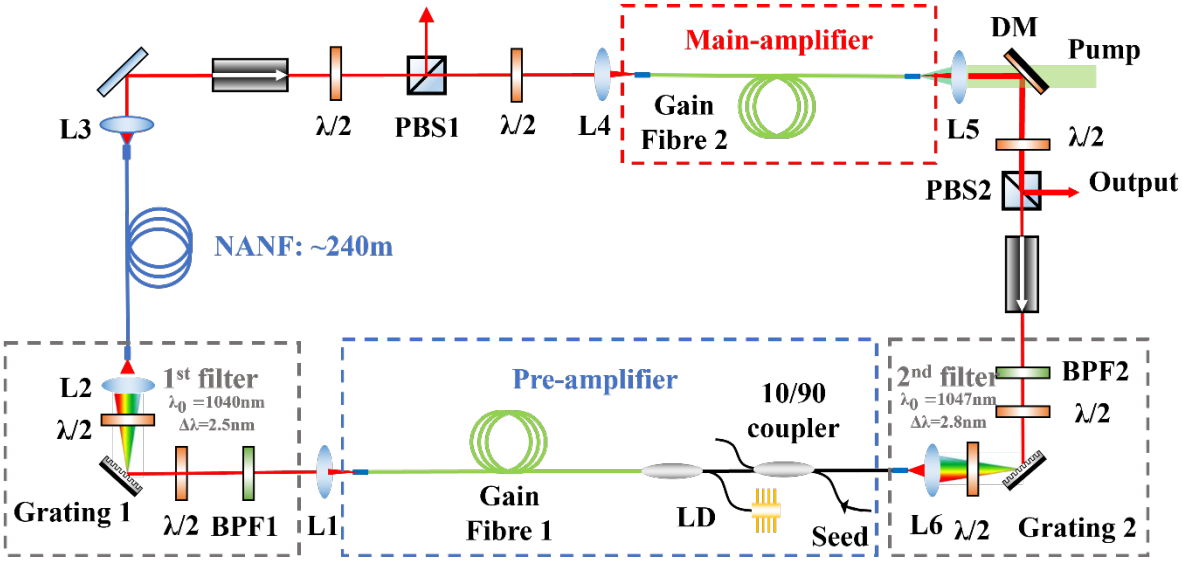

Figure 6.4 Schematic of the MO incorporating a 240 m-long in-house fabricated NANF to achieve ultra-low repetition rates. The NANF replaces the short PF segment after the first spectral filter, increasing the total cavity length to ~254 m and resulting in a repetition rate of ~1.18 MHz. The the λ_{c1}=1040 nm, with a 2.5 nm bandwidth, and the λ_{c2} =1047 nm, with a 2.8 nm bandwidth.

Under the single-pulse mode-locking regime, the variation of output power with respect to the absorbed pump power in the main amplifier was measured, as presented in Figure 6.5 (a). The maximum average output power reached 0.608 W, corresponding to a single-pulse energy of 514 nJ. Attempts to further increase the pump power led to disruption of stable mode-locking. This pulse energy, achieved at a repetition rate of 1.18 MHz, significantly surpasses that obtained from the 20.03 MHz MO configuration, and the improvement can be attributed to several factors. First, operating at a lower repetition rate reduces the average thermal load in the gain fibre of the main amplifier, thereby reducing thermally induced noise. More critically, the anomalous dispersion introduced by the NANF may modify the pulse chirp and influence the phase evolution, contributing to more efficient pulse formation. The output spectrum at maximum power, shown in Figure 6.5 (b), exhibits a central wavelength of 1046 nm and a 10-dB bandwidth of 91 nm. This bandwidth is narrower than that observed in the high-repetition-rate (20 MHz) MO, likely due to suppressed SPM in the presence of anomalous dispersion from the NANF. Pulse compression was performed using the same grating-based compressor as in previous experiments. The ACF of the compressed pulse and the TL Gaussian pulse are shown in Figure 6.6 (a). The FWHM of ACF is measured to be 64.5 fs, corresponding to pulse duration estimated at 45.7 fs under the Gaussian assumption. Compared to the 20 MHz case, this ACF features a significantly lower pedestal, indicating reduced NPS accumulation. Approximately 85% of the pulse energy is confined within the main lobe. Figure 6.6 (b) displays the ACF over a 5 ps window, showing no evidence of satellite pulses. The RF spectrum in Figure 6.7 (a) confirms a fundamental repetition

rate of 1.18 MHz with a SNR of 60.51 dB. The wideband spectrum, shown in Figure 6.7 (b), is flat and free of sidebands, evidencing stable and clean single-pulse mode-locking.

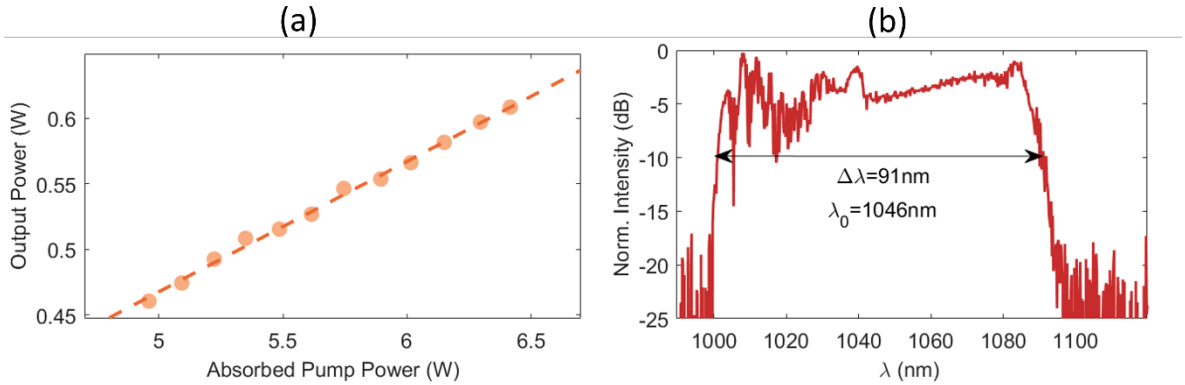

Figure 6.5 (a) Output power of single-pulse mode-locking at different pump power at the main-amplifier. (b) Output spectrum at 514 nJ pulse energy.

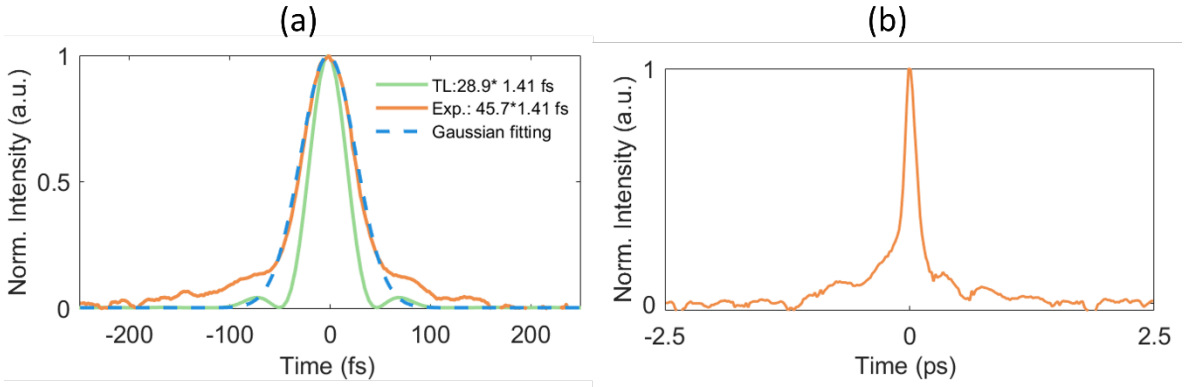

Figure 6.6 (a) The intensity AC traces of the compressed pulses (green) and TL pulses (orange) with a span of 500 fs. (b) The intensity AC traces of the compressed pulses with a span of 5 ps.

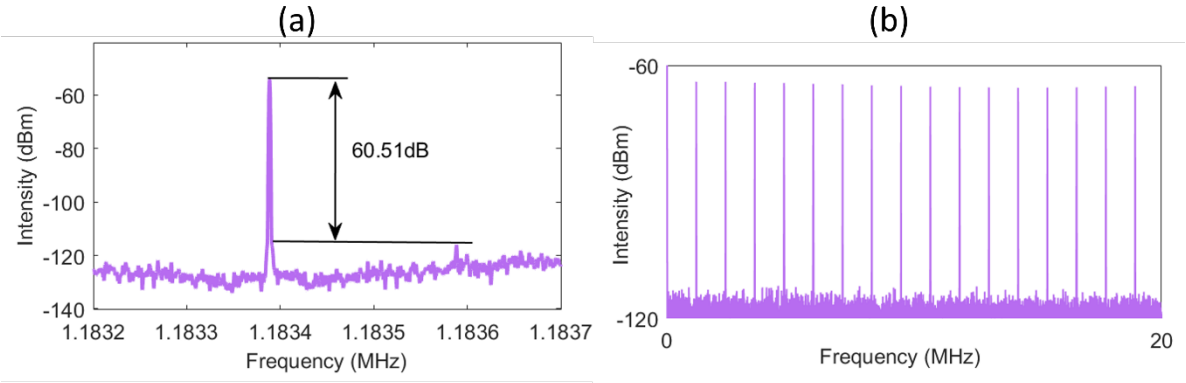

Figure 6.7 (a) RF spectrum with a NBW of 1 Hz and a span of 500 Hz. (b) RF spectrum with a NBW of 10kHz and a span of 20 MHz.

Single-pulse mode-locked operation was successfully achieved both in MOs using standard PM PFs and using NANFs. As expected, the introduction of NANF substantially reduced the repetition

frequency of the MO from 20.03 MHz to 1.18 MHz. It is notable that 35% more pulse energy was achieved in the MO using NANF. Less heat generated by the low average power at a low repetition rate partly contributes to this but should not be the main reason. The bandwidth of the output spectrum indicates that the negative dispersion introduced by NANF plays a crucial role in reaching a higher pulse energy. For a given MO, the bandwidth of the output spectrum is broadened at higher values of pump power in the main-amplifier. The MO using NANF delivers output pulses with a higher pulse energy (514nJ vs. 381nJ) but narrower bandwidth (91 nm vs. 120 nm) than the MO using standard PM PFs. Thus, the introduction of the NANF resulted in suppressions of spectral broadening and NPS accumulation simultaneously.

6.5 Simulation results

The spectral broadening process of the pulse in the gain fibre of the main-amplifier is likely dominated by the so-called gain-managed nonlinear amplification, which balances the nonlinearity and the longitudinal gain-shaping. To further investigate this phenomenon, we numerically modelled the MOs and simulated the intra-cavity pulse evolution by using the split-step method [160]. Given the low dispersion, low nonlinearity, and low loss characteristics of the 240 m NANF, it was modeled as a lumped dispersive element with an overall GDD of −0.34 ps^2 for simplification. To facilitate a fair comparison, both the PF- and NANF-based MOs were simulated to generate 300 nJ output pulse energy.

Figure 6.8 (a) displays the simulated spectrogram of the intra-cavity pulse immediately before entering the main amplifier in the NANF-based MO, showing a down-chirped profile. In contrast, Figure 6.8 (b) shows an up-chirped pulse for the PF-based MO, where a 0.4 m PM PF was used instead of the NANF. This is the essential impact brought about by the introduction of NANF. Figure 6.9 (a) presents the evolution of the spectral bandwidth along the gain fibre. In the PF-based MO, spectral broadening begins early due to the positively chirped input pulse, resulting in a final output bandwidth of 104 nm. However, in the NANF-based MO, spectral broadening is noticeably delayed, initiating after ~0.5 m of propagation and yielding a significantly narrower output bandwidth of 58 nm. This delayed spectral broadening explains the narrower output spectra despite higher pulse energy in the NANF-based MO. Figure 6.9 (b) illustrates the evolution of the pulse peak power in the main amplifier, which reflects the accumulation of NPS and is a key factor limiting pulse energy in ultrafast oscillators. The shaded area indicates the cumulative NPS, which is clearly smaller for the NANF-based MO. At 300 nJ, the calculated total NPS is approximately 20π for the NANF-based MO and 28π for the PF-based MO. In experimental conditions corresponding to maximum pulse energies of 514 nJ and 381 nJ for the NANF- and PF-based MOs, respectively, the accumulated NPS for both cases is approximately 35π. These results support the conclusion that lower NPS accumulation in the NANF-based MO facilitates

the generation of higher-energy pulses. Figure 6.10 compares the simulated output spectra with experimental results for both MO configurations, demonstrating good agreement and validating the simulation framework. Those results clearly prove that the negative dispersion introduced by the NANF can reduce the NPS accumulation and hence increase the maximum output pulse energy.

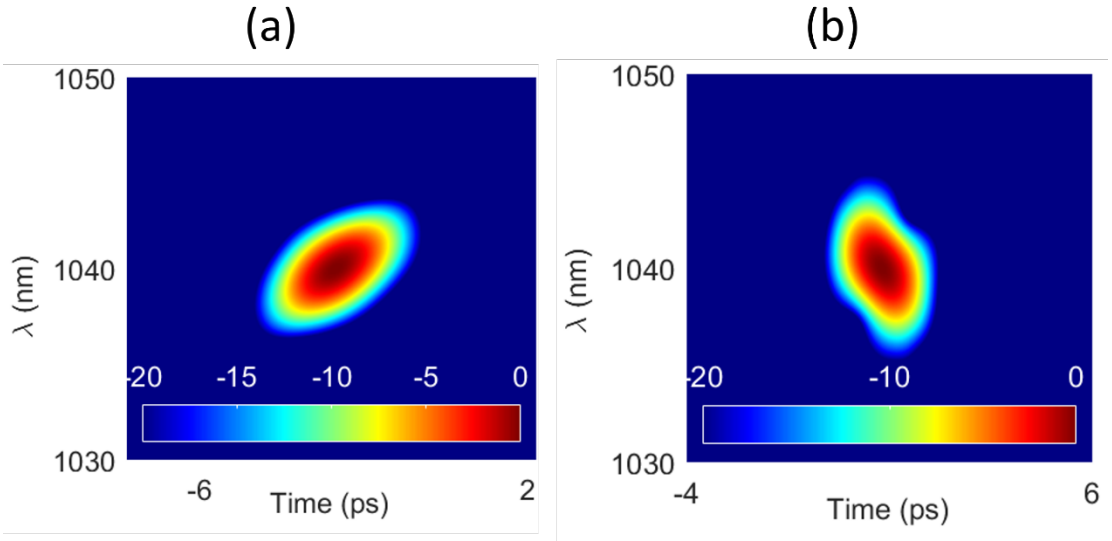

Figure 6.8 Numerical simulation results for MOs using PF and NANF, each delivering 300 nJ output pulse energy. (a) Spectrogram of the intra-cavity pulse before entering the main amplifier in the NANF-based MO, showing a negatively chirped (down-chirped) pulse. (b) Spectrogram of the intra-cavity pulse before entering the main amplifier in the PF-based MO, showing a positively chirped (up-chirped) pulse.

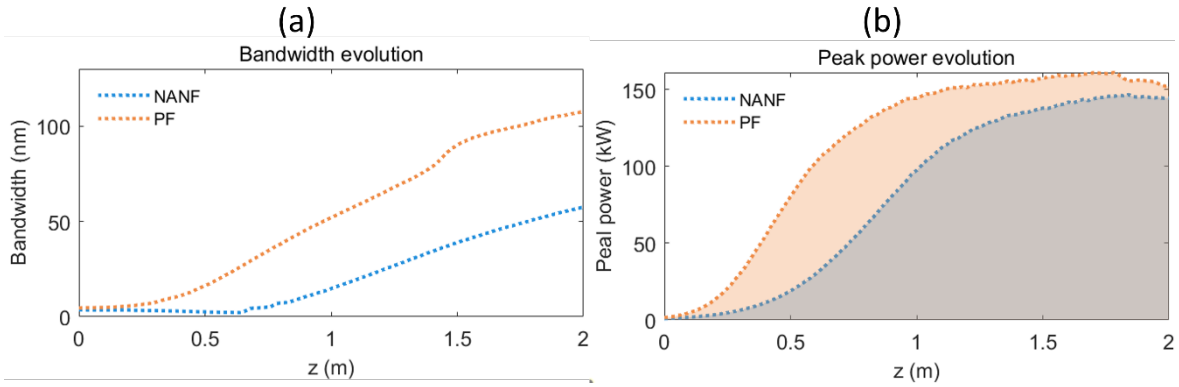

Figure 6.9 Numerical simulation results for MOs using PF and NANF, each delivering 300 nJ output pulse energy. (a) Evolution of the spectral bandwidth along the gain fibre of the main amplifier for both configurations (blue: NANF; orange: PF). (b) Evolution of the pulse peak power along the gain fibre, indicating NPS accumulation (blue: NANF; orange: PF).

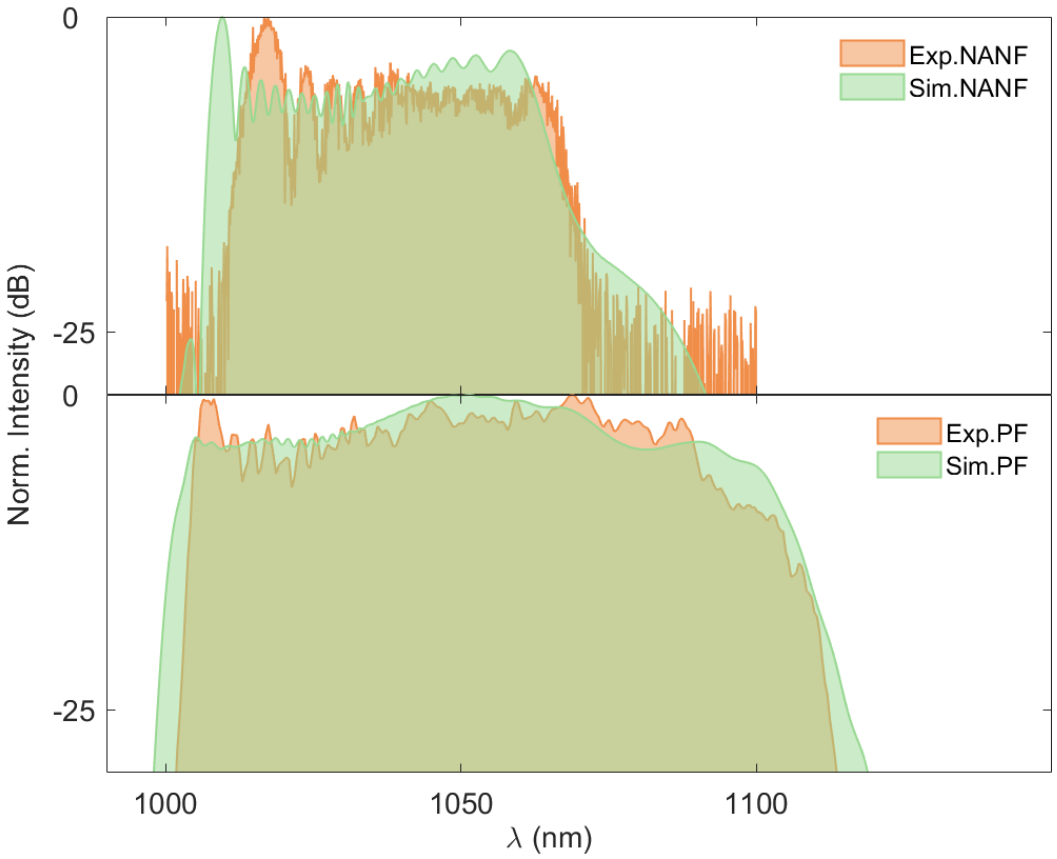

Figure 6.10 Numerical simulation results comparison between simulated and experimental output spectra for both Mos, each delivering 300 nJ output pulse energy. Upper panel: NANF-based MO; lower panel: PF-based MO.

In this work, NANF not only functions as a time delay line to reduce the pulse repetition rate but also provides chirp management functionality for the intra-cavity pulses to further enhance the output pulse energy. These findings confirm that the anomalous dispersion introduced by the NANF not only enables repetition rate reduction but also serves as an effective intra-cavity chirp management tool. This dual functionality helps suppress NPS accumulation and consequently enhances the achievable pulse energy in mode-locked oscillators.

6.6 Conclusion

In this chapter, we have implemented and analyzed a MO incorporating a long NANF to achieve low-repetition-rate operation. The combined experimental and numerical study confirms that the NANF segment provides both anomalous dispersion and ultra-low nonlinearity, which are essential for maintaining stable single-pulse operation in an extended cavity. Importantly, the introduction of the NANF does not degrade the pulse characteristics; instead, it facilitates a higher tolerance to nonlinear phase accumulation, thereby supporting an increase in the maximum achievable pulse energy. Our modelling clarified the pulse-evolution dynamics in this hybrid system, showing how the NANF suppresses nonlinear phase accumulation and enables

efficient gain-managed amplification by suitable negative chirp value. The consistency between simulation and experiment underlines the robustness of the approach. Beyond validating this concept, the results establish NANF-based MO integration as a powerful strategy for breaking the conventional trade-off between repetition rate, pulse energy, and pulse duration in fibre oscillators. This opens new opportunities for scaling ultrafast fibre lasers toward application regimes that demand simultaneously high pulse energy and low repetition rates, such as precision micromachining and nonlinear biomedical imaging.

Chapter 7 High-performance pulse compression based on hollow core nested antiresonant nodeless fibre

7.1 Introduction

The generation and manipulation of ultrashort laser pulses are essential in numerous scientific and industrial applications, ranging from high-resolution spectroscopy and micro-machining to nonlinear optics and biomedical imaging. To reach the temporal resolution required for such applications, post-compression techniques are often employed to shorten the pulse duration beyond the oscillator limit. Conventional free-space compression methods, such as grating pairs, prism pairs, and chirped mirrors (CMs), are capable of compensating spectral phase distortions accumulated during propagation. However, they typically involve complex optical alignment, large footprint, and sensitivity to mechanical perturbations. HCFs have emerged as a powerful alternative for pulse compression due to their low nonlinearity, high power handling, and favorable dispersion characteristics. Among various HCF types, the NANF offers exceptionally low propagation loss and broad transmission bandwidth, making it a strong candidate for high-performance compression. In particular, the negative GVD of NANF near 1 μm makes it well suited for compressing positively chirped pulses from Yb-based fibre oscillators. This chapter presents a comprehensive study of femtosecond pulse compression based on NANF. We first review the fundamental principles of conventional pulse compression techniques, followed by a detailed description of the NANF-based compression setup. Key challenges and optimization steps during implementation are analyzed, including spectral distortion control and nonlinear effects in diagnostics. Compression performance is experimentally characterized and compared with a benchmark grating pair compressor. Finally, we discuss dispersion limitations, integration potentials, and the future prospects of NANF in compact ultrafast systems.

7.2 Principles of conventional compression techniques

Ultrashort pulse compression is fundamentally based on compensating the spectral phase accumulated during pulse propagation through dispersive and nonlinear media. To achieve TL pulse durations, it is essential to introduce a dispersive optical element with an opposite sign of GDD and higher-order dispersion to that accumulated. This section introduces three widely used

pulse compression techniques: grating pairs, prism pairs, CMs, and pulse shaper, along with their physical principles and dispersion characteristics.

7.2.1 Grating pair based compressor

Grating pair compressors utilize angular dispersion and free-space propagation to introduce negative GDD, making them well-suited for compressing positively chirped pulses. By passing the ultrashort pulse through a pair of parallel reflective or transmissive diffraction gratings, different spectral components of a pulse propagate along different optical paths due to diffraction, where longer wavelengths propagating shorter distances and shorter wavelengths propagating longer paths. This results in a introduction of a negative GDD that can be expressed as:

$$GDD(\lambda_0) = -\frac{m^2\lambda_0^3 L}{2\pi c^2 d^2 cos^3\theta_0} \tag{7-1}$$

Where m is the diffraction order (usually -1 for compressors), λ_0 is the central wavelength, L is the separation between the gratings, c is the speed of light, d is the grating period, and θ_0 is the diffraction angle.

Figure 7.1 (a) and (b) show schematic diagrams of compressors using transmissive gratings and reflective gratings, respectively. Transmissive gratings tend to have higher compression efficiency. Grating compressors inherently introduce negative GDD and positive TOD, and both parameters scale with the separation distance between the gratings. By tuning this separation, one can flexibly adjust the amount of dispersion. Grating pair compressors have a very mature device supply and can also provide flexible and efficient dispersion compensation, but they usually rely on good spatial optical path alignment. In the case of large dispersion compensation, the size and space occupation of the grating are relatively high.

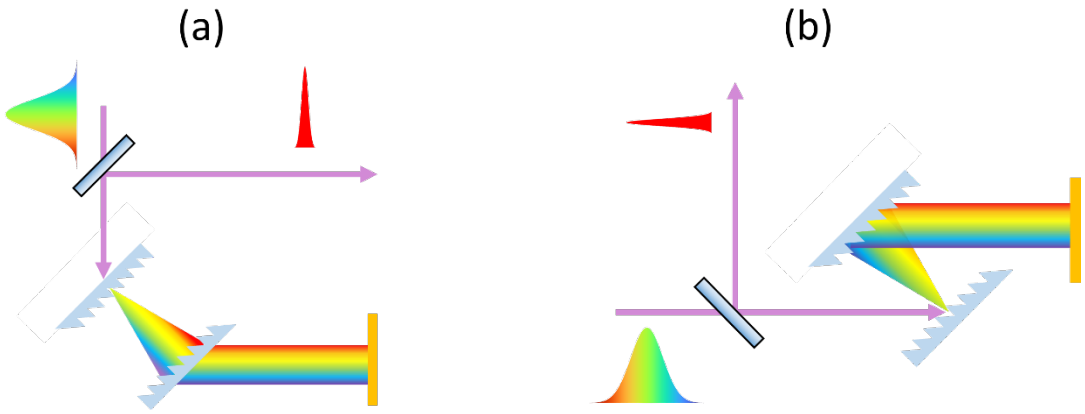

Figure 7.1 Schematic diagrams of grating pair compressors. (a) Configuration using transmissive diffraction gratings, which offers higher efficiency. (b) Configuration

using reflective diffraction gratings. In both cases, angular dispersion separates spectral components, and path length differences among wavelengths introduce negative GDD and positive TOD for pulse compression.

7.2.2 Prism pair based compressor

Prism pair compressors operate on the principle of material dispersion and angular separation through refraction. The GDD generated by the ultrashort pulse passing through the prism pair is partly due to the angular dispersion caused by refraction and partly due to the material dispersion of the prism medium that can be expressed as:

$$GDD(\lambda_0) = -4L_{sep}\frac{\lambda_0^3}{2\pi c^2}\left(\frac{dn}{d\lambda}\Big|_{\lambda_0}\right)^2 + L_{prism}\frac{\lambda_0^3}{2\pi c^2}\frac{d^2n}{d\lambda^2}\Big|_{\lambda_0} \quad (7\text{-}2)$$

Where L_{sep} is the separation between prisms, n is the refractive index of the prisms, L_{prism} is the insertion thickness of the prism.

Figure 7.2 (a) and (b) are schematic diagrams of a prism compressor without and with a folded structure, respectively. The latter has a more compact structure. Unlike grating pairs, due to the combined effects of material dispersion and angular dispersion, prism pairs can introduce negative GDD and negative TOD by finely adjusting the insertion thickness of the prisms and the prism spacing. This gives prism pairs an advantage in compressing pulses below 100fs or even shorter pulses. For compensation of large amounts of dispersion, large grating pairs and footprint are also required.

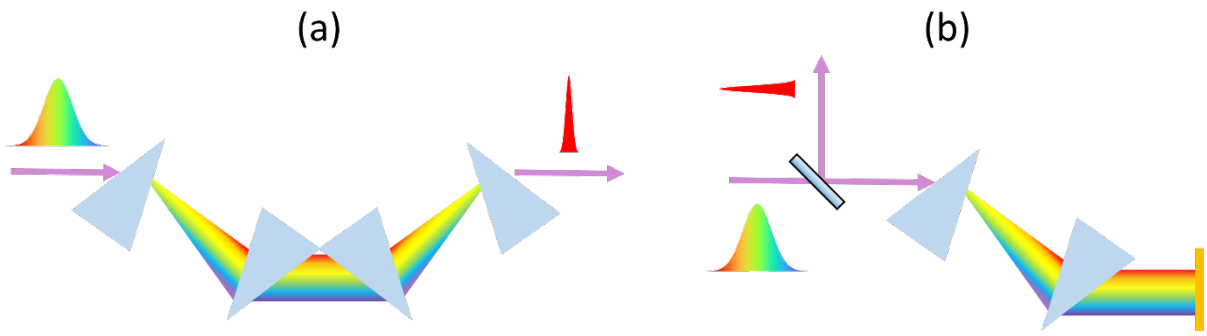

Figure 7.2 Schematic diagrams of prism pair compressors. (a) Standard unfolded geometry where the beam propagates through two prisms and experiences material and angular dispersion. (b) Folded configuration that enhances compactness by folding the beam path with mirrors. Prism compressors generate negative GDD and negative TOD by adjusting prism separation and insertion depth, making them suitable for compressing sub-100 fs pulses.

7.2.3 Chirped mirror based compressor

CMs are multilayer dielectric mirrors engineered to provide tailored spectral phase shifts upon reflection. By designing the layer thicknesses to vary (chirp) in depth, the mirror causes different spectral components to reflect at different depths, leading to wavelength-dependent group delays. This enables precise control over GDD and higher-order dispersion. An important feature of CM is that the depth and material can be designed to customize GDD and TOD more freely, which is different from grating and prism pairs, where GDD and TOD are usually coupled. There are also CM products on the market that have zero net GDD and are only used for TOD compensation.

Figure 7.2 (a) and (b) respectively show the schematic diagram of the structure of the CM and the schematic diagram of the compressor based on the CM. CMs are more convenient to collimate and can provide ultra-high compression efficiency. The single-shot reflectivity is almost always over 99%. CMs can also provide ultra-wide spectral bandwidth. Therefore, CMs are often used to compress sub-hundred-femtosecond or even few-cycle pulses. The GDD introduced by a single reflection of a CM is relatively limited and fixed (~ -50 - -100 fs^2 typically), unlike grating pairs and prism pairs that can be continuously adjusted. When compensating for large dispersion, cascading is sometimes required to achieve complete dispersion compensation.

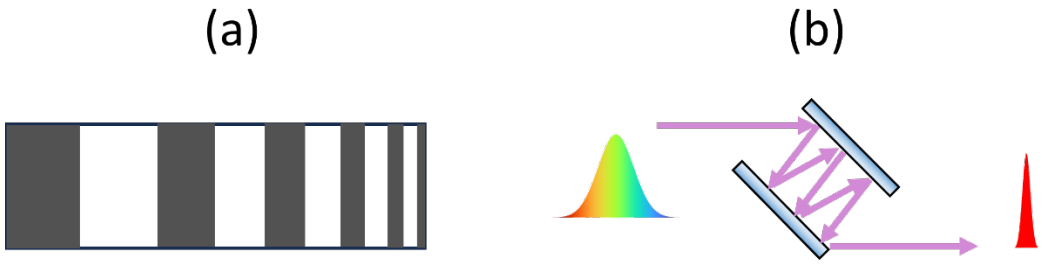

Figure 7.3 Schematics of CM design and CM-based pulse compressor. (a) Layer structure of a CM, where dielectric layers are chirped in thickness to induce wavelength-dependent reflection delays. (b) CM compressor configuration using a sequence of reflections to accumulate dispersion compensation. CMs offer precise, high-efficiency dispersion control and are widely used for few-cycle pulse compression.

7.2.4 Spatial light modulators based compressor

Pulse shapers based on spatial light modulators (SLMs) offer a highly flexible approach to pulse compression by directly manipulating the spectral phase and amplitude of ultrashort pulses in a programmable fashion. These systems typically employ a $4f$ compressor geometry, as shown in Figure 7.4, where the pulse is dispersed spatially in the frequency domain using a diffraction

grating and a focusing lens, then modulated by an SLM located at the Fourier plane. The SLM acts as a programmable mask that can imprint desired phase and/or amplitude modulation onto each frequency component of the pulse. After recombination by a symmetric optical path, the resulting time-domain waveform reflects the imposed spectral phase, enabling full or partial compensation of high-order dispersions, or even arbitrary waveform shaping. This pulse shaper can achieve arbitrary and programmable dispersion compensation, including GDD, TOD, FOD, etc. The pulse shaper can theoretically achieve full compensation of any order of dispersion. It can also adaptively compensate the pulse through the feedback algorithm. However, in practice, the spectral resolution and shaping fidelity of this method are affected by the number of pixels of the SLM, and precise optical path alignment is required. Due to the limited damage threshold of the SLM, this technology is not suitable for use in the field of high-energy pulses.

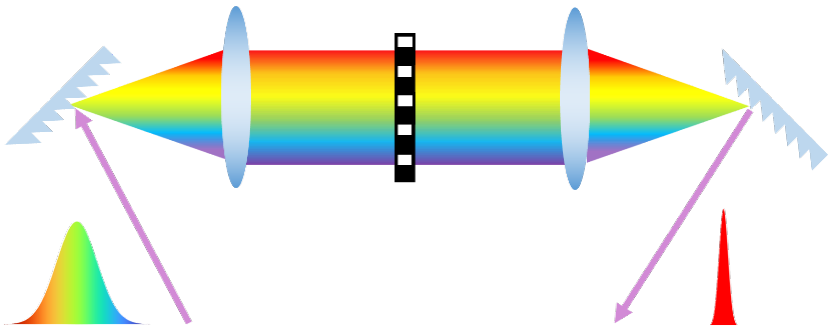

Figure 7.4 Pulse shaping compressor based on a SLM in a $4f$ configuration. The input pulse is angularly dispersed by a diffraction grating and focused by a lens onto the SLM placed at the Fourier plane. The SLM modulates the spectral phase and/or amplitude of each frequency component. After symmetric recombination, the output pulse exhibits the desired time-domain waveform. This approach enables arbitrary dispersion compensation and waveform shaping, but is limited by the SLM's spectral resolution and damage threshold.

7.2.5 Hollow-core fibre based compressor

The pulse compressors mentioned above are usually composed of bulk components. These free-space optics require precise alignment, occupy significant space, and introduce undesired power loss due to their multi-pass configuration. However, traditional solid-core fibres face challenges in compressing high-energy pulses due to strong nonlinearity. In contrast, NANFs, which guide light through air rather than glass, significantly reduce nonlinearity, enabling efficient pulse compression and ultrashort pulse delivery. Moreover, NANFs can be designed to provide anomalous dispersions at 1 μm, making them ideal for compressing up-chirped pulses from ytterbium-fibre-based MOs. Previous studies have demonstrated pulse compression from 1.6 ps

to 158 fs using a photonic bandgap HCF (PB-HCF) for a 5.3-nJ Yb fibre laser[211]. The propagation loss and transmission bandwidth of HCFs are critical factors in achieving high-energy pulse compression with minimal dispersion. Compared to PB-HCF, NANF offers lower loss and broader transmission bandwidth[10], which provides a promising solution for compressing and delivering ultrashort pulses. For example, pulse delivery at 800 nm has been demonstrated using an NANF with a Ti:Sapphire laser[212]. Due to the high pulse energy of 200 μJ, pre-chirp of the input pulses is required to compensate for the dispersion of the NANF, and a complex vacuum system is necessary to prevent plasma formation during the pulse delivery. Nevertheless, these results highlight the high-power handling capability and promising ultrashort pulse compressing performance of the NANF. Combining NANFs with Yb fibre lasers offers a potential route to realizing a monolithic, fibre-based system capable of delivering compressed pulses for end-user applications.

7.3 Experimental setup of pulse compression using NANF

7.3.1 Description of the setup

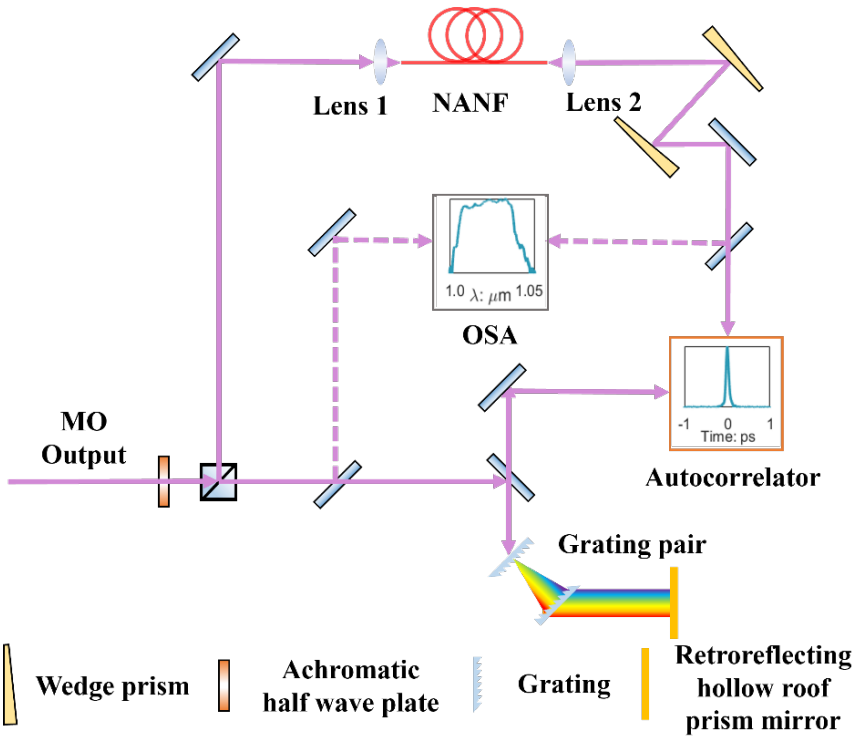

Figure 7.5 Schematic layout of the experimental setup for pulse compression using NANF. The setup includes two compression branches (NANF and grating pair), polarization-based beam splitting, power control optics, and diagnostic tools (OSA and autocorrelator). Attenuation optics are inserted before diagnostic tools to prevent damage from high-energy pulses.

To compress the output pulses of a MO, we present in this section a post-compression stage based on NANF in an atmospheric environment. The schematic layout of the compression system is shown in Figure 7.5. In order to evaluate the actual effect of the NANF-based compressor, a grating pair compressor was also built. An achromatic HWP and a broadband PBS were used to reflect almost all the energy into the optical path of the NANF-based compressor, and only a small part of the energy was transmitted into the optical path of the grating pair compressor. The two compressors share an autocorrelator and an optical spectrum analyzer (OSA) for measurement. The pulses are coupled into the OSA through a MMF for spectral measurement. In order to avoid damage to the measurement device by high energy pulses, a wedge mirror is used to attenuate the energy of the pulses output by the NANF. The transmission efficiency of a single wedge mirror is measured to be ~86%, and the reflectivity is about 7%. Therefore, two wedge mirrors are used. The total energy attenuation is about 0.5%. The NANF used is the same as that described in Section 6.3. The Chromatic Dispersion Parameter, D shown in Figure 6.1 (c) is converted to the Group Velocity Dispersion Parameter, β_2 parameter as shown in Figure 7.6. The orange dashed line marks the location of the zero-dispersion point.

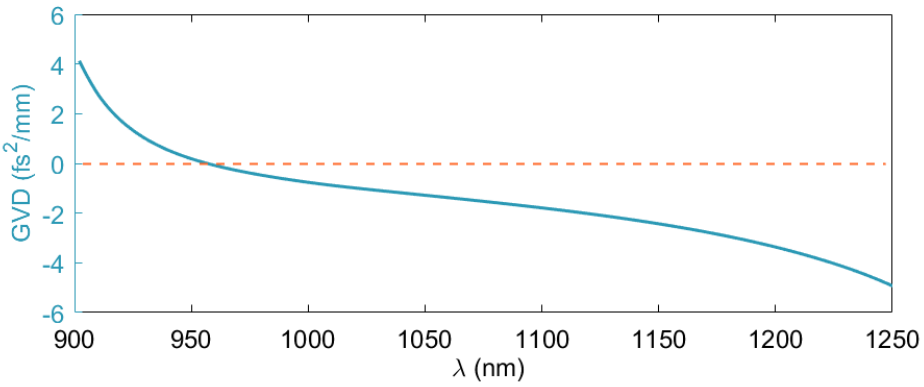

Figure 7.6 GVD curve of the NANF, derived from the chromatic dispersion parameter shown in Figure 6.1 (c). The orange dashed line indicates the zero-dispersion wavelength.

As shown in Figure 7.7, the structure of MO is basically the same as that in Section 5.2.1. The difference is that in order to increase the output energy, the gain fibre of the main amplifier is replaced from a 25um core diameter to a 30um core diameter PLMA 30/250, with a length of about 2.4m. The fibre was coiled with a bending diameter of 5 cm for ensuring single-mode operation. In order to better match the mode field, the focal length of lens3 was replaced with 8.0mm. The recorded stable pulse train of the MO, operating in single-pulse mode-locking, is shown in Figure 7.8 (a). The repetition rate was 19.34 MHz, matching well with the measured total optical cavity path length of ~ 15.50 m. With a pump power fixed at 5.69 W in the 1st arm, the output power of the MO was controlled by adjusting the pump power in the 2nd arm. Figure 7.8 (b) shows the increase of the output power and pulse energy with respect to the absorbed pump power,

reaching a maximum of 10.2 W and 527.2 nJ, respectively. Output spectrum of the MO broadened with the increase of the pump power, showing an expand of the 10-dB spectral bandwidth from 61 nm to 91 nm, as illustrated in Figure 7.8 (c). The MO generated mode-locked pulses with an upchirp due to the all-normal dispersion cavity. Autocorrelation of the output pulses at the maximum power was measured and shown in Figure 7.8 (d), unveiling a pulse width of 2 ps with a Gaussian assumption.

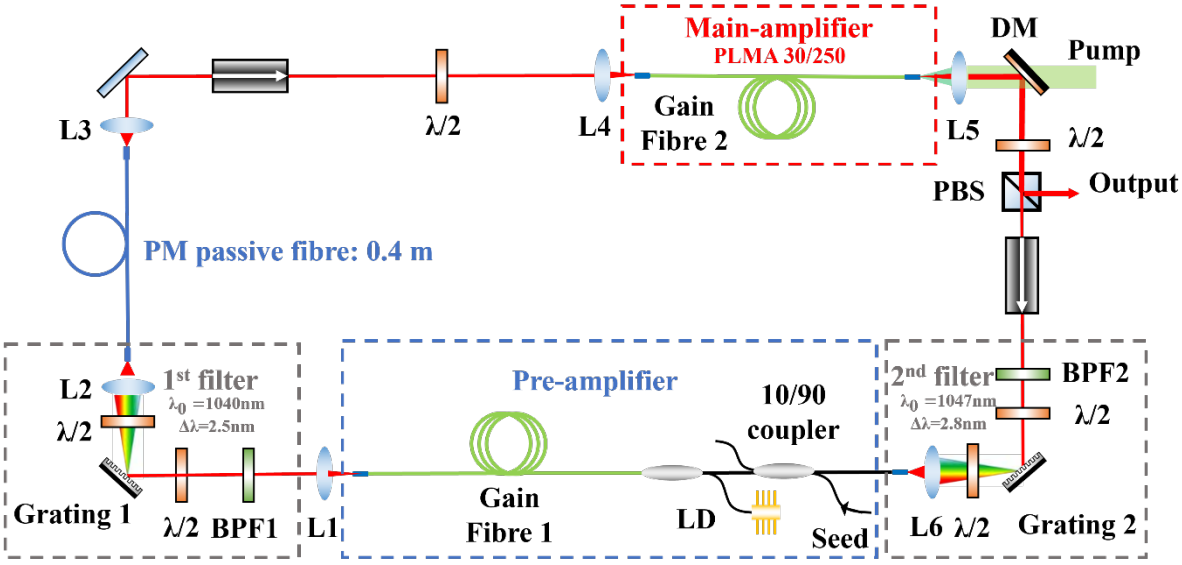

Figure 7.7 Modified MO structure used in the compression experiment. Compared with the setup in Section 5.2.1, the main amplifier uses a PLMA 30/250 fibre (30 μm core diameter) for higher output energy. The beam coupling optics were also adjusted for better mode-field matching.

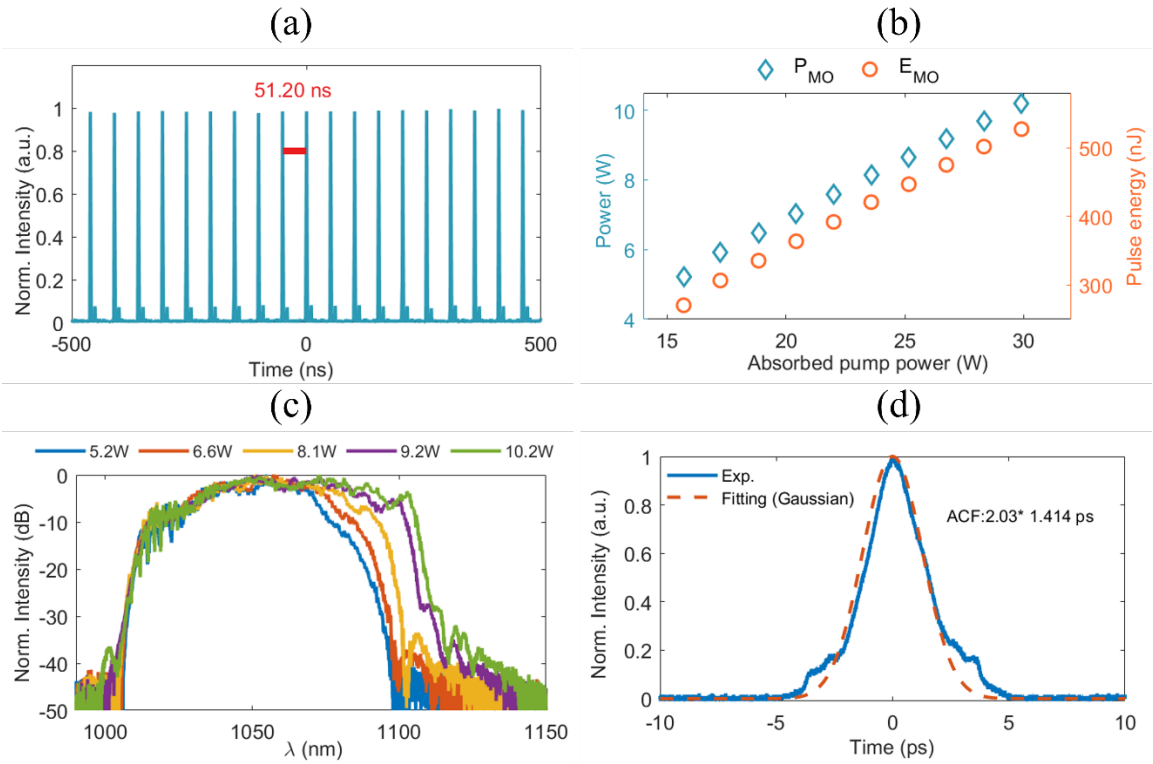

Figure 7.8 Characterization of the MO performance.(a) Oscilloscope trace showing stable mode-locked pulse train at 19.34 MHz.(b) Output power and single-pulse energy as functions of absorbed pump power.(c) 10-dB spectral bandwidth broadening with increasing pump power.(d) Measured autocorrelation of the output pulse at maximum power, yielding a 2 ps pulse width under Gaussian assumption.

7.3.2 Optimization for pulse measurement

During the experiment, some errors occurred in data collection due to errors in the device settings. Therefore, the optimization process of the device is recorded in this section.

7.3.2.1 Spectral distortion in the PBS reflection path

In the initial experimental setup, the spectroscopic branch was constructed using a standard PBS and a common HWP. During initial setup, we observed that the spectral shape at the reflection port of the PBS deviated from the original MO output, particularly when the reflected power was reduced via rotation of the HWP. As shown in Figure 7.9, the output spectrum of the MO is shown in (a), while (b)-(g) present the reflected spectra at different power levels from 6.84 W down to 0.40 W. As the reflected power decreased, the deviation from the original MO spectrum became increasingly pronounced, with the spectral center shifting towards shorter wavelengths. This indicates that the beam-splitting optics,the PBS and HWP, exhibit wavelength-dependent extinction behavior, suppressing the longer-wavelength components more effectively than the

shorter ones. Such spectral distortion poses a challenge when evaluating pulse compression performance using different methods (e.g., NANF and grating pair), because it prevents consistent comparison based on the same input spectrum. In our case, since the compressed pulse spectrum is highly sensitive to the spectral shape, these inhomogeneities must be minimized to ensure meaningful comparison.

To address the spectral distortion observed in the reflected branch of the polarization beamsplitter (PBS) during earlier measurements as shown in Figure 7.9, we replaced the conventional HWP with an achromatic HWP, and the narrowband PBS with a broadband PBS. To ensure overall spectral fidelity throughout the compression setup, all reflective optics, including steering mirrors, were selected as broadband dielectric mirrors. We then repeated the power-tuning process by rotating the HWP from 0° to 45°, corresponding to a gradual decrease in reflected power. The corresponding reflected spectra are shown in Figure 7.10. It is evident that with the upgraded optics, the normalized spectral shape remains highly consistent across different HWP angles. Only at the minimum reflection setting (45°) does the spectrum exhibit noticeable distortion, primarily due to the extremely high extinction ratio which results in a strong attenuation of longer-wavelength components. This behavior contrasts significantly with the previous configuration, where even moderate reductions in reflection power led to asymmetric spectral deformation.

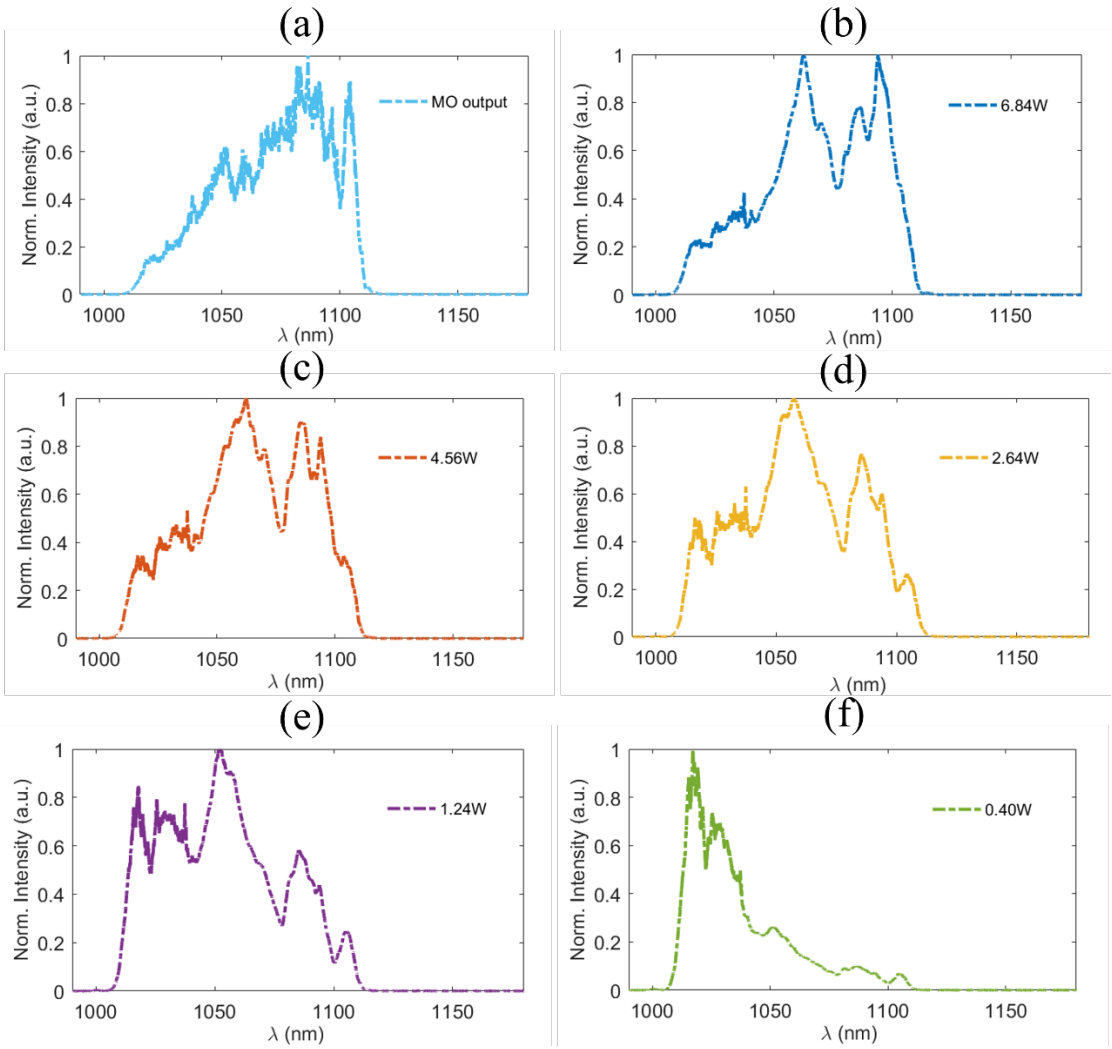

Figure 7.9 Normalized spectra measured at the reflection port of the PBS under different reflected power levels. (a) Original output spectrum of the MO. (b-g) Reflected spectra corresponding to decreasing reflected powers: 6.84 W, 4.56 W, 2.64 W, 1.24 W, and 0.40 W, respectively. As the reflected power decreases, the spectrum exhibits increasing distortion relative to the original MO spectrum, with a progressive shift of the spectral center towards shorter wavelengths and suppression of long-wavelength components. This effect arises from the wavelength-dependent extinction of the beam-splitting optics and highlights the need for careful polarization control to maintain spectral fidelity when comparing the performance of different pulse compression techniques.

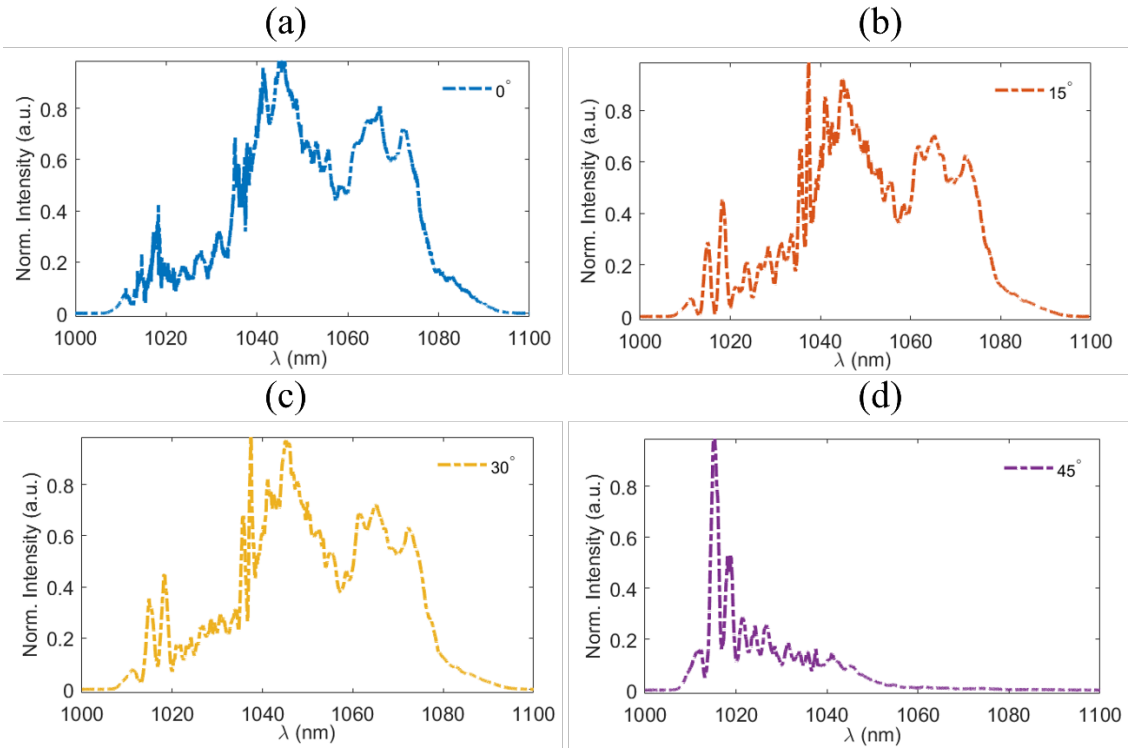

Figure 7.10 Normalized reflection spectra at different HWP angles (0°, 15°, 30°, and 45°) after replacing the conventional HWP and PBS with an achromatic HWP and a broadband PBS. The reflected power is adjusted from maximum to minimum by rotating the HWP. The recorded spectra exhibit excellent spectral fidelity across most settings, with only the 45° case (corresponding to the minimum reflected power) showing noticeable spectral distortion due to the extremely high extinction ratio. This result demonstrates that the upgraded polarization optics significantly reduce wavelength-dependent reflection bias, enabling fair spectral comparison between subsequent compression branches. However, the extinction at minimal reflection power still limits the spectral integrity, suggesting that practical measurement should be performed at a slightly lower-than-maximum reflection power.

This improvement confirms that the wavelength-dependent transmission imbalance in the earlier setup originated from the limited bandwidths of the standard HWP and PBS. By employing achromatic and broadband components, we achieve high-fidelity power tuning with minimal spectral bias. In practice, this optimization is critical when comparing different compression branches, such as the NANF and grating pair lines, ensuring that both branches receive comparable spectral content. However, the slight spectral clipping at the lowest power setting suggests that in actual measurements, the reflected power should be tuned to slightly below its maximum to ensure both spectral integrity and accurate compression comparison.

7.3.2.2 Mitigation of nonlinear distortion in spectral acquisition

To ensure accurate spectral characterization at the NANF output, we systematically optimized the length of the MMF used for coupling light into the spectrometer. After full compression, the pulse duration was below 100 fs, resulting in relatively high peak power even after attenuation. In this regime, excessive MMF length may introduce nonlinear effects such as SPM or Raman scattering, which distort the collected spectrum.

Initially, a 5 m MMF was used for spectral acquisition. As shown in Figure 7.11 (a), under low pulse energy (narrow spectrum), the collected output spectrum from the NANF closely matched the input spectrum. However, as the pulse energy increased and dispersion was more effectively compensated, spectral broadening became significant. Under these conditions, the 5 m MMF led to noticeable distortions, including the emergence of a Raman shoulder near the long-wavelength edge, as illustrated in Figure 7.11 (b). To minimize these nonlinear distortions, the MMF was shortened to 1 m. As shown in Figure 7.11 (c), the spectrum collected with this configuration exhibited much better agreement with the original input spectrum, even at high peak powers. Consequently, all subsequent spectral measurements at the NANF output were performed using a 1 m MMF.

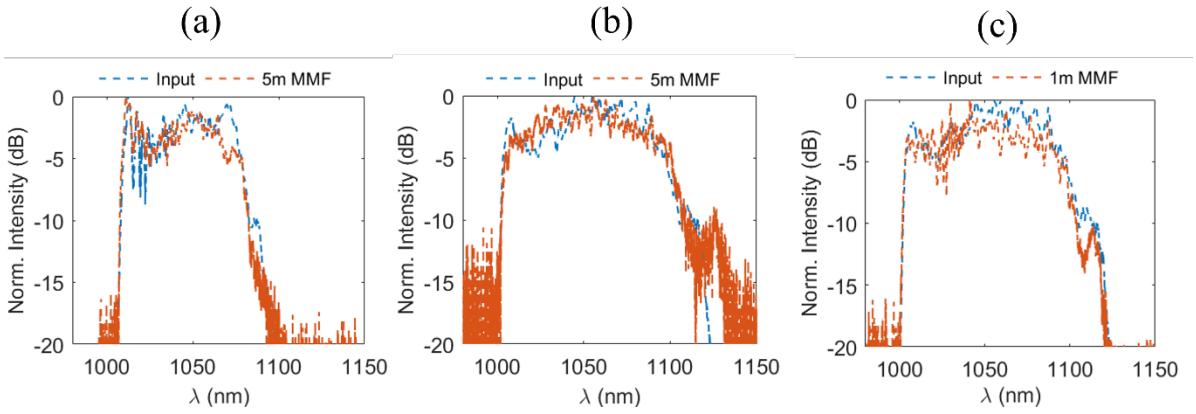

Figure 7.11 Comparison of the collected spectra at the output of the NANF using different lengths of MMF. The input spectrum (blue dashed line) is shown for reference in each panel.(a) Spectral collection using a 5 m MMF at low pulse energy, where minimal spectral broadening is observed.(b) Collection with the same 5 m MMF at higher pulse energy after near-full compression, revealing additional spectral features including a prominent Raman shoulder.(c) Spectral collection using a shortened 1 m MMF at high pulse energy, which effectively preserves the original spectral shape. All spectra are normalized in power for comparison.

7.4 Compression performance and analysis

Based on the estimated group velocity dispersion of −1.38 fs^2/mm at the central wavelength of the laser, a fibre length of 12 m was selected for pulse compression using the NANF. Power measurements were performed at both the input and output ends of the fibre to evaluate the overall transmission efficiency. The output beam exhibited a near-circular Gaussian profile in the far field, which is shown in Figure 7.14, indicating that the fundamental mode of the NANF was successfully excited.

It is worth noting that the spectral bandwidth of the pulse increased with the output power of the mode-locked oscillator (MO). To characterize the transmission behavior of the NANF under different input conditions, we measured the pulse energies at both ends of the fibre across a range of incident spectral bandwidths. Figure 7.12 (a) shows the input and output pulse energies as a function of spectral bandwidth, where the input energy is denoted by diamond markers and the output by circles. At the highest input energy of 492 nJ, an output energy of 424 nJ was achieved, corresponding to an overall transmission efficiency of 86.2%. Figure 7.12 (b) presents the transmission efficiency as a function of spectral bandwidth. As the bandwidth increased from 61 nm to 91 nm, the transmission efficiency decreased slightly from 90.4% to 86.2%. This minor decline is primarily attributed to axial chromatic aberration introduced by the coupling lens. This limitation can potentially be mitigated by replacing the refractive lens with a reflective concave mirror, which eliminates wavelength-dependent focal shifts and improves broadband coupling efficiency.

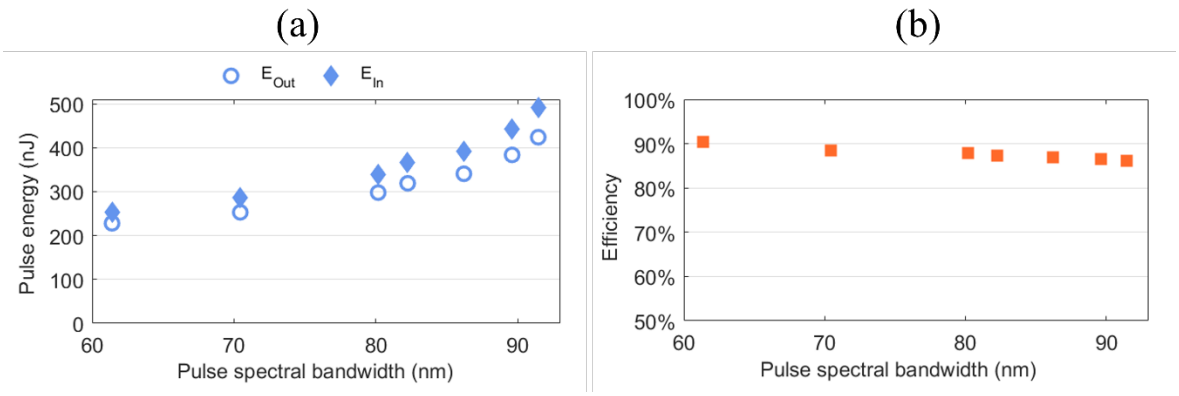

Figure 7.12 Characterization of the NANF transmission performance under different input pulse conditions.(a) Measured input and output pulse energies as a function of the input spectral bandwidth. Diamond markers indicate the input pulse energy before the NANF, and circle markers indicate the corresponding output energy after the fibre.(b) Overall transmission efficiency of the NANF as a function of the pulse spectral

bandwidth. The slight decrease in efficiency with broader spectra is attributed to chromatic aberration from the coupling lens.

At the maximum input pulse energy of 492 nJ, the output pulse from the 12 m NANF was measured to have a duration of 181.6 fs. To determine the optimum fibre length for pulse compression, we performed a cut-back measurement by progressively shortening the fibre and recording the resulting pulse durations. As shown in Figure 7.13 (a), the pulse duration decreased monotonically as the fibre was shortened from 12 m to 10.8 m, reaching a minimum of 55.9 fs. Further reduction in fibre length resulted in pulse broadening due to over-compression. For comparison, the grating-based compressor produced a minimum pulse duration of 52.9 fs, as indicated by the green line inFigure 7.13 (a). Given the broad spectral bandwidth of the pulses, the TL pulse width was calculated to be 33.6 fs. The dependence of the compressed pulse duration on GVD can be described by the following expression[213]:

$$\tau_{out} = \tau_{in}\sqrt{1+\left(\frac{4ln(2)\times GVD\times L}{{\tau_{in}}^2}\right)^2} \tag{7-3}$$

where τ_{in} is the input pulse duration (assuming a Gaussian pulse), τ_{out} is the output duration, GVD is the group velocity dispersion, and L is the propagation length. Using this equation, the evolution of the pulse duration with fibre length was calculated assuming a TL input (τ_{in}=33.6 fs) and a GVD of −1.38 fs^2/mm. The resulting theoretical curve is shown as the orange dashed line in Figure 7.13 (a). Fitting the experimental data yields the blue dashed curve, which exhibits a good match with the theoretical prediction. The fit suggests that the shortest achievable pulse duration from the NANF would be approximately 48.9 fs at a fibre length of 10.6 m. The discrepancy between the theoretical and experimental curves may be attributed to residual higher-order dispersion present in the oscillator output. Figure 7.13 (b) presents the input and output spectra at the optimal compression condition (10.8 m fibre, 424 nJ output energy). The similarity in spectral shape indicates the absence of strong nonlinear effects during propagation, even at this high energy level. Figure 7.13 (c) shows the autocorrelation traces of compressed pulses from the NANF and grating-pair compressors, along with the TL trace. The compressed pulse durations from both methods closely approach the transform limit, validating the effectiveness of both compression schemes. To further confirm the spatial quality of the output pulse, the far-field beam profile was recorded at the fibre output under optimal compression conditions. As shown in Figure 7.14, some noise patterns in the beam image are likely caused by interference from the thin-film filter mounted in front of the camera sensor. To suppress the influence of such noise, horizontal and vertical cross-sections of the beam profile were extracted through the beam center and fitted with Gaussian functions. The resulting X-Y profiles exhibit a well-defined circular

Gaussian distribution, confirming effective excitation of the fundamental mode and the absence of spatial distortion throughout the pulse compression process.

In addition to temporal and spatial characterization, the dispersion properties of the NANF impose further constraints on its compression capability. Based on the measured GVD characteristics, the corresponding TOD curve was calculated and is shown in Figure 7.15. Within the operational spectral range near 1 μm, the NANF exhibits negative GVD and positive TOD. This dispersion profile implies that the fibre cannot compensate the positive TOD originating from the oscillator's solid-core fibre components. On the contrary, it introduces additional TOD, which becomes a limiting factor when attempting sub-50 fs pulse compression. Moreover, the dispersion compensation provided by the NANF is inherently fixed for a given fibre length, unlike grating- or prism-based compressors that offer continuous tunability. This restricts the flexibility of the NANF when dealing with input pulses of varying bandwidths or chirp. Nevertheless, this limitation can be addressed by cascading multiple fibre-based components with discrete, pre-defined dispersion values, allowing coarse tuning of the overall dispersion compensation.

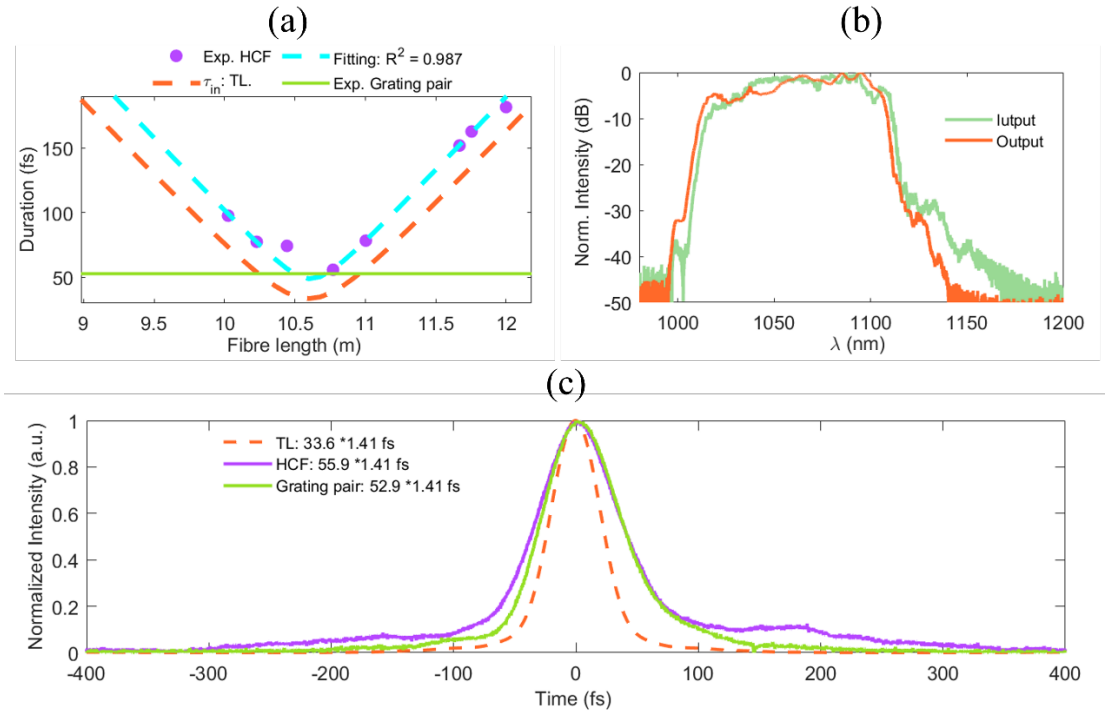

Figure 7.13 Pulse compression performance using NANF and a grating-based compressor.(a) Measured compressed pulse durations as a function of NANF length (purple dots), fitted using the GVD model (blue dashed line), and compared with the theoretical curve based on TL input pulses (orange dashed line). The shortest experimental duration from the grating-based compressor is also shown (green line).(b) Normalized spectra before and after NANF compression at the optimum condition

(10.8 m fibre length, 424 nJ output).(c) Autocorrelation traces of compressed pulses from the NANF and grating-pair compressors, along with the TL trace.

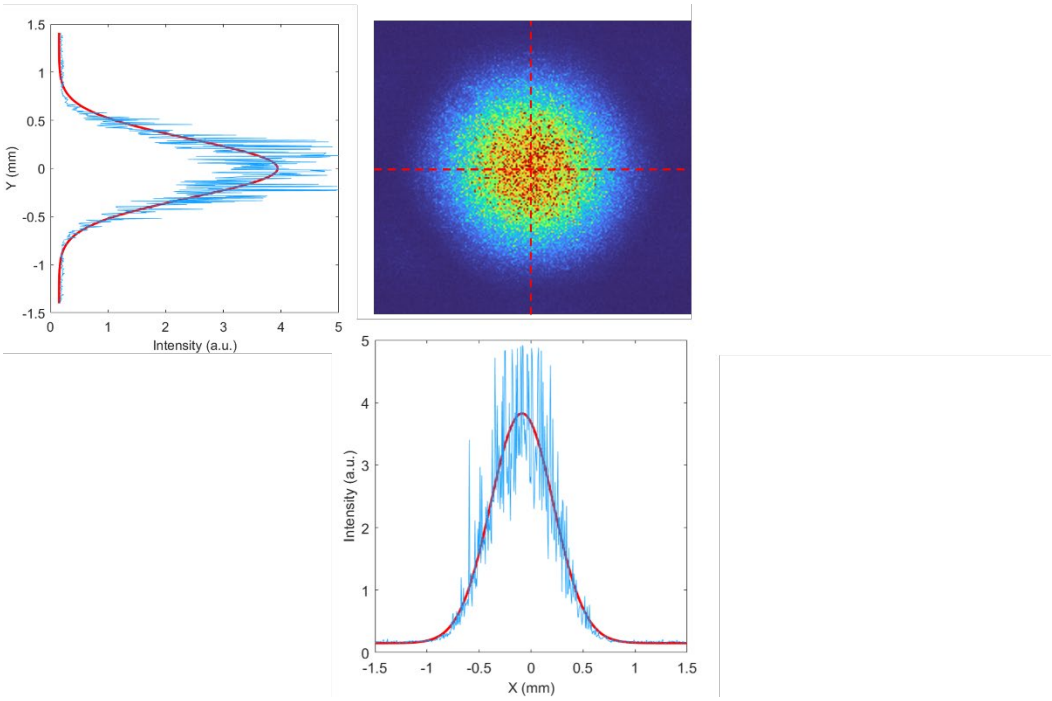

Figure 7.14 Far-field beam profile of the NANF output, exhibiting a near-Gaussian mode shape. The noise pattern in the beam image is likely caused by interference from the thin-film filter mounted in front of the camera sensor. To mitigate the influence of such noise, horizontal and vertical cross-sections through the beam center were extracted and fitted with Gaussian functions (red line), confirming the symmetric Gaussian profile and effective excitation of the fundamental mode.

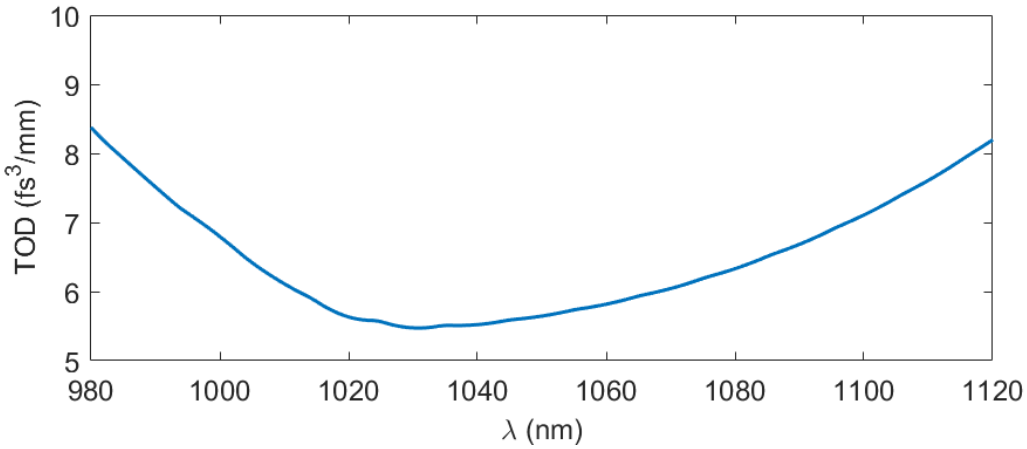

Figure 7.15 Calculated TOD curve of the NANF based on its GVD characteristics (see Figure 7.6). In the 1 μm spectral region, the NANF exhibits positive TOD while providing negative GVD.

Despite these limitations, the NANF remains a promising platform for ultrafast pulse delivery and compression, owing to its low loss, broad transparency window, and customizable dispersion. Recent studies have demonstrated low-loss NANF designs with transmission windows exceeding 68 THz and attenuation below 0.1 dB/km, as well as coupling efficiencies up to 97% with single-frequency lasers[212]. Furthermore, several works have reported successful fusion splicing between NANF and standard silica fibres, paving the way toward all-fibre architectures with minimized insertion loss and back-reflection[214]. With continued progress in splicing techniques and dispersion engineering, NANF-based pulse compressors hold strong potential for future integration into compact, alignment-free ultrafast systems, including on-chip mode-locked laser platforms[215].

7.5 Conclusion

In this chapter, we have demonstrated a high-efficiency femtosecond pulse compression scheme based on NANF, achieving sub-60 fs pulse durations with energy up to 424 nJ and a total transmission efficiency exceeding 86%. The NANF exhibits negative GVD around 1 μm and supports fundamental mode propagation, as confirmed by far-field beam profile measurements. Through systematic optimization, including beam polarization control and suppression of diagnostic-induced nonlinear distortions, we ensured reliable comparison with conventional grating-pair compression. A cut-back measurement revealed the optimal NANF length to be ~10.8 m, yielding compressed pulses as short as 55.9 fs. Experimental results aligned well with dispersion-based modeling, indicating the presence of residual TOD that currently limits compression performance. While grating compressors achieved slightly shorter durations (52.9 fs), the NANF offered superior beam quality, higher energy throughput, and a compact configuration. Limitations such as fixed dispersion compensation and positive TOD can be mitigated by cascading multiple fibre segments or through dispersion engineering. Recent advances in broadband NANF designs, fusion splicing with solid-core fibres, and low-loss coupling indicate strong potential for full fibre integration. These developments pave the way for compact, robust, and potentially on-chip femtosecond laser systems leveraging NANF-based compression.

Chapter 8 Pulse dynamics in the Mamyshev oscillator

8.1 Introduction

Understanding the transient dynamics during the startup of MOs is important for improving their controllability, stability, and reproducibility. Previous theoretical work has suggested that the initial gain distribution, particularly the timing between population inversion and seed injection, may influence the transition from noise to a coherent mode-locked state. Concepts such as coherence memory and coherence amnesia have been proposed to describe divergent evolutionary pathways under different starting conditions[216]. The idea for this study was initially motivated by experimental observations in Chapter 6, where direct single-pulse seeding of a 1 MHz MO proved nontrivial. Although detailed investigation of seed-cavity synchronization is beyond the scope of this chapter, the challenge highlighted the importance of startup conditions, including gain and seed timing, in determining the success and pathway of mode-locking. This led us to explore, in a more controlled setting, how different gain initialization scenarios affect the evolution from seed signal to a stable MO regime.

To this end, this chapter investigates how the temporal order of gain activation and seed injection influences the buildup dynamics of an MO. Two representative scenarios are considered: a steady-state start, where the amplifier gains are pre-established before allowing optical circulation, and a cold start, where seed injection coincides with the onset of gain. Rather than aiming to distinguish strict attractor types, our goal is to observe whether different initial gain conditions lead to observable differences in the evolution speed or coherence characteristics. To capture these transient dynamics, a real-time DFT-based measurement system was developed, enabling spectral and energy evolution to be tracked over thousands of roundtrips. A key focus is placed on the spectral cross-correlation coefficient (sXC), which provides a practical measure of spectral stability from shot to shot. Complementary simulations were also performed to examine the role of gain conditions under idealized assumptions, where both sXC and the first-order coherence function $g_{12}^{(1)}$ can be evaluated. These two parameters are taken from the methodology reported in Ref. [216]. While the present study does not aim to deliver definitive conclusions, it serves as a preliminary investigation into how gain-seed timing may shape mode-locking evolution. The system and methodologies developed here lay the groundwork for more targeted studies on coherence dynamics and start-up optimization in complex laser oscillators.

8.2 Experimental setup

To capture the real-time dynamics during the initiation of mode-locking in the MO, a DFT-based measurement system was constructed, as illustrated in Figure 8.1. The setup comprises three main components: the seed generation and modulation unit, the MO cavity, and a diagnostic platform for both spectral and temporal monitoring. A seed pulse with a repetition rate of approximately 40 MHz, as introduced in Section 5.3.3.5, is externally modulated before being injected into the MO cavity. The configuration of the MO system is described in Section 7.3.1, with a repetition rate of about 20MHz. An additional chopper is placed before the main amplifier to enable active control over the cavity's opening and closing. The output from the MO is split using a PBS. One arm is directed to an OSA for average spectral characterization. The other arm is fed into a fibre coupler. The tap port (1%) is connected to a 5 GHz PD, which provides a low-resolution pulse train used as both a mode-locking trigger and a temporal alignment reference. The main port of the coupler (99%) delivers the signal into a long segment of dispersive fibre, which maps the optical spectrum into a time-stretched waveform via chromatic dispersion. This waveform is then detected by a 32 GHz photodetector (83440D, Agilent) for high-speed measurement, enabling detailed observation of spectral fluctuations and transient features. Finally, all signals are recorded using a real-time oscilloscope with a 50 GHz sampling rate and a maximum acquisition window of 1.25 ms. This setup enables simultaneous observation of coarse triggering signals and fine temporal features, providing a complete picture of the build-up dynamics under different start-up conditions.

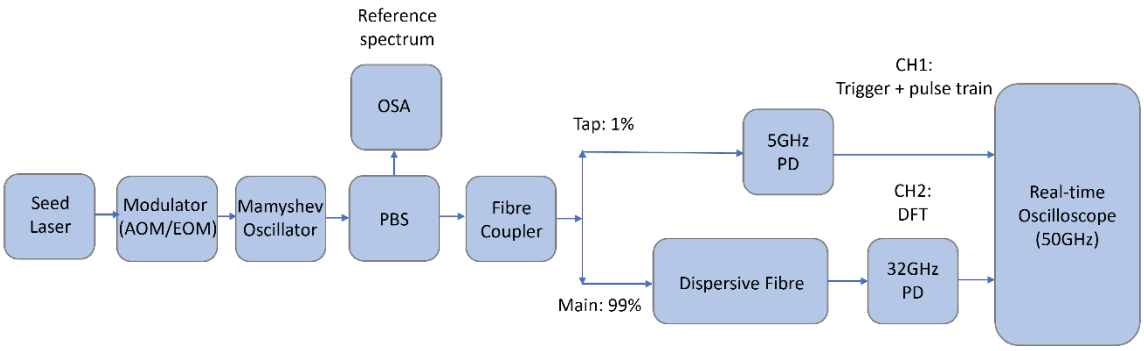

Figure 8.1 Schematic of the experimental setup for investigating the build-up dynamics of the MO using DFT. The output of the MO is split into two branches: one is directed to an OSA, optical spectrum analyzer, for average spectral characterization, while the other is processed through a dispersive fibre and detected by high-speed photodetectors to reconstruct spectral evolution in real time.

8.3 Key components in the DFT characterization system

8.3.1 Dispersive fibre for time-stretch mapping

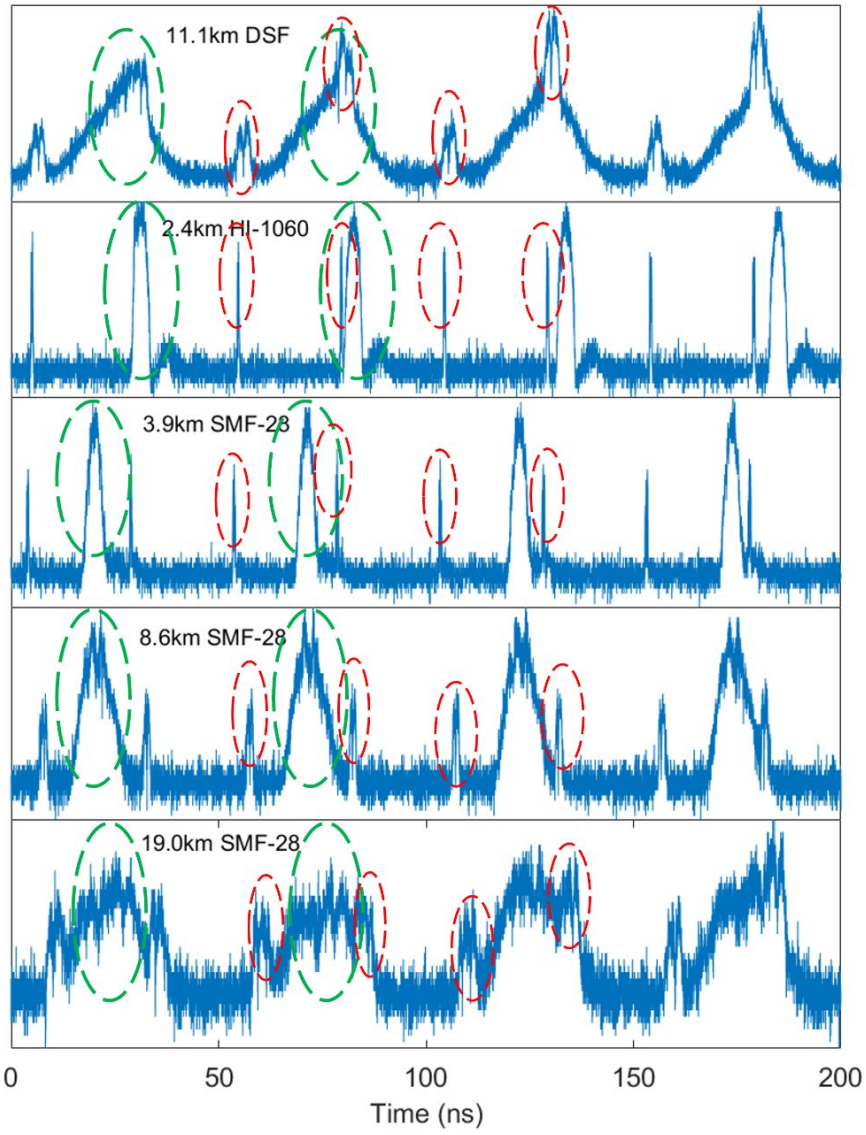

Figure 8.2 Time-domain traces of the MO output after DFT using different fibre configurations. The main MO pulse train at ~20 MHz is marked by green circles, while residual seed pulses at 40 MHz are indicated by red circles. Shorter fibres provide insufficient dispersion, whereas excessively long fibres degrade the temporal contrast. The results highlight the need for seed-pulse modulation and the trade-off between dispersion length and signal quality in DFT measurements.

In DFT-based measurement schemes, the choice of dispersive fibre is crucial for determining the temporal resolution and fidelity of spectral mapping. To evaluate its effectiveness in time-stretch transformation, we tested a range of fibre types with varying dispersion characteristics and lengths available in our laboratory. The corresponding experimental results are presented in

Figure 8.2, where the MO output is mapped into the time domain using five different fibre configurations. Each trace shows a periodic structure corresponding to the MO pulse train at a repetition rate of ~20 MHz, highlighted by the green circles. In addition, residual peaks originating from the continuously injected seed pulses at 40 MHz are clearly visible, marked by the red circles. These unwanted features can interfere with the DFT measurement and, in some cases, even alias into the main signal, thereby compromising the reliability of the temporal characterization. To address this issue, active modulation of the seed pulse using an AOM or EOM is required to suppress the background injection and improve the temporal contrast of the DFT signal. Due to their short lengths, the 2.4 km HI-1060 and 3.9 km SMF-28 fibres offer limited temporal stretching. Dispersion-shifted fibre (DSF), which provides greater dispersion per unit length at 1 μm, enables comparable stretching to that of 19.0 km SMF-28 using only 11.1 km. However, greater dispersion is not inherently advantageous: aside from transmission loss, excessive temporal stretching reduces the optical signal per unit time, thereby diminishing the temporal contrast and detection sensitivity.

Table 8.1 summarizes the tested fibre types and their associated propagation losses. After balancing spectral resolution and transmission loss, we selected a standard SMF-28 fibre with a length of 8.6 km as the optimal dispersive element. This configuration provides sufficient stretching for clear spectral unfolding while maintaining acceptable optical throughput. If available, a HI-1060 fibre with a length of approximately 10 km would potentially offer improved performance by combining low loss and higher dispersion efficiency.

Table 8.1 Insertion loss of dispersive fibres used for DFT-based spectral mapping.

Fibre type	Fibre length	Insertion loss
DSF	11.1km	20.5dB
HI-1060	2.4km	1.4dB
SMF-28	3.9km	2.0dB
SMF-28	8.6km	11.0dB
SMF-28	19.0km	22.2dB

To evaluate the wavelength resolution of the DFT system with the selected 8.6 km SMF-28 fibre, a mode-locked pulse with a pulse energy of 150 pJ was injected into the dispersive fibre. The input pulse had a center wavelength of 1041.83 nm and a 10-dB spectral width of 27.64 nm, as measured by the OSA. Figure 8.3 (a) shows the time-domain waveform captured by the real-time oscilloscope after dispersion. At a sampling rate of 50 GHz, the stretched signal occupies 384 sampling points. Based on the known spectral width and temporal span, the effective wavelength

resolution of the DFT signal is estimated to be approximately 0.72 nm per point. Figure 8.3 (b) shows the original spectrum recorded by the OSA, and Figure 8.3 (c) displays the DFT signal after remapping to the wavelength axis. The DFT-based reconstruction aligns well with the OSA spectrum, confirming the reliability of the calibrated dispersion-to-wavelength mapping.

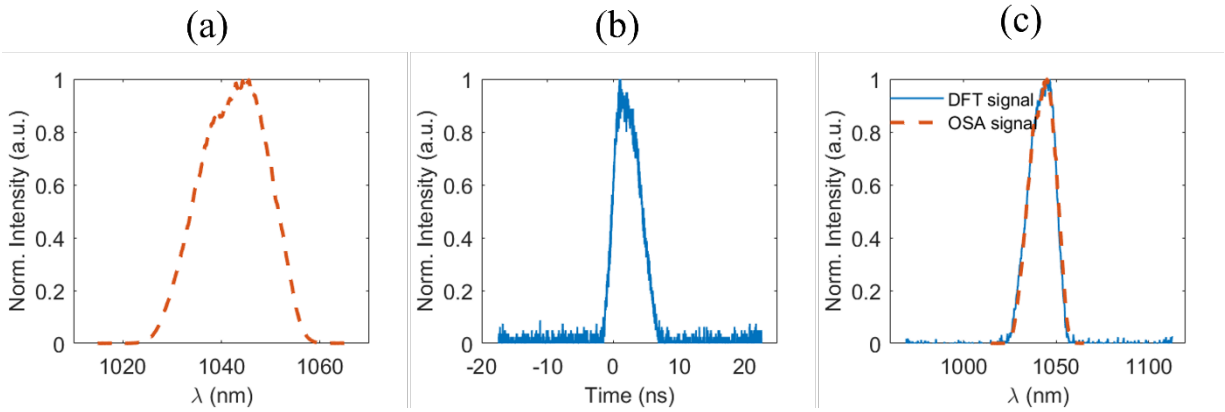

Figure 8.3 Wavelength calibration of the DFT signal using 8.6 km SMF-28. (a) Time-domain trace of a mode-locked pulse after passing through the dispersive fibre, captured by a real-time oscilloscope. (b) Optical spectrum of the same pulse measured directly using an OSA. (c) The DFT signal is remapped to the wavelength axis using the calibrated dispersion coefficient and compared with the OSA spectrum, showing good agreement.

8.3.2 Pulse injection via AOM vs. EOM

To address the interference caused by continuously injected seed pulses, external amplitude modulation was applied to temporally gate the seed source. Considering that the seed pulse has a repetition rate of 40 MHz and the maximum acquisition window of the oscilloscope is 1.25 ms, a gate width of 20 ns was implemented using a high-speed optical switch with a repetition rate of 500 Hz. This configuration ensures that, in principle, each recorded trace corresponds to the build-up dynamics initiated by a single seed pulse.

To evaluate the effectiveness of different modulators, we compared the use of an electro-optic modulator (EOM) and an AOM under the same gating parameters. Figure 8.4 (a) shows the temporal output of the MO when gated with an EOM, while Figure 8.4 (b) shows the result with an AOM. In both cases, the detection was performed using a 5 GHz photodetector to monitor the overall temporal envelope of the pulse train. Due to its lower extinction ratio, the EOM allowed residual seed pulses to leak through outside the intended gate window. These unwanted pulses can re-seed the MO cavity and obscure the true single-pulse-triggered dynamics. In contrast, the AOM provided significantly better isolation, effectively eliminating residual injection and enabling

more reliable observation of clean build-up events. As a result, the AOM was selected as the preferred external modulator for subsequent experiments.

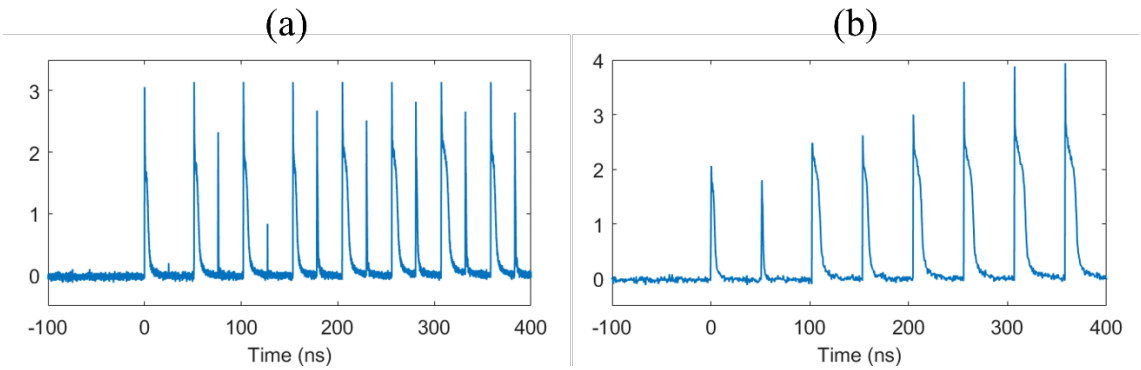

Figure 8.4 Temporal response of the MO under single-pulse seed injection using different modulators. (a) EOM: Due to limited extinction ratio, residual seed pulses are observed outside the gate window, leading to potential multi-pulse triggering. (b) AOM: The seed is well confined within the gate window, enabling cleaner observation of the build-up process.

8.4 Locking behavior under different start-up conditions

The transient behavior of a mode-locked MO depends strongly on the initial conditions under which the cavity is seeded. Recent studies have suggested that the level of population inversion at the moment of seed injection can influence the system's route toward stable mode-locking. In particular, different initial gain levels may lead to varying coherence evolution dynamics, sometimes described under the framework of coherence memory versus coherence amnesia[216]. Although our aim is not to directly classify the observed dynamics into these categories, we are motivated by the same fundamental question: How does the initial upper-state population affect the temporal and spectral pathway through which coherence is established? To address this, we investigate two representative start-up schemes: In the steady-state start, both preamplifier and main amplifier pumps are turned on well before seed injection, allowing the gain medium to reach a relatively high level of population inversion. In contrast, the cold start involves injecting the seed before activating the pump sources, resulting in a much lower initial inversion level. To facilitate quantitative comparisons between these conditions, we introduce two diagnostic metrics proposed in the literature: The spectral cross-correlation coefficient $sXC(N)$, which characterizes the similarity between adjacent power spectra across roundtrips. It is defined as:

$$sXC(N) = \frac{\max\left[\int I(\omega,N)I(\omega+\delta\omega,N+1)d\omega\right]}{\sqrt{\int I^2(\omega,N)d\omega \int I^2(\omega,N+1)d\omega}} \tag{8-1}$$

Where $I(\omega, N)$ denotes the power spectrum at roundtrip N, and the maximization is taken over frequency shift $\delta\omega$ to account for center-wavelength drift. And the first-order spectral coherence $g_{12}^{(1)}(\lambda, N)$, which evaluates the phase correlation at a fixed wavelength between field samples. It is given by:

$$g_{12}^{(1)}(\lambda, N) = \frac{|\langle E_1^*(\lambda, N) E_2(\lambda, N+m)\rangle|}{\sqrt{\langle |E_1(\lambda, N)|^2\rangle \langle |E_2(\lambda, N+m)|^2\rangle}} \tag{8-2}$$

where E_1 and E_2 represent optical field samples from different roundtrips or ensemble realizations. In our experiments, only sXC is evaluated, as it requires only power spectra and is compatible with DFT-based measurements. The spectral coherence $g_{12}^{(1)}$, which demands full phase information, will be discussed and simulated in a later section.

In the following subsections, we compare the evolution of the MO under the steady-state and cold start conditions, using these metrics to assess how different gain levels at startup affect the system's trajectory toward mode-locking.

8.4.1 Mode-locking initiation from a steady-state start

In the steady-state start configuration, the seed pulses are continuously injected, and both the preamplifier and main amplifier are fully pumped in advance. However, the optical path between the preamplifier and main amplifier is blocked by a mechanical chopper. This ensures that the gain in both stages has reached a high population inversion before pulse injection into the full cavity. The system is triggered by rotating the chopper to open the optical path, allowing the preamplified seed to enter the main amplifier, initiating the mode-locking process. The first Q-switched burst is used to define roundtrip 0.

Figure 8.5 shows the real-time evolution of the pulse train recorded by a 5 GHz photodetector. A large Q-switched spike is followed by a sequence of smaller pulses, gradually stabilizing in shape and spacing. The temporal position of the pulses shows a noticeable drift toward later times, which is attributed to a shift in the center wavelength. Since the output is measured through a dispersive fibre, any spectral shift translates directly into a temporal shift in the DFT signal. Figure 8.6 displays the corresponding spectral evolution. The initial Q-switched spike generates a broad and irregular spectrum. As the cavity dynamics evolve, the spectrum becomes narrower and shifts toward longer wavelengths. After roughly 1000 roundtrips, the spectral shape appears more regular, although minor variations persist beyond 2000 roundtrips. A small but visible change occurs near 2800 roundtrips, indicating that the system continues to adjust even after the main relaxation phase.

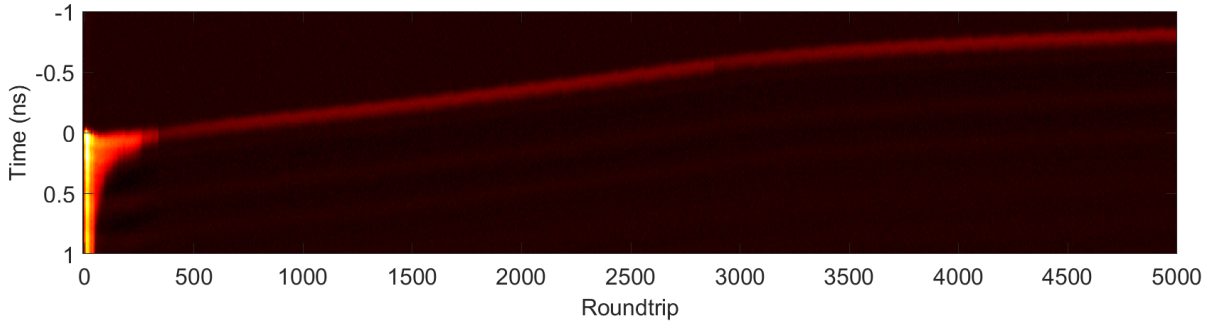

Figure 8.5 Real-time temporal evolution of the MO output under steady-state start conditions, recorded with a 5 GHz photodetector. An initial Q-switched spike is followed by pulse narrowing and a visible temporal drift caused by spectral red-shift.

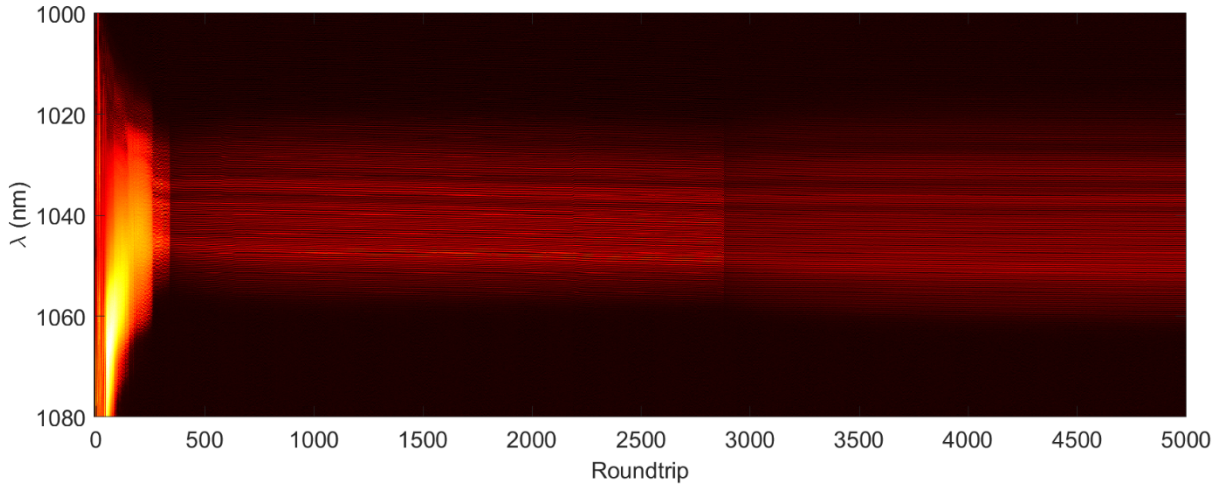

Figure 8.6 Spectral evolution retrieved via DFT, showing strong broadening during the initial build-up and gradual stabilization of the spectral shape.

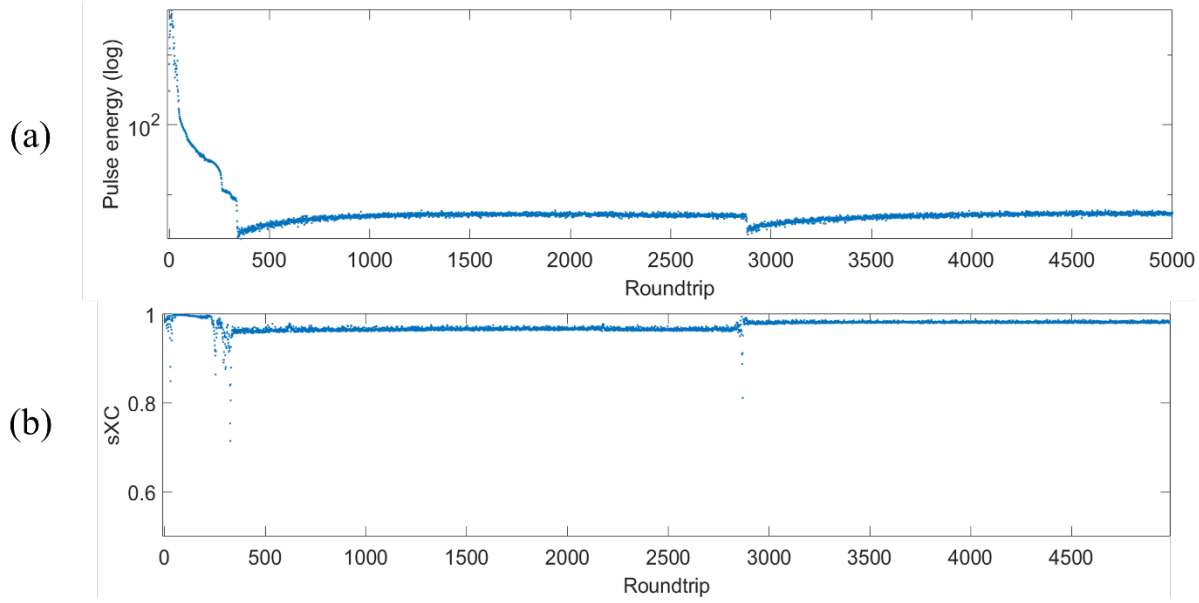

Figure 8.7 Quantitative parameters of the steady-state start process: (a) Pulse energy (log scale) showing relaxation and a subtle secondary transition; (b) sXC parameter indicating steady convergence but with residual fluctuations.

To quantify the stabilization process, Figure 8.7 shows the evolution of pulse energy and the spectral cross-correlation coefficient (sXC). The pulse energy in Figure 8.7 (a) drops rapidly after the Q-switched burst and gradually approaches a steady level. A secondary adjustment is again visible around roundtrip 2800. Figure 8.7 (b) plots sXC, which reflects the spectral similarity between adjacent roundtrips. It increases steadily and reaches above 0.95 after ~1000 roundtrips, but does not fully converge to 1. This indicates that the system achieves high spectral stability, though small fluctuations or jitter remain.

8.4.2 Mode-locking initiation from a cold start

In the cold-start configuration, the seed pulses and preamplifier pump are kept on continuously, and the optical path between stages remains open. However, the main amplifier pump is initially turned off. The mode-locking process is initiated by switching on the main amplifier pump, allowing the seed and preamplified signal to enter a cavity with zero initial gain in the second stage. This method is adopted due to hardware limitations that prevent precise synchronization of both pump channels.

Figure 8.8 shows the evolution of the MO output captured by the 5 GHz photodetector. The initial stage is dominated by a series of noisy and irregular pulses, lacking clear periodicity. These pulses gradually organize into a pulse train, and the timing stabilizes after several hundred roundtrips. Compared to the steady-state case, the cold-start path exhibits greater pulse shape variability and less-defined timing in the early stages. The corresponding spectral evolution obtained from DFT is presented in Figure 8.9. The spectrum fluctuates dramatically in both bandwidth and central wavelength over the first ~1000 roundtrips. Several stages of spectral collapse and re-expansion are visible, with abrupt changes in spectral shape. Despite the chaotic onset, the spectrum eventually stabilizes after approximately 1500 roundtrips, reaching a steady structure with minimal variation thereafter.

To evaluate the convergence quantitatively, Figure 8.10 shows the pulse energy and spectral cross-correlation coefficient sXC. In Figure 8.10 (a), the pulse energy increases in bursts, followed by a more gradual stabilization. In Figure 8.10 (b), the sXC value oscillates strongly throughout the first 1000-1200 roundtrips, with multiple sharp drops and recoveries. These features indicate significant shot-to-shot variations in spectral content. After roundtrip ~1500, sXC steadily increases and eventually exceeds 0.98, indicating convergence to a stable and reproducible spectral profile.

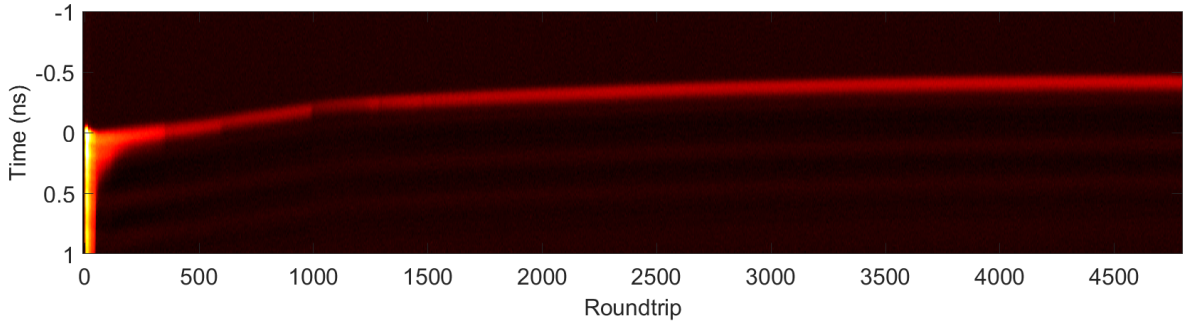

Figure 8.8 Temporal evolution of the MO output under cold-start conditions, recorded with a 5 GHz photodetector. The early-stage pulses are irregular and noisy, gradually stabilizing into a periodic train.

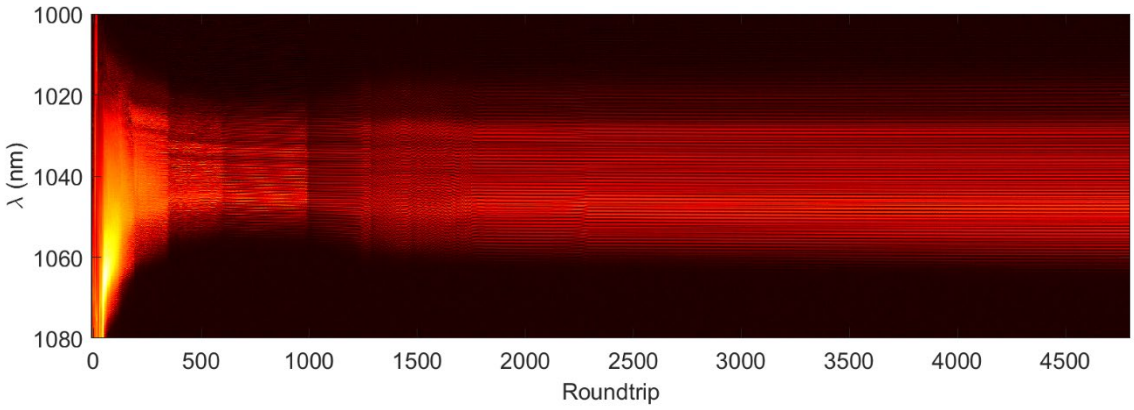

Figure 8.9 Spectral evolution captured via DFT during the cold-start build-up. Strong spectral fluctuations, collapses, and red-shifts are observed before the spectrum stabilizes around roundtrip 1500.

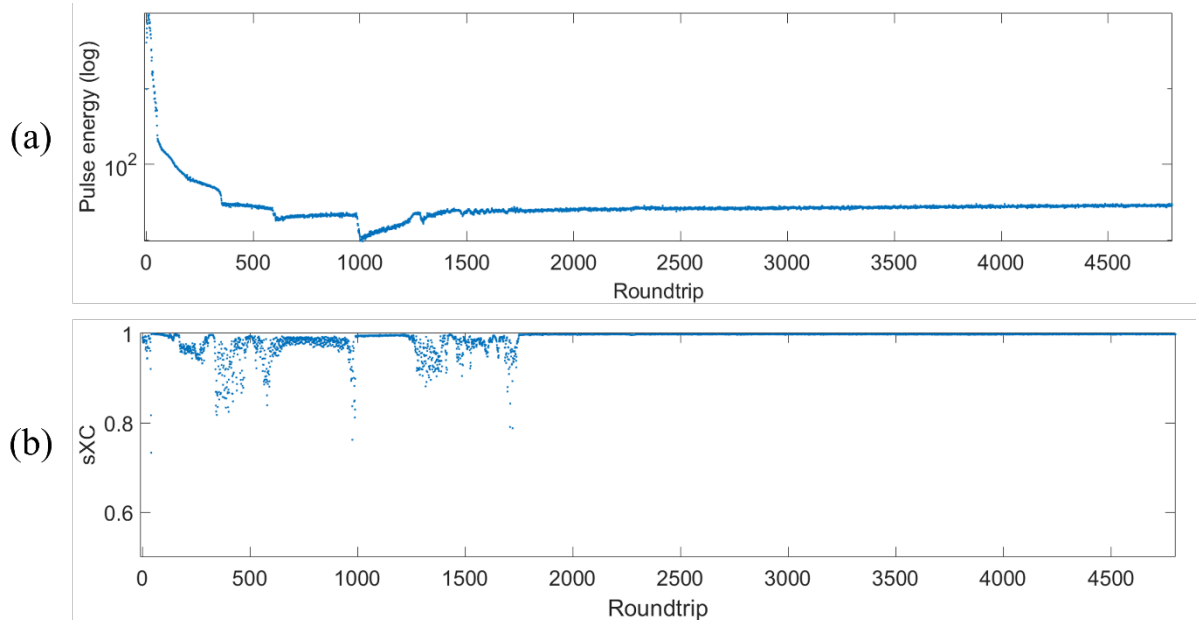

Figure 8.10 Quantitative metrics of the cold-start process: (a) Pulse energy evolution showing bursts followed by gradual convergence; (b) Spectral cross-correlation sXC showing strong early oscillations and eventual stabilization above 0.98 after ~1500 roundtrips.

Compared to the steady-state start, the cold-start configuration exhibits stronger early-stage spectral oscillations, but it converges to a spectrally stable state more quickly. This observation suggests that a lower initial population inversion may reduce nonlinear mode competition and facilitate a more deterministic evolution path. Surprisingly, despite its more chaotic onset, the cold-start case reaches full spectral stability faster than the smoother, steady-state start described in Section 8.4.1.

8.4.3 Numerical simulation of start-up dynamics

To further understand the role of gain conditions in the mode-locking evolution of the MO, numerical simulations were performed under two representative scenarios: steady-state start and cold start. These simulations were based on a GNLSE model incorporating gain dynamics. The detailed simulation framework is described in Section 4.3.2.

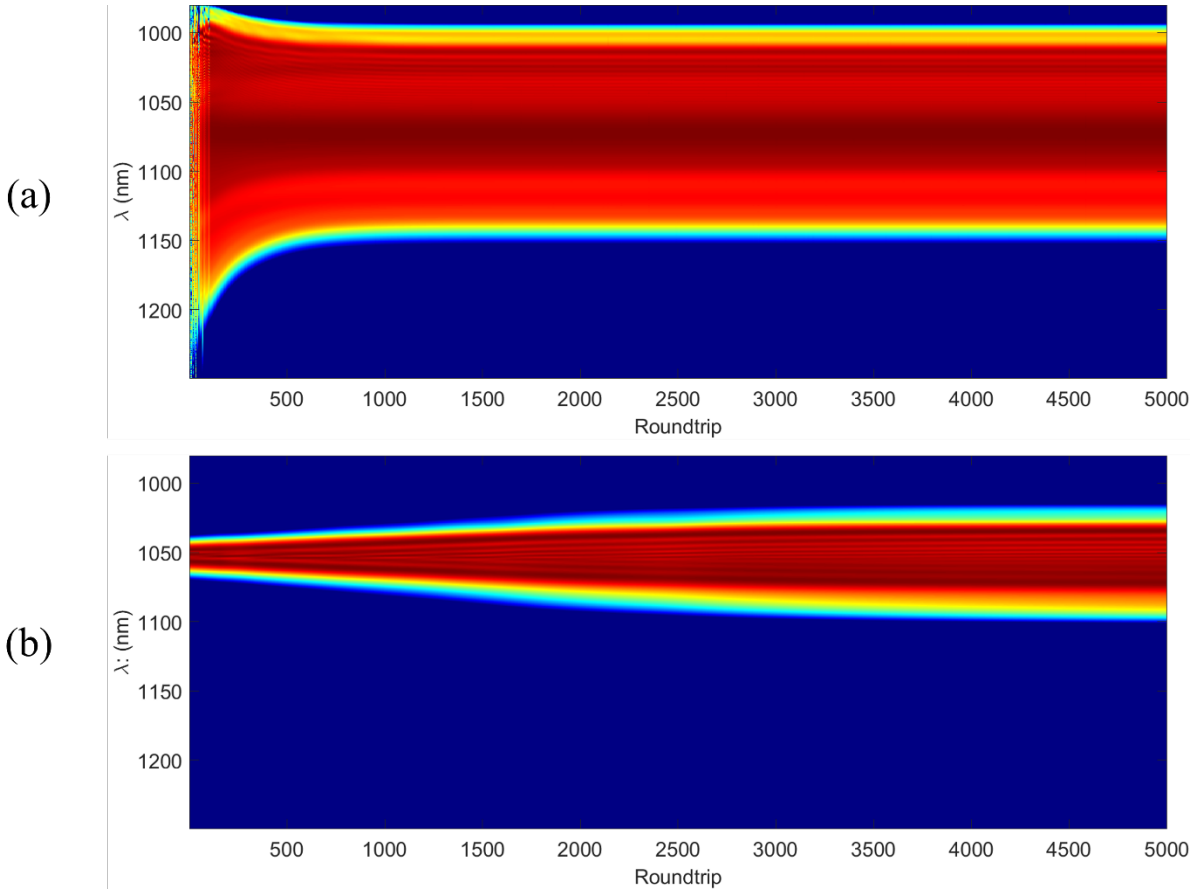

Figure 8.11 Simulated spectral evolution of the MO under two start-up conditions. (a) steady-state start: both the preamplifier and main amplifier are fully pumped (5 W), with no seed injection prior to startup. (b) Cold start: both amplifiers are initially unpumped and the seed pulse is injected simultaneously with the activation of the pumps. Each plot shows the evolution of output spectra over 5000 roundtrips. The cold-start case exhibits faster spectral regularization, while the steady-state start leads to broader final spectra but with more fluctuations during the buildup phase.

In the steady-state start, both the preamplifier and the main amplifier are fully pumped at 5 W from the beginning, resulting in high population inversion throughout the system. However, no seed pulse is injected prior to startup, and thus no circulating optical field exists in the cavity. In this sense, the system is optically cold despite being energetically charged. In contrast, the cold-start simulation begins with both amplifiers unpumped, corresponding to zero population inversion. The seed pulse is injected simultaneously with the activation of both pump sources, representing a cavity that is cold in both optical and energetic senses.

Figure 8.11 shows the simulated spectral evolution over 5000 roundtrips. Both scenarios exhibit progressive spectral broadening and eventual stabilization. Notably, the cold-start case reaches a spectrally regular state more rapidly, while the steady-state start displays slower buildup and more pronounced early-time fluctuations. Interestingly, the final output spectrum of the cold-start case appears narrower than that of the steady-state start, which is somewhat counterintuitive. This observation suggests that the system may not have reached full stability within the simulated time window, and requires further evidence to substantiate this interpretation.

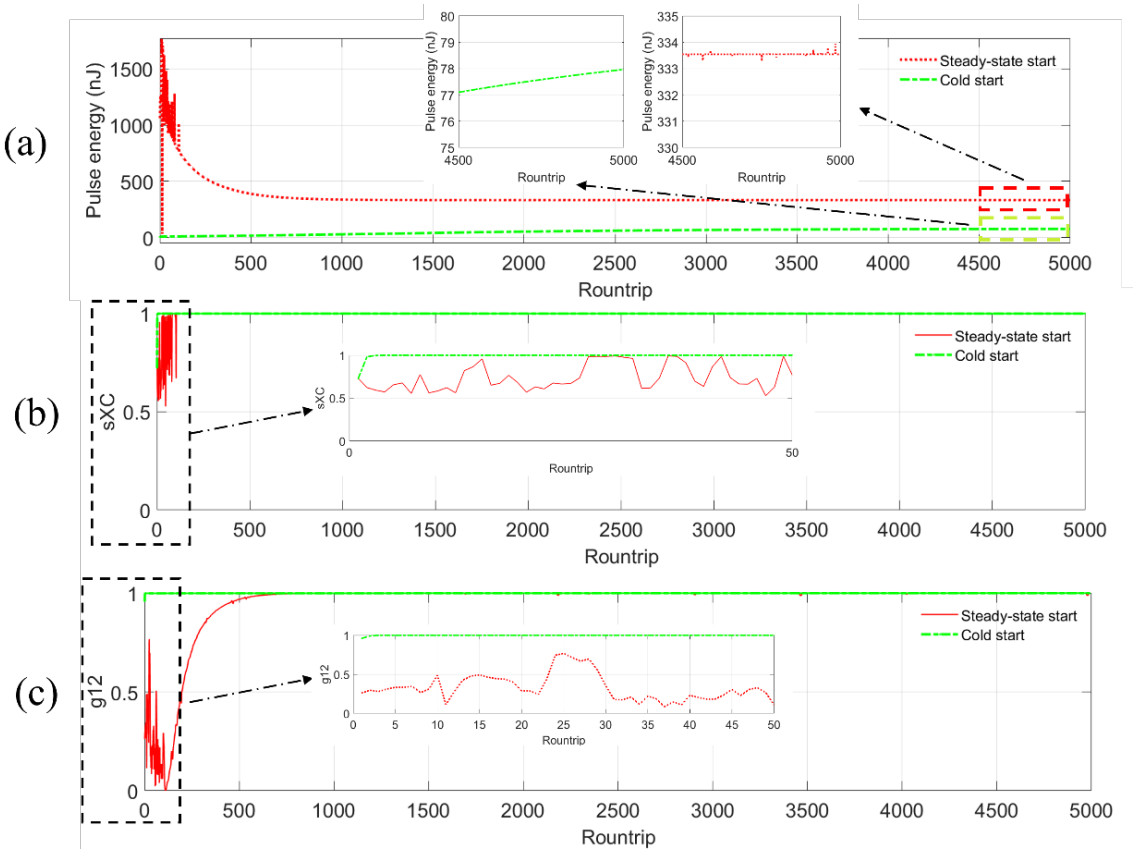

Figure 8.12 Quantitative comparison of output dynamics under steady-state and cold-start conditions. (a) Simulated pulse energy evolution over 5000 roundtrips. Inset: zoom-in of the last 500 roundtrips (4500-5000), showing that energy in the steady-state case has saturated while the cold-start case continues to grow. (b) Evolution of spectral

cross-correlation coefficient sXC within the first 50 roundtrips. (c) Evolution of first-order coherence function $g_{12}^{(1)}$ over the same time window. The cold-start pathway rapidly reaches a coherent state, whereas the steady-state start exhibits a slower and more fluctuation-prone coherence buildup.

Figure 8.12 provides a quantitative comparison of the two cases. Figure 8.12 (a) shows the evolution of pulse energy. The steady-state start reaches saturation earlier, whereas the cold-start case does not reach equilibrium within the simulated time window, with the pulse continuing to accumulate energy. As highlighted in the zoomed-in inset, the pulse energy of the steady-state start stabilizes between 4500 and 5000 roundtrips, while that of the cold-start remains lower and increases slowly but persistently. This behavior also explains why the spectral width of the cold-start in Figure 8.11 is narrower than that of the steady-state start, indicating ongoing energy build-up and the absence of full stability. Although this convergence is not observed within the present simulation window, the cold-start is expected to eventually reach the same stable state as the steady-state start. Figure 8.12 (b) and (c) show the evolution of spectral coherence during the first 50 roundtrips, in terms of the spectral cross-correlation coefficient sXC and the first-order coherence function $g_{12}^{(1)}$. The cold-start case reaches high coherence values significantly faster than the steady-state case, indicating that, under the current simulation conditions, the cold-start pathway enables a more direct and rapid transition from seed injection to a coherent MO signal.

Regarding the steady-state start, the simulation conditions differ slightly from those in the experiment. Experimentally, the seed is continuously injected and the preamplifier already produces amplified pulses, while the optical path to the main amplifier is blocked using a mechanical chopper. This means that although the main amplifier is optically cold, the preamplifier is not. In contrast, the simulation assumes that no seed pulse is present anywhere in the cavity prior to startup. Despite this discrepancy, the simulated results, such as gradual energy buildup and delayed spectral stabilization, are qualitatively consistent with the experimental traces (Section 8.4.1), where similar trends are observed. In the cold-start case, the simulated evolution appears smoother and more monotonic than the experimental results. Experimentally, this pathway often displays more segmented or stepwise behavior, with abrupt changes in coherence or spectral width. Such discrepancies likely arise from differences in initial conditions. In the simulation, both amplifiers start from complete inversion absence, while in the experiment, the preamplifier is already pumped and the seed is continuously injected. As a result, the initial seed may be partially amplified before reaching the main amplifier. Furthermore, it remains unclear whether the MO is triggered by the very first injected seed pulse or by a subsequent one, meaning that the effective gain distribution could have already evolved beyond the modeled initial condition. These practical factors may account for the richer dynamics

observed experimentally. Future simulations incorporating partially pre-amplified seeds and intermediate gain levels may help bridge this gap. Despite the differences in transient behavior, both simulations ultimately converge toward stable, mode-locked states. The cold-start configuration continues to exhibit slow energy growth at the end of the simulation window, suggesting that it is approaching, but has not fully reached, its spectral steady state. Nevertheless, the spectral coherence has already been established. These findings agree qualitatively with experimental results, where both start-up methods can yield stable operation, albeit through different transient pathways.

In summary, the numerical results highlight the distinct dynamics induced by different gain initialization conditions. Under the same pump power, the cold-start scenario, despite its energetically unfavorable start, leads to faster coherence formation and a more monotonic buildup process. In contrast, the steady-state start features stronger early fluctuations and a slower convergence. These results reinforce the view that the initial gain landscape not only influences the build-up speed, but also determines the characteristic route by which mode-locking is achieved.

8.5 Conclusion

In this chapter, we explored the build-up dynamics of MOs under different gain initialization conditions using a combination of real-time DFT diagnostics and numerical simulations. Two representative scenarios were studied: a steady-state start, where both amplifier stages are pre-pumped before allowing optical circulation, and a cold start, where gain and seed injection occur simultaneously from an initially unexcited state. A real-time DFT-based measurement system was constructed to capture single-shot spectral and temporal dynamics over thousands of cavity roundtrips. Experimental results revealed distinct spectral and energy evolution behaviors under the two startup scenarios. In particular, the cold-start case often exhibited a faster rise in spectral coherence and pulse energy, while the steady-state start showed a more gradual transition with prolonged early-time fluctuations. These differences were further quantified using the spectral cross-correlation coefficient (sXC), extracted from single-shot DFT traces. The cold-start pathway consistently reached higher sXC values earlier, suggesting a more rapid transition toward a coherent mode-locked state. Complementary simulations incorporating gain dynamics were performed to interpret these observations. The results reproduced the key trends observed experimentally: faster coherence buildup in the cold-start case, and more gradual energy evolution in the steady-state case. The simulation also enabled access to the first-order spectral coherence function $g_{12}^{(1)}$, which further supported the view that cold-start conditions can accelerate the establishment of spectral and phase stability. However, the simulations did not

fully replicate certain features seen in the experiments, such as segmented or abrupt spectral changes in cold-start evolution. This discrepancy likely stems from differences in the initial gain distribution: in experiments, the preamplifier is already active before main amplification begins, and the exact moment of successful mode-locking may vary depending on which seed pulse triggers the transition. In contrast, the simulations assume idealized starting conditions with zero inversion and a single seed pulse, which smooths out some of the real-world variability. Future work could incorporate more realistic gain-seed timing to bridge this gap. It is also worth emphasizing that this chapter serves primarily as a technical validation and exploratory investigation. Rather than aiming to categorize all possible startup pathways, our goal was to develop and test a measurement framework capable of resolving transient dynamics, and to examine whether gain conditions lead to measurable differences in the mode-locking evolution. The insights gained here lay the foundation for future studies on start-up control, attractor dynamics, and coherence engineering in ultrafast fibre lasers.

Chapter 9 Beam coupling for multi-core fibre

9.1 Introduction

In addition to using gain fibres with larger mode fields, CBC technology can also be implemented on MCF platforms to further increase the output energy of MO. In high-power fibre laser systems, MCFs extend fibre laser scaling by integrating multiple amplification channels into a single cladding, which greatly suppresses relative phase fluctuations compared to arrays of discrete fibres. This property facilitates CBC with reduced stabilization requirements. Proof-of-principle demonstrations have already shown phase-locked operation in 7-core fibres[139]. Furthermore, MCF naturally meets the stringent requirements of femtosecond pulse coherent pulse combining for optical path difference[217], which is particularly important for broadband pulses generated by MO. Beyond energy scaling through CBC, MCFs also enable flexible control over amplitude, phase, and polarization across the individual cores, allowing the generation of reconfigurable structured light beams[141]. And the generation of femtosecond optical vortex beams based MO has also been proved in experiment. These capabilities make MCFs promising candidates not only for high-power ultrafast amplification in MO but also for applications requiring tailored beam profiles in MO. Building upon these developments, this work advances the scaling from previously demonstrated 7-core systems to a 32-core MCF platform. Such an increase in core count holds significant potential for further energy scaling and beam tailoring, but it also imposes stringent requirements on coupling: all cores must be excited with high efficiency and uniformity to fully exploit the available gain volume and to enable reliable phase control across the array. In this chapter, we present a systematic investigation of coupling strategies into a 32-core MCF using phase-only SLMs to generate tailored multi-beam arrays, establishing a foundation for high-energy amplification and CBC with large-core-count MCFs.

We first describe the physical structure of the MCF used in the experiment, including geometric parameters and inter-core characteristics. A reflective LCoS SLM optimized for 1550 nm is then introduced as the primary beam-shaping device, along with its Fourier optics-based operating principles. Based on this foundation, three representative beam modulation strategies, namely Overlap, Subregion, and Hybrid, are proposed and evaluated both numerically and experimentally. Each method involves distinct design trade-offs in terms of interference suppression, beam quality, and system robustness. To quantify performance, two key metrics are defined: efficiency (η), representing the ratio of coupled power to incident power, and uniformity (σ), describing the energy distribution balance across all cores. These parameters are computed at both the pattern-generation stage (η_p, σ_p) and the fibre output stage (η, σ), enabling a detailed evaluation of each method’s effectiveness. All experimental results presented have

undergone phase management optimization when needed, ensuring consistent benchmarking across methods. The chapter concludes with a full-core coupling demonstration using the best-performing strategy, validating the practical feasibility of SLM-based beam shaping for high-density MCF excitation.

9.2 Multi-core fibre structure and parameters

In this section, a 1550 nm single-mode CW laser was used as the input source to investigate beam coupling into a 32-core multi-core fibre (MCF). The cross-sectional image and structural parameters of the MCF are shown in Figure 9.1 and Table 9.1, respectively [218]. Each core supports single-mode operation around 1550 nm with an average MFD of approximately 9.9 μm. The cores are arranged in a nearly square lattice with an average pitch of 28.8 μm (standard deviation of 0.2 μm), and the total cladding diameter is 241.2 μm. The MCF features a heterogeneous core design, with slightly different effective refractive indices among adjacent cores. To minimize inter-core coupling, each core is surrounded by an index trench. The resulting inter-core crosstalk is estimated to be below −60 dB over a 10 m fibre length, which is sufficiently low to be considered negligible in this experiment. Notably, the cores are labelled numerically in the microscope image (Figure 9.1) to facilitate one-to-one mapping with the sub-beams later generated by the SLM. This labelling supports per-core phase control in subsequent beam steering simulations in Section 9.4.2.

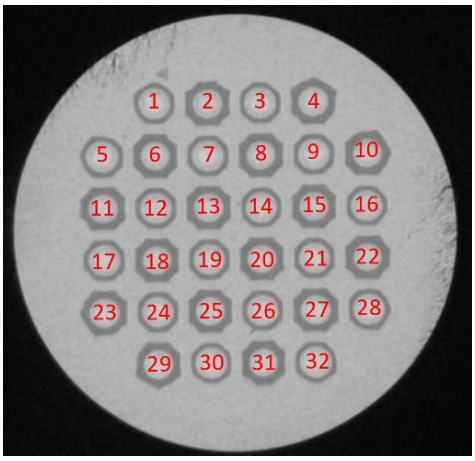

Figure 9.1 Cross-sectional microscope image of the 32-core multi-core fibre (MCF). The cores form a near-square lattice with a pitch of ~28.8 μm and cladding diameter of 241.2 μm. Numerical labels are added to the cores for phase management and mapping to sub-beams generated via SLM.

Table 9.1 Geometric parameters of the 32-core fibre used in the experiment.

Avg. pitch	28.8μm

Max./Min. pitch	29.1/28.4μm
Standard deviation (SD)	0.2 μm
Cladding diameter	241.2 μm
MFD	9.9 μm

The goal of the experiment is to simultaneously couple light into all 32 cores of the MCF using a phase-only SLM. A single laser beam is modulated to produce an array of individually shaped beams, which are then focused onto the MCF facet through a lens. Two key performance metrics are used to evaluate the actual coupling performance at the fibre output: 1. Efficiency (η): defined as the ratio of the total optical power measured from all fibre cores to the total optical power injected into the SLM; 2. Uniformity (σ): defined as the standard deviation of the output power distribution among the 32 individual fibre cores. These metrics reflect the final coupling result and are denoted without subscripts. Additionally, precise control over the relative phase of each sub-beam is required for applications involving coherent beam combination or phase-sensitive coupling. The symmetric spatial layout and geometry of the fibre core array impose key design constraints on the construction of appropriate SLM phase masks, which will be addressed in the following sections.

9.3 Spatial phase modulation using SLM

9.3.1 SLM configuration and operating principle

A SLM is an electronically addressable optical device capable of modulating light spatially in amplitude, phase, or polarization. Depending on the configuration of the liquid crystal (LC) material and alignment, SLMs can be designed to provide phase-only, amplitude-only, or complex modulation. Reflective SLMs based on liquid crystal on silicon (LCoS) technology offer high spatial resolution and are widely used in applications such as optical communication, microscopy, and wavefront shaping [219-223]. Figure 9.2 illustrates the internal structure of a LCoS-based SLM. The device consists of a thin LC layer sandwiched between alignment layers atop a complementary metal-oxide-semiconductor (CMOS) backplane. The voltage applied to each electrode individually controls the orientation of LC molecules, modulating the local refractive index for the extraordinary ray, thereby introducing a phase delay:

$$\Delta\phi(V) = \frac{2\pi}{\lambda}(n_e - n_o)d \tag{9-1}$$

Here, λ is the wavelength of incident light, d is the thickness of the LC layer, and n_e, n_o are the effective refractive indices of the extraordinary and ordinary rays, respectively. Commercial

phase-only SLMs typically implement 8-bit grayscale control to map gray levels (0-255) to phase shifts in the range of 0-2π. This enables high-resolution, pixel-wise programmable phase modulation. In this experiment, a reflective phase-only SLM (HOLOEYE PLUTO-TELCO) optimized for 1550 nm was used. Its specifications are summarized in Table 9.2.

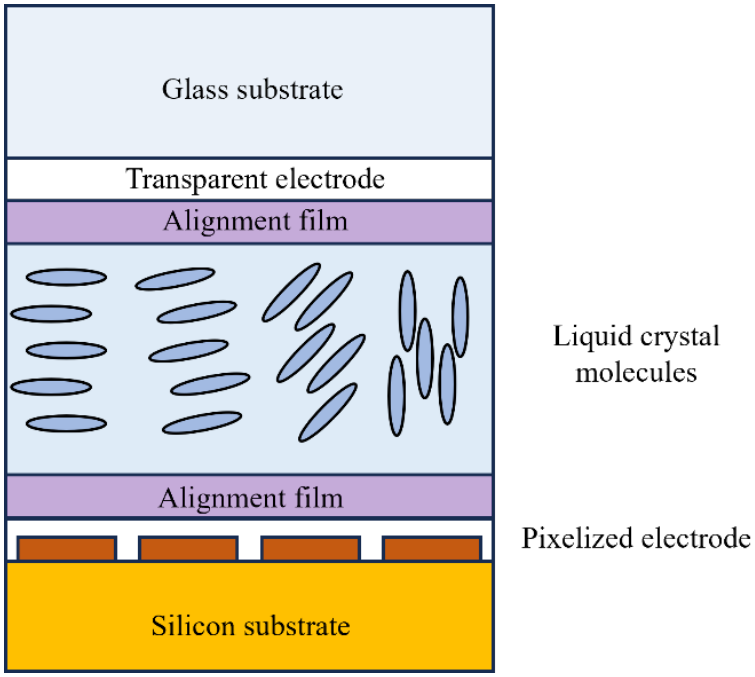

Figure 9.2 Schematic diagram of a reflective LCoS SLM. The device consists of a LC layer modulated by individual CMOS electrodes, enabling phase-only control of incident light.

Table 9.2 Specifications of the reflective phase-only SLM used in this study.

Part No.	HES 7020 6010-TELCO-013-C (HOLOEYE)
Wavelength range	1400 - 1700 nm
Resolution	1920 × 1080
Active area	15.36 mm × 8.64 mm
Pixel pitch	8.0 μm
Fill factor	93%
Reflectivity	~80%

9.3.2 Fourier optics basis for phase mask design

Figure 9.3 illustrates the working principle of a transmissive phase-only beam shaping system, where a SLM is used in conjunction with a focusing lens to control the beam distribution at the

output (focal) plane. In this setup, the SLM modulates only the phase of the incident wavefront. The optical field immediately after the SLM can be expressed as:

$$U_o'(x,y) = U_o(x,y) \cdot exp[j\varphi(x,y)], \tag{9-2}$$

where, $U_o(x,y)$ is the complex amplitude of yhe incedent field, and $\varphi(x,y)$ denotes the applied phase mask.

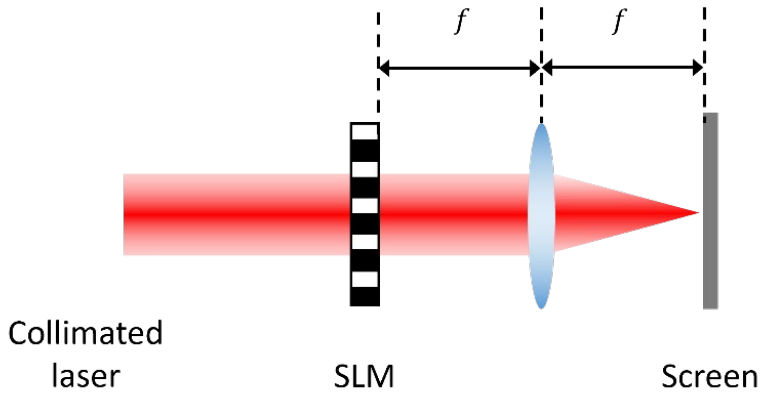

Figure 9.3 Schematic representation of a transmissive phase-only beam shaping device based on a SLM.

Assuming the modulated beam propagates a distance d and is then incident onto a thin lens of focal length f, the field just before the lens is denoted by $U_l(x_l,y_l)$, and the field immediately after the lens becomes[224]:

$$U_l'(x_l,y_l) = U_l(x_l,y_l) \cdot exp\left[-j\frac{k}{2f}\left(x_l^2+y_l^2\right)\right], \tag{9-3}$$

where, $k = \frac{2\pi}{\lambda}$ is the wave number. The exponential term represents the phase modulation introduced by the lens under the thin-lens approximation. Assuming scalar wave propagation and invoking the Fresnel diffraction integral under the paraxial approximation, the field distribution at the focal plane (u,v) is given by[224]:

$$U_f(u,v) = \frac{exp\left(j\frac{k}{2f}\left(1-\frac{d}{f}\right)(u^2+v^2)\right)}{j\lambda f} \cdot \iint_{-\infty}^{\infty} U_o'(x,y) exp\left[-j\frac{k}{f}(xu+yv)\right] dxdy. \tag{9-4}$$

This expression shows that the focal-plane field $U_f(u,v)$ is proportional to the Fourier transform of the modulated field $U_o'(x,y)$, up to a quadratic phase factor. When the propagation distance d between the input plane (SLM plane) and the lens satisfies $d = f$, meaning that the input plane is conjugate to the front focal plane of the lens, the quadratic phase term vanishes and the lens performs a pure Fourier transform:

$$U_f(u,v) = \frac{1}{j\lambda f} \cdot \mathcal{F}\{U_o'(x,y)\}. \tag{9-5}$$

This relationship forms the theoretical foundation for phase mask design: to achieve a desired field profile $U_f(u,v)$ at the focal plane, one can calculate its inverse Fourier transform and encode the resulting phase profile $\varphi(x,y)$ onto the SLM.

9.4 Beam control via phase mask design

In addition to conventional passive optical elements such as lenses and gratings, a phase-only SLM allows pixel-level control over the wavefront, enabling dynamic beam shaping in programmable systems. This capability is crucial for simultaneously coupling a single laser source into multiple targets, such as the individual cores of a MCF, with precise control over the beam direction and relative phase. In this section, two beam control functionalities are demonstrated: 1. generating a single beam at an arbitrary off-axis position; 2. producing multiple coherent beams directed toward predefined locations. These functions are both realized using computer-generated phase masks that encode a prescribed spatial frequency onto the wavefront. Importantly, these phase masks are derived from an inverse Fourier mapping between the target distribution in the focal plane and the modulated field at the SLM plane. Since the SLM operates on a discrete pixel grid, a numerical implementation based on the discrete Fourier transform is employed throughout this section. The key goal is to map a target pattern in the focal plane to a phase-only mask defined on the SLM pixel grid, with a focus on spatial precision, uniformity, and implementation efficiency.

9.4.1 Single-beam offset demonstration

To verify the basic beam steering capability, we start with the generation of a single beam shifted away from the optical axis by applying a linear phase ramp across the SLM surface. The SLM plane is defined by a 2D grid of size $M \times N$, with physical side lengths L_X and L_Y given by:

$$L_\mathrm{X} = M\Delta x, \quad L_\mathrm{Y} = N\Delta y. \tag{9-6}$$

Here, Δx and Δy are the pixel pitches in the horizontal and vertical directions, respectively. The sampling grid defines the total extent and resolution of the modulated field. According to the discrete Fourier transform framework, the spatial frequency domain is sampled as[225]:

$$F_\mathrm{X} = 1/\Delta x, \quad F_\mathrm{Y} = 1/\Delta y, \quad \Delta f_\mathrm{X} = 1/L_\mathrm{X}, \quad \Delta f_\mathrm{Y} = 1/L_\mathrm{Y}. \tag{9-7}$$

Here, F_X and F_Y are referred to as the side length of the frequency domain, Δf_X and Δf_Y are the sampling intervals. This implies that the focal plane resolution is directly tied to the physical dimensions of the SLM and the pixel sampling rate. Each spatial frequency component is mapped to a physical location in the output (Fourier) plane, as described in Ref. [224]. The transformation between spatial coordinates in the focal plane and the coordinates in the frequency domain follow the following relationship:

$$f_X = u/\lambda f, \quad f_Y = v/\lambda f. \tag{9-8}$$

Where f_X and f_Y are the spatial frequencies of the blazed grating , (u, v) are the spatial coordinates in the focal plane, λ is the wavelength, and$f$ is the focal length of the Fourier-transforming lens. To shift the beam center from the origin to a point (u_1, v_1) , the following phase mask is encoded onto the SLM:

$$\varphi_1(\xi, \eta) = mod[2\pi(f_{X1} \cdot \xi + f_{Y1} \cdot \eta), 2\pi], \tag{9-9}$$

here $f_{X1} = u_1/\lambda f, \quad f_{Y1} = v_1/\lambda f.$

To validate the beam steering capability enabled by SLM phase encoding, a series of single-beam offset simulations were conducted. Figure 9.4 presents the simulation results for four distinct beam directions, corresponding to the core positions #6, #9, #24, and #27 of the 32-core MCF. The top row (a-d) shows the linear phase ramps applied on the SLM, while the bottom row (e-h) displays the resulting far-field intensity distributions calculated via 2D discrete Fourier transform. The emergence of distinct intensity peaks at the expected offset positions confirms the accuracy of the phase design and the feasibility of precise beam placement in the MCF plane. Note: In simulation, the SLM is assumed to have an ideal fill factor and reflectivity of 100%. The number of pixels used was 960*960.

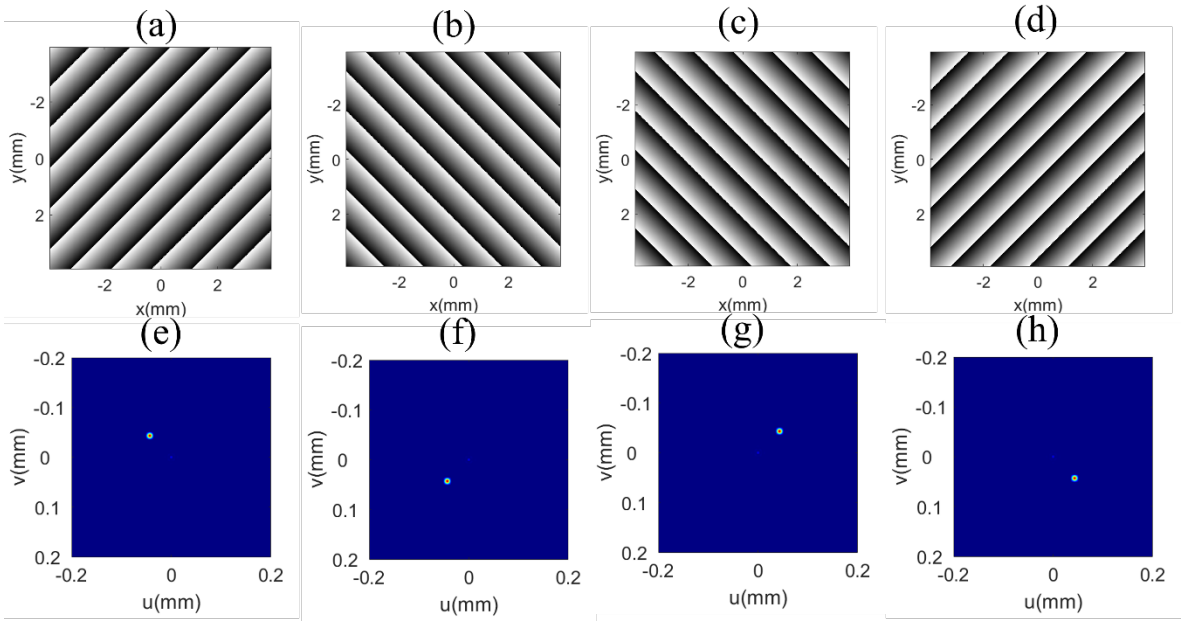

Figure 9.4 Simulated single-beam offset using linear phase ramps encoded on the SLM. (a-d) Linear phase profiles designed to steer the beam toward four different directions. (e-h) Corresponding far-field intensity distributions obtained from 2D discrete Fourier transform simulations, demonstrating localized beam formation at positions corresponding to MCF core #6, #9, #24, and #27.

9.4.2 Multi-beam generation approaches

For MCF applications, it is often necessary to generate not only multiple beams, but also to arrange them in symmetric and periodic patterns. In such cases, suppressing the undesired interference among target beams becomes a critical concern. In this section, we introduce and compare three distinct beam generation methods, aiming to identify an optimized strategy.

9.4.2.1 Overlap method

A straightforward approach to generating multiple beams is to superimpose several linear phase ramps on the SLM, each steering light to a specific focal plane location. We refer to this approach as the Overlap Method, in which all beams are encoded across the entire aperture of the SLM without spatial separation. While this method is simple and convenient to implement, it inevitably leads to coherent interference between different phase ramps, especially when the beam array is highly symmetric.

Suppose the desired focal-plane positions are (u_1, v_1), $(u_2, v_2), \cdots$, (u_n, v_n), corresponding to spatial frequencies $(f_{\mathrm{X1}}, f_{\mathrm{Y1}})$, $(f_{\mathrm{X2}}, f_{\mathrm{Y2}})$, ..., $(f_{\mathrm{Xn}}, f_{\mathrm{Yn}})$. The total complex field on the SLM plane can be expressed as the sum of n individually tilted plane waves:

$$U_{SLM}(x, y) = \sum_{i=1}^{n} exp[j2\pi(f_{\mathrm{X1}} \cdot x + f_{\mathrm{Y1}} \cdot y)] \tag{9-10}$$

The corresponding phase mask to be encoded on the SLM is then given by the argument of this complex sum:

$$\varphi_{Overlap}(x, y) = mod\left\{\sum_{i=1}^{n} exp[j2\pi(f_{\mathrm{X1}} \cdot x + f_{\mathrm{Y1}} \cdot y)], 2\pi\right\} \tag{9-11}$$

Figure 9.5 shows the simulation results obtained using the Overlap Method without any phase optimization. In this configuration, the incident beam is simultaneously tilted toward the positions corresponding to cores #6, #9, #24, and #27 of the MCF, as indicated in Figure 9.5 (a). The phase values assigned to each target beam are all set to 0, i.e., no relative phase difference is introduced between beams. Compared with the single-beam tilts shown in Figure 9.4, the key difference here lies in the simultaneous generation of multiple beams. Figure 9.5 (b) reveals the presence of additional intensity

peaks that were not part of the design. These arise due to coherent interference among the beams, which is particularly pronounced under symmetric target patterns when no phase control is applied. Figure 9.5 (c) analyzes the energy performance of the generated beam array. While the energy distribution across the four target spots is perfectly uniform (standard deviation σ_p = 0), the overall generation efficiency η_p reaches only 63.48%. Here, η_p refers to the ratio of energy within all valid target spots to the total output energy in the simulated far field, and σ_p quantifies the standard deviation of the energy ratio among those target spots. To evaluate the effectiveness of SLM-based phase modulation independently of experimental imperfections, we apply the same set of performance metrics, efficiency and uniformity, to the generated far-field pattern. These simulation-level values are consistently denoted with the subscript "p" (standing for *pattern*), to distinguish them from the experimentally measured coupling metrics at the fibre output, which are denoted without subscripts. These results serve as a baseline for comparison with subsequent methods involving phase management, which aim to mitigate interference and improve efficiency.

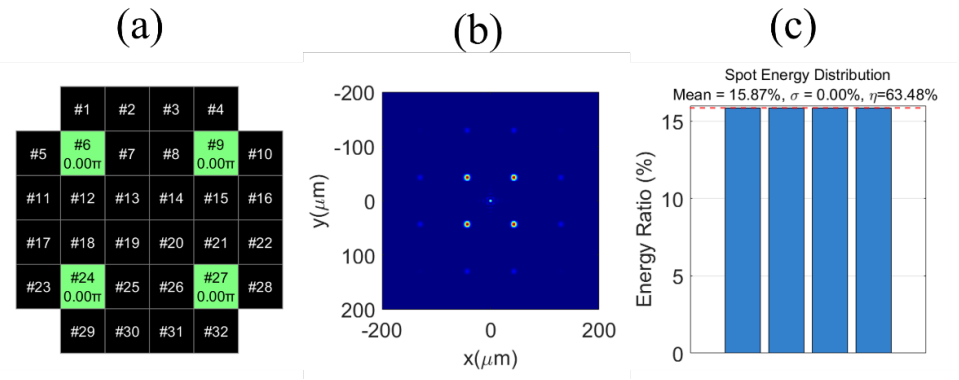

Figure 9.5 Simulation results using the Overlap Method without phase management. (a) Assigned phase values for selected cores (#6, #9, #24, and #27), all set to 0.00π, indicating no phase adjustment between beams. (b) Simulated far-field intensity distribution reveals additional unwanted interference spots due to coherent overlap. (c) Spot energy distribution; the four bars correspond left-to-right to cores #6, #9, #24, and #27. The total efficiency improves perfect uniformity (σ_p = 0.00%) but limited efficiency (η_p = 63.48%) without phase control.

Proper phase management can effectively suppress the detrimental interference effects among sub-beams. Figure 9.6 (a) illustrates a phase arrangement strategy in which distinct relative phases are assigned to the four target beams. As shown in Figure 9.6 (b), the resulting far-field pattern demonstrates a significant reduction in interference artifacts compared to the unmanaged case. The corresponding energy analysis in Figure 9.6 (c) indicates a marked improvement in total efficiency, with η_p increasing to 83.17%, while perfect uniformity is maintained (σ_p = 0). However, not all phase management configurations lead to favorable

outcomes. As shown in in Figure 9.6 (d) and (e), an alternative phase arrangement produces a far-field pattern that closely resembles the case without any phase management. In this case, the performance metrics shown in Figure 9.6 (f) reveal a slight degradation in both energy uniformity (σ_p = 0.01%) and efficiency (η_p = 62.96%). This comparison highlights the critical role of appropriate phase design in optimizing multi-beam generation performance.

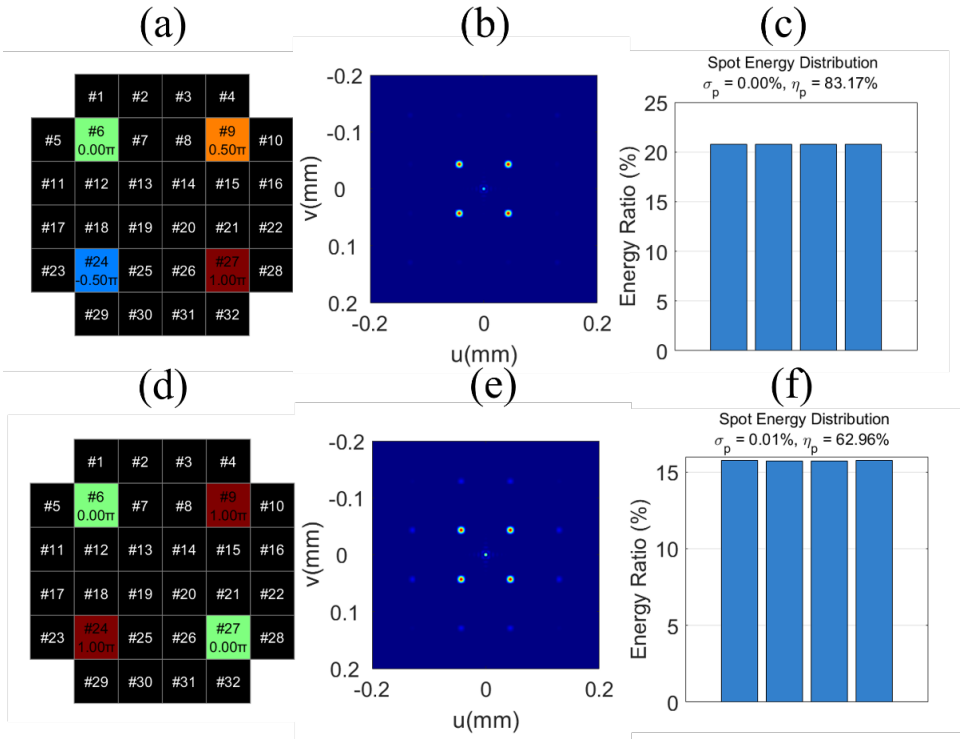

Figure 9.6 Comparison of different phase management schemes for generating a 2×2 sub-beam array. (a,d) Spatial phase arrangements corresponding to the four selected target cores (#6, #9, #24, #27), with individual blocks annotated by core number and relative phase (in units of π). (b,e) Simulated far-field intensity patterns under the two phase configurations. (c,f) Corresponding evaluations of power uniformity and total pattern efficiency, denoted as σ_p and η_p, respectively. The four bars correspond left-to-right to cores #6, #9, #24, and #27.

To further evaluate the interference effect in more complex symmetric multi-beam generation, we simulated two beam arrays, in which one comprising 16 beams and the other spanning all 32 MCF cores, using the overlap method, with and without relative phase control. In the first case, a 4×4 square array of sub-beams was generated. Figure 9.7 (a) shows a configuration where all beams were assigned the same phase (0π). The resulting far-field intensity distribution in Figure 9.7 (b) exhibits prominent side lobes and strong interference fringes. The quantitative analysis in Figure 9.7 (c) reveals poor energy concentration, with a low pattern efficiency of η_p = 41.51% and a standard deviation of σ_p = 2.40%. When appropriate relative phases are applied, as illustrated in Figure 9.7 (d), the beam pattern becomes significantly cleaner, as shown in Figure 9.7 (e), and

the energy distribution among the target beams improves accordingly. The corresponding metrics shown in Figure 9.7 (f) indicate η_p = 80.56% and σ_p = 1.41%, confirming that phase optimization enhances both energy efficiency and uniformity.

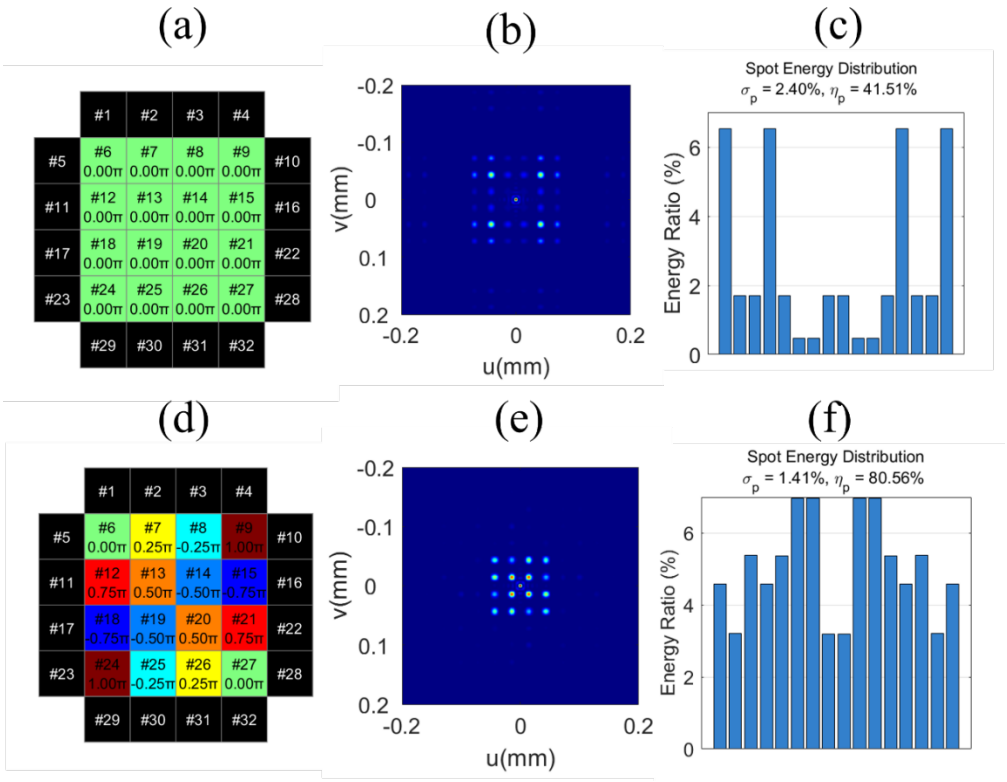

Figure 9.7 Simulation results for a 4×4 beam array using the Overlap Method. (a,d) Assigned relative phase maps, aligned with the MCF core indices. (b,e) Simulated far-field intensity distributions. (c,f) Statistical evaluation of energy performance using pattern efficiency η_p and uniformity σ_p. Results show that phase control significantly improves both efficiency and uniformity. The 16 bars correspond left-to-right to cores #6, #7, #8, #9, #12, #13, #14, #15, #18, #19, #20, #21, #24, #25, #26 and #27.

The same trend is observed in the 32-beam case. Without any phase management, as illustrated in Figure 9.8 (a), the far-field distribution in Figure 9.8 (b) is cluttered with strong interference. The analysis in Figure 9.8 (c) confirms this degradation, with η_p = 44.52% and σ_p = 1.05%. In contrast, when a designed phase distribution is applied, as shown in Figure 9.8 (d), the far-field pattern in Figure 9.8 (e) exhibits substantial improvement, with the final evaluation in Figure 9.8 (f) yielding η_p = 73.01% and σ_p = 0.99%. These results clearly demonstrate that the Overlap Method, though simple, is highly sensitive to interference, particularly in symmetric configurations. Effective phase management is therefore essential to achieving high-quality beam arrays.

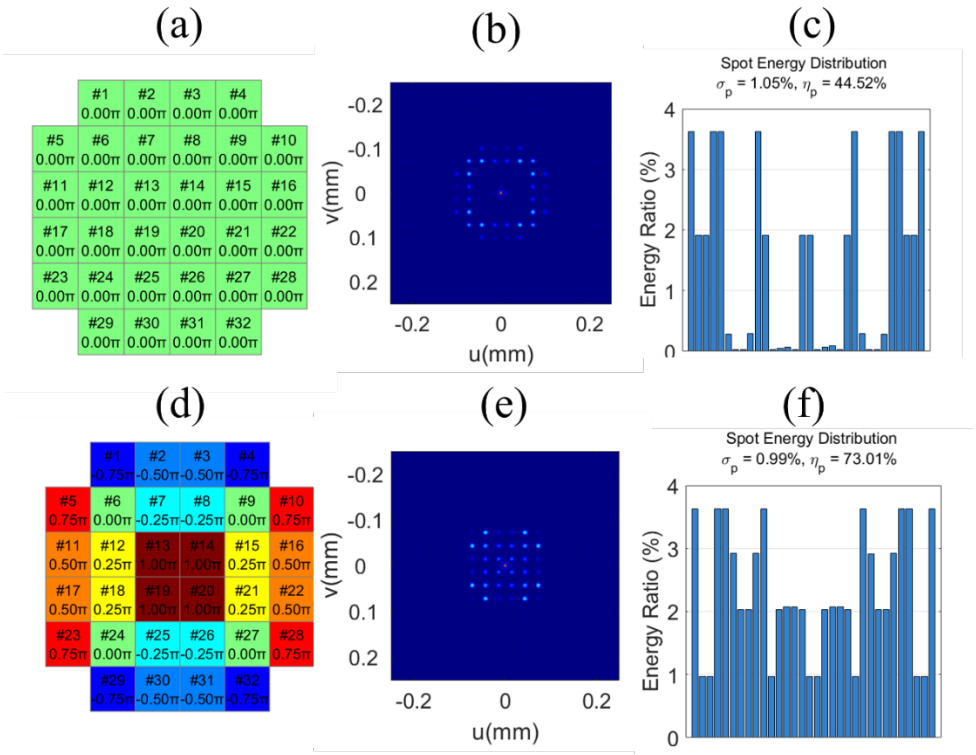

Figure 9.8 Simulation results for a full 32-core beam array using the Overlap Method. (a,d) Phase patterns with and without relative phase management. (b,e) Corresponding far-field intensity distributions. (c,f) Energy analysis confirms that optimized phase assignment suppresses interference and enhances performance. The 32 bars correspond left-to-right to cores from #1 to #32.

9.4.2.2 Subregion method

To further mitigate the interference caused by coherent superposition in the Overlap Method, we adopt an alternative strategy referred to as the Subregion Method. This approach spatially separates the encoding regions for different sub-beams on the SLM, thereby eliminating mutual interference among them.

Figure 9.9 (a) and (b) illustrate the fundamental difference between these two strategies. In the Overlap Method, multiple linear phase ramps are superimposed over the full SLM aperture, as shown in Figure 9.9 (a). In the Subregion Method, illustrated in Figure 9.9 (b), the SLM area is partitioned into multiple subregions, each independently encoding a single beam. This spatial isolation breaks the coherent interference mechanism and allows for independent beam shaping. Figure 9.9 (c) shows the relative phase assignment corresponding to the 32-core MCF configuration, all set to 0 for demonstration. The simulated far-field intensity pattern in Figure 9.9 (d) assumes equal focal lengths for the collimating and focusing lenses, the same configuration as used in the Overlap Method. However, due to the spatially localized modulation of the Subregion Method, the Fourier plane distribution exhibits strong aperture effects, so that only a

limited number of sub-beams are formed and the energy is not efficiently directed toward the desired 32-core positions. This result highlights that the optical configuration for the Subregion Method must be adapted to account for its spatial encoding structure. Additionally, due to the presence of a strong intensity peak in the vicinity of the origin in the focal plane, the colorbar range was adjusted to enhance the visibility of surrounding regions. Maintaining the default 0-1 scale would suppress much of the detail in lower-intensity areas.

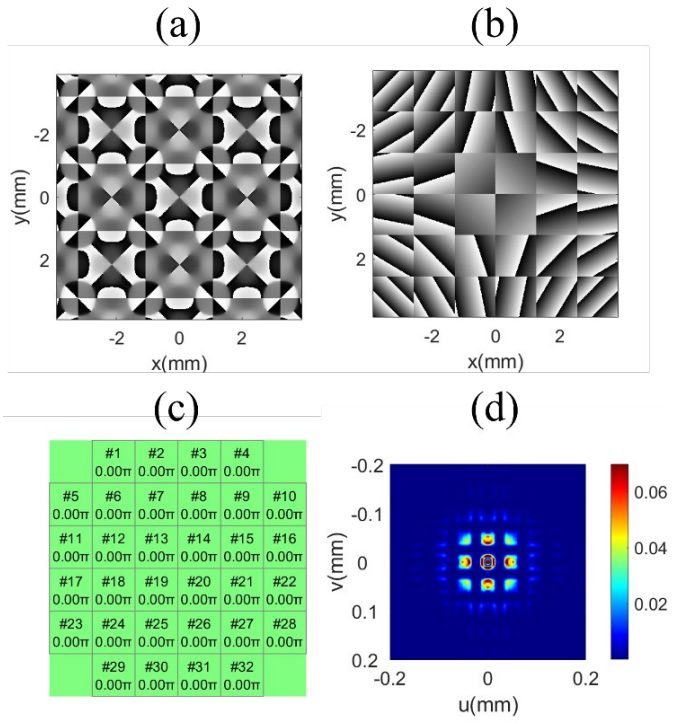

Figure 9.9 Comparison between the Overlap Method and the Subregion Method for 32-beam generation. (a) Phase profile of the Overlap Method: full-aperture encoding. (b) Phase profile of the Subregion Method: localized encoding with isolated regions. (c) Assigned relative phase map for 32 sub-beams (all set to 0). (d) Simulated far-field intensity under identical optical conditions as the Overlap case, showing significant aperture truncation and incomplete beam formation. The colorbar range was adjusted to enhance the visibility of weaker features near the origin of the focal plane, where strong intensity components are present.

To mitigate coherent interference in the subregion method, the focal length of the focusing lens is adjusted to match the reduced sub-aperture size. For the 32-core configuration, this corresponds to a six-fold reduction in focal length relative to the collimation lens. Figure 9.10 presents the simulation results under this modified configuration using a standard Gaussian input beam. The top row shows the case without phase management, and the bottom row incorporates a specific phase arrangement. In both cases, clear sub-beam arrays are successfully generated, confirming that spatial decoupling via subregion encoding effectively

suppresses interference, even for complex patterns. Due to the high peak intensity near the optical axis (central spot), the color range of the second column is selectively adjusted for better visibility. In contrast, all other intensity plots use default scaling unless otherwise noted. Moreover, zoom-in views of the far-field intensity profiles (third column) reveal pronounced spatial features. The sub-beams exhibit non-circular, petal-shaped contours with prominent Airy-type sidelobes. These features arise from the diffraction effect caused by abrupt truncation of the Gaussian beam by the square subregion apertures. Such structural artifacts introduce moderate energy leakage and can affect coupling quality if beam shapes do not match the acceptance profile of the MCF cores.

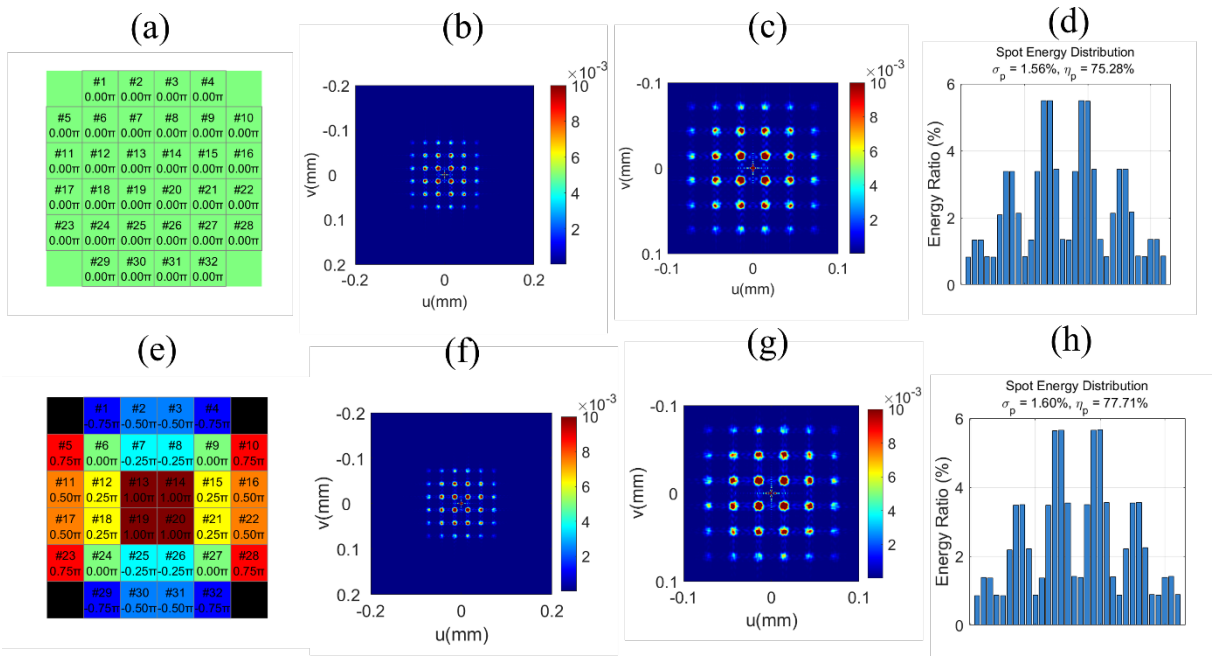

Figure 9.10 Simulation results of the subregion method using a Gaussian incident beam. (a, d) Phase maps of the 32-beam array without and with phase management, respectively. (b, e) Far-field intensity distributions with the color range adjusted for visualization due to strong central peak. (c, f) Zoomed-in views (0.1 mm × 0.1 mm) showing individual sub-beam contours. (g, h) Statistical analysis of energy uniformity and efficiency. The 32 bars correspond left-to-right to cores from #1 to #32. Notably, each sub-beam exhibits hexagonal or petal-like envelopes with evident Airy sidelobes caused by subregion aperture diffraction.

To further optimize spatial uniformity, a flat-top illumination scheme is introduced using an 8th-order super-Gaussian beam, as illustrated in Figure 9.11. Compared with the Gaussian beam shown in Figure 9.11 (a), the super-Gaussian beam illustrated in Figure 9.11 (b) provides a more uniform intensity distribution across the SLM aperture while maintaining sharp edge roll-off.

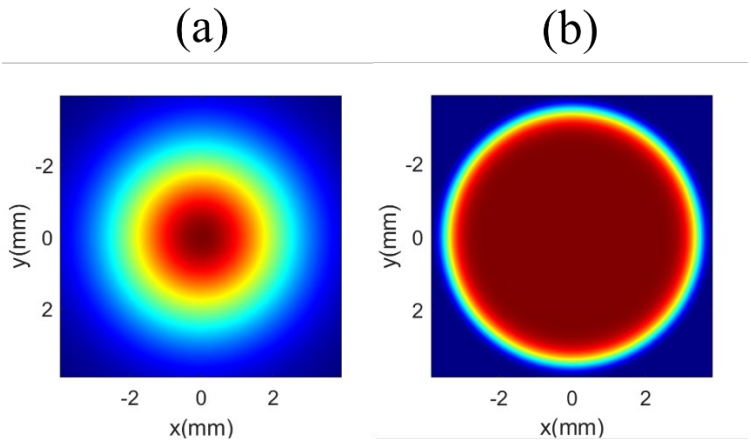

Figure 9.11 Incident beam profiles at the SLM plane. (a) Conventional Gaussian beam used in previous simulations. (b) Eighth-order super-Gaussian (flat-top) beam with sharp edge roll-off and uniform center intensity, designed to improve sub-beam uniformity in the subregion method.

Figure 9.12 shows the resulting beam arrays under super-Gaussian (flat-top) illumination, comparing phase-unmanaged (top row) and phase-managed (bottom row) conditions. Compared with the Gaussian-illuminated results in Figure 9.10, the most notable improvement lies in the enhanced uniformity of individual sub-beams. The sidelobes are significantly reduced, and the beam profiles become smoother and more symmetric. These results confirm that flat-top beams improve energy confinement within each sub-beam and suppress inter-spot leakage more effectively. Meanwhile, under flat-top illumination, the performance gap between the unmanaged and managed cases becomes negligible, as evidenced by the similar values of energy efficiency (η_{p}) and uniformity (σ_{p}). This highlights the robustness of the subregion method when the input beam profile is properly shaped.

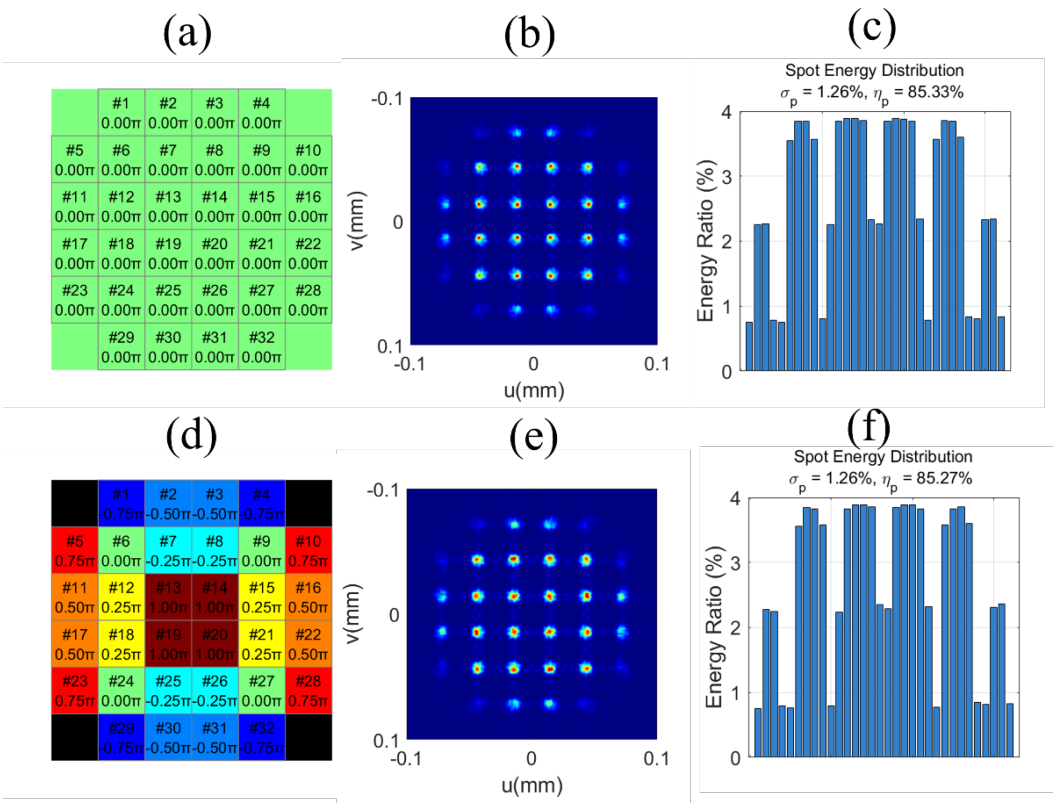

Figure 9.12 Simulation results of the subregion method using a flat-top incident beam. Top row: without phase management; Bottom row: with phase management. (a, d) Phase profiles for the 32-beam array. (b, e) Far-field intensity distributions under uniform color scaling. (c, f) Energy ratio and distribution across all target beams. The 32 bars correspond left-to-right to cores from #1 to #32. The sub-beams display smooth circular contours with suppressed sidelobes. Phase management offers minimal additional benefit in this condition, indicating the intrinsic stability of the flat-top subregion scheme.

Figure 9.13 explores the impact of increasing the beam size on the SLM by simultaneously enlarging both the collimating and focusing lens focal lengths by 1.2× (top row) and 1.4× (bottom row), compared to the baseline configuration. This modification results in a broader illumination area on the SLM and, consequently, larger sub-beams in the output plane. Given the proven decoupling capability of the subregion method, no phase management is applied here. The resulting beam arrays demonstrate improved uniformity, as shown in the rightmost column, where the standard deviation (σ_p) of the energy distribution decreases. However, the total efficiency (η_p) also drops, indicating increased optical loss. The far-field intensity patterns (second column) reveal pronounced aperture effects, with visible clipping and sidelobe distortion. A closer look at the sub-beams (second column) highlights additional spatial features: in Figure 9.13 (b), each sub-beam exhibits a structured intensity distribution featuring a local minimum at the center and four surrounding high-intensity regions aligned along the horizontal and vertical

axes. In contrast, the sub-beams in Figure 9.13 (e) transition into polygonal shapes with peak intensity shifting toward their edges. These behaviors stem from diffraction and edge truncation caused by limited aperture size and increased sub-beam diameter.

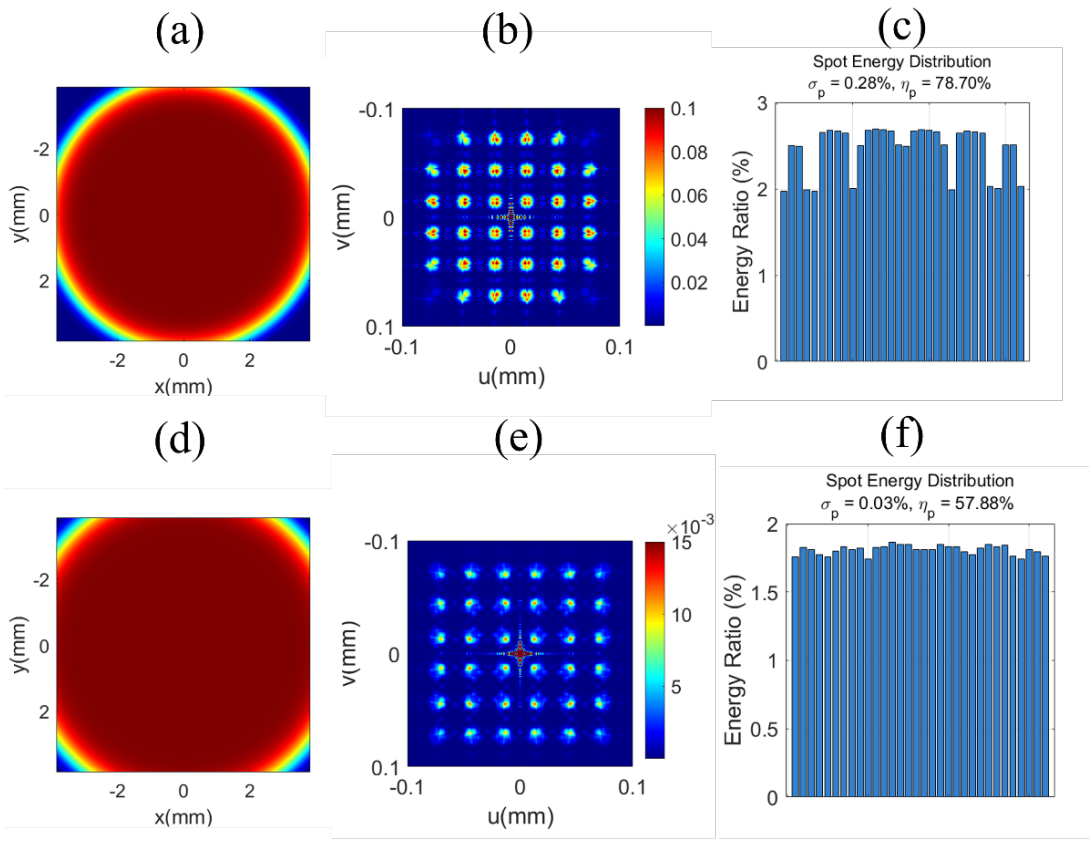

Figure 9.13 Simulation results of subregion-based beam array generation under expanded beam sizes. (a-c) Results for a beam size increased by 1.2×; (d-f) results for a 1.4× increase. First column: encoded phase masks on the SLM. The 32 bars correspond left-to-right to cores from #1 to #32. Second column: simulated far-field intensity distributions. Third column: magnified views of individual sub-beam profiles. Rightmost column: quantitative evaluation of uniformity (σ_p) and efficiency (η_p). No phase management is applied. Note: Color scale in the second column is adjusted for visualization due to high-intensity central lobe.

9.4.2.3 Hybrid method

To mitigate the limitations of the subregion method, particularly its sensitivity to the input beam profile, a hybrid strategy is proposed. As illustrated in Figure 9.14, the SLM aperture is divided into four quadrants, each assigned an independent periodic phase modulation pattern. This design leverages the central symmetry of a Gaussian input beam to retain global coherence, while partially suppressing interference among sub-beams. It aims to combine the robustness of subregion encoding with the improved uniformity seen in the overlap method.

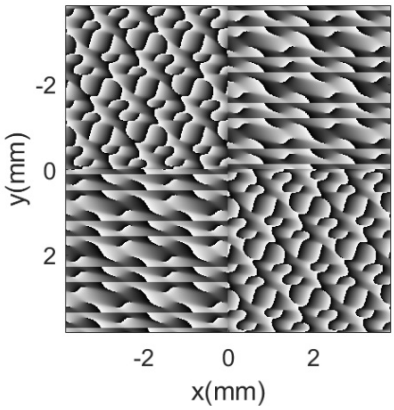

Figure 9.14 Schematic of the hybrid phase mask design: the SLM plane is divided into four quadrants, each with distinct periodic modulations.

Simulation results are presented in Figure 9.15 (a-f). The upper and bottom rows compare performance with and without phase management, respectively. Compared with the overlap method, the hybrid approach improves energy uniformity, particularly in the phase-managed case where σ_{p} reduces to 0.80%. However, this comes at a cost. First, the structured symmetry of the individual sub-beam profiles is disrupted. Rather than a smooth and symmetric core, each sub-beam exhibits irregular or elongated intensity shapes, and the peak no longer resides at the center. This indicates that spatial coherence is not fully preserved within each quadrant. Second, as shown in the far-field intensity distribution, multiple side lobes emerge around both the center and edges of the array. These residual sidelobes imply incomplete spatial decoupling and more complex inter-spot interference patterns. In effect, although the hybrid scheme improves energy balance across the array, it sacrifices sub-beam integrity and leads to lower energy confinement. The overall efficiency η_{p}, while improved compared to subregion without phase control, still lags behind that of the overlap method.

Thus, while the hybrid method inherits some benefits of both strategies, it also compounds their limitations, namely the need for sophisticated phase management and the difficulty of maintaining well-defined beam profiles.

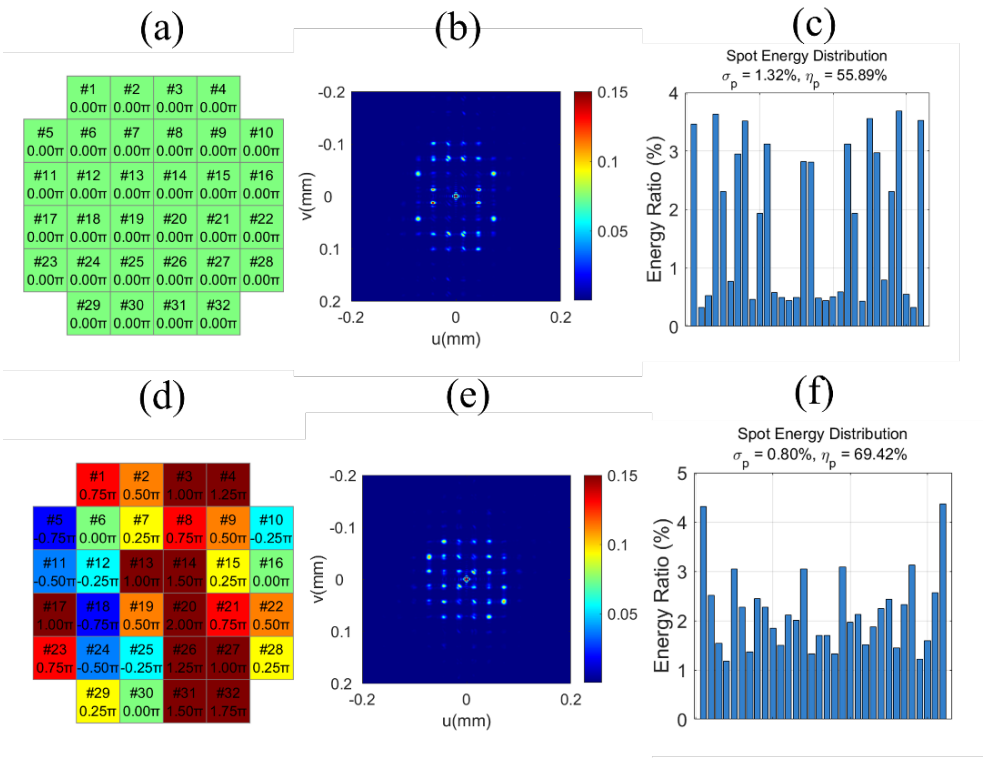

Figure 9.15 Far-field performance of the hybrid method under Gaussian illumination. (a-c) Results without phase management: (a) assigned phase shifts for 32 target beams, (b) far-field intensity distribution, (c) energy ratio per spot with uniformity σ_p = 1.32% and efficiency η_p = 55.89%. (d-f) Results with phase management: (d) optimized phase shifts, (e) far-field pattern showing improved energy distribution, (f) corresponding histogram with σ_p = 0.80%, η_p = 69.42%. The 32 bars in (c) and (f) correspond left-to-right to cores from #1 to #32. Although phase optimization improves uniformity, sub-beam integrity is degraded and residual sidelobes persist, indicating incomplete spatial decoupling.

9.4.2.4 Method comparison summary

To summarize, three representative methods: Overlap, Subregion, and Hybrid were evaluated for generating multi-beam arrays suitable for coupling into MCFs. Each approach presents a distinct trade-off between beam quality, energy uniformity, interference suppression, and implementation complexity. 1. The Overlap method, while sensitive to coherent interference, exhibits excellent beam quality and is inherently spatial coherent and minimal beam shaping distortion. However, its performance relies on precise phase management, which may require additional algorithmic support in more complex configurations. 2. The Subregion method offers robust interference suppression by spatially decoupling the phase regions but suffers from significant beam distortion, aperture clipping effects, and strong sensitivity to input beam profile and alignment. Its coherence is compromised. 3. The Hybrid method, although conceptually aiming to combine the advantages of the previous two, results in poor beam fidelity and degraded

energy concentration. It retains the complexity of phase control while failing to achieve a substantial improvement in either uniformity or robustness. In practice, it inherits the drawbacks of both methods, with limited practical benefit. Overall, the Overlap method remains the most promising scheme when phase control is properly managed, offering the best balance between optical quality and system compatibility. Having established the design principles and simulated performance of various multi-beam generation strategies, we next turn to their experimental validation using a custom-built coupling setup.

9.5 Experimental setup and results

9.5.1 Optical layout

In this setup shown in Figure 9.16, a Gaussian beam from an input single-mode fibre (SMF) is first collimated into a parallel beam using a collimation lens. A $\lambda/2$ plate is placed before the SLM to optimize its reflective efficiency. A portion of the modulated beam is then diverted by a beam splitter (BS) and monitored, while the remaining beam is coupled into the receiving fibre, either a single-mode fibre or a 32-core fibre, via a coupling lens. The MFDs of the SMF and each core of the 32-core fibre are 10.4 μm and 9.9 μm, respectively, both with a NA of 0.14. The focal lengths of the collimation and coupling lenses are f_1 = 40 mm, and f_2 = 40 mm or 9.6 mm, depending on the array configuration. Specifically, f_2 = 40 mm is used for the overlap method, while f_2 = 9.6 mm is applied to the subregion and hybrid methods with 4×4 beam arrays. The powers P_1, P_2, and P_3 represent the input power to the system, the power before coupling, and the power after coupling into the output fibre, respectively. For this experiment, P_1 = 20 dBm and P_2 = 13.62 dBm, indicating an insertion loss of 6.38 dB. The ratio $\eta = P_3/P_2$ is used to evaluate the overall system efficiency, which includes both beam-shaping and coupling performance. Since the output fibres are only a few meters long, transmission losses are neglected. Two cameras are used for real-time monitoring: Camera 1 captures the far-field beam pattern before coupling, and Camera 2 observes the coupled output from the 32-core fibre. It is important to note two clarifications regarding Figure 9.16. First, the SLM used in our experiment is a reflective type; however, a transmissive SLM is illustrated in the schematic for drawing clarity. Second, practical optical systems inevitably suffer from aberrations, which degrade the image quality and coupling efficiency. Such aberrations may arise from imperfect optical alignment, defocus, surface irregularities of optical elements, or intrinsic limitations of lenses and other imaging components. To address this, a home-built software developed by a former group member enables phase compensation by applying an additional wavefront correction on the SLM. Each time the beam is re-collimated or any optical component is replaced, the aberration correction must be re-optimized. With f_2 = 40 mm, the measured coupling power P_3 was 9.76 dBm for SMF and 8.23

dBm for the 32-core fibre. For f_2 =9.6 mm, P_3 was 8.34 dBm for SMF and 7.17 dBm for the 32-core fibre. For the MCF case, the reported value corresponds to coupling into a single core as a reference measurement, rather than simultaneous excitation of all 32 cores with a generated beam pattern. The difference in coupling efficiency across focal lengths arises from MFD and NA mismatches. The optimized SMF result provides an upper-bound benchmark for the coupling performance achievable with the 32-core fibre.

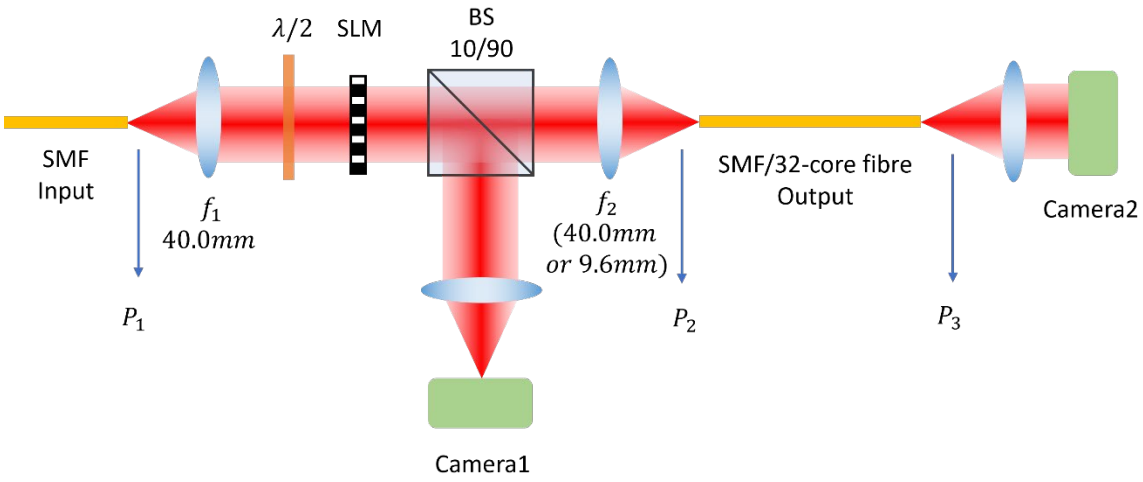

Figure 9.16 Schematic of the experimental setup. A Gaussian beam is collimated, modulated by a reflective SLM, and then coupled into a receiving fibre. A beam splitter is used to monitor the modulated pattern. The SLM is illustrated as a transmissive device for clarity. Camera 1 monitors the modulated far-field pattern, and Camera 2 captures the output from the fibre.

Due to the fixed geometry of the 32-core fibre, spatial alignment between the generated pattern and fibre core positions is crucial. Since mechanical rotation of the fibre was not feasible, we programmed a rotational adjustment to the holographic pattern itself. Figure 9.17 illustrates the setup used to determine the rotation angle of the fibre endface. White light is injected backward from the output end of the fibre to visualize the core structure, as shown in Figure 9.18 (a). Figure 9.18 (b) presents a simulated beam array rotated by 30° to match the fibre orientation, with the original unrotated array shown in the inset. Experimental optimization of the rotation angle is shown in Figure 9.18 (c), where the x-axis indicates rotation angle and the y-axis shows the coupled power P_3. The optimal alignment was achieved at approximately 3° for this setup. In addition, mismatch between the designed beam pitch d_{des} and the actual inter-core spacing d_{cores} may occur due to imperfect optical alignment or deviations from the ideal focal planes. To address this, d_{des} must be adjusted such that the actual beam spacing $d_{act} \approx d_{cores}$. A scaling factor, defined as d'_{des}/d_{des} , is introduced to quantify the adjustment. Figure 9.18 (d) summarizes the optimization results. For f_2 = 9.6mm, the optimal ratio is approximately 0.91,

while for f_2 = 40mm, it is approximately 0.94. This scaling compensates for slight beam divergence and alignment errors in the optical path.

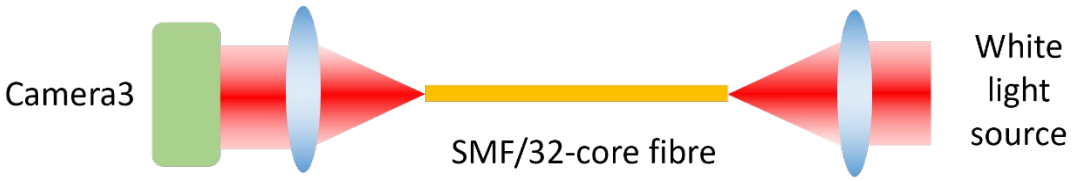

Figure 9.17 Schematic for visualizing the 32-core fibre's output facet. White light is injected from the output side of the fibre to identify core positions for alignment. The rotation angle of the generated pattern is adjusted accordingly.

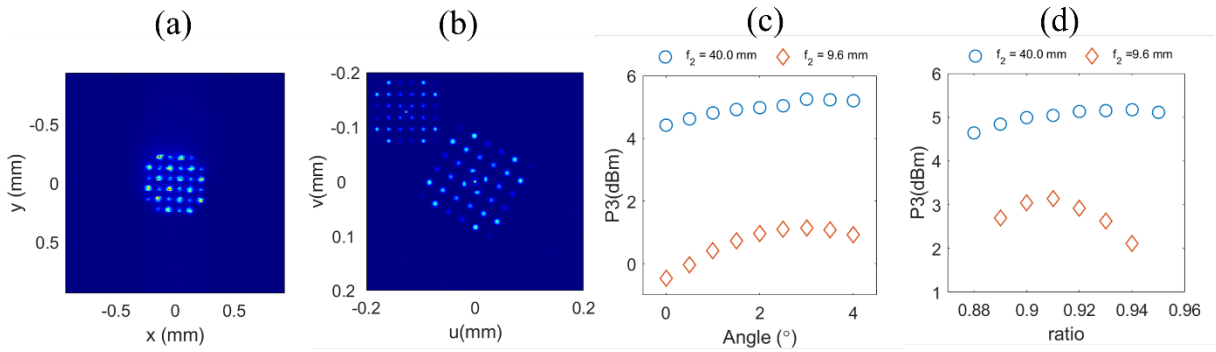

Figure 9.18 Optimization of rotation angle and pitch distance for coupling to a 32-core fibre. (a) Captured fibre core image using white-light back-illumination. (b) Simulated beam pattern rotated by 30°; the original unrotated array is shown in the inset. (c) Coupling efficiency P_3 versus rotation angle. (d) Coupling efficiency $P3$ versus pitch scaling ratio. Optimal values are 3° and 0.91 (for f_2 = 9.6 mm) and 0.94 (for f_2 = 40 mm), respectively.

9.5.2 Experimental demonstration of coupling

All experimental results presented in this section were obtained after phase management optimization was applied, when necessary, to enhance beam generation and coupling performance. Figure 9.19 presents the experimental results using the overlap method. In this configuration, a specially designed sub-beam array was generated on the SLM, as shown in Figure 9.19 (a). The inset illustrates the corresponding target cores on the 32-core fibre. This pattern features a 4×4 square array in which the four corner beams are omitted, resulting in 12 active sub-beams. Additionally, the array is deliberately offset from the center, testing the method's robustness against large spatial deflections. The bright central spot corresponds to the zeroth-order diffraction, which is not involved in coupling. Figure 9.19 (b) shows the statistical distribution of the 12 intended sub-beams at the generation plane. The uniformity is high, with a standard deviation of σ_{p} = 2.66%, and the overall pattern efficiency η_p = 84.64%. Figure 9.19 (c)

presents the output pattern captured at the 32-core fibre's end facet. Despite the spatial shift and irregular geometry of the pattern, successful coupling into the designated cores is achieved. The energy distribution across the coupled beams is shown in Figure 9.19 (d), yielding a standard deviation of σ = 2.99% and a measured coupling efficiency η = 17.86% based on the output power P_3 = 6.14 dBm.

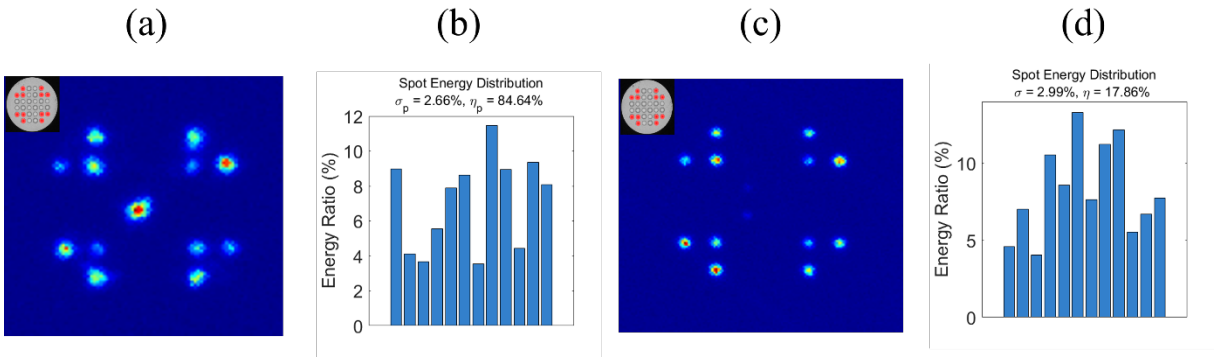

Figure 9.19 Experimental results using the overlap method. (a) Sub-beam array generated on the SLM; the inset shows the target cores to be coupled. The array comprises 12 beams in a 4×4 configuration with omitted corners and large spatial deflection. The central bright spot is the zeroth-order diffraction. (b) Energy distribution of the 12 sub-beams at the generation plane, with calculated standard deviation σ_p = 2.66% and pattern efficiency η_p = 84.64%. (c) Coupled output pattern from the 32-core fibre. (d) Energy distribution of the coupled beams, with σ = 2.99% and measured coupling efficiency η = 17.86% (based on P_3 = 6.14 dBm). The 12 bars correspond left-to-right to cores #1, #4, #5, #6, #9, #10, #23, #24, #27, #28, #29 and #32.

Figure 9.20 presents the experimental results for the subregion method under the same target beam configuration as in Figure 9.19. Figure 9.20 (a) shows the generated sub-beam array, where the eight peripheral beams visibly deviate from their intended positions. Despite applying a modified color range, these beams remain faint or undetectable in the coupled output image. Figure 9.20 (b) provides the corresponding statistical analysis, indicating a uniformity of σ_p = 9.14% and energy efficiency η_p = 83.89%. Figure 9.20 (c) captures the actual output from the 32-core fibre. The intensity scale has been adjusted to highlight weaker outputs; nevertheless, the eight outermost cores exhibit no detectable signal. This suggests that the corresponding beams were not coupled into the intended fibre cores, likely due to spatial misalignment caused by inaccurate beam positioning, as seen in (a). The output energy distribution is summarized in Figure 9.20 (d), where only four spots show significant intensity, yielding a coupling efficiency of η = 5.22%. The measured output power in this case is P_3 = 0.8 dBm, indicating a notable degradation in coupling performance compared to the overlap method.

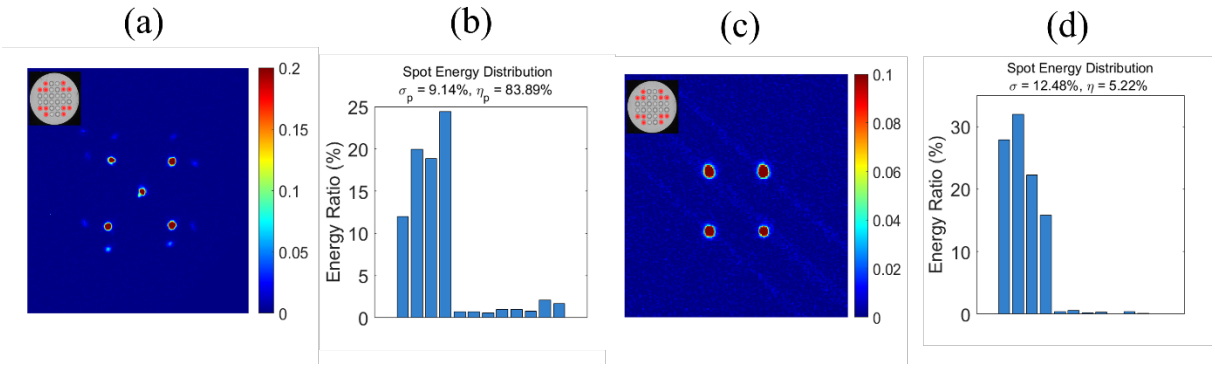

Figure 9.20 Experimental results using the subregion method for coupling into a selected 12-core configuration. (a) SLM-generated sub-beam array, with the target pattern indicated in the inset (four corner beams omitted by design). The eight outer beams exhibit noticeable spatial deviation from intended positions. (b) Energy distribution analysis of the 12 generated sub-beams, with σ_{p} = 9.14%, η_p= 83.89%. (c) Output intensity image from the 32-core fibre. Despite contrast adjustment, the outer eight cores show no detectable output, confirming failed coupling. (d) Statistical analysis of coupled output beams, revealing significant energy imbalance with σ = 12.48%, η = 5.22%. The measured coupled power is P_3 = 0.8 dBm. The 12 bars in (b) and (d) correspond left-to-right to cores #1, #4, #5, #6, #9, #10, #23, #24, #27, #28, #29 and #32.

To experimentally evaluate the hybrid modulation strategy, a 4×4 sub-beam array (excluding the four corner beams) was generated on the SLM using the same target configuration as in previous experiments. The resulting pattern is shown in Figure 9.21, where the inset illustrates the corresponding target cores in the 32-core fibre. As observed, the central zeroth-order diffraction spot dominates the intensity distribution, overwhelming the surrounding sub-beams. This strong residual beam indicates that the hybrid method suffers from ineffective phase modulation, resulting in poor energy allocation to the target beams. Unlike the overlap and subregion methods, where the pattern efficiency η_{p} exceeded 80%, the hybrid method fails to concentrate energy into the desired locations. Consequently, the power ratio between the zeroth-order and the target beams could not be accurately extracted, and no further coupling experiments were performed for this method due to its subpar performance.

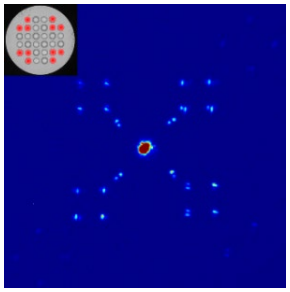

Figure 9.21 Sub-beam array generated by the hybrid method. A 4×4 beam array (excluding corners) was produced using the hybrid modulation strategy. The inset indicates the corresponding core positions in the 32-core fibre. The zeroth-order diffraction is significantly stronger than the target beams, preventing a meaningful evaluation of pattern efficiency. This strong central spot reflects the poor modulation performance of the hybrid method. As a result, no coupling tests were conducted for this configuration.

The experimental results clearly validate the distinct performance characteristics of the three beam modulation strategies. Among them, the overlap method exhibits the most balanced performance, achieving both high pattern uniformity and coupling efficiency. Even for beam arrays with large spatial offsets, this method maintains robust energy allocation and coherence, making it ideal for precise MCF excitation. The subregion method, while offering relatively high efficiency in generating multiple beams, is highly sensitive to spatial alignment errors and beam shape variations. This sensitivity results in positional deviations of the outer beams, leading to coupling failures in several outer cores, as confirmed by the absence of signal in the corresponding output positions. The hybrid method, though conceptually designed to combine the strengths of overlap and subregion encoding, performed the worst in practice. Its inability to effectively suppress the zeroth-order diffraction beam significantly reduced usable energy for the target sub-beams. Consequently, no meaningful coupling results were obtained. Based on these findings, the overlap strategy is selected as the sole method for subsequent experiments involving full-core coupling into the 32-core fibre.

To further evaluate the practical performance of the overlap method, a full 32-core excitation pattern was generated and coupled into the 32-core fibre. Figure 9.22 (a) shows the SLM-generated sub-beam array at the focal plane. The central zeroth-order diffraction spot partially overlaps with one of the sub-beams, making it difficult to distinguish and quantify the energy assigned to that beam. As a result, both η_p and σ_{p} are not provided in Figure 9.22 (b). Nonetheless, the qualitative uniformity of the pattern indicates a generally well-distributed energy allocation. This overlap issue also highlights the need for introducing a global offset to the entire sub-beam array in future implementations, so as to spatially separate the signal beams from the zeroth-order diffraction. Figure 9.22 (c) displays the output of the 32-core fibre, with all cores clearly

activated. The corresponding energy distribution in Figure 9.22 (d) shows σ = 1.80% and η = 18.37%, reflecting satisfactory overall uniformity and coupling efficiency despite the central interference.

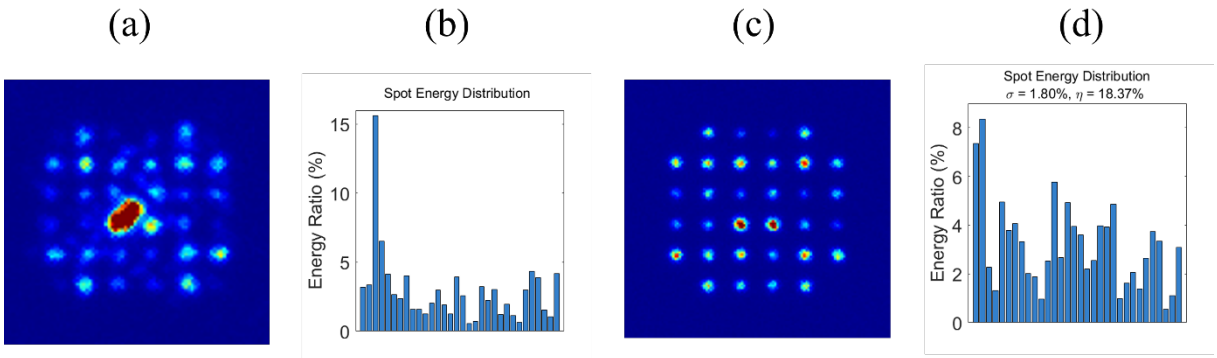

Figure 9.22 Experimental demonstration of full 32-core excitation using the overlap method. (a) SLM-generated sub-beam array at the focal plane. The zeroth-order diffraction overlaps with a signal beam, obscuring accurate energy estimation. (b) Statistical energy distribution of the generated pattern. Both η_p and σ_p are omitted due to the overlap. (c) Output from the 32-core fibre showing successful coupling across all cores. (d) Statistical energy distribution of output spots; σ = 1.80%, η = 18.37%. The 32 bars correspond left-to-right to cores from #1 to #32. This result also indicates that future designs should incorporate a global shift to the sub-beam array to avoid interference from the zeroth-order component.

9.6 Conclusion

This chapter presented a systematic investigation into multi-beam generation and fibre coupling strategies for a 32-core MCF using a phase-only SLM. By leveraging the Fourier transform relationship between the SLM plane and the focal plane, programmable phase masks were employed to steer and distribute optical beams with high spatial precision.

Three beam modulation strategies were explored and compared: 1. Overlap Method: Offers high beam quality and spatial coherence but is highly sensitive to coherent interference. With appropriate phase management, it provides the best balance between energy efficiency and power uniformity. 2. Subregion Method: Achieves robust suppression of interference by spatially decoupling encoding regions, but suffers from beam distortion, aperture clipping, and strong sensitivity to input beam profile and alignment. 3. Hybrid Method: Aims to combine the advantages of the previous two methods but yields poor practical performance, exhibiting residual interference, degraded beam quality, and low efficiency. Through simulation and experimental validation, the overlap method with optimized phase management was found to

deliver the most reliable performance in generating dense, high-fidelity beam arrays. Experimental implementation demonstrated successful coupling into all 32 fibre cores with a total coupling efficiency of η = 18.37% and a standard deviation of power uniformity σ = 1.80%, confirming the effectiveness of the proposed system under realistic conditions.

These findings establish a solid foundation for advanced spatial beam control in MCF-based systems and pave the way for future research into dynamic beam steering, real-time feedback control, and adaptive modulation techniques for complex beam shaping tasks. However, none of the three methods examined in this chapter is readily compatible with CBC under the current optical configuration based on a single Gaussian input beam. This limitation arises from the need for precise and stable phase control across multiple sub-beams, which is hindered by interference management strategies that compromise phase consistency and beam fidelity. The realization of CBC in MCF architectures will thus require the development of new optical designs that can support phase-stable, high-quality beam arrays, potentially through the integration of adaptive feedback, stochastic parallel gradient descent optimization algorithm, or machine learning algorithms.

Chapter 10 Conclusion and future work

10.1 Summary of the thesis

This thesis has explored the design, optimization, and extension of MOs as a pathway toward high-energy femtosecond fibre lasers. A unifying numerical framework was first developed based on the GNLSE, incorporating both steady-state and dynamic gain models together with split-step Fourier and Runge–Kutta solvers. This framework clarified the limitations of the steady-state approximation and demonstrated the necessity of dynamic gain modelling at high repetition rates, where incomplete inversion recovery plays a decisive role. On this basis, a 20-MHz MO was realized, delivering pulse energies up to 381 nJ and supporting compression to sub-40 fs durations. Numerical simulations reproduced both spectral and temporal characteristics with high fidelity, validating the predictive capability of the model and enabling systematic cavity optimization. To extend energy scaling toward lower repetition rates, a 1-MHz MO incorporating an NANF was implemented. The intrinsically low dispersion, weak nonlinearity, and broad transmission bandwidth of the NANF enabled effective intracavity chirp management, higher pulse energies, and efficient external compression, resulting in sub-60 fs pulses with >400nJ. Beyond steady-state performance metrics, the thesis investigated the formation dynamics of MOs using single-shot DFT diagnostics. By contrasting steady-state and cold-start conditions, distinct routes toward spectral coherence and pulse-energy buildup were identified, providing new insight into the controllability, reproducibility, and robustness of mode-locking in highly nonlinear fibre systems. In parallel, spatial scaling was addressed through programmable beam shaping with a phase-only spatial light modulator, enabling efficient and uniform excitation of all 32 cores in a multi-core fibre and demonstrating a viable route toward spatially multiplexed ultrafast fibre sources. The demonstrated performance metrics, including hundreds of nanojoules pulse energy, sub-50 fs pulse durations, and operation from the MHz to tens-of-MHz repetition-rate regime, are well aligned with the requirements of a range of application domains, including multiphoton microscopy and biological imaging, ultrafast spectroscopy, and precision materials processing. In particular, the combination of high peak power, flexible repetition-rate scaling, and fibre-based delivery enabled by NANFs is attractive for applications requiring compact, alignment-tolerant, and robust ultrafast sources. Furthermore, the insights gained into startup dynamics and coherence control are directly relevant to applications where operational stability and reproducibility are critical, such as medical imaging and industrial deployment.

In conclusion, this work establishes practical design strategies for Mamyshev oscillators spanning gain modelling, dispersion engineering, repetition-rate scaling, and diagnostic-guided optimization. Together with the demonstrated advances in temporal and spatial scaling, these

results provide a solid foundation for the future development of ultrafast fibre lasers and their translation toward multi-core architectures and application-driven systems in science, medicine, and advanced manufacturing.

10.2 Future work

10.2.1 Dispersive Fourier transform for MO startup dynamics

A natural extension of the present work is to apply DFT to investigate the startup dynamics of MOs operating at a lower repetition rate, such as 1 MHz. By modulating the repetition rate of the injected seed pulses, one can realize synchronous injection, second-harmonic injection, and higher-order harmonic injection. This would enable systematic studies of seed competition under the gain landscape of the MO, particularly when the pump-induced inversion dynamics are taken into account. In the short term, this work could contribute to optimized single-pulse startup strategies for low-repetition-rate MOs. In the longer term, it could serve as a platform for exploring the role of periodic external perturbations in nonlinear dynamical systems.

10.2.2 Toward high-energy all-fibre low-repetition-rate Mamyshev oscillators

Current all-fibre Mamyshev oscillator (MO) architectures typically rely on amplifier stages with core diameters of approximately 10 μm, which limits the achievable pulse energy to around 150 nJ. Building on the present work, the adoption of large-mode-area (LMA) fibres, such as PLMA 25/250 or PLMA-YDF 25/250, represents a promising route toward further energy scaling while maintaining an all-fibre architecture. Larger mode areas reduce nonlinear phase accumulation and enable higher pulse energies, while also improving mode-field compatibility with hollow-core fibres. A key step toward a fully fibreized high-energy MO is the seamless integration of anti-resonant NANFs with LMA gain and passive fibres. Achieving reliable, low-loss, and low-back-reflection splicing between NANFs and fibres such as PM25/250 or PLMA-YDF 25/250 remains a central technical challenge. Such splices must preserve beam quality, minimize Fresnel reflections that can destabilize mode-locking, and ensure long-term mechanical and environmental stability. Further improvements in system robustness could be realized through the development of PM-NANFs, which would enable better control of the intracavity polarization state and reduce sensitivity to environmental perturbations. In addition, the practicality of a fully fibreized MO platform would be greatly improved by developing dispersion-tuning techniques for NANFs, enabling a tunable, NANF-based pulse compressor. This requires controllable dispersion engineering and reliable tuning mechanisms that preserve the low nonlinearity, broad transmission bandwidth, and high-power handling capability of the NANF while allowing precise adjustment of the delivered pulse chirp. Addressing these challenges would enable a fully

fibreized Mamyshev oscillator platform combining high pulse energy, efficient compression, and robust operation without free-space optics. Such a system would be highly attractive for applications requiring compact, alignment-free, and high-performance ultrafast fibre laser sources.

10.2.3 MCF integration for energy scaling and coherent combining

A further avenue for energy scaling is to incorporate MCFs into the amplification stage of MOs. Two complementary strategies can be envisioned. First, MCFs may be directly embedded in the MO cavity, where the presence of multiple cores can substantially increase the effective mode area, thereby enabling higher pulse energies without sacrificing beam quality. Second, extrinsic amplification schemes: MCF-based gain-managed amplification (GMA) can be employed. GMA, a technique that harnesses the spectral evolution of chirped pulses under strong normal dispersion and nonlinearity, has recently been recognized as a powerful route toward high-energy ultrashort pulse generation. Its conceptual similarity to the nonlinear spectral filtering in MOs. Furthermore, MCFs offer a natural platform for CBC, where multiple amplified channels can be phase-locked to generate ultrashort pulses with energies well beyond the single-core limit. Furthermore, it can achieve customized output of vector beams. Collectively, these strategies may open a path toward a new class of fibre-based ultrafast lasers that are simultaneously compact, scalable, and capable of delivering extreme pulse parameters.

10.2.4 Machine learning-assisted optimization and control

Given the strongly nonlinear and history-dependent nature of the Mamyshev oscillator (MO), conventional optimization strategies based on parameter scanning or local feedback control often become inefficient or unreliable. The system response is frequently non-smooth and path-dependent, with multiple coexisting operating states that cannot be uniquely identified by instantaneous output metrics alone. Similar challenges arise in coherent beam combining (CBC) systems, where a large number of coupled degrees of freedom and the presence of multiple local optima complicate stable and rapid convergence using model-based control. In this context, machine learning techniques offer a fundamentally different approach by enabling data-driven mappings between observable system outputs and control actions without requiring an explicit, tractable physical model. For example, neural networks could be trained to correlate spectral or time–frequency diagnostics with optimal adjustments of cavity parameters such as pump power, spectral filtering, or phase bias, thereby accelerating the identification of favorable operating regimes. In CBC architectures, learning-based controllers could assist in stabilizing relative phases or mitigating slow environmental drifts by exploiting correlations that are difficult to capture with conventional control algorithms. Nevertheless, the applicability of such approaches

is subject to important limitations. The presence of abrupt transitions between distinct dynamical states implies that large and diverse training datasets are required to adequately sample the relevant regions of parameter space. Generalization beyond the trained operating conditions remains challenging, particularly when the system crosses bifurcation boundaries or enters new attractor regimes. Moreover, the limited interpretability of many neural-network-based models may obscure the underlying physical mechanisms governing pulse formation and stability. Finally, practical deployment in experimental systems must contend with constraints imposed by measurement noise, actuator bandwidth, and control-loop latency, which may limit the achievable performance gains in real-time operation.

10.3 Conclusion

In summary, the proposed future work spans a broad spectrum, ranging from fundamental investigations of MO startup dynamics using DFT to practical strategies for energy scaling through all-fibre architectures, MCF integration, and coherent combining. In parallel, the incorporation of machine learning approaches offers a forward-looking route to address the challenges of nonlinear optimization and feedback control. Collectively, these directions not only promise to deepen the physical understanding of MOs but also pave the way toward compact, robust, and high-energy ultrafast fibre laser systems.

Appendix A List of publications

A.1 Journal Publications

1. **Yan, J.**, et al., Chirp‐Managed, High‐Energy, Low‐Repetition Mamyshev Oscillator Based on Hollow Core Fibre. Laser & Photonics Reviews, 2025. 19(7): p. 2401910.

2. **Yan, J.**, et al., High-performance pulse compression for ytterbium-fibre Mamyshev oscillator through anti-resonant hollow-core fibre. Optics & Laser Technology, 2025. 192: p. 113859.

A.2 Conference Publications

1. **Yan, J.**, et al. 1-MHz 500-nJ Mamyshev Oscillator with Hollow Core Fibre. in CLEO 2024. 2024. Charlotte, North Carolina: Optica Publishing Group.

2. **Yan, J.**, et al. Efficient Anti-Resonant Hollow-Core Fibre-Based Pulse Compressor for High-Energy Ytterbium Fibre Laser. in 2025 Conference on Lasers and Electro-Optics Europe & European Quantum Electronics Conference (CLEO/Europe-EQEC). 2025.

List of References

[1] Zipfel, W.R., R.M. Williams, and W.W. Webb, *Nonlinear magic: multiphoton microscopy in the biosciences*. Nature biotechnology, 2003. **21**(11): p. 1369-1377.

[2] Crespi, A., et al., *Integrated multimode interferometers with arbitrary designs for photonic boson sampling*. Nature photonics, 2013. **7**(7): p. 545-549.

[3] Devadas, M.S., et al., *Imaging nano-objects by linear and nonlinear optical absorption microscopies*. Nanotechnology, 2015. **26**(35): p. 354001.

[4] Cao, T., et al., *Femtosecond Laser Assisted Chemical Ionization Mass Spectrometry: Toward Sub-ppq Detection Limits for Organic Molecules*. Analytical Chemistry, 2024. **96**(43): p. 17235-17243.

[5] Weber, R., et al., *Heat accumulation during pulsed laser materials processing*. Optics express, 2014. **22**(9): p. 11312-11324.

[6] Wang, T. and C. Xu, *Three-photon neuronal imaging in deep mouse brain*. Optica, 2020. **7**(8): p. 947-960.

[7] Macias-Romero, C., et al., *Wide-field medium-repetition-rate multiphoton microscopy reduces photodamage of living cells*. Biomedical optics express, 2016. **7**(4): p. 1458-1467.

[8] Liu, W., et al., *Femtosecond Mamyshev oscillator with 10-MW-level peak power*. Optica, 2019. **6**(2): p. 194-197.

[9] Lin, D., et al., *The generation of 1.2 μJ pulses from a Mamyshev oscillator based on a high concentration, large-mode-area Yb-doped fibre*. Journal of Lightwave Technology, 2022. **40**(21): p. 7175-7179.

[10] Petrovich, M., et al., *Broadband optical fibre with an attenuation lower than 0.1 decibel per kilometre*. Nature Photonics, 2025: p. 1-6.

[11] Maiman, T.H., *Stimulated Optical Radiation in Ruby*. Nature, 1960. **187**(4736): p. 493-494.

[12] Einstein, A., *Strahlung-Emission und-Absorption nach der Quantentheorie*. Verh. d. Deutsche Physik. Ges., 1916. **18**: p. 318-328.

[13] Javan, A., W.R. Bennett, and D.R. Herriott, *Population Inversion and Continuous Optical Maser Oscillation in a Gas Discharge Containing a He-Ne Mixture*. Physical Review Letters, 1961. **6**(3): p. 106-110.

[14] Purohit, G., *Overview of lasers*. Applied Innovative Research, 2020. **2**: p. 193-203.

[15] Ishikawa, M., et al., *High-power visible semiconductor lasers*. Optics, Electro-Optics, and Laser Applications in Science and Engineering. Vol. 1418. 1991: SPIE.

[16] He, W.L., et al., *A systematic review and meta-analysis on the efficacy of low-level laser therapy in the management of complication after mandibular third molar surgery*. Lasers in Medical Science, 2015. **30**(6): p. 1779-1788.

[17] Metwally, S.A., B.H.A. Leila, and M.S. Gaballah, *Laser application in agriculture and its physiological effect on plant: a review*. 2020.

[18] Geusic, J., H. Marcos, and L. Van Uitert, *Laser oscillations in Nd - doped yttrium aluminum, yttrium gallium and gadolinium garnets*. Applied Physics Letters, 1964. **4**(10): p. 182-184.

[19] Byer, R.L., *Diode laser—pumped solid-state lasers*. Science, 1988. **239**(4841): p. 742-747.

[20] Cho, C.Y., et al., *24-W cryogenically cooled Nd:YAG monolithic 946-nm laser with a slope efficiency >70%*. Optics Express, 2015. **23**(8): p. 10126-10131.

[21] Allan, R., *Industry: Lasers in the factory: Nd: YAG and CO2 lasers are growing in popularity for cutting, drilling, welding, scribing, and heat-treating a host of metals and nonmetals*. IEEE spectrum, 1979. **16**(5): p. 42-51.

[22] Dubey, A.K. and V. Yadava, *Experimental study of Nd: YAG laser beam machining—An overview*. Journal of materials processing technology, 2008. **195**(1-3): p. 15-26.

[23] Myers, T. and J. McDaniel, *The pulsed Nd: YAG dental laser: review of clinical applications*. Journal of the California Dental Association, 1991. **19**(11): p. 25-30.

[24] Modena, D.A.O., et al., *Efficacy and safety of ND:YAG 1064 nm lasers for photoepilation: a systematic review*. Lasers in Medical Science, 2020. **35**(4): p. 797-806.

[25] Patel, C.K.N., *Continuous-Wave Laser Action on Vibrational-Rotational Transitions of C${\mathrm{O}}_{2}$*. Physical Review, 1964. **136**(5A): p. A1187-A1193.

[26] Gerry, E.T., *Gasdynamic lasers*. IEEE spectrum, 1970. **7**(11): p. 51-58.

[27] DeMaria, A.J., *Review of CW high-power CO 2 lasers*. Proceedings of the IEEE, 2005. **61**(6): p. 731-748.

[28] Duley, W., *CO2 lasers effects and applications*. 2012.

[29] Mushtaq, R.T., et al., *State-Of-The-Art and Trends in CO2 Laser Cutting of Polymeric Materials—A Review*. Materials, 2020. **13**(17): p. 3839.

[30] Umroh, B., A. Ginting, and M.N.A. Rahman, *CO2 laser machining on alumina ceramic: a review*. IOP Conference Series: Materials Science and Engineering, 2020. **1003**(1): p. 012131.

[31] Basov, N.G., V. Danilychev, and Y.M. Popov, *Stimulated emission in the vacuum ultraviolet region*. Soviet Journal of quantum electronics, 1971. **1**(1): p. 18.

[32] Stamm, U., et al. *Recent developments in industrial excimer laser technology*. in *XI International Symposium on Gas Flow and Chemical Lasers and High-Power Laser Conference*. 1997. SPIE.

[33] Jain, K., *Advances in excimer laser lithography*. Lasers in Microlithography, 1987. **774**: p. 115-123.

[34] Jain, K., C. Willson, and B. Lin, *Ultrafast deep UV lithography with excimer lasers*. IEEE Electron Device Letters, 2005. **3**(3): p. 53-55.

[35] Levinson, H.J., *High-NA EUV lithography: current status and outlook for the future*. Japanese Journal of Applied Physics, 2022. **61**(SD): p. SD0803.

[36] Pfleging, W., M. Przybylski, and H. Brückner, *Excimer laser material processing: state-of-the-art and new approaches in microsystem technology*. Laser-based Micropackaging, 2006. **6107**: p. 144-158.

[37] Trokel, S.L., R. Srinivasan, and B. Braren, *Excimer laser surgery of the cornea*. American journal of ophthalmology, 1983. **96**(6): p. 710-715.

[38] Pidro, A., et al., *Excimer lasers in refractive surgery*. Acta Informatica Medica, 2019. **27**(4): p. 278.

[39] Sorokin, P.P. and J.R. Lankard, *Stimulated Emission Observed from an Organic Dye, Chloro-aluminum Phthalocyanine*. IBM Journal of Research and Development, 1966. **10**(2): p. 162-163.

[40] Schäfer, F.P., W. Schmidt, and J. Volze, *Organic dye solution laser*. Applied Physics Letters, 1966. **9**(8): p. 306-309.

[41] Soffer, B. and B. McFarland, *Continuously tunable, narrow - band organic dye lasers*. Applied physics letters, 1967. **10**(10): p. 266-267.

[42] Hänsch, T.W., *Repetitively Pulsed Tunable Dye Laser for High Resolution Spectroscopy*. Applied Optics, 1972. **11**(4): p. 895-898.

[43] Ippen, E., C. Shank, and A. Dienes, *Passive mode locking of the cw dye laser*. Applied Physics Letters, 1972. **21**(8): p. 348-350.

[44] Fork, R., B. Greene, and C.V. Shank. *Generation of optical pulses shorter than 0.1 psec by colliding pulse mode-locking*. in *Conference on Lasers and Electro-Optics*. 1981. Optica Publishing Group.

[45] Fattahi, H., et al., *Third-generation femtosecond technology*. Optica, 2014. **1**(1): p. 45-63.

[46] Moulton, P.F., *Spectroscopic and laser characteristics of Ti:Al2O3*. Journal of the Optical Society of America B, 1986. **3**(1): p. 125-133.

[47] Spence, D.E., P.N. Kean, and W. Sibbett, *60-fsec pulse generation from a self-mode-locked Ti:sapphire laser*. Optics Letters, 1991. **16**(1): p. 42-44.

[48] Ell, R., et al., *Generation of 5-fs pulses and octave-spanning spectra directly from a Ti: sapphire laser*. Optics letters, 2001. **26**(6): p. 373-375.

[49] Li, W., et al., *339 J high-energy Ti: sapphire chirped-pulse amplifier for 10 PW laser facility*. Optics letters, 2018. **43**(22): p. 5681-5684.

[50] Lureau, F., et al., *High-energy hybrid femtosecond laser system demonstrating 2× 10 PW capability*. High Power Laser Science and Engineering, 2020. **8**: p. e43.

[51] Holonyak, N. and S. Bevacqua, *COHERENT (VISIBLE) LIGHT EMISSION FROM Ga (As1−xPx) JUNCTIONS*. Applied Physics Letters, 1962. **1**(4): p. 82-83.

[52] Hall, R.N., et al., *Coherent light emission from GaAs junctions*. Physical Review Letters, 1962. **9**(9): p. 366.

[53] Ujager, F.S., S. Zaidi, and U. Younis. *A review of semiconductor lasers for optical communications*. in *7th International Symposium on High-capacity Optical Networks and Enabling Technologies*. 2010. IEEE.

[54] Mehuys, D.G., *High-power semiconductor lasers*. Semiconductor Lasers II, 1999: p. 259-321.

[55] Latham, W.P., et al., *High-power semiconductor lasers: applications and progress*. Advanced High-Power Lasers, 2000. **3889**: p. 34-44.

[56] Deacon, D.A., et al., *First operation of a free-electron laser*. Physical Review Letters, 1977. **38**(16): p. 892.

[57] Freund, H.P. and T.M. Antonsen, *Principles of free-electron lasers*. 1992: Springer.

[58] O'Shea, P.G. and H.P. Freund, *Free-electron lasers: Status and applications*. Science, 2001. **292**(5523): p. 1853-1858.

[59] Seddon, E., et al., *Short-wavelength free-electron laser sources and science: a review*. Reports on Progress in Physics, 2017. **80**(11): p. 115901.

[60] Snitzer, E., *Proposed fibre cavities for optical masers*. Journal of Applied Physics, 1961. **32**(1): p. 36-39.

[61] Snitzer, E., *Optical maser action of Nd+ 3 in a barium crown glass*. Physical review letters, 1961. **7**(12): p. 444.

[62] Koester, C.J. and E. Snitzer, *Amplification in a Fibre Laser*. Applied Optics, 1964. **3**(10): p. 1182-1186.

[63] Kao, K.C. and G.A. Hockham. *Dielectric-fibre surface waveguides for optical frequencies*. in *Proceedings of the Institution of Electrical Engineers*. 1966. IET.

[64] Kapron, F.P., D.B. Keck, and R.D. Maurer, *Radiation losses in glass optical waveguides*. Applied Physics Letters, 1970. **17**(10): p. 423-425.

[65] Poole, S., D.N. Payne, and M.E. Fermann, *Fabrication of low-loss optical fibres containing rare-earth ions*. Electronics Letters, 1985. **21**(17): p. 737-738.

[66] Mears, R., et al., *Neodymium-doped silica single-mode fibre lasers*. Electronics letters, 1985. **21**(17): p. 738-740.

[67] Mears, R.J., et al., *Low-noise erbium-doped fibre amplifier operating at 1.54 μm*. Electronics Letters, 1987. **23**(19): p. 1026-1028.

[68] Richardson, D.J., J. Nilsson, and W.A. Clarkson, *High power fibre lasers: current status and future perspectives [Invited]*. Journal of the Optical Society of America B, 2010. **27**(11): p. B63-B92.

[69] Snitzer, E., et al. *Double clad, offset core Nd fibre laser*. in *Optical fibre sensors*. 1988. Optica Publishing Group.

[70] Maurer, R., *Optical waveguide light source*. 1974, Google Patents.

[71] Kafka, J.D., *Laser diode pumped fibre lasers with pump cavity*. 1989, Google Patents.

[72] Osowski, M., et al. *Advances in high-brightness semiconductor lasers*. in *Laser Source Technology for Defense and Security IV*. 2008. SPIE.

[73] Pask, H., et al., *Ytterbium-doped silica fibre lasers: versatile sources for the 1-1.2/spl mu/m region*. IEEE Journal of Selected Topics in Quantum Electronics, 1995. **1**(1): p. 2-13.

[74] Paschotta, R., et al., *Ytterbium-doped fibre amplifiers*. IEEE Journal of quantum electronics, 2002. **33**(7): p. 1049-1056.

[75] Dominic, V., et al., *110 W fibre laser*. Electronics letters, 1999. **35**(14): p. 1158-1160.

[76] Minelly, J., et al. *High-gain fibre power amplifier tandem-pumped by a 3-W multistripe diode*. in *Optical Fibre Communication Conference*. 1992. Optica Publishing Group.

[77] Jeong, Y., et al. *Ytterbium-doped large-core fibre laser with 1 kW continuous-wave output power*. in *Advanced Solid-State Photonics*. 2004. Optica Publishing Group.

[78] Stiles, E. *New developments in IPG fibre laser technology*. in *Proceedings of the 5th International Workshop on Fibre Lasers*. 2009.

[79] Du, S., et al., *10 kW Fibre Amplifier Seeded by Random Fibre Laser With Suppression of Spectral Broadening and SRS*. IEEE Photonics Technology Letters, 2022. **34**(14): p. 721-724.

[80] Boyd, R.W., A.L. Gaeta, and E. Giese, *Nonlinear Optics*, in *Springer Handbook of Atomic, Molecular, and Optical Physics*, G.W.F. Drake, Editor. 2023, Springer International Publishing: Cham. p. 1097-1110.

[81] Krause, J.L., K.J. Schafer, and K.C. Kulander, *High-order harmonic generation from atoms and ions in the high intensity regime*. Physical Review Letters, 1992. **68**(24): p. 3535-3538.

[82] Macklin, J.J., J.D. Kmetec, and C.L. Gordon, *High-order harmonic generation using intense femtosecond pulses*. Physical Review Letters, 1993. **70**(6): p. 766-769.

[83] Ghimire, S., et al., *Observation of high-order harmonic generation in a bulk crystal*. Nature Physics, 2011. **7**(2): p. 138-141.

[84] Phillips, K.C., et al., *Ultrafast laser processing of materials: a review*. Advances in Optics and Photonics, 2015. **7**(4): p. 684-712.

[85] Malinauskas, M., et al., *Ultrafast laser processing of materials: from science to industry*. Light: Science & Applications, 2016. **5**(8): p. e16133-e16133.

[86] Hargrove, L., R.L. Fork, and M. Pollack, *Locking of He–Ne laser modes induced by synchronous intracavity modulation*. Applied Physics Letters, 1964. **5**(1): p. 4-5.

[87] Kuizenga, D.J. and A.E. Siegman, *FM and AM mode locking of the homogeneous laser. Part I. Theory*. IEEE J. Quant. Electron.; (United States), 1970. **QE-6:11**(None; Journal ID: ISSN IEJQA).

[88] Kuizenga, D.J. and A.E. Siegman, *FM and AM mode locking of the homogeneous laser. Part II. Experimental results in a Nd:YAG laser with internal FM modulation*. IEEE J. Quant. Electron.; (United States), 1970. **QE-6:11**(None; Journal ID: ISSN IEJQA).

[89] Haus, H., *A theory of forced mode locking*. IEEE Journal of Quantum Electronics, 1975. **11**(None; Journal ID: ISSN 0018-9197).

[90] Ishida, Y., N. Sarukura, and H. Nakano. *Soliton-like Pulse Shaping in cw Passively Mode-Locked Ti:Al2O3 Laser*. in *Ultrafast Phenomena*. 1990. Monterey, California: Optica Publishing Group.

[91] Stingl, A., et al., *Sub-10-fs mirror-dispersion-controlled Ti: sapphire laser*. Optics letters, 1995. **20**(6): p. 602-604.

[92] Maiuri, M., M. Garavelli, and G. Cerullo, *Ultrafast Spectroscopy: State of the Art and Open Challenges*. Journal of the American Chemical Society, 2020. **142**(1): p. 3-15.

[93] Keller, U., *Recent developments in compact ultrafast lasers*. Nature, 2003. **424**(6950): p. 831-838.

[94] Strickland, D. and G. Mourou, *Compression of amplified chirped optical pulses*. Optics communications, 1985. **55**(6): p. 447-449.

[95] Liu, J., et al., *Diode-pumped high energy and high average power all-solid-state picosecond amplifier systems*. Applied Sciences, 2015. **5**(4): p. 1590-1602.

[96] Reagan, B.A., et al. *Demonstration of a 1 Joule, 500 W average power picosecond laser*. in *Solid State Lasers XXVI: Technology and Devices*. 2017. SPIE.

[97] Denk, W., J.H. Strickler, and W.W. Webb, *Two-photon laser scanning fluorescence microscopy*. Science, 1990. **248**(4951): p. 73-76.

[98] Cundiff, S.T. and J. Ye, *Colloquium: Femtosecond optical frequency combs*. Reviews of Modern Physics, 2003. **75**(1): p. 325.

[99] Hänsch, T.W., *Nobel lecture: passion for precision*. Reviews of Modern Physics, 2006. **78**(4): p. 1297-1309.

[100] Krausz, F. and M. Ivanov, *Attosecond physics*. Reviews of modern physics, 2009. **81**(1): p. 163-234.

[101] Mourou, G.A., T. Tajima, and S.V. Bulanov, *Optics in the relativistic regime*. Reviews of modern physics, 2006. **78**(2): p. 309-371.

[102] Bueno, J.M., F.J. Ávila, and P. Artal, *Comparing the performance of a femto fibre-based laser and a Ti:sapphire used for multiphoton microscopy applications*. Applied Optics, 2019. **58**(14): p. 3830-3835.

[103] Fermann, M.E. and I. Hartl, *Ultrafast fibre lasers*. Nature Photonics, 2013. **7**(11): p. 868-874.

[104] Ranka, J.K., R.S. Windeler, and A.J. Stentz, *Visible continuum generation in air–silica microstructure optical fibres with anomalous dispersion at 800 nm*. Optics letters, 2000. **25**(1): p. 25-27.

[105] Agrawal, G.P., *Nonlinear fibre optics*, in *Nonlinear Science at the Dawn of the 21st Century*. 2000, Springer. p. 195-211.

[106] Clarkson, W., *Thermal effects and their mitigation in end-pumped solid-statelasers*. Journal of Physics D: Applied Physics, 2001. **34**(16): p. 2381.

[107] Jauregui, C., J. Limpert, and A. Tünnermann, *High-power fibre lasers*. Nature photonics, 2013. **7**(11): p. 861-867.

[108] Dzhibladze, M.I., et al., *Mode locking in a fibre laser*. Soviet Journal of Quantum Electronics, 1983. **13**(2): p. 245.

[109] Wigley, P., P. French, and J. Taylor, *Mode locking of a continuous wave neodymium doped fibre laser with a linear external cavity*. Electronics Letters, 1990. **26**(16): p. 1238-1240.

[110] Fermann, M., et al., *Femtosecond fibre laser*. Electronics Letters, 1990. **26**(20): p. 1737-1739.

[111] Bingham, S.P., et al. *Output pulse energy from pulsed single-mode fibre amplifiers*. in *Fibre Lasers XXII: Technology and Systems*. 2025. SPIE.

[112] Stock, M., et al. *Generation of high-power femtosecond optical pulses by chirped pulse amplification in erbium doped fibres*. in *Nonlinear Guided-Wave Phenomena*. 1993. Optica Publishing Group.

[113] Chang, G. and Z. Wei, *Ultrafast Fibre Lasers: An Expanding Versatile Toolbox*. iScience, 2020. **23**(5).

[114] Haus, H., *Theory of mode locking with a slow saturable absorber*. IEEE Journal of Quantum Electronics, 2003. **11**(9): p. 736-746.

[115] Tamura, K., H. Haus, and E. Ippen, *Self-starting additive pulse mode-locked erbium fibre ring laser*. Electronics Letters, 1992. **28**(24): p. 2226-2228.

[116] Matsas, V., et al., *Selfstarting passively mode-locked fibre ring soliton laser exploiting nonlinear polarisation rotation*. Electronics Letters, 1992. **28**(15): p. 1391-1393.

[117] Fermann, M., et al., *Passive mode locking by using nonlinear polarization evolution in a polarization-maintaining erbium-doped fibre*. Optics letters, 1993. **18**(11): p. 894-896.

[118] Hofer, M., et al., *Characterization of ultrashort pulse formation in passively mode-locked fibre lasers*. IEEE Journal of Quantum Electronics, 1992. **28**(3): p. 720-728.

[119] Doran, N. and D. Wood, *Nonlinear-optical loop mirror*. Optics letters, 1988. **13**(1): p. 56-58.

[120] Fermann, M.E., et al., *Nonlinear amplifying loop mirror*. Optics Letters, 1990. **15**(13): p. 752-754.

[121] Duling, I.N., *All-fibre ring soliton laser mode locked with a nonlinear mirror*. Optics Letters, 1991. **16**(8): p. 539-541.

[122] Richardson, D.J., et al., *Selfstarting, passively modelocked erbium fibre ring laser based on the amplifying Sagnac switch*. Electronics Letters, 1991. **27**(6): p. 542-544.

[123] Wu, S., et al., *High-power passively mode-locked Er-doped fibre laser with a nonlinear optical loop mirror*. Optics Letters, 1993. **18**(17): p. 1444-1446.

[124] Wang, Y., et al., *Cross-splicing method for compensating fibre birefringence in polarization-maintaining fibre ring laser mode locked by nonlinear polarization evolution*. Applied Optics, 2016. **55**(21): p. 5766-5770.

[125] Keller, U., et al., *Semiconductor saturable absorber mirrors (SESAM's) for femtosecond to nanosecond pulse generation in solid-state lasers*. IEEE Journal of selected topics in QUANTUM ELECTRONICS, 1996. **2**(3): p. 435-453.

[126] Set, S.Y., et al., *Laser mode locking using a saturable absorber incorporating carbon nanotubes*. Journal of lightwave Technology, 2004. **22**(1): p. 51.

[127] Sun, Z., et al., *Graphene mode-locked ultrafast laser*. ACS nano, 2010. **4**(2): p. 803-810.

[128] Jeong, Y.-C., et al., *Multi-kilowatt single-mode ytterbium-doped large-core fibre laser*. Journal of the Optical Society of Korea, 2009. **13**(4): p. 416-422.

[129] Jeong, Y., et al., *Ytterbium-doped large-core fibre laser with 1.36 kW continuous-wave output power*. Optics Express, 2004. **12**(25): p. 6088-6092.

[130] Deng, D., et al., *112-μJ 180-fs pulses at 1-kHz repetition rate from Yb-doped laser based on strictly all-fibre CPA structure*. IEEE Photonics Journal, 2019. **11**(6): p. 1-7.

[131] Wang, T., et al., *High-power femtosecond laser generation from an all-fibre linearly polarized chirped pulse amplifier*. High Power Laser Science and Engineering, 2023. **11**: p. e25.

[132] Röser, F., et al., *Millijoule pulse energy high repetition rate femtosecond fibre chirped-pulse amplification system*. Optics Letters, 2007. **32**(24): p. 3495-3497.

[133] Eidam, T., et al., *Fibre chirped-pulse amplification system emitting 3.8 GW peak power*. Optics Express, 2011. **19**(1): p. 255-260.

[134] Poletti, F., M.N. Petrovich, and D.J. Richardson, *Hollow-core photonic bandgap fibres: technology and applications*. Nanophotonics, 2013. **2**(5-6): p. 315-340.

[135] Chen, Y., et al. *Hollow core DNANF optical fibre with< 0.11 dB/km loss*. in *Optical Fibre Communication Conference*. 2024. Optica Publishing Group.

[136] Nisoli, M., et al., *Compression of high-energy laser pulses below 5 fs*. Optics Letters, 1997. **22**(8): p. 522-524.

[137] Russell, P.S.J., et al., *Hollow-core photonic crystal fibres for gas-based nonlinear optics*. Nature Photonics, 2014. **8**(4): p. 278-286.

[138] Hanna, M., et al., *Coherent combination of ultrafast fibre amplifiers*. Journal of Physics B: Atomic, Molecular and Optical Physics, 2016. **49**(6): p. 062004.

[139] Ramirez, L.P., et al., *Coherent beam combining with an ultrafast multicore Yb-doped fibre amplifier*. Optics Express, 2015. **23**(5): p. 5406-5416.

[140] Klenke, A., et al., *500 W rod-type 4× 4 multicore ultrafast fibre laser*. Optics Letters, 2022. **47**(2): p. 345-348.

[141] Lin, D., et al., *Reconfigurable structured light generation in a multicore fibre amplifier*. Nature Communications, 2020. **11**(1): p. 3986.

[142] Noda, J., K. Okamoto, and Y. Sasaki, *Polarization-maintaining fibres and their applications*. Journal of Lightwave Technology, 2003. **4**(8): p. 1071-1089.

[143] Mollenauer, L.F. and R.H. Stolen, *The soliton laser*. Optics letters, 1984. **9**(1): p. 13-15.

[144] Kelly, S.M. *Characteristic Sideband Instability of the Periodically Amplified (Average) Soliton*. in *International Quantum Electronics Conference*. 1992. Optica Publishing Group.

[145] Mollenauer, L., J. Gordon, and M. Islam, *Soliton propagation in long fibres with periodically compensated loss*. IEEE Journal of Quantum Electronics, 2003. **22**(1): p. 157-173.

[146] Tamura, K., et al., *77-fs pulse generation from a stretched-pulse mode-locked all-fibre ring laser*. Optics letters, 1993. **18**(13): p. 1080-1082.

[147] Nelson, L., et al., *Efficient frequency doubling of a femtosecond fibre laser*. Optics letters, 1996. **21**(21): p. 1759-1761.

[148] Ilday, F., et al., *Self-similar evolution of parabolic pulses in a laser*. Physical review letters, 2004. **92**(21): p. 213902.

[149] Buckley, J., et al., *Femtosecond fibre lasers with pulse energies above 10 nJ*. Optics letters, 2005. **30**(14): p. 1888-1890.

[150] Chong, A., et al., *All-normal-dispersion femtosecond fibre laser*. Optics express, 2006. **14**(21): p. 10095-10100.

[151] Chong, A., W.H. Renninger, and F.W. Wise, *All-normal-dispersion femtosecond fibre laser with pulse energy above 20 nJ*. Optics letters, 2007. **32**(16): p. 2408-2410.

[152] Renninger, W., A. Chong, and F. Wise, *Dissipative solitons in normal-dispersion fibre lasers*. Physical Review A—Atomic, Molecular, and Optical Physics, 2008. **77**(2): p. 023814.

[153] Kieu, K., et al., *Sub-100 fs pulses at watt-level powers from a dissipative-soliton fibre laser.* Optics letters, 2009. **34**(5): p. 593-595.

[154] Piche, M. *Mode locking through nonlinear frequency broadening and spectral filtering*. in *Mode-locked and Other Ultrashort Laser Designs, Amplifiers, and Applications*. 1994. SPIE.

[155] Mamyshev, P. *All-optical data regeneration based on self-phase modulation effect*. in *24th European Conference on Optical Communication. ECOC'98 (IEEE Cat. No. 98TH8398)*. 1998. IEEE.

[156] Pitois, S., et al., *Generation of localized pulses from incoherent wave in optical fibre lines made of concatenated Mamyshev regenerators.* Journal of the Optical Society of America B, 2008. **25**(9): p. 1537-1547.

[157] Regelskis, K., et al., *Ytterbium-doped fibre ultrashort pulse generator based on self-phase modulation and alternating spectral filtering.* Optics Letters, 2015. **40**(22): p. 5255-5258.

[158] Liu, Z., et al., *Megawatt peak power from a Mamyshev oscillator.* Optica, 2017. **4**(6): p. 649-654.

[159] Li, Y.-Y., et al., *Generation of High-Peak-Power Femtosecond Pulses in Mamyshev Oscillators: Recent Advances and Future Challenges.* Laser & Photonics Reviews, 2023. **17**(4): p. 2200596.

[160] Sidorenko, P., et al., *Self-seeded, multi-megawatt, Mamyshev oscillator.* Optics Letters, 2018. **43**(11): p. 2672-2675.

[161] Olivier, M., et al., *Femtosecond fibre Mamyshev oscillator at 1550 nm.* Optics letters, 2019. **44**(4): p. 851-854.

[162] Zheng, J.-C., et al., *Low mode-locking threshold and sub-90 fs Er-doped Mamyshev oscillator.* Optics Communications, 2022. **508**: p. 127711.

[163] Wen, X., et al. *Broadband Mamyshev Oscillator at 1.7 μm*. in *CLEO: Fundamental Science*. 2024. Optica Publishing Group.

[164] Tarasov, N., et al., *Mode-locking via dissipative Faraday instability.* Nature Communications, 2016. **7**(1): p. 12441.

[165] Samartsev, I., A. Bordenyuk, and V. Gapontsev. *Environmentally stable seed source for high power ultrafast laser*. in *Components and Packaging for Laser Systems III*. 2017. SPIE.

[166] Wang, T., et al., *Over 80 nJ Sub-100 fs All-Fibre Mamyshev Oscillator.* IEEE Journal of Selected Topics in Quantum Electronics, 2021. **27**(6): p. 1-5.

[167] Haig, H., et al., *Megawatt pulses from an all-fibre and self-starting femtosecond oscillator.* Optics Letters, 2022. **47**(4): p. 762-765.

[168] Wang, T., et al., *All-PM fibre Mamyshev oscillator delivers hundred-nanojoule and multi-watt sub-100 fs pulses*. Ultrafast Science, 2023. **3**.

[169] Yang, S., et al., *All - Fibre 2 μm Mamyshev Oscillator: Mapping of Different Operating Regimes*. Laser & Photonics Reviews, 2025: p. 2500074.

[170] Boulanger, V., et al., *All-fibre Mamyshev oscillator enabled by chirped fibre Bragg gratings*. Optics Letters, 2020. **45**(12): p. 3317-3320.

[171] Luo, X., et al., *All-fibre mode-locked laser based on Mamyshev mechanism with high-energy pulse generation at 1550 nm*. Journal of Lightwave Technology, 2020. **38**(6): p. 1468-1473.

[172] Chen, Y.-H., et al., *Starting dynamics of a linear-cavity femtosecond Mamyshev oscillator*. Journal of the Optical Society of America B, 2021. **38**(3): p. 743-748.

[173] Yan, D., et al., *Pulse dynamic patterns in a self-starting Mamyshev oscillator*. Optics Express, 2021. **29**(7): p. 9805-9815.

[174] Liu, J., et al., *Pulse buildup dynamics in a self-starting Mamyshev oscillator*. Optics Express, 2024. **32**(4): p. 5851-5861.

[175] Li, T.-J., et al., *Revealing the pulse dynamics in a Mamyshev oscillator: from seed signal to oscillator pulse*. Optics Express, 2023. **31**(23): p. 39250-39260.

[176] Xu, Q., et al., *Revealing the Ultrafast Soliton Dynamics in an All-Fibre Self-Starting Er Mamyshev Oscillator*. Journal of Lightwave Technology, 2025. **43**(5): p. 2304-2311.

[177] Dong, Y., et al., *Dynamic characteristics and conversion process of solitons in a Mamyshev oscillator*. Chaos, Solitons & Fractals, 2024. **189**: p. 115667.

[178] Qi, Y., et al., *Dissipative Pure-Quartic Solitons Generation and Evolution Dynamics in a Mamyshev Oscillator*. Journal of Lightwave Technology, 2025. **43**(8): p. 4000-4006.

[179] Nigam, A., et al., *Multipulse operation in Mamyshev oscillator: influence of external seed source*. Laser Physics, 2023. **34**(1): p. 015101.

[180] Ma, K., et al., *Revealing switchable pulse dynamics in an all-fibre Mamyshev oscillator*. Applied Optics, 2025. **64**(19): p. 5325-5332.

[181] Yan, D., et al., *Routes from stationary dissipative solitons to chaos in a Mamyshev oscillator*. Chaos, Solitons & Fractals, 2023. **177**: p. 114250.

[182] Wang, A., et al., *Solitons, bifurcation and chaotics in a bidirectional mamyshev oscillator*. Optics Communications, 2024. **567**: p. 130730.

[183] Ma, C., et al., *Ultrabroadband, few-cycle pulses directly from a Mamyshev fibre oscillator*. Photonics Research, 2020. **8**(1): p. 65-69.

[184] Kang, D., et al., *Sub-10-fs pulse generation from 10 nJ Yb-fibre laser with cascaded nonlinear pulse compression*. Optics Express, 2024. **32**(4): p. 5214-5219.

[185] Luo, X., et al., *Intracavity supercontinuum generation in a mode-locked erbium-doped fibre laser based on the Mamyshev mechanism with highly nonlinear fibre*. Optics Letters, 2020. **45**(9): p. 2530-2533.

[186] Lin, D., et al., *The generation of femtosecond optical vortex beams with megawatt powers directly from a fibre based Mamyshev oscillator*. 2022. **11**(4): p. 847-854.

[187] Xu, H., et al., *Generation of ultrashort cylindrical vector beams from a Mamyshev oscillator*. Optics Letters, 2024. **49**(21): p. 6121-6124.

[188] Cao, B., et al., *Self-starting spatiotemporal mode-locking using Mamyshev regenerators*. Optics Letters, 2022. **47**(17): p. 4584-4587.

[189] Liu, Y., et al., *All-fibre spatiotemporal mode-locked based on Mamyshev mechanism with high energy noise-like pulse generation at 1550 nm*. Optics Communications, 2024. **552**: p. 130074.

[190] Malitson, I.H., *Interspecimen Comparison of the Refractive Index of Fused Silica*,†*. Journal of the Optical Society of America, 1965. **55**(10): p. 1205-1209.

[191] Woodward, R.I., *Dispersion engineering of mode-locked fibre lasers*. Journal of Optics, 2018. **20**(3): p. 033002.

[192] Chang, H., et al., *172-fs, 27-µJ, Yb-doped all-fibre-integrated chirped pulse amplification system based on parabolic evolution by passive spectral amplitude shaping*. Optics Express, 2019. **27**(23): p. 34103-34112.

[193] Guo, K., et al., *Monolithic gain-managed nonlinear fibre amplifier delivering 2.7-μJ ultrashort pulse with broad spectrum seeding*. Optics & Laser Technology, 2025. **192**: p. 113610.

[194] Godin, T., et al., *Recent advances on time-stretch dispersive Fourier transform and its applications*. Advances in Physics: X, 2022. **7**(1): p. 2067487.

[195] Guo, K., et al., *Highly stable Q-switched and mode-locked pulse generation from an all-PM figure-9 fibre laser*. Optics Express, 2022. **30**(20): p. 35636-35646.

[196] Theeg, T., et al. *Side pumping scheme for all-fibre counter-pumping of high power single-frequency fibre amplifiers*. in *2013 Conference on Lasers & Electro-Optics Europe & International Quantum Electronics Conference CLEO EUROPE/IQEC*. 2013.

[197] He, J., et al., *High Peak Power Tunable Visible Source at 550 nm from a Frequency Doubled Nanosecond Yb-doped Fibre MOPA*.

[198] Teh, P.S., et al., *200 W Diffraction limited, single-polarization, all-fibre picosecond MOPA*. Optics Express, 2013. **21**(22): p. 25883-25889.

[199] Sakr, H., et al., *Hollow core optical fibres with comparable attenuation to silica fibres between 600 and 1100 nm*. Nature communications, 2020. **11**(1): p. 6030.

[200] Zhang, Y., et al., *Double-pass pre-chirp managed amplification with high gain and high average power*. Optics Letters, 2021. **46**(13): p. 3115-3118.

[201] Debarre, D., et al., *Mitigating phototoxicity during multiphoton microscopy of live Drosophila embryos in the 1.0–1.2 μ m wavelength range*. PLoS One, 2014. **9**(8): p. e104250.

[202] Yang, P., et al., *Highly stable Yb-fibre laser amplifier of delivering 32-μJ, 153-fs pulses at 1-MHz repetition rate*. Applied Physics B, 2018. **124**(8): p. 169.

[203] Sayinc, H., et al., *Sub-100 fs pulses from a low repetition rate Yb-doped fibre laser*. Optics Express, 2009. **17**(7): p. 5731-5735.

[204] Boivinet, S., et al., *All-Fibre 1-\(\mu\) m PM Mode-Lock Laser Delivering Picosecond Pulses at Sub-MHz Repetition Rate*. IEEE Photonics Technology Letters, 2014. **26**(22): p. 2256-2259.

[205] Mortag, D., et al. *Low repetition rate high-energy fibre oscillator*. in *Conference on Lasers and Electro-Optics*. 2010. Optica Publishing Group.

[206] Erkintalo, M., et al., *Environmentally stable all-PM all-fibre giant chirp oscillator*. Optics express, 2012. **20**(20): p. 22669-22674.

[207] Bowen, P., et al., *Mode-locked Yb-doped fibre laser emitting broadband pulses at ultralow repetition rates*. Optics Letters, 2016. **41**(22): p. 5270-5273.

[208] Olivier, M., et al. *Low repetition rate Yb-doped all-fibre Mamyshev oscillator*. in *2023 Photonics North (PN)*. 2023. IEEE.

[209] Sollapur, R., et al., *Resonance-enhanced multi-octave supercontinuum generation in antiresonant hollow-core fibres*. Light: Science & Applications, 2017. **6**(12): p. e17124-e17124.

[210] Feng, Z., et al., *Stable Optical Frequency Comb Distribution Enabled by Hollow‐Core Fibres*. Laser & Photonics Reviews, 2022. **16**(11): p. 2200167.

[211] Nielsen, C.K., K.G. Jespersen, and S.R. Keiding, *A 158 fs 5.3 nJ fibre-laser system at 1 μm using photonic bandgap fibres for dispersion control and pulse compression*. Optics Express, 2006. **14**(13): p. 6063-6068.

[212] Lekosiotis, A., et al., *On-target delivery of intense ultrafast laser pulses through hollow-core anti-resonant fibres*. Optics express, 2023. **31**(19): p. 30227-30238.

[213] Diels, J.-C. and W. Rudolph, *Ultrashort laser pulse phenomena*. 2006: Elsevier.

[214] Shi, B., et al., *Splicing Hollow-Core Fibre with Standard Glass-Core Fibre with Ultralow Back-Reflection and Low Coupling Loss*. ACS photonics, 2024. **11**(8): p. 3288-3295.

[215] Guo, Q., et al., *Ultrafast mode-locked laser in nanophotonic lithium niobate*. Science, 2023. **382**(6671): p. 708-713.

[216] Cao, B., et al., *Coherence memory and amnesia in a mode-locked Mamyshev oscillator*. Optica, 2024. **11**(12): p. 1673-1681.

[217] Fathi, H., M. Närhi, and R. Gumenyuk, *Towards Ultimate High-Power Scaling: Coherent Beam Combining of Fibre Lasers*. Photonics, 2021. **8**(12): p. 566.

[218] Jain, S., et al., *32-core erbium/ytterbium-doped multicore fibre amplifier for next generation space-division multiplexed transmission system*. Optics Express, 2017. **25**(26): p. 32887-32896.

[219] Forbes, A., A. Dudley, and M. McLaren, *Creation and detection of optical modes with spatial light modulators*. Advances in optics and photonics, 2016. **8**(2): p. 200-227.

[220] Willner, A.E., et al., *Optical communications using orbital angular momentum beams*. Advances in optics and photonics, 2015. **7**(1): p. 66-106.

[221] Maurer, C., et al., *What spatial light modulators can do for optical microscopy*. Laser & Photonics Reviews, 2011. **5**(1): p. 81-101.

[222] Nehmetallah, G. and P.P. Banerjee, *Applications of digital and analog holography in three-dimensional imaging*. Advances in Optics and Photonics, 2012. **4**(4): p. 472-553.

[223] Memmolo, P., et al., *Recent advances in holographic 3D particle tracking*. Advances in Optics and Photonics, 2015. **7**(4): p. 713-755.

[224] Goodman, J.W., *Introduction to Fourier optics*. 2005: Roberts and Company publishers.

[225] Voelz, D.G., *Computational fourier optics: a MATLAB tutorial*. (No Title), 2011: p. 51.

List of References